

N° d'ordre : 04ISAL0035

Année 2004

N° attribué par la bibliothèque

\_\_\_\_/\_\_\_\_/\_\_\_\_/\_\_\_\_/\_\_\_\_/\_\_\_\_/\_\_\_\_/\_\_\_\_/\_\_\_\_/\_\_\_\_/

# THESE

En co-tutelle avec l'université de Helsinki

Présentée devant

**L'INSTITUT NATIONAL DES SCIENCES APPLIQUEES DE LYON**

Pour obtenir

## LE GRADE DE DOCTEUR

**FORMATION DOCTORALE : Images & Systèmes**

**ECOLE DOCTORALE : Electronique, Electrotechnique et Automatique**

Par

**TIMO MÄKELÄ**

Ingénieur de l'université de Technologie de Helsinki

**Titre :**

**Mise en correspondance en imagerie cardiaque multimodale : vers un  
modèle anatomo-fonctionnel individualisé du cœur**

***Directeurs de Thèse :***

Patrick CLARYSSE et Isabelle E. MAGNIN

Soutenue le 05 Juillet 2004 devant la Commission d'Examen

### JURY

M. Philippe CINQUIN  
M. Nicholas AYACHE  
Mme Isabelle E. MAGNIN  
M. Patrick CLARYSSE  
M. Toivo KATILA  
Mme Ulla RUOTSALAINEN

Rapporteur  
Rapporteur  
Directeur de thèse  
Co-Directeur  
Examineur  
Examineur

Mai 2003

## INSTITUT NATIONAL DES SCIENCES APPLIQUEES DE LYON

**Directeur : STORCK A.**

**Professeurs :**

AUDISIO S.	PHYSICOCHEMIE INDUSTRIELLE
BABOT D.	CONT. NON DESTR. PAR RAYONNEMENTS IONISANTS
BABOUX J.C.	GEMPPM***
BALLAND B.	PHYSIQUE DE LA MATIERE
BAPTISTE P.	PRODUCTIQUE ET INFORMATIQUE DES SYSTEMES MANUFACTURIERS
BARBIER D.	PHYSIQUE DE LA MATIERE
BASTIDE J.P.	LAEPSI****
BAYADA G.	MECANIQUE DES CONTACTS
BENADDA B.	LAEPSI****
BETEMPS M.	AUTOMATIQUE INDUSTRIELLE
BIENNIER F.	PRODUCTIQUE ET INFORMATIQUE DES SYSTEMES MANUFACTURIERS
BLANCHARD J.M.	LAEPSI****
BOISSON C.	VIBRATIONS-ACOUSTIQUE
BOIVIN M. (Prof. émérite)	MECANIQUE DES SOLIDES
BOTTA H.	UNITE DE RECHERCHE EN GENIE CIVIL - Développement Urbain
BOTTA-ZIMMERMANN M. (Mme)	UNITE DE RECHERCHE EN GENIE CIVIL - Développement Urbain
BOULAYE G. (Prof. émérite)	INFORMATIQUE
BOYER J.C.	MECANIQUE DES SOLIDES
BRAU J. CENTRE DE THERMIQUE DE LYON - Thermique	du bâtiment
BREMOND G.	PHYSIQUE DE LA MATIERE
BRISAUD M.	GENIE ELECTRIQUE ET FERROELECTRICITE
BRUNET M.	MECANIQUE DES SOLIDES
BRUNIE L.	INGENIERIE DES SYSTEMES D'INFORMATION
BUREAU J.C.	CEGELY*
CAVAILLE J.Y.	GEMPPM***
CHANTE J.P.	CEGELY*- Composants de puissance et applications
CHOCAT B.	UNITE DE RECHERCHE EN GENIE CIVIL - Hydrologie urbaine
COMBESCURE A.	MECANIQUE DES CONTACTS
COUSIN M.	UNITE DE RECHERCHE EN GENIE CIVIL - Structures
DAUMAS F. (Mme)	CENTRE DE THERMIQUE DE LYON - Energétique et Thermique
DOUTHEAU A.	CHIMIE ORGANIQUE
DUFOUR R.	MECANIQUE DES STRUCTURES
DUPUY J.C.	PHYSIQUE DE LA MATIERE
EMPTOZ H.	RECONNAISSANCE DE FORMES ET VISION
ESNOUF C.	GEMPPM***
EYRAUD L. (Prof. émérite)	GENIE ELECTRIQUE ET FERROELECTRICITE
FANTOZZI G.	GEMPPM***
FAVREL J.	PRODUCTIQUE ET INFORMATIQUE DES SYSTEMES MANUFACTURIERS
FAYARD J.M.	BIOLOGIE FONCTIONNELLE, INSECTES ET INTERACTIONS
FAYET M.	MECANIQUE DES SOLIDES
FERRARIS-BESSO G.	MECANIQUE DES STRUCTURES
FLAMAND L.	MECANIQUE DES CONTACTS
FLORY A.	INGENIERIE DES SYSTEMES D'INFORMATIONS
FOUGERES R.	GEMPPM***
FOUQUET F.	GEMPPM***
FRECON L.	REGROUPEMENT DES ENSEIGNANTS CHERCHEURS ISOLÉS
GERARD J.F.	INGENIERIE DES MATERIAUX POLYMERES
GERMAIN P.	LAEPSI****
GIMENEZ G.	CREATIS**
GOBIN P.F. (Prof. émérite)	GEMPPM***
GONNARD P.	GENIE ELECTRIQUE ET FERROELECTRICITE
GONTRAND M.	PHYSIQUE DE LA MATIERE
GOUTTE R. (Prof. émérite)	CREATIS**
GOUJON L.	GEMPPM***
GOURDON R.	LAEPSI****.
GRANGE G.	GENIE ELECTRIQUE ET FERROELECTRICITE
GUENIN G.	GEMPPM***
GUICHARDANT M.	BIOCHIMIE ET PHARMACOLOGIE
GUILLOT G.	PHYSIQUE DE LA MATIERE
GUINET A.	PRODUCTIQUE ET INFORMATIQUE DES SYSTEMES MANUFACTURIERS
GUYADER J.L.	VIBRATIONS-ACOUSTIQUE
GUYOMAR D.	GENIE ELECTRIQUE ET FERROELECTRICITE
HEIBIG A.	MATHEMATIQUE APPLIQUEES DE LYON
JACQUET-RICHARDET G.	MECANIQUE DES STRUCTURES
JAYET Y.	GEMPPM***
JOLION J.M.	RECONNAISSANCE DE FORMES ET VISION
JULLIEN J.F.	UNITE DE RECHERCHE EN GENIE CIVIL - Structures
JUTARD A. (Prof. émérite)	AUTOMATIQUE INDUSTRIELLE
KASTNER R.	UNITE DE RECHERCHE EN GENIE CIVIL - Géotechnique
KOULOUMDJIAN J.	INGENIERIE DES SYSTEMES D'INFORMATION
LAGARDE M.	BIOCHIMIE ET PHARMACOLOGIE
LALANNE M. (Prof. émérite)	MECANIQUE DES STRUCTURES
LALLEMAND A.	CENTRE DE THERMIQUE DE LYON - Energétique et thermique
LALLEMAND M. (Mme)	CENTRE DE THERMIQUE DE LYON - Energétique et thermique
LAUGIER A.	PHYSIQUE DE LA MATIERE
LAUGIER C.	BIOCHIMIE ET PHARMACOLOGIE
LAURINI R.	INFORMATIQUE EN IMAGE ET SYSTEMES D'INFORMATION
LEJEUNE P.	UNITE MICROBIOLOGIE ET GENETIQUE
LUBRECHT A.	MECANIQUE DES CONTACTS

<b>MASSARD N.</b>	INTERACTION COLLABORATIVE TELEFORMATION TELEACTIVITE
<b>MAZILLE H.</b>	PHYSICOCHIMIE INDUSTRIELLE
<b>MERLE P.</b>	GEMPPM***
<b>MERLIN J.</b>	GEMPPM***
<b>MIGNOTTE A. (Mle)</b>	INGENIERIE, INFORMATIQUE INDUSTRIELLE
<b>MILLET J.P.</b>	PHYSICOCHIMIE INDUSTRIELLE
<b>MIRAMOND M.</b>	UNITE DE RECHERCHE EN GENIE CIVIL - Hydrologie urbaine
<b>MOREL R.</b>	MECANIQUE DES FLUIDES ET D'ACOUSTIQUES
<b>MOSZKOWICZ P.</b>	LAEPSI****
<b>NARDON P. (Prof. émérite)</b>	BIOLOGIE FONCTIONNELLE, INSECTES ET INTERACTIONS
<b>NIEL E. AUTOMATIQUE INDUSTRIELLE</b>	
<b>NORTIER P.</b>	DREP
<b>ODET C.</b>	CREATIS**
<b>OTTERBEIN M. (Prof. émérite)</b>	LAEPSI****
<b>PASCAULT J.P.</b>	INGENIERIE DES MATERIAUX POLYMERES
<b>PAVIC G.</b>	VIBRATIONS-ACOUSTIQUE
<b>PELLETIER J.M.</b>	GEMPPM***
<b>PERA J. UNITE DE RECHERCHE EN GENIE CIVIL - Matériaux</b>	
<b>PERRIAT P.</b>	GEMPPM***
<b>PERRIN J.</b>	INTERACTION COLLABORATIVE TELEFORMATION TELEACTIVITE
<b>PINARD P. (Prof. émérite)</b>	PHYSIQUE DE LA MATIERE
<b>PINON J.M.</b>	INGENIERIE DES SYSTEMES D'INFORMATION
<b>PONCET A.</b>	PHYSIQUE DE LA MATIERE
<b>POUSIN J.</b>	MODELISATION MATHEMATIQUE ET CALCUL SCIENTIFIQUE
<b>PREVOT P.</b>	INTERACTION COLLABORATIVE TELEFORMATION TELEACTIVITE
<b>PROST R.</b>	CREATIS**
<b>RAYNAUD M.</b>	CENTRE DE THERMIQUE DE LYON - Transferts Interfaces et Matériaux
<b>REDARCE H.</b>	AUTOMATIQUE INDUSTRIELLE
<b>RETIF J-M.</b>	CEGELY*
<b>REYNOUARD J.M.</b>	UNITE DE RECHERCHE EN GENIE CIVIL - Structures
<b>RIGAL J.F.</b>	MECANIQUE DES SOLIDES
<b>RIEUTORD E. (Prof. émérite)</b>	MECANIQUE DES FLUIDES
<b>ROBERT-BAUDOUY J. (Mme) (Prof. émérite)</b>	GENETIQUE MOLECULAIRE DES MICROORGANISMES
<b>ROUBY D.</b>	GEMPPM***
<b>ROUX J.J.</b>	CENTRE DE THERMIQUE DE LYON – Thermique de l'Habitat
<b>RUBEL P.</b>	INGENIERIE DES SYSTEMES D'INFORMATION
<b>SACADURA J.F.</b>	CENTRE DE THERMIQUE DE LYON - Transferts Interfaces et Matériaux
<b>SAUTEREAU H.</b>	INGENIERIE DES MATERIAUX POLYMERES
<b>SCAVARDA S.</b>	AUTOMATIQUE INDUSTRIELLE
<b>SOUROUILLE J.L.</b>	INGENIERIE INFORMATIQUE INDUSTRIELLE
<b>THOMASSET D.</b>	AUTOMATIQUE INDUSTRIELLE
<b>THUDEROZ C.</b>	ESCHIL – Equipe Sciences Humaines de l'Insa de Lyon
<b>UBEDA S.</b>	CENTRE D'INNOV. EN TELECOM ET INTEGRATION DE SERVICES
<b>VELEX P.</b>	MECANIQUE DES CONTACTS
<b>VIGIER G.</b>	GEMPPM***
<b>VINCENT A.</b>	GEMPPM***
<b>VRAY D.</b>	CREATIS**
<b>VUILLERMOZ P.L. (Prof. émérite)</b>	PHYSIQUE DE LA MATIERE
 <b>Directeurs de recherche C.N.R.S. :</b>	
<b>BAIETTO-CARNEIRO M-C. (Mme)</b>	MECANIQUE DES CONTACTS ET DES SOLIDES
<b>BERTHIER Y.</b>	MECANIQUE DES CONTACTS
<b>CONDEMIN G.</b>	UNITE MICROBIOLOGIE ET GENETIQUE
<b>COTTE-PATAT N. (Mme)</b>	UNITE MICROBIOLOGIE ET GENETIQUE
<b>ESCUDIE D. (Mme)</b>	CENTRE DE THERMIQUE DE LYON
<b>FRANCIOSI P.</b>	GEMPPM***
<b>MANDRAND M.A. (Mme)</b>	UNITE MICROBIOLOGIE ET GENETIQUE
<b>POUSIN G.</b>	BIOLOGIE ET PHARMACOLOGIE
<b>ROCHE A.</b>	INGENIERIE DES MATERIAUX POLYMERES
<b>SEGUELA A.</b>	GEMPPM***
 <b>Directeurs de recherche I.N.R.A. :</b>	
<b>FEBVAY G.</b>	BIOLOGIE FONCTIONNELLE, INSECTES ET INTERACTIONS
<b>GRENIER S.</b>	BIOLOGIE FONCTIONNELLE, INSECTES ET INTERACTIONS
<b>RAHBE Y.</b>	BIOLOGIE FONCTIONNELLE, INSECTES ET INTERACTIONS
 <b>Directeurs de recherche I.N.S.E.R.M. :</b>	
<b>PRIGENT A.F. (Mme)</b>	BIOLOGIE ET PHARMACOLOGIE
<b>MAGNIN I. (Mme)</b>	CREATIS**
 <b>* CEGELY</b>	<b>CENTRE DE GENIE ELECTRIQUE DE LYON</b>
<b>** CREATIS</b>	<b>CENTRE DE RECHERCHE ET D'APPLICATIONS EN TRAITEMENT DE L'IMAGE ET DU SIGNAL</b>
<b>***GEMPPM</b>	<b>GROUPE D'ETUDE METALLURGIE PHYSIQUE ET PHYSIQUE DES MATERIAUX</b>
<b>****LAEPSI</b>	<b>LABORATOIRE D'ANALYSE ENVIRONNEMENTALE DES PROCEDES ET SYSTEMES INDUSTRIELS</b>

## Ecoles Doctorales et Diplômes d'Etudes Approfondies habilités pour la période 1999-2003

ECOLE DOCTORALE n° code national	RESPONSABLE PRINCIPAL	CORRESPONDANT INSA	DEA INSA n° code national	RESPONSABLE DEA INSA
<b>CHIMIE DE LYON</b>  (Chimie, Procédés, Environnement)  EDA206	M. D. SINOUC UCBL1 04.72.44.62.63 Sec 04.72.44.62.64 Fax 04.72.44.81.60	M. R. GOURDON 87.53 Sec 84.30 Fax 87.17	Chimie Inorganique <b>910643</b>	
			Sciences et Stratégies Analytiques <b>910634</b>	
			Sciences et Techniques du Déchet <b>910675</b>	M. R. GOURDON Tél 87.53 Fax 87.17
<b>ECONOMIE, ESPACE ET MODELISATION DES COMPORTEMENTS</b>  (E <sup>2</sup> MC)  EDA417	M.A. BONNAFOUS LYON 2 04.72.72.64.38 Sec 04.72.72.64.03 Fax 04.72.72.64.48	Mme M. ZIMMERMANN 60.91 Fax 87.96	Villes et Sociétés <b>911218</b>	Mme M. ZIMMERMANN Tél 60.91 Fax 87.96
			Dimensions Cognitives et Modélisation <b>992678</b>	M. L. FRECON Tél 82.39 Fax 85.18
<b>ELECTRONIQUE, ELECTROTECHNIQUE, AUTOMATIQUE</b>  (E.E.A.)  EDA160	M. D. BARBIER INSA DE LYON 85.47 Fax 60.82		Automatique Industrielle <b>910676</b>	M. M. BETEMPS Tél 85.59 Fax 85.35
			Dispositifs de l'Electronique Intégrée <b>910696</b>	M. D. BARBIER Tél 85.47 Fax 60.82
			Génie Electrique de Lyon <b>910065</b>	M. J.P. CHANTE Tél 87.26 Fax 85.30
			Images et Systèmes <b>992254</b>	Mme I. MAGNIN Tél 85.63 Fax 85.26
<b>EVOLUTION, ECOSYSTEME, MICROBIOLOGIE, MODELISATION</b>  (E2M2)  EDA403	M. J.P. FLANDROIS UCBL1 04.78.86.31.50 Sec 04.78.86.31.52 Fax 04.78.86.31.49	M. S. GRENIER 79.88 Fax 85.34	Analyse et Modélisation des Systèmes Biologiques <b>910509</b>	M. S. GRENIER Tél 79.88 Fax 85.34
<b>INFORMATIQUE ET INFORMATION POUR LA SOCIETE</b>  (EDIHS)  EDA 407	M. L. BRUNIE INSA DE LYON 87.59 Fax 80.97		Documents Multimédia, Images et Systèmes d'Information Communicants <b>992774</b>	M. A. FLORY Tél 84.66 Fax 85.97
			Extraction des Connaissances à partir des Données <b>992099</b>	M. J.F. BOULICAUT Tél 89.05 Fax 87.13
			Informatique et Systèmes Coopératifs pour l'Entreprise <b>950131</b>	M. A. GUINET Tél 85.94 Fax 85.38
<b>INTERDISCIPLINAIRE SCIENCES- SANTÉ</b>  (EDISS)  EDA205	M. A.J. COZZONE UCBL1 04.72.72.26.72 Sec 04.72.72.26.75 Fax 04.72.72.26.01	M. M. LAGARDE 82.40 Fax 85.24	Biochimie <b>930032</b>	M. M. LAGARDE Tél 82.40 Fax 85.24
<b>MATERIAUX DE LYON</b>  UNIVERSITE LYON 1  EDA 034	M. J. JOSEPH ECL 04.72.18.62.44 Sec 04.72.18.62.51 Fax 04.72.18.60.90	M. J.M. PELLETIER 83.18 Fax 85.28	Génie des Matériaux : Microstructure, Comportement Mécanique, Durabilité <b>910527</b>	M. J.M. PELLETIER Tél 83.18 Fax 85.28
			Matériaux Polymères et Composites <b>910607</b>	M. H. SAUTERAU Tél 81.78 Fax 85.27
			Matière Condensée, Surfaces et Interfaces <b>910577</b>	M. G. GUILLOT Tél 81.61 Fax 85.31
<b>MATHEMATIQUES ET INFORMATIQUE FONDAMENTALE</b>  (Math IF)  EDA 409	M. F. WAGNER UCBL1 04.72.43.27.86 Fax 04.72.43.00.35	M. J. POUSIN 88.36 Fax 85.29	Analyse Numérique, Equations aux dérivées partielles et Calcul Scientifique <b>910281</b>	M. G. BAYADA Tél 83.12 Fax 85.29
<b>MECANIQUE, ENERGETIQUE, GENIE CIVIL, ACOUSTIQUE</b>  (MEGA)  EDA162	M. F. SIDOROFF ECL 04.72.18.61.56 Sec 04.72.18.61.60 Fax 04.78.64.71.45	M. G. DALMAZ 83.03 Fax 04.72.89.09.80	Acoustique <b>910016</b>	M. J.L. GUYADER Tél 80.80 Fax 87.12
			Génie Civil <b>992610</b>	M. J.J. ROUX Tél 84.60 Fax 85.22
			Génie Mécanique <b>992111</b>	M. G. DALMAZ Tél 83.03 Fax 04.78.89.09.80
			Thermique et Energétique <b>910018</b>	M. J. F. SACADURA Tél 81.53 Fax 88.11

En grisé : Les Ecoles doctorales et DEA dont l'INSA est établissement principal

## Sommaire

<b>RESUME</b>	<b>6</b>
<b>PREFACE</b>	<b>7</b>
<b>LISTE DES PUBLICATIONS</b>	<b>9</b>
<b>LISTES DES ABREVIATIONS ET SYMBOLES</b>	<b>11</b>
<b>1. INTRODUCTION</b>	<b>12</b>
<b>2. METHODES DE RECALAGE POUR LES IMAGES THORACIQUES ET CARDIAQUES : REVUE DU PROBLEME</b>	<b>16</b>
2.1 Transformations de l'image	17
2.2 Principes de la mise en correspondance ou recalage	20
2.3 Obtention de la transformation optimale	22
2.4 Evaluation du recalage	23
2.5 Conclusions	23
<b>3. RECALAGE DE DONNEES CARDIAQUES ANATOMIQUES ET FONCTIONNELLES</b>	<b>24</b>
3.1 Données cardiaques	24
3.2 Recalage d'images cardiaques anatomiques RM et métaboliques TEP	27
3.2.1 Segmentation des structures thoraciques	30
3.2.2 Calcul de la transformation optimale du recalage	32
3.2.3 Résultats des recalages rigides	34
3.2.4 Evaluation de la méthode de recalage rigide IRM-TEP	36
3.3 Méthode basée sur des repères externes pour les images RM et les données MCG	39
<b>4. CARTOGRAPHIES FONCTIONNELLES EN 3-D</b>	<b>41</b>
4.1 Principe	41
4.2 Résultats des fusions de données	43
<b>5. METHODE DE RECALAGE ELASTIQUE POUR LES IMAGES CARDIAQUES RM ET PET</b>	<b>45</b>
5.1 Principe	45
5.2 Résultats des recalages élastiques	48
<b>6. DISCUSSION</b>	<b>50</b>
<b>7. CONCLUSIONS</b>	<b>57</b>
<b>REFERENCES</b>	<b>60</b>

## RESUME

### **Mise en correspondance en imagerie cardiaque multimodale : vers un modèle anatomo-fonctionnel individualisé du cœur**

L'objectif de cette thèse était de développer des méthodes destinées au recalage et à la fusion en imagerie cardiaque multi-modale. Une méthode de recalage rigide a été mise au point pour recaler des images par Résonance Magnétique (IRM) et en Tomographie d'Emission de Positons (TEP) cardiaques. La méthode est basée sur le recalage des structures thoraciques segmentées à partir des images TEP de transmission et IRM transverses. Les structures thoraciques ont été segmentées à partir des images à l'aide de modèles déformables. Le recalage d'images par RM avec des images de TEP d'émission selon les orientations anatomiques (en petit axe) est également possible. La méthode de recalage rigide a été évaluée en utilisant des images simulées et des données cliniques IRM et TEP de dix patients présentant des atteintes multitronculaires des artères coronaires. De même, une méthode de recalage élastique a été développée et appliquée au recalage d'images cardiaques intra-patient par RM et TEP et d'images inter-patients en IRM cérébrale. Dans cette méthode de recalage élastique, une combinaison du critère d'information mutuelle et d'informations de gradient a été introduite pour guider la déformation régularisée d'une image vers une image cible. Une approche pour la création de cartographies fonctionnelles en trois dimensions (3-D) du cœur a également été mise au point. Un modèle cardiaque anatomique individualisé bi-cavités a été extrait des images RM. Les images par RM anatomiques et TEP métaboliques ont été recalées en s'appuyant sur les surfaces des structures thoraciques. Les images RM et les données issues de la magnétocardiographie (MCG) sont mises en correspondance en utilisant des repères externes. La méthode permet d'obtenir un modèle individualisé anatomique et fonctionnel en 3-D du cœur incluant des informations structurelles issues de l'IRM et des informations fonctionnelles provenant de la TEP et de la MCG. Nous avons aussi évalué dans cette thèse différentes sources d'erreurs pour la méthode de recalage des images RM et des données de la MCG. Le recalage rigide IRM-TEP a été utilisé dans la comparaison de méthodes d'imagerie multimodale où la TEP sert de référence pour des études de la viabilité myocardique.

Mots-clés : recalage (mise en correspondance) d'images, imagerie thoracique et cardiaque multimodale, IRM, TEP, MCG, modèle anatomique et fonctionnel.

## Préface

Cette thèse est dédiée à ma chère épouse Ulla et à notre fils Mikael.

Le travail présenté dans cette thèse a été effectué à CREATIS, INSA de Lyon et au laboratoire d'ingénierie biomédicale de l'Université de Technologie d'Helsinki (HUT).

Je voudrais remercier mon responsable, Isabelle Magnin (Chef du laboratoire CREATIS de l'INSA à Lyon) et mon superviseur, Patrick Clarysse pour toutes les discussions offertes, les idées de recherche et les conseils fournis, ainsi que pour m'avoir proposé un excellent environnement de recherche pour ce travail à l'INSA de Lyon.

Je remercie aussi le professeur Toivo Katila, mon responsable en Finlande pour son soutien et les conditions de travail excellentes mises à ma disposition à l'université Technologique d'Helsinki (HUT), ainsi que Mme Outi Sipilä, D.Sc. (Tech.), mon professeur en Finlande, pour toutes les discussions et précieux conseils prodigués.

Je remercie les deux examinateurs préliminaires, Mme Ulla Ruotsalainen, chargée de cours universitaires, les Professeurs Philippe Cinquin et Nicholas Ayache pour leurs corrections et suggestions destinées à améliorer cette thèse.

Mille mercis également à Quoc Cuong Pham et à Nicoleta Pauna, de l'INSA de Lyon, ainsi qu'à Jyrki Lötjönen, chargé de cours du Centre de Recherche finlandais (VTT), pour leurs contributions nombreuses et essentielles et pour l'aide qu'ils m'ont apportée dans le cadre de ce travail.

De même, Jukka Nenonen, chargé de cours universitaires, les Docteurs Kirsi Lauerma et Helena Hänninen, ainsi que Eero Salli, D.Sc. (Tech.) reçoivent ici toute ma gratitude pour leurs nombreuses contributions et pour l'aide qu'ils m'ont apportée.

Je remercie également les personnes du laboratoire CREATIS de l'INSA de Lyon pour l'assistance dont ils ont fait preuve et pour m'avoir proposé une atmosphère de travail propice à la réflexion.

De même, que les personnes du laboratoire d'ingénierie biomédicale à l'Université Technologique de Helsinki, notamment les membres précédents et actuels du groupe de traitement de l'image, reçoivent mes remerciements pour leur assistance et leur gentillesse.

Je remercie également les membres du service de radiothérapie et d'oncologie de l'Hôpital Central Universitaire de Oulu pour leur bienveillance lors de la préparation de ce manuscrit.

Mes autres remerciements sincères sont destinés à la Région Rhône-Alpes pour son soutien financier, obtenu par l'intermédiaire du projet ADEMO, au département scientifique de l'Ambassade de France en Finlande, à la « Finnish Cultural

Foundation », la « Jenny and Antti Wihuri Foundation », la fondation de technologie en Finlande et à la fondation pour la recherche de l'université de technologie d'Helsinki.

Pour terminer, que mes parents, les membres de ma famille et mes amis trouvent ici l'expression de ma gratitude pour leur soutien.

Enfin, et ce n'est pas le moindre de mes remerciements, je remercie ma femme Ulla pour le soutien qu'elle m'a apporté et Mikael, notre fils âgé d'un an, pour la grande patience dont il a fait preuve lors la préparation de ce manuscrit.

Espoo et Oulu, mars 2004

Timo Mäkelä



## Liste des publications

### Publications dans des journaux avec comité de lecture

T.J. Mäkelä, P. Clarysse, O. Sipilä, N. Pauna, Q.C. Pham, T. Katila et I.E. Magnin. A review of cardiac image registration methods. *IEEE Trans. Med. Imaging*, vol. 21, no 9, pp. 1011-1021, 2002.

T.J. Mäkelä, Q.C. Pham, P. Clarysse, J. Nenonen, J. Lötjönen, O. Sipilä, H. Hänninen, K. Lauerma, J. Knuuti, T. Katila et I.E. Magnin. A 3-D model-based registration approach for the PET, MR and MCG cardiac data fusion. *Medical Image Analysis*, vol. 7, pp. 377-389, 2003.

K. Lauerma, P. Niemi, H. Hänninen, T. Janatuinen, L-M. Voipio-Pulkki, J. Knuuti, L. L. Toivonen, T.J. Mäkelä, M. Mäkijärvi et H.J. Aronen. Multimodality MR Imaging Assessment of Myocardial Viability: Combination of First-Pass and Late Contrast Enhancement to Wall Motion Dynamics and Comparison with FDG PET-Initial Experience. *Radiology*, vol. 217, pp. 729-736, 2000.

J. Nenonen, K. Pesola, H. Hänninen, K. Lauerma, P. Takala, T. J. Mäkelä, M. Mäkijärvi, J. Knuuti, L. Toivonen et T. Katila. Current-Density Estimation of Exercise-Induced Ischemia in Patients with Multivessel Coronary Artery Disease. *Journal of Electrocardiography*, vol. 34(supplement), pp. 37-42, 2001.

### Article dans des conférences avec comité de lecture

T.J. Mäkelä, P. Clarysse, J. Lötjönen, O. Sipilä, K. Lauerma, H. Hänninen, E. P. Pyökkimies, J. Nenonen, J. Knuuti, T. Katila et I.E. Magnin, A new method for the registration of cardiac PET and MR images using deformable model based segmentation of the main thorax structures. *Lect. Notes Comput. Sci. 2208:Medical Image Computing and Computer Assisted Intervention, MICCAI'01*, W. Niessen, M.A. Viergever (Eds.), Springer, pp. 557-564, 2001.

J. Lötjönen et T.J. Mäkelä, Elastic matching using a deformation sphere, *Lect. Notes Comput. Sci. 2208: Medical Image Computing and Computer Assisted Intervention, MICCAI'01*, W. Niessen, M.A. Viergever (Eds.), Springer, pp. 541-548, 2001.

T.J. Mäkelä, J. Lötjönen, O. Sipilä, K. Lauerma, J. Nenonen, T. Katila et I.E. Magnin, Error Analysis of Registering of Anatomical and Functional Cardiac Data Using External Markers, *Int. Conf. on Biomagnetism, BIOMAG'02*, H. Nowak, J. Haueisen, F. Giesler, R. Huonker (Eds.). Verlag, pp. 842-845, 2002.

T. J. Mäkelä, Q.-C. Pham, P. Clarysse, J. Lötjönen, K. Lauerma, H. Hänninen, J. Knuuti, T. Katila et I. E. Magnin. A 3-D model-based approach for the PET-functional and MR-anatomical cardiac imaging data fusion, Lect. Notes Comput. Sci. 2230: International Workshop on Functional Imaging and Modeling of the Heart, FIMH'01, Springer, pp. 83-90, 2001.

T. Mäkelä, M. Pollari, J. Lötjönen, N. Pauna, A. Reilhac, P. Clarysse, I.E. Magnin et T. Katila. Evaluation and comparison of surface and intensity based rigid registration methods for thorax and cardiac MR and PET images. Lect. Notes Comput. Sci. 2674: International Workshop on Functional Imaging and Modeling of the Heart, FIMH'03, Springer, pp. 224-233, 2003.

N. Pauna, P. Croisille, N. Costes, A. Reilhac, T. Mäkelä, O. Cozar, M. Janier et P. Clarysse. A strategy to quantitatively evaluate MRI/PET cardiac registration methods using a Monte Carlo simulator. Lect. Notes Comput. Sci. 2674: International Workshop on Functional Imaging and Modeling of the Heart, FIMH'03, Springer, pp. 194-204, 2003.

M. Pollari, J. Lötjönen, T. Mäkelä, N. Pauna, A. Reilhac et P. Clarysse. Evaluation of cardiac MR-PET registration methods using a numerical breathing phantom, IEEE International Symposium on Biomedical Imaging, 2004, pp. 1447-1450.

## Autres publications

T. J. Mäkelä, P. Clarysse, J. Lötjönen, O. Sipilä, K. Lauerma, H. Hänninen, J. Nenonen, J. Knuuti, T. Katila et I. E. Magnin. A Method for Registration of Cardiac MR and PET Images for Assessing Myocardial Viability. Understanding Cardiac Imaging Techniques - From Basic Pathology to Image Fusion, Paolo Marzullo, Ed., IOS Press, pp. 155-165, 2001.

## Listes des abréviations et symboles

2-D	Two-dimensional	2-D	En deux dimensions
3-D	Three-dimensional	3-D	En trois dimensions
4-D	Four-dimensional	4-D	En quatre dimensions
BSPM	Body surface potential mapping	CPSC	Cartographie du potentiel de surface corporelle
CR	Correlation ratio	RC	Rapport de corrélation
ECG	Electrocardiography	ECG	Examen électrocardiographique
CDE	Current density estimates	EDC	Estimations des densités de courant
FBP	Filtered back projection algorithm	ARPF	Algorithme de rétroprojection filtrée
18F-FDG	2-[fluorine 18]fluoro-2-deoxy-D-glucose	18F-FDG	Fluoro-déoxy-D-glucose marqué au fluor 18
FEM	Finite element method	MEF	Méthode des éléments finis
HUCH	Helsinki university central hospital	HUCH	Hôpital central de l'université d'Helsinki
[MR]I	[Magnetic resonance] imaging	I[RM]	Imagerie par [résonance magnétique]
LA	Long axis	GA	Grand Axe
LV	Left ventricle	VG	Ventricule gauche
MAP	Maximum a posteriori	MAP	Maximum a posteriori
MCG	Magnetocardiography	MCG	Magnétocardiographie
NMI	Normalized mutual information	IMN	Informations mutuelles normalisées
PET	Positron emission tomography	TEP	Tomographie d'émission de positons
NMR	Nuclear magnetic resonance	RMN	Résonance magnétique nucléaire
RMS	Root mean square	RMS	Racine carrée de la valeur moyenne du carré de l'élément étudié
RV	Right ventricle	VD	Ventricule droit
SA	Short axis	PA	Petit axe
SDV	Standard deviation	ET	Ecart-type
SPECT	Single photon emission computed tomography	TEMP	Tomographie d'émission monophotonique
SQUID	Superconducting magnetometer	SQUID	Magnétomètre supraconducteur
T	Tesla	T	Tesla
CT	X-ray computed tomography	TDM	Tomodensitométrie
US	Ultrasonography	US	Ultrasonographie/échographie
VTK	Visualization toolkit software library	VTK	Librairie de visualisation graphique VTK

# 1. Introduction

L'intégration de données provenant de différentes modalités d'imagerie médicale est souvent souhaitée à des fins diagnostiques et de recherche en cardiologie. Une première étape de ce processus d'intégration est d'amener les modalités impliquées dans un alignement spatial, une procédure dénommée *recalage* [Maintz et Viergever, 1998]. Après le recalage, une étape de fusion est nécessaire pour visualiser les informations intégrées à partir des données impliquées.

Le principal objectif de cette thèse était de développer des méthodes pour combiner des informations provenant de différentes modalités en imagerie cardiaque. Dans le recalage d'images cardiaques et dans la fusion de données, l'intégration d'informations complémentaires multiples dans une référence commune permet une analyse plus approfondie des fonctions et des pathologies cardiaques. De façon plus spécifique, le recalage d'images cardiaques et la fusion de données multimodales contribuent à la détermination et la quantification de la viabilité des tissus dans les maladies cardiaques ischémiques. Un tissu viable est un tissu pathologique dont la fonction peut être au moins en partie restaurée après le rétablissement du débit sanguin. La quantification de la viabilité peut aider à décider si un patient présentant une coronaropathie pourra, ou non, bénéficier d'une procédure de revascularisation.

Le diagnostic d'ischémie et l'estimation de la viabilité reposent sur l'analyse conjointe de la perfusion, du métabolisme, et de la fonction contractile, chacun de ces paramètres étant quantifié par des modalités d'imagerie spécifiques (Fig. 1).

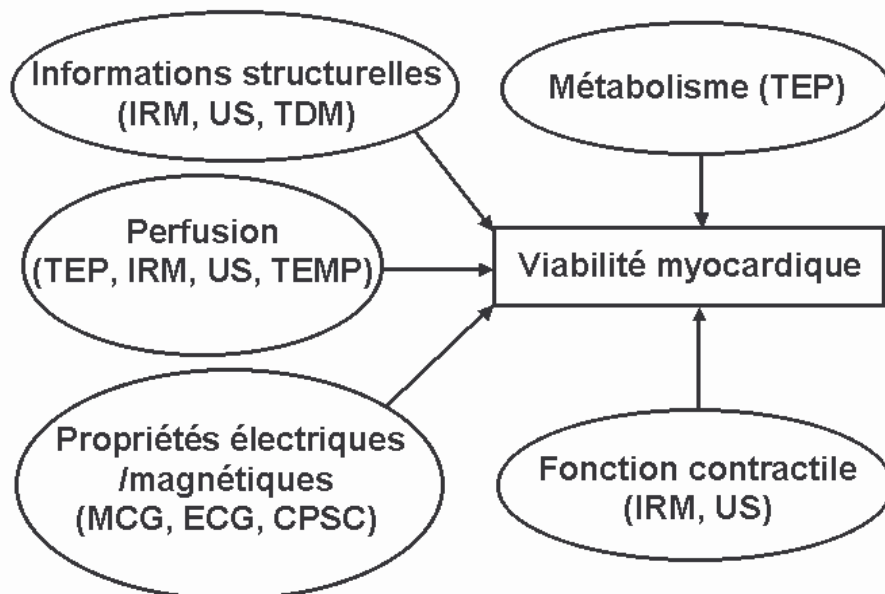


Figure 1 : Recalage et fusion de données cardiaques pour des études de viabilité myocardique [Mäkelä, 2003a].

Des informations structurales sur le cœur peuvent être obtenues en utilisant l'imagerie par résonance magnétique (IRM), la tomодensitométrie (TDM) et l'échographie (US).

Des informations fonctionnelles peuvent être obtenues en analysant le métabolisme en tomographie d'émission de positons (TEP), la perfusion en tomographie d'émission monophotonique (TEMP) au thallium, en IRM, US ou TEP, et la fonction contractile en IRM et US. L'activité électrique fonctionnelle du cœur crée à la fois des champs électriques et magnétiques et ceux-ci peuvent être mesurés respectivement par l'électrocardiographie (ECG) et la magnéto-cardiographie (MCG) [Siltanen, 1988]. L'ECG, la MCG et les techniques de cartographie multicanaux par ECG, telles que la cartographie du potentiel de surface corporelle (CPSC) [Ambroggi, 1989], [Simelius, 1998] donnent des informations supplémentaires uniques sur les manifestations électromagnétiques de l'ischémie et sur la viabilité myocardique.

Dans cette thèse, nous avons considéré des données cardiaques obtenues par IRM, TEP et MCG. *L'IRM* [Lauterbur, 1973] est basée sur les principes de la résonance magnétique nucléaire (RMN). Dans des applications cliniques, le signal provenant du noyau hydrogène est normalement utilisé pour l'imagerie [Webb, 1995]. En IRM cardiaque (on trouve aussi le terme « cardio-rem-nographie »), on obtient habituellement des images selon les axes anatomiques du cœur identifiés par petit axe (PA) et grand axe (GA). Des images de repérage (scout views) sont tout d'abord acquises pour définir les orientations cardiaques GA et PA. Ensuite, des séquences temporelles d'images cardiaques (mode ciné) en petit axe sont généralement réalisées. Elles consistent en plusieurs coupes partant du plan des valves en descendant vers l'apex du VG. Ces acquisitions sont en général synchronisées à l'ECG et obtenues au cours d'une apnée afin d'améliorer la qualité des images et réduire les erreurs de recalage provoquées par le mouvement cardiaque et respiratoire. L'imagerie par RM présente l'avantage d'être non invasive, d'offrir une sélection libre des plans d'imagerie et un bon contraste entre les différents types de tissus mous [Conolly, 1995]. L'IRM marquée est une technique précise pour l'analyse des déformations de la paroi cardiaque [Zerhouni, 1988], [Axel, 1989]. Les anomalies de mobilité de la paroi cardiaque sont des indicateurs sensibles d'une anomalie du débit sanguin myocardique [Ratib, 2000]. Le développement de séquences IRM plus rapides a aussi permis de déterminer la circulation de premier passage du bolus de contraste par IRM, et ouvert la voie à des études de perfusion myocardique [Hartiala, 1995]. Comparée aux ultrasons, l'imagerie par RM est plus précise pour l'évaluation de la viabilité. En effet, les images RM peuvent être acquises avec une qualité reproductible indépendante de l'examineur et de l'anatomie du patient [Baer, 1996].

*L'imagerie de TEP* [Sweet, 1951], [Wrenn, 1951], [Brownell, 1953] peut donner des informations sur la perfusion et l'activité métabolique du cœur [VanBrockling, 1995]. L'imagerie TEP a été utilisée pour évaluer le bénéfice apporté par des interventions

chirurgicales de pontage coronarien et dans les études de viabilité [Hartiala, 1995]. L'imagerie TEP par le fluoro-déoxy-D-glucose marqué au fluor18 (18F-FDG) donne des informations sur le métabolisme du glucose dans le cœur. Cette méthode est considérée comme étant la référence pour déterminer les zones tissulaires viables du cœur [Hartiala, 1995]. L'imagerie TEP permet de quantifier la perfusion myocardique régionale en termes absolus. Dans les acquisitions TEP, les images sont habituellement statiques, c'est-à-dire qu'elles représentent des informations intégrées au cours du temps. Cependant, avec les appareils modernes de tomodensitométrie, il est possible d'acquérir des images en synchronisation à l'ECG. Avec des acquisitions dynamiques, l'évolution dans le temps de la captation du radiotraceur est suivie dans des régions d'intérêt [Gilardi, 1996].

Outre des images fonctionnelles TEP en émission, on acquiert aussi des images en transmission à l'aide d'une source radioactive externe (par exemple, le germanium 68) pour la correction d'atténuation de l'image d'émission. Les images TEP de transmission ressemblent à une image de tomodensitométrie X de faible qualité. Elle offre cependant des informations structurelles qui peuvent être utilisées à des fins de segmentation et de recalage [Kim, 1991], [Pallotta, 1995], [Mäkelä, 2001].

La *Magnétocardiographie* (MCG) permet l'étude approfondie des champs électromagnétiques du cœur. En MCG, les champs magnétiques produits par l'activité électrique du cœur sont enregistrés de façon non agressive en utilisant un magnétomètre supraconducteur (SQUID) [Hämäläinen, 1999]. Les champs magnétiques mesurés en dehors du corps sont d'amplitude extrêmement faible (10 fT à 100 pT). Les signaux mesurés sont générés par les courants électriques des cellules myocardiques et, par conséquent, les mesures donnent des informations fonctionnelles directes en temps réel sur le cœur [Hämäläinen, 1999]. L'échelle de temps des signaux détectables varie d'une milliseconde à plusieurs secondes ou même à des durées plus longues. La région de l'activité de la source est calculée en utilisant les données obtenues à partir des capteurs SQUID. Dans la plupart des cas, l'objectif de l'analyse des données est de résoudre le problème inverse, c'est-à-dire d'estimer la densité du courant source sous-jacente aux champs externes mesurés [Nenonen, 1994]. En d'autres termes, on calcule la distribution d'un courant qui donnerait le résultat de la mesure. Une estimation minimum normée est souvent utilisée pour estimer la distribution du courant principal, mais étant donné que le problème inverse est mal posé, il est nécessaire d'appliquer une régularisation [Nenonen, 1997]. La MCG est actuellement utilisée dans certains hôpitaux pour évaluer et développer plus encore son utilisation clinique [Hämäläinen, 1999]. Les études MCG multicanaux sont particulièrement prometteuses pour localiser de façon non agressive des activités cardiaques anormales critiques pour la survenue de l'arythmie [Nenonen, 1997].

L'objectif de cette thèse était de développer des méthodes pour le recalage et la fusion de données cardiaques multimodales pour une meilleure compréhension de la

physiologie du cœur et des pathologies associées et l'amélioration du diagnostic des cardiopathies ischémiques [Mäkelä, 2002a]. Plus précisément, l'objectif de cette thèse était de mettre au point des méthodes pour combiner des données cardiaques anatomiques de l'IRM, et des données fonctionnelles du métabolisme mesurées en 18F-FDG TEP et de l'activité électromagnétique provenant de la MCG. Dans ce but, une nouvelle méthode de recalage rigide a été développée pour mettre en correspondance des images par RM et TEP-FDG cardiaques [Mäkelä, 2001], [Mäkelä, 2003a]. La méthode proposée est présentée et évaluée dans le chapitre 3.2. La méthode de recalage des données anatomiques IRM et fonctionnelles issues de la MCG, ainsi que l'évaluation de différentes sources d'erreurs influençant le recalage sont décrites dans le chapitre 3.3 [Mäkelä, 2002b], [Mäkelä, 2003a].

Les techniques de recalage rigide IRM-TEP, d'une part et IRM-MCG, d'autre part, ont été utilisés conjointement pour établir une procédure complète de construction d'un modèle anatomique et fonctionnel en trois dimensions spécifique du cœur du patient [Mäkelä, 2003a]. Ce modèle est présenté au chapitre 4.

Enfin, une nouvelle méthode de recalage élastique a été développée [Lötjönen and Mäkelä, 2001] et appliquée, par exemple, pour compenser le mouvement cardiaque dans des études intra-individuelles (chapitre 5). L'ensemble des résultats est discuté dans le chapitre 6 avant la conclusion générale (chapitre 7).



## 2. Méthodes de recalage pour les images thoraciques et cardiaques : état de l'art

Plusieurs articles de synthèse et ouvrages ont été publiés dans le domaine du recalage des images médicales [Brown, 1992], [Maurer, 1993], [van den Elsen, 1993], [Maintz, 1998], [Lester, 1998], [Fitzpatrick, 2000], [Audette, 2000], [Bankman, 2000], [Hill, 2001], [Frangi, 2001], [Hajnal, 2001]. Seuls quelques articles de revue se concentrent sur le recalage des images cardiaques [Habboosh, 1992], [Gilardi, 1996]. Gilardi et al. [Gilardi, 1996] ont présenté une revue des techniques et des applications cliniques pour l'intégration des images biomédicales multimodales du cœur et Habboosh [Habboosh, 1992] a discuté brièvement des aspects du recalage cardiaque TEP et IRM. De même, dans l'article de revue de Maintz et Viergever [Maintz, 1998], les méthodes de recalage des images cardiaques sont étudiées dans une section à part. [Mäkelä, 2002a] présentent une revue des méthodes de recalage des images cardiaques, y compris les plus récentes. Les problèmes liés à l'implantation et à la validation des méthodes sont aussi discutés.

Les méthodes de recalage comportent habituellement les principaux éléments suivants :

- 1) la transformation (au sens mathématique) d'une image vers une autre ;
- 2) un critère de similarité qui indique lorsqu'une image ressemble le plus à une image de référence
- 3) un processus d'optimisation qui estime les meilleurs paramètres de transformation.

L'évaluation de la méthode de recalage est un problème important, difficile du fait de l'absence de référence parfaite (gold standard en anglais). Elle est souvent négligée dans les publications.

Dans le recalage d'images cardiaques, la plupart des approches a tenté d'appliquer des méthodes de recalage existantes qui pour leur grande majorité ont été développées dans le cadre de l'imagerie cérébrale. La caractéristique principale du cas de l'imagerie thoracique et cardiaque est relative aux mouvements combinés de la respiration et du cœur. C'est ce qui en fait également la grande difficulté. Dans les sections suivantes, nous passons en revue la littérature du recalage en imagerie cardiaque et thoracique en fonction des trois composants précités en soulignant les problèmes spécifiques du recalage d'images cardiaques qui sont principalement dus à la mobilité des structures anatomiques (mouvements respiratoires et mouvements cardiaques). Ce chapitre est issu de l'article que nous avons publiée récemment [Mäkelä, 2002a].

Les principales méthodes de recalage d'images cardiaques et leurs principaux paramètres, y compris des informations relatives à la précision des méthodes, sont résumés dans le tableau 1.



## 2.1 Transformations de l'image

Les méthodes de recalage sont généralement classées en méthodes rigides, affines, projectives, ou non rigides selon la nature de la transformation du recalage [Maintz, 1998] (Fig. 2). Une transformation est dite « globale » si elle s'applique à toute l'image, et « locale » si elle s'applique à des sous-régions de l'image qui ont alors chacune leur propre transformation.

Dans le recalage rigide global, seules les translations et les rotations sont admises. Les distances entre les points et les angles entre les lignes ne changent pas pendant le recalage [van den Elsen, 1993]. Les méthodes de recalage affines transforment des lignes parallèles en lignes parallèles. Les transformations projectives conservent les lignes. Les méthodes de recalage non rigide font intervenir des transformations plus générales [Maintz, 1998], [Fitzpatrick, 2000].

L'étude du tableau 1 montre clairement que la plupart des méthodes considèrent des transformations rigides. Quelques travaux font appel à des transformations affines globales [Slomka, 1995] ou même élastiques [Wirth, 1997], [Declerck, 1997], [Gallippi, 2001], [Klein, 2002a, 2002b]. Slomka *et al.* [Slomka, 1995, 2001] ont comparé les critères de similarité de *la somme des différences absolues* et de *changement stochastique de signe* pour un recalage affine d'images en TEMP d'émission cardiaque. Un recalage initial a été obtenu à partir de l'alignement des axes principaux. Ils en déduisent que la méthode de *la somme des différences absolues* donnait de meilleurs résultats que la méthode de *changement stochastique de signe*. Cette méthode a ensuite été améliorée et proposée comme outil clinique pour la quantification voxel par voxel des images TEMP [Slomka, 2001].

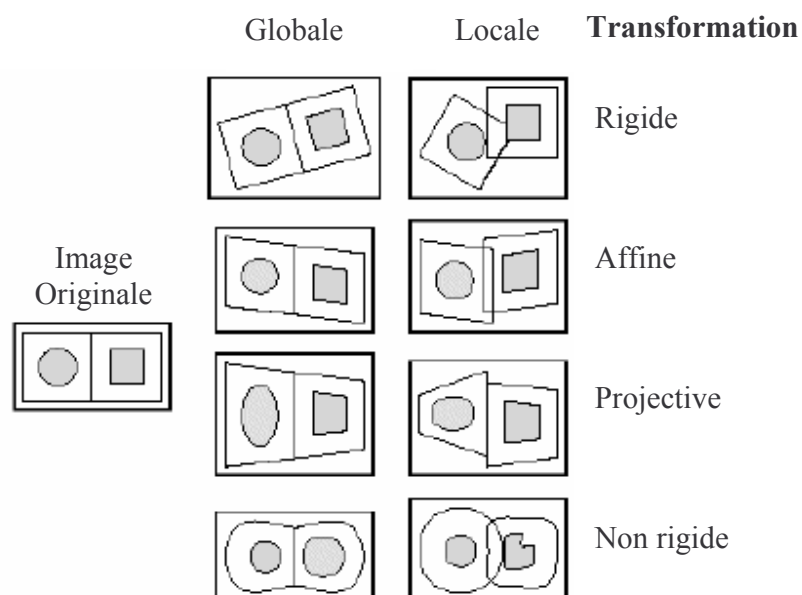


Figure 2 : Transformations d'images 2-D [Maintz, 1998].

Dans cette dernière, l'algorithme de recalage compense les différences de forme par recalage affine, et inclue une technique d'érosion dont l'action est similaire à des déformations de l'image (ou warping) pour affiner le recalage. Wirth *et al.* [Wirth, 1997] ont utilisé un recalage élastique pour mettre en correspondance des images RM thoraciques et des images tomodensitométriques du même sujet. Dans cette méthode, 36 repères correspondants dans le thorax et les surfaces pulmonaires sont appariés de façon élastique. La transformation des autres points est déterminée par une fonction d'interpolation élastique. La validation de la précision de la méthode n'a pas été effectuée.

Declerck *et al.* [Declerck, 1996a, 1996b, 1997] ont présenté une méthode automatisée pour aligner les images TEMP obtenues dans des études de perfusion myocardique au repos et à l'effort. Dans cette méthode, les points caractéristiques des surfaces des images cardiaques TEMP sont extraits à l'aide d'un détecteur de contour [Canny, 1986], [Deriche, 1987]. Ces primitives sont recalées par la méthode ICP (Iterative Closest Point) [Besl, 1992]. Les images sont recalées plus finement de façon élastique sur une image modèle en utilisant des transformations locales splines. Gallippi *et al.* [Gallippi, 2001] ont utilisé la mesure de la corrélation modifiée pour apparier statistiquement l'intensité locale des images recalées. La méthode a été appliquée pour le recalage rigide de séries chronologiques intramodalité cardiaque en IRM et US. Dans la publication récente de Klein *et al.* [Klein, 2002a, 2002b], un nouvel algorithme élastique de recalage en 4-D a été proposé pour la compensation du mouvement d'images TEP d'émissions cardiaques synchronisées afin de donner une meilleure estimation conjointe des paramètres métaboliques et de perfusion. La méthode recalcule différentes séquences temporelles d'images d'émission cardiaques TEP avec une image télé-diastolique. Elle utilise un modèle élastique non uniforme (modèle de mouvement affine global à 12 paramètres) et calcule de façon itérative les paramètres de recalage du modèle à partir d'une fonction de coût qui combine une mesure quadratique de la différence des intensités des images avec un terme de contrainte de la continuité temporelle faisant l'hypothèse d'une vitesse constante entre les images de la séquence et imposant un modèle affine de mouvement. La méthode ne nécessite pas de segmentation précise *a priori* de l'objet. En général, une transformation élastique est nécessaire pour mettre en correspondance deux images acquises à différents moments du cycle cardiaque pour tenir compte du mouvement entre deux images successives d'une séquence temporelle. Cette transformation est aussi nécessaire pour le recalage inter-sujets, un domaine d'étude qui représente certainement un grand défi pour l'avenir.

**Tableau 1 : VUE D'ENSEMBLE DES METHODES DE RECALAGE DES IMAGES  
THORACIQUES ET CARDIAQUES [MÄKELÄ, 2002A]**

Reference	Modalities	Object	Trans.	Struc.	Method	Valid.	Error	Error type
<b>Registration methods based on geometric image features</b>								
<b>Point-based registration</b>								
Wirth et al. (1997)	CT-MR	Thorax	Elastic	LM	int. & elast.	-	-	-
<b>Thorax surface based registration</b>								
Yu et al. (1995)	CT-PET	Thorax	Rigid	T&L	h&h	P	(x,y) 2.3 mm, (y) 3.0 mm	mean (RMS)
Cai et al. (1999)	CT-PET	Lungs	Rigid	T&L	CM	P&Pa.&SU	(x,y) 2-3 mm, (y) 3 - 4 mm, (rot.) 1.5°	mean
Pallotta et al. (1995)	PET-PET	Heart	Rigid	T&L	CM	P&SI	3 mm, (rot.) 1°	mean (RMS)
Gilardi et al. (1998)	SPECT-PET	Heart	Rigid	T&L	CM	P&Pa.	2.19 ± 0.52 mm	mean(RMS)±SDV
(Mäkelä et al., 2001)	MR-PET	Heart	Rigid	T&L	CM	SU	(x,y,z) 3 mm, 5 mm (z)	(x,y)mean (RMS), (z)mean
Mäkelä et al. (2003b)	MR-PET	Heart	Rigid	T&L	CM	SI	(x,y,z) 2.8 ± 0.5 mm	mean±SDV (RMS)
<b>Heart surface based registration</b>								
Faber et al. (1991)	MR-SPECT	Heart	Rigid	HS	h&h	P	2.7 mm	mean (RMS)
Sinha et al. (1995)	MR-PET	Heart	Rigid	HS	h&h	LM	1.95 mm ± 1.6 mm	mean (RMS)
Nekolla et al. (2000)	PET-SPECT	Heart	Rigid	HS	-	SU	2.5 mm	mean
Declercq et al. (1997)	SPECT-SPECT	Heart	Elastic	HS	ICP	Pa.	-	-
<b>Registration methods based on voxel similarity measures</b>								
<b>Intensity difference and correlation methods</b>								
Callippi et al. (2001)	MR-MR	Heart	Rigid & Elastic	-	C	M	1.23 ± 0.06 mm	left-right(mean) ant.-post.(mean)
Bidaut et al. (2001)	MR-MR	Heart	Rigid	-	SSD	LM	3.0 mm (x), 1.6 mm (y), 2.2 mm (z)	mean (RMS)
Bacharach et al. (1993)	PET-PET	Heart	Rigid	-	CC	M	(x,y,z) 1 mm, (rot.) 1.5°	(maximum) mean
Turkington et al. (1997)	PET-PET	Heart	Rigid	-	C	P	(x,y) 1.7 mm, (z) 4.2 mm	mean
Klein et al. (2002)	PET-PET	Heart	Elastic	-	LS	P	(x) 1.9 mm, (y) 2.4 mm, (z) 6.8 mm	mean (max.)
Hoh et al. (1993)	MR-SPECT	Heart	(4-D) Rigid	-	SAD, SSC	M	(x,y) 0.5 ± 0.5 mm, (z) 1.1 ± 1.1 mm, (rot) 0.9 ± 1.1°	mean ± SDV
Dey et al. (1999)	CT-SPECT	Heart&Thorax	Rigid	-	SAD VIR	P	2.5 ± 1.2 mm	mean (RMS)
Eberl et al. (1998)	SPECT-SPECT	Heart	Rigid	-	SAD	P	3.3 ± 1.3 mm	mean (RMS)
Slomka et al. (1995)	SPECT-SPECT	Heart	Affine	-	SAD	P	3.1 ± 1.7 mm	mean ± SDV
							1.3° (rot)	
							1.5 mm(x,y,z), 2.0° (rot), 5.3 % (size)	mean (max.)
<b>Mutual information</b>								
Carrillo et al. (2001)	MR-MR	Abdom.	Rigid	-	MI	LM	(x,y,z) 3.05 mm	mean
Mäkelä et al. (2003b)	MR-PET	Heart	Rigid	-	NMI	SI	(x,y,z) 4.8 ± 1.4 mm	mean±SDV (RMS)

#### **Abréviations utilisées Tableau I. :**

**Object** = Principales structures anatomiques à mettre en correspondance

**Trans.** = Méthode de transformation (rigide, affine, non rigide).

**Struc.** = Structures recalées (T = Thorax, L = Poumons, LM = Repères, HS = Surfaces cardiaques).

**Method** = Méthode utilisée dans le recalage: CM = distance de chanfrein, élast. = transformation non rigide ; h&h = « head-and-hat », int. = interpolation, LS = estimation aux moindres carrés,

**et les mesure de similarité** : C = corrélation croisée, CC = coefficient de corrélation, MI = information mutuelle, NMI = information mutuelle normalisée, SAD = somme des différences absolues, SSC = changement stochastique du signe, SSD = somme du carré des différences d'intensité, VIR = variance du rapport d'intensité.

**Valid.** = méthode de validation (P = fantôme, Pa. = patient, SI = images simulées, M = images non alignées, LM = repères anatomiques, SU = surfaces).

**Erreur** : rot. = erreur en rotation.

## 2.2 Principes de mise en correspondance

Le choix d'une méthode de recalage d'image cardiaque est difficile. En effet, il n'existe à l'heure actuelle aucune méthode complètement automatisée qui pourrait prendre en charge la grande variété des situations cliniques rencontrées (modalités, protocoles d'acquisition, etc.).

Les méthodes de recalage des images cardiaques et thoraciques peuvent être réparties en deux catégories principales : (1) les méthodes de recalage basées sur les caractéristiques géométriques de l'image et (2) les méthodes basées sur des mesures de similarité de voxels [Mäkelä, 2002a].

- **Méthodes basées sur des caractéristiques géométriques**

Les méthodes basées sur les caractéristiques géométriques de l'image peuvent être divisées en le recalage d'un *ensemble de points* et des méthodes qui recalent *les bords/contours ou les surfaces*. Les méthodes de recalage d'images cardiaques sont souvent validées à l'aide d'expériences pratiquées sur un fantôme dans lesquelles des jeux correspondants de points de repère externes sont recalés [Pallotta, 1995], [Yu, 1995], [Eberl, 1996], [Gilardi, 1998], [Dey, 1999]. De même, des validations basées sur des repères utilisent typiquement le recalage de jeux de points de repère correspondants ou homologues [Kramer, 1989], [Savi, 1995], [Sinha, 1995], [Eberl, 1996], [Gilardi, 1998], [Carrillo, 2001], [Bidaut, 2001]. Des repères ont aussi été utilisés pour la mise en correspondance élastique d'IRM thoraciques avec des images TDM [Wirth, 1997]. Dans [Mäkelä, 2002b], une méthode de recalage basée sur des repères cutanés a été utilisée pour mettre en correspondance des images RM cardiaques et des données de MCG. La méthode des moindres carrés non itérée [Arun, 1987] a été utilisée pour mettre en correspondance les deux jeux de points de repères homologues.

Les méthodes de recalage basées sur les contours et les surfaces incluent des méthodes qui recalent les surfaces cardiaques [Faber, 1991], [Thirion, 1995], [Sinha, 1995], [Andersson, 1995], [Declerck, 1997], [Thirion, 2001], [Nekolla, 2000] et les surfaces thoraciques [Pallotta, 1995], [Yu, 1995], [Tai, 1997], [Gilardi, 1998], [Cai, 1999], [Mäkelä, 2001]. Les méthodes de recalage où une image de transmission (TEP, TEMP) est utilisée comme médiateur pour recaler l'image d'émission correspondante, reposent sur l'hypothèse que le patient ne bouge pas pendant et entre les acquisitions des images de transmission et d'émission [Kim, 1991], [Pallotta, 1995], [Yu, 1995], [Tai, 1997], [Gilardi, 1998], [Cai, 1999], [Mäkelä, 2001]. Étant donné que les temps d'acquisition de l'image dans les images cardiaques TEP et TEMP de transmission et d'émission sont souvent de plusieurs minutes, des artefacts de mouvement sont fréquents. Pour l'imagerie TEMP, un mouvement supérieur à 2-3 cm entre l'acquisition de l'image TEMP cardiaque de transmission et d'émission altère sérieusement la

correction de l'atténuation de l'image d'émission et, par conséquent, sa qualité [Stone, 1998]. La méthode d'appariement par carte de distance de chanfrein [Borgefors, 1986, 1988] est souvent utilisée pour recalcr des surfaces et des jeux de points. Cette méthode minimise la somme des distances entre les points transformés et une carte de distances, établie à partir des surfaces segmentées à l'aide de la transformation des distances de chanfrein [Herk, 2000]. Les méthodes d'appariement à partir des cartes de chanfrein ont été principalement utilisées pour le recalcr des structures thoraciques [Pallotta, 1995], [Gilardi, 1998], [Cai, 1999], [Mäkelä, 2001]. De même, l'algorithme ICP de Besl et McKay [Besl, 1992] a été utilisé pour recalcr des lignes et des surfaces [Declerck, 1996b, 1997]. Dans l'algorithme ICP, les distances entre les structures sont explicitement calculées à chaque itération de l'algorithme de recalcr en vue de la minimisation de la somme des distances. L'algorithme « head-and-hat » [Pelizzari, 1989], [Levin, 1988] a également été fréquemment utilisé pour recalcr des images médicales et en premier lieu pour recalcr des images du cerveau. L'algorithme représente les contours d'une image (habituellement une image à haute résolution) sous la forme d'une surface (la tête ; « head ») et les contours de l'autre image sous la forme d'une série de points (le chapeau ; « hat »). La méthode « head-and-hat » détermine la transformation optimale qui minimise la somme des distances entre les points du chapeau « hat » et les surfaces de la tête « head » dans un processus itératif (méthode de Powell). Cette méthode a été appliquée au recalcr d'images cardiaques [Faber, 1991], [Sinha, 1995] et thoraciques [Yu, 1995]. Dans [Mäkelä, 2001], une méthode de recalcr d'images cardiaques RM et TEP-FDG a été présentée. Elle est basée sur la mise en correspondance des surfaces thoraciques et pulmonaires. La méthode diffère des méthodes de recalcr précédemment introduites (par exemple, [Pallotta, 1995], [Gilardi, 1998]), car elle inclue notamment une segmentation automatique, basée sur un modèle déformable, des surfaces thoraciques et pulmonaires dans les images thoraciques RM et TEP de transmission. Un autre avantage de cette méthode de recalcr est qu'elle peut recalcr des images par RM transverses, et également en PA avec la TEP.

- **Méthodes basées sur des mesures similarité**

Les méthodes de recalcr basées sur des mesures de similarité d'intensité de voxels incluent des méthodes de type « *moments et axes principaux d'inertie* », « *différences d'intensité* », « *corrélacion* », ainsi que des méthodes basées sur « *l'information mutuelle* ». Les méthodes basées sur les *moments* sont principalement utilisées dans les étapes d'initialisation d'autres méthodes plus précises [Slomka, 1995], [Dey, 1999]. Les méthodes de « *différences d'intensité* » ont été principalement utilisées pour des recalcrs intramodalités [Hoh, 1993], [Slomka, 1995, 2001], [Bidaut, 2001], [Klein, 2002a, 2002b] et aussi dans quelques cas pour des recalcrs intermodalités SPECT-PET [Eberl, 1996], SPECT-CT [Dey, 1999].

Les « *méthodes de corrélacion* » ont été principalement utilisées pour des recalcrs intramodalités [Bettinardi, 1993], [Bacharach, 1993], [Turkington, 1997], [O'Connor, 1998, 2000], [Gallippi, 2001] et aussi pour le recalcr intermodalité de structures

thoraciques segmentées [Kim, 1991]. A ce jour, les méthodes de recalage d'images cardiaques et thoraciques basées sur l'*information mutuelle* ne sont pas très nombreuses dans la littérature [Carrillo, 2001], [Zhenghong, 2002], [McLeish, 2003], [Shekhar, 2002], [Mattes, 2003], [Lötjönen and Mäkelä 2001], [Mäkelä, 2003b]. Dans [Lötjönen and Mäkelä, 2001], une méthode de recalage élastique d'images cardiaques RM-TEP, combinant l'information mutuelle, des informations de gradient et un lissage de la transformation, a été mise au point pour guider la déformation d'une image vers une image de référence. Cette méthode est détaillée dans le chapitre 5. Le principe des méthodes de recalage utilisant des mesures de similarité de voxels repose sur les transformations itératives de l'image source vers l'image cible [Maes, 1997], [Hajnal, 2001], [Woods, 2000a]. Ces approches nécessitent l'évaluation de la transformation à chaque fois qu'un nouveau jeu des paramètres de transformation est sélectionné. La vitesse de l'algorithme de recalage dépend de facteurs comme la nécessité de pratiquer un prétraitement, la complexité de la fonction coût et le nombre d'évaluations de la fonction coût effectuées par l'algorithme d'optimisation [Herk, 2000]. Avec des méthodes de recalage basées sur la similarité de voxels, le nombre d'évaluations de fonctions coût est habituellement élevé. Des techniques rapides d'évaluation de la fonction coût et des schémas multi-résolutions accélèrent généralement la convergence de ce type d'algorithmes de recalage [Lötjönen and Mäkelä 2001].

Les méthodes manuelles [Waiter, 2000], [Behloul, 2001] peuvent être considérées comme une catégorie à part de méthodes de recalage. Elles reposent habituellement sur l'aptitude d'un expert à recaler des images de façon interactive. Les images sont généralement interpolées aux mêmes dimensions de voxel avant le recalage manuel.

## 2.3 Obtention de la transformation optimale

Pour l'optimisation du recalage rigide d'une image en 3-D, une fonction coût de 6 paramètres (3 translations et 3 révolutions) est généralement minimisée. Dans des méthodes de recalage affines, projectives et non rigides, la fonction coût présente davantage de paramètres. Une recherche globale pour trouver le minimum (ou le maximum) de la fonction de coût est habituellement trop coûteuse du point de vue des calculs. Le but des méthodes d'optimisation est la recherche rapide d'un optimum de cette fonction de coût. Les méthodes qui ne nécessitent pas l'évaluation du gradient de la fonction coût sont généralement privilégiées. La méthode d'optimisation de Powell [Powell, 1962], [Press, 1992] a donc été largement utilisée dans les méthodes de recalage cardiaque et thoracique [Faber, 1991], [Yu, 1995], [Cai, 1999], [Dey, 1999], [Carrillo, 2001], tout comme la méthode d'optimisation du Simplexe [Nelder, 1965], [Press, 1992] pour le recalage des images cardiaques [Hoh, 1993], [Slomka, 1995, 2001], [Eberl, 1996], [Dey, 1999]. De même, les techniques multi-résolution peuvent être adoptées avec succès pour augmenter la probabilité de trouver l'optimum global



dans l'espace des paramètres et pour accélérer le processus de recalage [Pallotta, 1995], [Bidaut 2001], [Lötjönen and Mäkelä 2001].

## 2.4 Evaluation du recalage

L'évaluation de la précision du recalage est une tâche difficile en imagerie médicale, en raison généralement de l'absence de référence [Fitzpatrick, 2000], [Woods, 2000b], [Hajnal, 2001]. L'évaluation des méthodes de recalage est souvent effectuée à l'aide de repères externes ou de repères anatomiques servant de référence [Woods, 2000b]. L'inspection visuelle est la méthode la plus évidente d'évaluation qualitative de la précision du recalage, mais elle doit être considérée comme étant une approche informelle et insuffisante. Pour les méthodes de recalage basées sur les surfaces thoraciques, la précision du recalage a été évaluée à l'aide de fantômes thoraciques [Bettinardi, 1993], [Pallotta, 1995], [Yu, 1995], [Eberl, 1996], [Gilardi, 1998], [Kramer, 1989], [Cai, 1999], [Dey, 1999] ou de fantômes cardiaques [Turkington, 1997]. Klein *et al.* [Klein, 2002a, 2002b] ont utilisé un fantôme cardiaque numérique et dynamique (fantôme MCAT) [Pretorius, 1997] pour évaluer un algorithme de correction du mouvement en 4-D d'images cardiaques TEP. Des images simulées peuvent aussi être utilisées pour estimer la précision du recalage d'images cardiaques [Pallotta, 1995], [Tai, 1997], [Pauna, 2003], [Mäkelä, 2003b]. Des dispositifs d'imagerie intégrés, tels que les scanners TEP/TDM [Beyer, 1999], [Patton, 2000] pourraient aussi fournir des références pour l'évaluation de méthodes de recalage [Goerres, 2002].

## 2.5 Conclusions

A la lecture de cette brève vue d'ensemble, il est clair que le recalage d'images cardiaques et thoraciques a été envisagé dans différents contextes cliniques impliquant des modalités et des objectifs différents. Dans la plupart des cas, des transformations rigides sont considérées, ce qui signifie en général une simplification du problème de recalage. De même, il est très difficile, à ce jour, de comparer les méthodes en raison de l'absence de procédures d'évaluations communes. Des informations issues des publications concernant l'évaluation des méthodes figurent dans le tableau 1 et peuvent être considérées comme premiers indicateurs de performance.

Dans l'objectif de construire un modèle cardiaque spécifique au patient, nous introduisons dans le prochain chapitre, une nouvelle méthode permettant de combiner des informations anatomiques à partir de l'imagerie par RM et des informations fonctionnelles à partir à la fois de l'imagerie TEP et MCG. Comme nous le verrons, il s'agit d'une méthode basée sur le recalage rigide des surfaces de structures anatomiques extraites. En nous basant sur un travail dans le cadre d'une autre thèse, la méthode est évaluée et l'influence de différents paramètres de la méthode peut alors être étudiée.

### 3. Recalage de données cardiaques anatomiques et fonctionnelles

Dans le cadre d'études de viabilité myocardique, des médecins de l'Hôpital Central Universitaire de Helsinki (Helsinki University Central Hospital - HUCH) ont acquis des données anatomiques et fonctionnelles auprès d'une dizaine de patients présentant une ischémie aiguë.

Une nouvelle méthode de recalage des données acquises a été développée pour aider l'analyse par les cliniciens. Cette méthode permet la superposition des informations anatomiques et fonctionnelles pour un patient donné. Les données cardiaques, les méthodes et leurs principes sont décrits dans les sections suivantes. L'évaluation de la méthode de recalage IRM-TEP est aussi présentée. Elle repose sur une simulation numérique réaliste.

#### 3.1 Données cardiaques

Dans ce travail, des données IRM et TEP-18F-FDG d'émission et de transmission [Mäkelä, 2001, 2003a], [Lötjönen and Mäkelä 2001], [Lauerma, 2000] et des données MCG [Mäkelä, 2003a] ont été obtenues chez dix patients (E1 - E10, âge moyen de 69 ans, 8 hommes, 2 femmes) souffrant de coronaropathie multitrunculaire, diagnostiquée par angiographie coronarienne et par la présence d'une dyskinésie régionale sur des ciné-angiogrammes [Lauerma, 2000]. Tous les patients ont eu un bilan par imagerie RM et 18F-FDG TEP dans un délai de 10 jours. Ils ont ensuite subi une intervention chirurgicale de pontage coronarien. Six mois plus tard, l'examen IRM a été répété pour l'évaluation de la réponse myocardique après revascularisation. Dans ce travail, nous utilisons les images RM préopératoires.

- **Données IRM**

Les données IRM ont été acquises avec un imageur Siemens, Magnetom Vision 1.5 T (Siemens, Erlangen, Allemagne) au service de radiologie de l'Hôpital Central Universitaire de Helsinki (Helsinki University Central Hospital - HUCH). Deux séries d'images ont été acquises : une série d'images thoraciques transverses avec synchronisation à l'ECG, comprenant 40 coupes environ, en partant du cou vers le pelvis, et une série dynamique d'images en mode ciné petit axe, comportant 5 à 10 coupes débutant au niveau du plan des valves en descendant vers l'apex du VG. Les images thoraciques transverses ont été acquises pendant une respiration libre à l'aide d'une séquence TurboFLASH [Siemens, 2001], [Raichura, 2001] avec une antenne corps. La taille des pixels et l'épaisseur de coupe pour les images transverses sont respectivement de 1.95 x 1.95 mm<sup>2</sup> et de 10 mm (Fig. 3a). Les coupes IRM en petit axe (Fig. 3b) comportent 10 à 15 phases du cycle cardiaque et ont été acquises en



synchronisation à l'ECG et en apnée. La taille des pixels pour les coupes PA est de  $1.25 \text{ mm} \times 1.25 \text{ mm}^2$  et l'épaisseur de coupe est de 7 mm avec une distance de 15 mm entre les coupes. Les données IRM utilisées dans certaines évaluations [Mäkelä, 2002b] ont été acquises avec des paramètres un peu différents (voir [Mäkelä, 2002b] pour de plus amples détails).

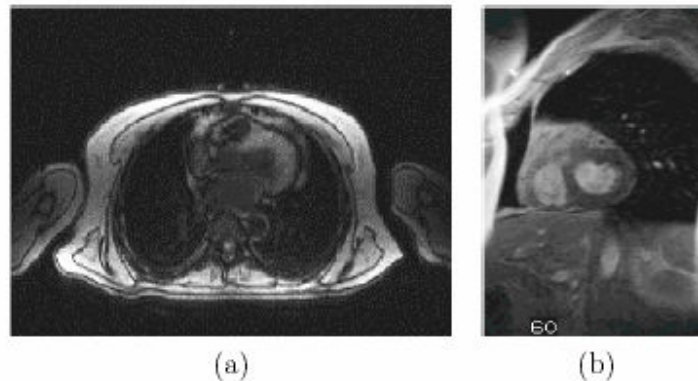


Figure 3 : Images par RM (a) transverses et (b) en petit axe.

Un protocole d'acquisition typique d'images RM cardiaques avec synchronisation à l'ECG est présenté en Fig. 4. Il existe un problème de localisation spatio-temporelle des plans de coupes: on n'observe pas la même région anatomique à un même niveau de coupe pendant la séquence temporelle. Entre la télé-diastole et la télé-systole, le plan des valves cardiaques descend de 9 à 14 mm en direction de l'apex, et les parois myocardiques s'épaississent de 10 mm à plus de 15 mm environ [Rogers, 1991], [O'Dell, 1995], [Klein, 2002a, 2002b].

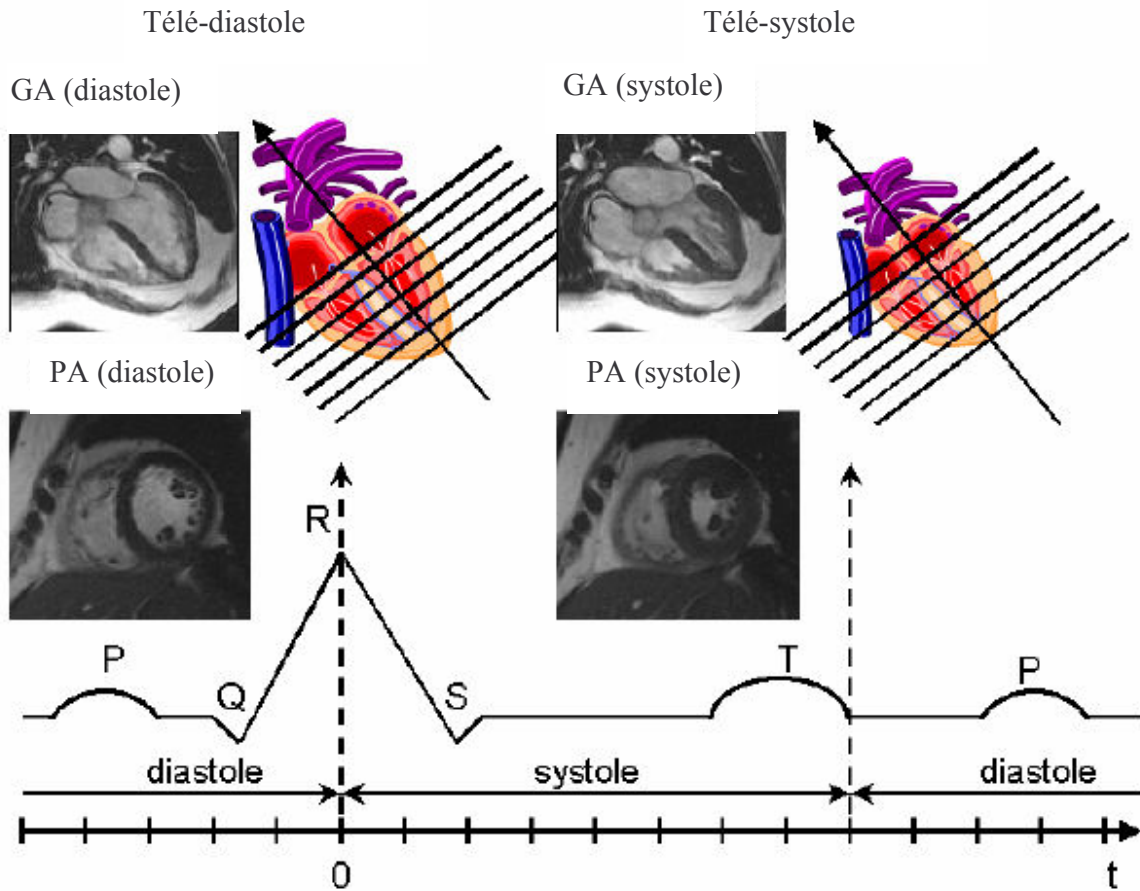


Figure 4 : Acquisition d'images RM en petit axe et en grand axe en mode ciné, synchronisée à l'ECG. Les images RM en PA et GA sont présentées en télé-diastole et télé-systole. En raison du mouvement 3-D du cœur, une même coupe n'observe pas la même région anatomique [Mäkelä, 2002a].

- **Données TEP**

Les données TEP cardiaques d'émission statiques marquées au  $^{18}\text{F}$ -FDG et les données TEP de transmission ont été acquises avec un imageur TEP Siemens, ECAT 931/08-12 (Siemens/CTI, Knoxville, USA) au Turku PET center. Une série de 15 images TEP contiguës de transmission et d'émission  $^{18}\text{F}$ -FDG a été obtenue (Fig. 5a, 5b). Pour les images de transmission et d'émission, la taille des pixels et l'épaisseur de coupe sont respectivement de  $2.41 \times 2.41 \text{ mm}^2$  et de 6,75 mm.

Les images TEP de transmission sont utilisées pour la correction de l'atténuation des images d'émission, mais fournissent aussi des informations structurales qui seront utilisées pour le recalage [Mäkelä, 2001].

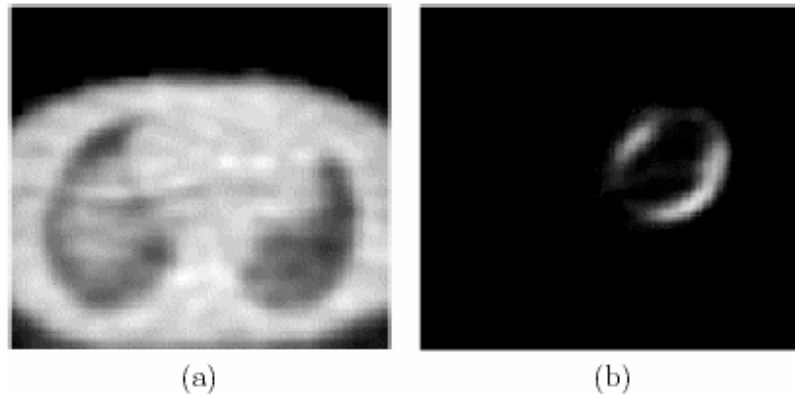


Figure 5 : Images TEP de (a) transmission et (b) d'émission 18F-FDG [Mäkelä, 2001].

L'image TEP d'émission 18F-FDG représente le métabolisme glucidique dans le tissu myocardique. Les images TEP d'émission et de transmission ont été acquises l'une après l'autre sans déplacer le patient. Si aucun mouvement significatif ne survient entre et pendant les acquisitions des images, on estime que l'image TEP d'émission 18F-FDG est recalée avec l'image de transmission correspondante [Kim, 1991], [Bacharach, 1993], [Bettinardi, 1993], [Pallotta, 1995], [Gilardi, 1996].

- **Données MCG**

Les mesures MCG ont été réalisées au repos et à l'effort avec un cardiomagnétomètre à 67 canaux (4-D NeuroImaging, Helsinki, Finlande) au laboratoire BioMag de HUCH [Montonen, 2000]. Une ischémie aiguë a été induite par test d'effort avec un ergomètre non magnétique d'effort [Hänninen, 2001] et pédalage en décubitus dorsal. Les signaux de différence du segment ST des enregistrements moyennés au repos et après effort sont exploités pour l'estimation des densités de courant (EDC) [Nenonen, 2001]. Dans ce travail, nous avons utilisé les données de dépolarisation (complexe QRS) au repos. Des modèles de thorax patient-spécifiques ont été obtenus à partir des images RM. Ils incluent les surfaces triangulées du thorax et du ventricule gauche (VG) [Lötjönen, 1999], [Pham, 2001]. Le thorax se voit assigner une conductivité électrique constante. Les valeurs discrètes des densités de courant ont été estimées sur le VG à mi-paroi. Un estimateur du maximum *a posteriori* (MAP) est utilisé pour la régularisation du problème inverse [Nenonen, 2001].

### 3.2 Recalage d'images RM cardiaques anatomiques et TEP métaboliques

Pour le diagnostic précis des pathologies ischémiques et les études de viabilité, on pratique actuellement l'acquisition d'images par RM cardiaques en petit axe. Dans certains cas, l'examen TEP est réalisée afin de fournir une référence pour l'estimation

de la viabilité. En raison du manque de repères anatomiques fiables correspondants, le recalage direct d'images RM en petit axe avec des images TEP est un problème difficile. Les résultats des expériences que nous avons réalisées dans cette situation particulière de recalage sont médiocres et ne sont pas exploitables [Pauna, 2003]. Nous avons donc décidé de considérer le recalage des structures thoraciques visibles à la fois sur les images TEP de transmission et les images RM transverses.

Les principales étapes de la méthode de recalage que nous proposons sont présentées à la figure 6 et décrites ci-dessous :

- 1) Redimensionnement des image qui est réalisé pour avoir des dimensions de voxel isotropes pour les images TEP de transmission, d'émission 18F-FDG et RM transverses . Une interpolation trilineaire est utilisée pour redimensionner les images TEP de transmission et d'émission pour les faire correspondre à la taille isotrope des voxels de l'image RM ( $1.95 \times 1.95 \times 1.95 \text{ mm}^3$ ).
- 2) Segmentation automatique du thorax et des poumons qui est effectuée pour les images TEP de transmission et RM transverses, à l'aide d'une méthode basée sur des modèles déformables 3-D [Lötjönen, 1999]. Les surfaces extraites sont représentées par des triangulations.
- 3) Sélection automatique d'un jeu de points provenant des surfaces segmentées du thorax et des poumons dans le modèle TEP. Il s'agit des nœuds uniformément distribués du modèle triangulé déformé [Lötjönen, 1998].
- 4) Calcul des paramètres rigides de recalage (3 translations, 3 rotations) pour trouver le meilleur recalage entre le jeu de points et les surfaces de l'image RM segmentée en utilisant la méthode d'appariement par cartes de distance de chanfrein [Borgefors, 1988].
- 5) Recalage de l'image TEP-FDG d'émission avec l'image RM transverse, obtenu à l'aide des paramètres de recalage calculés.
- 6) Recalage des images RM en petit axe avec les données TEP d'émission 18F-FDG . Les informations relatives aux positions des coupes présentes dans l'en-tête de l'image RM donnent la transformation entre les coupes RM transverses et en PA. Des coupes TEP d'émission 18F-FDG en petit axe correspondant aux coupes IRM-PA sont calculées à partir des images TEP transverses recalées.

La méthode est entièrement décrite dans [Mäkelä, 2001]. Les étapes de segmentation et de recalage sont développées ci-après.

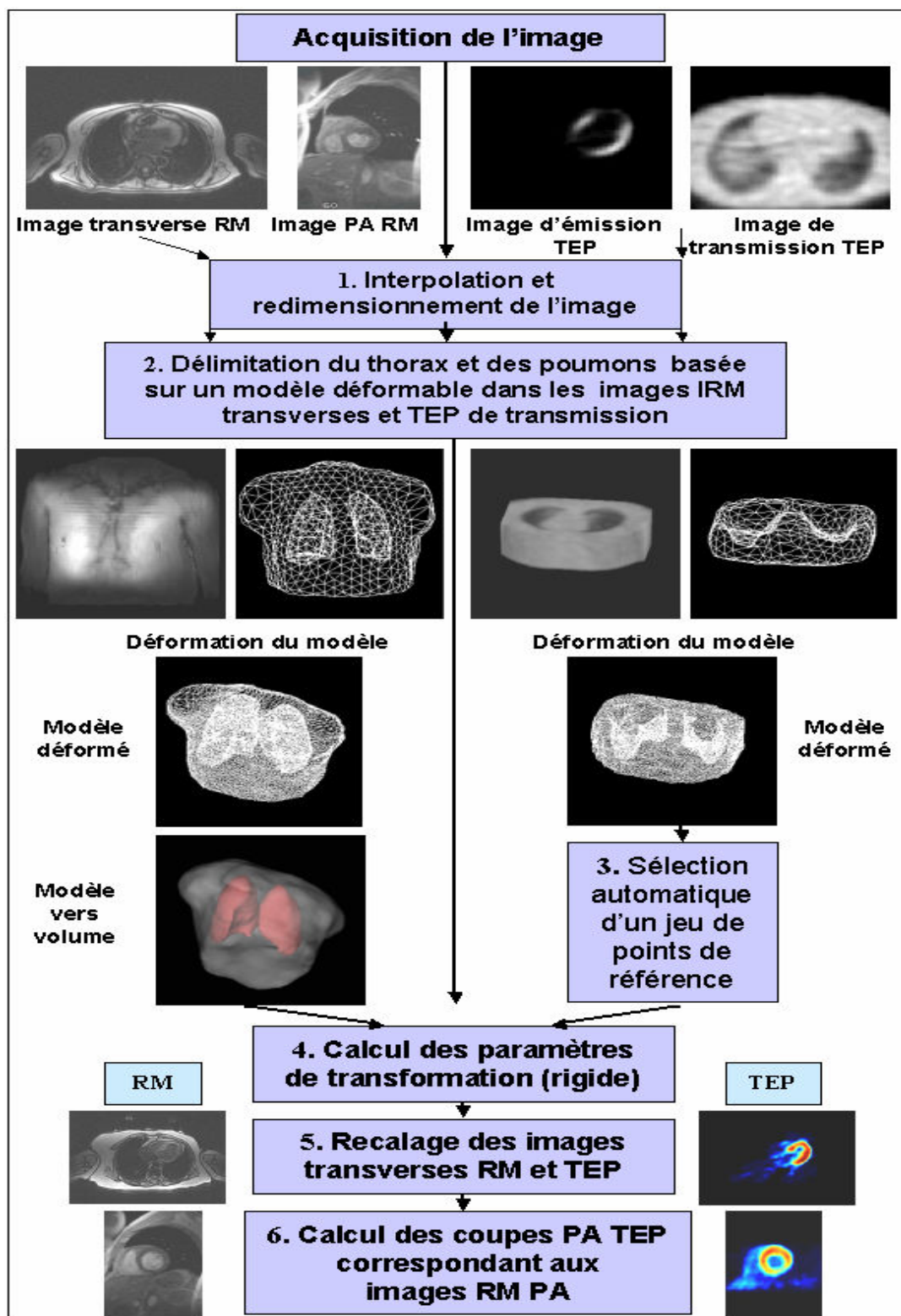


Figure 6 : Principales étapes de la méthode rigide de recalage d'images RM et TEP thoraciques et cardiaques

### 3.2.1 Segmentation des structures thoraciques

La segmentation des structures thoraciques est basée sur la déformation élastique (déformations de forme libre) d'un modèle *a priori* topologique et géométrique 3D à l'aide d'une approche multi-résolution [Lötjönen, 1999]. Un modèle de thorax incluant un thorax triangulé et les surfaces pulmonaires est utilisé avec les images RM transverses (Fig. 7a). Avec les images TEP de transmission, en raison d'un champ de vue réduit, on utilise un modèle tronqué qui ne comporte qu'une partie du thorax (Fig. 7b).

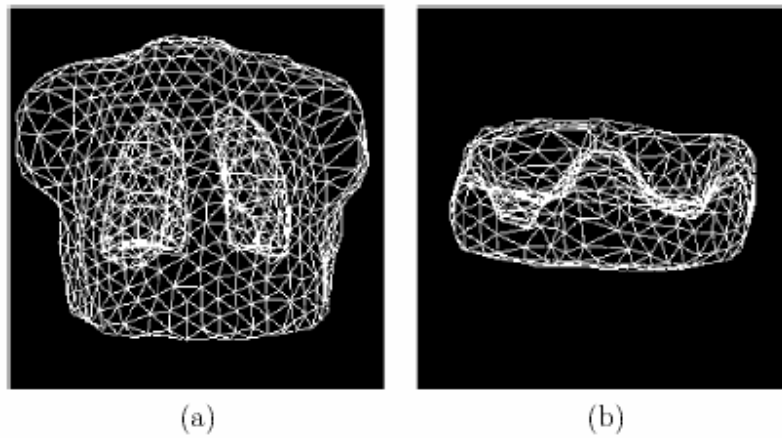


Figure 7 : Modèle *a priori* topologique et géométrique du thorax pour la segmentation 3D de l'image (a) RM transverse et de l'image (b) TEP de transmission .

L'algorithme de déformation adapte le modèle *a priori* pour le faire correspondre localement aux contours dans l'image via un processus de minimisation d'énergie. L'énergie à minimiser est ;

$$E_{total} = E_{image} + \gamma E_{modèle} \quad (1)$$

où  $E_{image}$  représente l'erreur de recalage entre le modèle préalable et les contours partiels dans l'image. Le terme d'énergie  $E_{modèle}$  tend à préserver la forme du modèle en limitant la déformation du modèle *a priori*. Il décrit la déviation des normales à la surface du modèle par rapport à leur orientation d'origine. Le paramètre  $\gamma \in [0,1]$  fixe la contribution relative des deux composantes d'énergie. Une approche multi-résolution est utilisée pour la minimisation de la fonction énergie. L'énergie de l'image est calculée à l'aide de cartes de distance orientées [Lötjönen, 1999] construites sur les contours extraits obtenus à partir d'une détection de contour (estimateur de Canny-Deriché [Canny, 1986], [Deriché, 1987]) ou du seuillage de l'image. En pratique, la détection des contours par l'opérateur de Canny-Deriché est préférée pour les images RM ainsi qu'avec la plupart des images TEP de transmission . Les contours du thorax et des poumons sont en général bien détectés (inspection visuelle), à la fois dans les images RM transverses



et les images TEP de transmission, même si les contours des images TEP de transmission sont plus lisses qu'en IRM (Fig. 8 et Fig. 9). Avec des images RM, une erreur maximum de 7 à 10 voxels (erreur moyenne de 1 voxel) a été obtenue pour les résultats des segmentations basées sur le modèle déformable par rapport à des segmentation réalisées par un expert [Lötjönen, 1999].

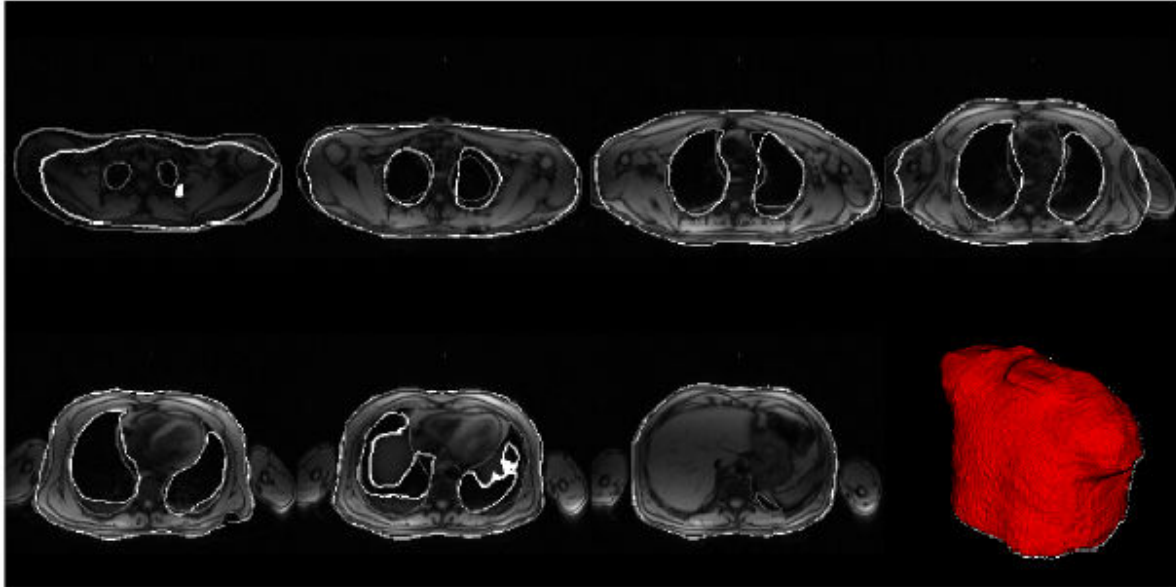


Figure 8 : Image RM segmentée . Les contours blancs représentent le résultat de la segmentation obtenue avec le modèle déformable et les contours gris, le résultat de la segmentation manuelle (visualisation du résultat de la segmentation en 3-D dans l'angle inférieur droit).

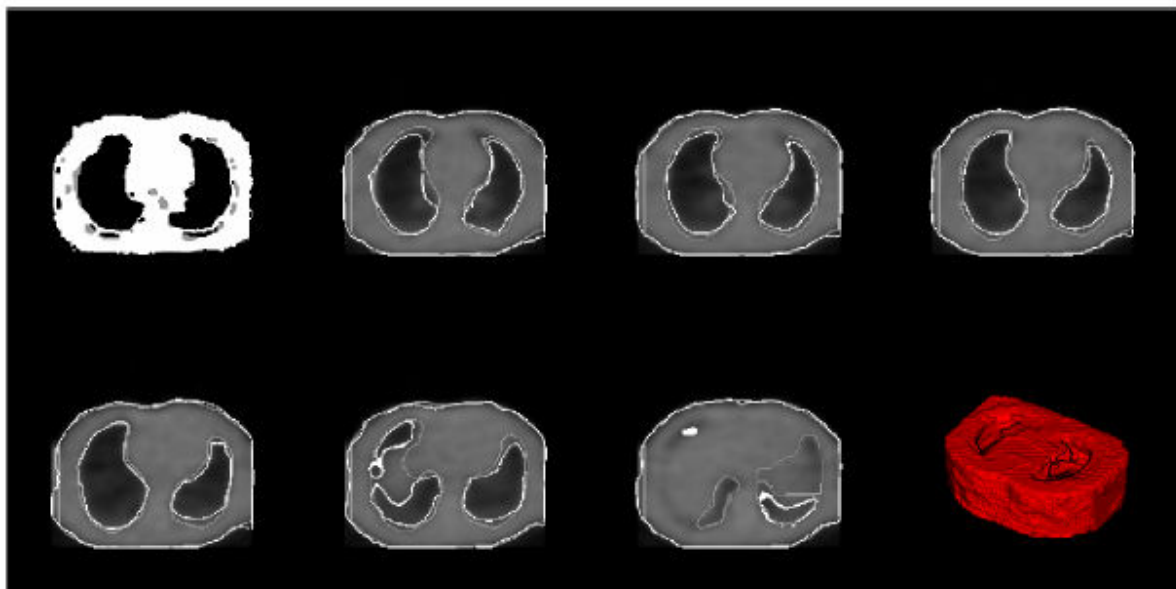


Figure 9 : Image TEP de transmission segmentée . Les contours blancs représentent le résultat de la segmentation obtenue avec le modèle déformable et les contours gris, le résultat de la segmentation manuelle (visualisation du résultat de la segmentation en 3-D dans l'angle inférieur droit).

### 3.2.2 Calcul de la transformation optimale du recalage

L'optimisation des paramètres rigides de recalage est effectuée à l'aide d'une méthode non standard, intitulée ici *méthode d'optimisation sur grille discrète* [Mäkelä, 2001]. Les paramètres de recalage optimaux minimisent la distance d'un jeu de points nodaux issus de la surface de l'image TEP de transmission aux surfaces extraites des structures de l'image RM. Les distances entre les points nodaux transformés et les surfaces segmentées sont calculées à l'aide de l'algorithme de cartes de distance de chanfrein [Borgefors, 1988]. Dans la figure 10, on peut voir un exemple de carte de distance calculée à partir des surfaces issues de l'IRM.



Figure 10 : Deux vues orthogonales d'une carte de distance 3D calculée à partir des surfaces thoracique et pulmonaires extraites des IRM. L'algorithme de recalage minimise la distance de ces surfaces avec les points des surfaces issues de l'image TEP de transmission en utilisant la carte de distance [Mäkelä, 2003a].

Dans la méthode d'optimisation sur grille discrète, on recherche l'optimum d'un vecteur de 6 paramètres (3 translations, 3 rotations) de façon itérative dans un espace de recherche discret. L'espace discret de recherche est tout d'abord partitionné à l'aide d'une grille dont la densité est définie par l'utilisateur (Fig. 11, voir [Mäkelä, 2001] pour de plus amples détails). La fonction de coût à minimiser dépend des 6 paramètres de la transformation. Par souci de simplicité, l'algorithme de minimisation n'est décrit ici que pour 2 paramètres de translation selon les directions  $x$  et  $y$  du plan 2-D. L'extension à 6 paramètres est directe. Les paramètres à optimiser forment le vecteur de paramètres  $(t_1, t_2)$ . Le vecteur optimal est recherché de façon itérative dans l'espace de recherche discret. La position initiale de ce vecteur est  $(t_{10}, t_{20})$  (Fig. 11).



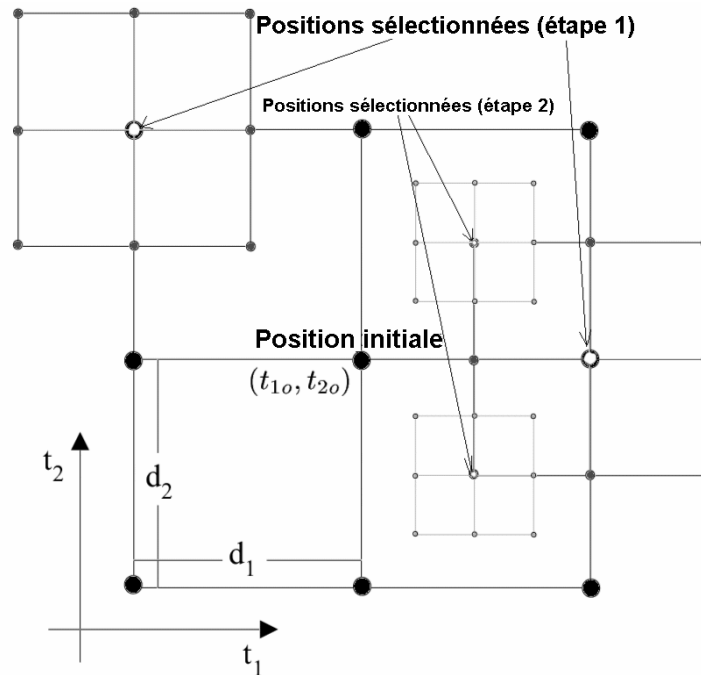


Figure 11 : Principe de recherche des paramètres optimaux de translation (voir texte pour symboles et explications)

Les étapes itératives pour la recherche d'un nouveau vecteur de paramètres sont les suivantes à l'itération  $k$ :

- 1) Détermination des valeurs possibles pour le paramètre de translation  $t_k$ ,  $ke[1,2]$  :  $t_k - gd_k$ ,  $t_k - (g-1)d_k, \dots, t_k, \dots, t_k + gd_k$ , où  $g$  est un paramètre entier positif défini par l'utilisateur modifiant le nombre de nouvelles valeurs possibles, et où le paramètre  $d_k$  (nombre réel positif) représente le pas de variation du paramètre  $t_k$ .
- 2) La fonction de coût est calculée pour les  $(2g+1)^n$  combinaisons du vecteur de paramètres, où  $n$  est le nombre de paramètres (gros points dans la Fig. 11, dans cet exemple  $n = 2$ ),.
- 3) Un nombre  $m$  ( $m=2$ , ici) de combinaisons défini par l'utilisateur, ayant l'erreur de recalage la plus faible est sélectionné en tant que nouveaux vecteurs de paramètres initiaux de l'itération  $k+1$  (positions sélectionnées de l'étape 1, points en blanc, Fig. 11).
- 4) Chaque pas  $d_k$  est divisé par 2.

- 5) Les étapes 1-2 sont répétées pour les  $m$  vecteurs de paramètres initiaux. Ensuite, les étapes 3-4 donnent à nouveau  $m$  optima locaux. Ainsi, le nombre de vecteurs de paramètres initiaux reste constant au cours des itérations. L'algorithme itère jusqu'à ce que la fonction de coût ne diminue pas de plus d'une faible valeur prédéfinie.

L'algorithme ne converge pas nécessairement vers le minimum global de la fonction coût. Cependant, la méthode échantillonne davantage l'espace de recherche que la méthode de base de descente de gradient et permet de trouver le minimum avec une probabilité plus importante. La méthode permet aussi de limiter l'espace de recherche; il est en effet très facile de borner les rotations et les translations. Des optimisations plus standard comme les méthodes multidimensionnelles de Powell et du Simplexe ont également été comparées lors de l'évaluation décrite au paragraphe 3.3.

### **3.2.3 Résultats des recalages rigides**

Dix jeux de données de patients comportant des images RM et TEP de transmission et d'émission ( $^{18}\text{F}$ -FDG) ont été recalés de façon rigide dans [Mäkelä, 2001]. Les figures 12 et 13 présentent des images TEP-FDG d'émission recalées de façon rigide à des images RM transverses et en petit axe en télé-diastole pour le cas E1 (voir [Mäkelä, 2001] pour plus de détails). Les résultats en petit axe sont présentés en mode mosaïque en figure 14. La figure 15 présente le recalage rigide d'images RM-PA avec des images TEP-FDG d'émission, en télé-diastole pour le cas E2.

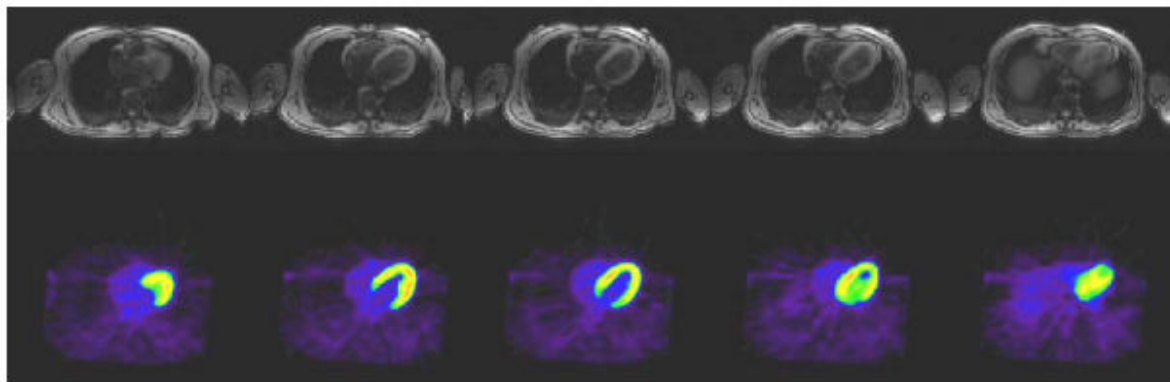


Figure 12 : Coupes IRM transverses (en haut) recalées à des images TEP 18F-FDG (en bas) en télédiastole pour le cas E1.

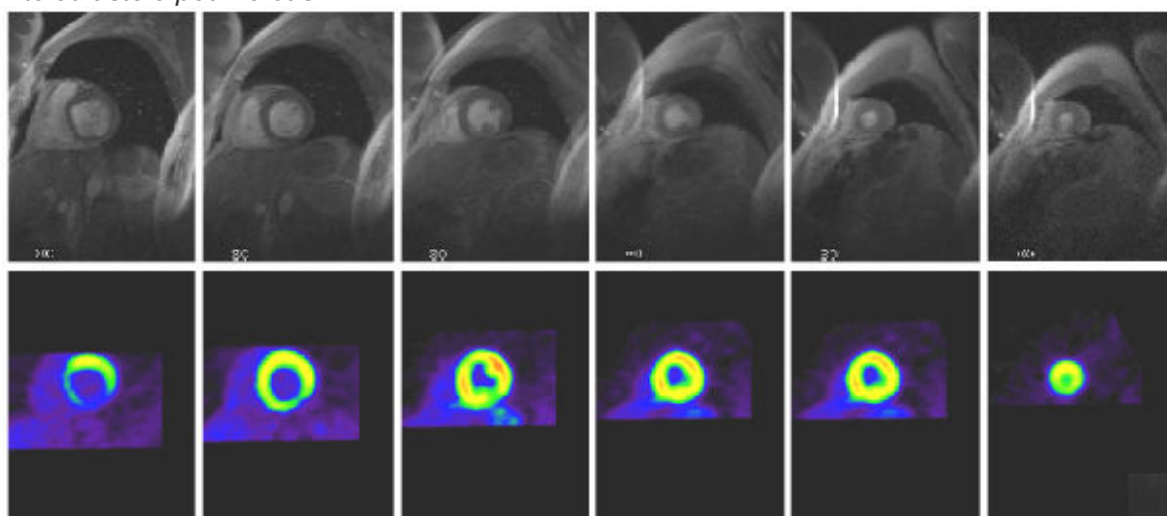


Figure 13 : Coupes IRM en petit axe (en haut) recalées à des images TEP 18F-FDG (en bas) en télédiastole pour le cas E1.

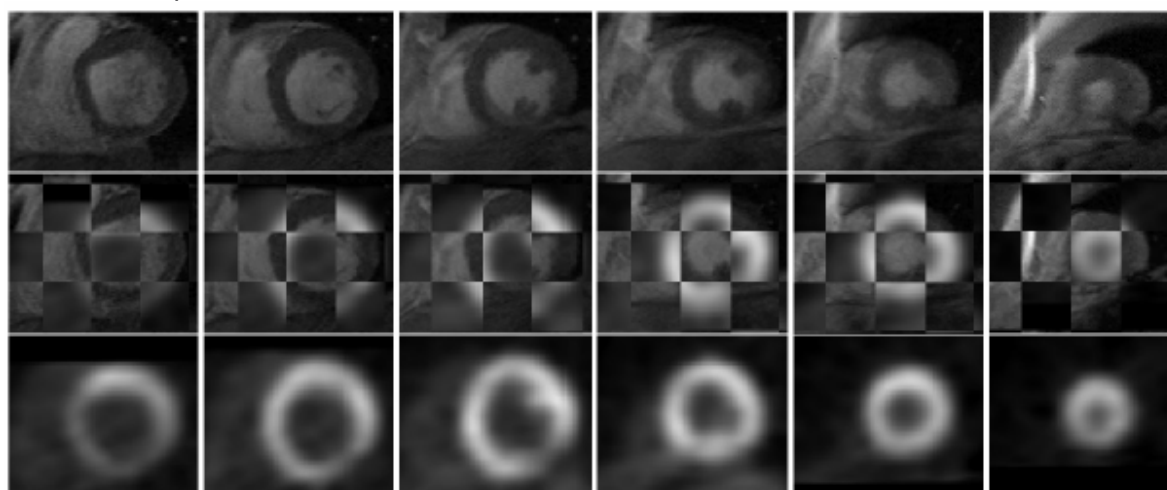


Figure 14 : Coupes IRM-PA centrées sur la région du cœur (en haut) recalées à des images TEP-FDG (en bas) pour le cas E1 en télédiastole. La rangée du milieu est une présentation en mosaïque du recalage où l'on peut juger de la superposition des données IRM et TEP.

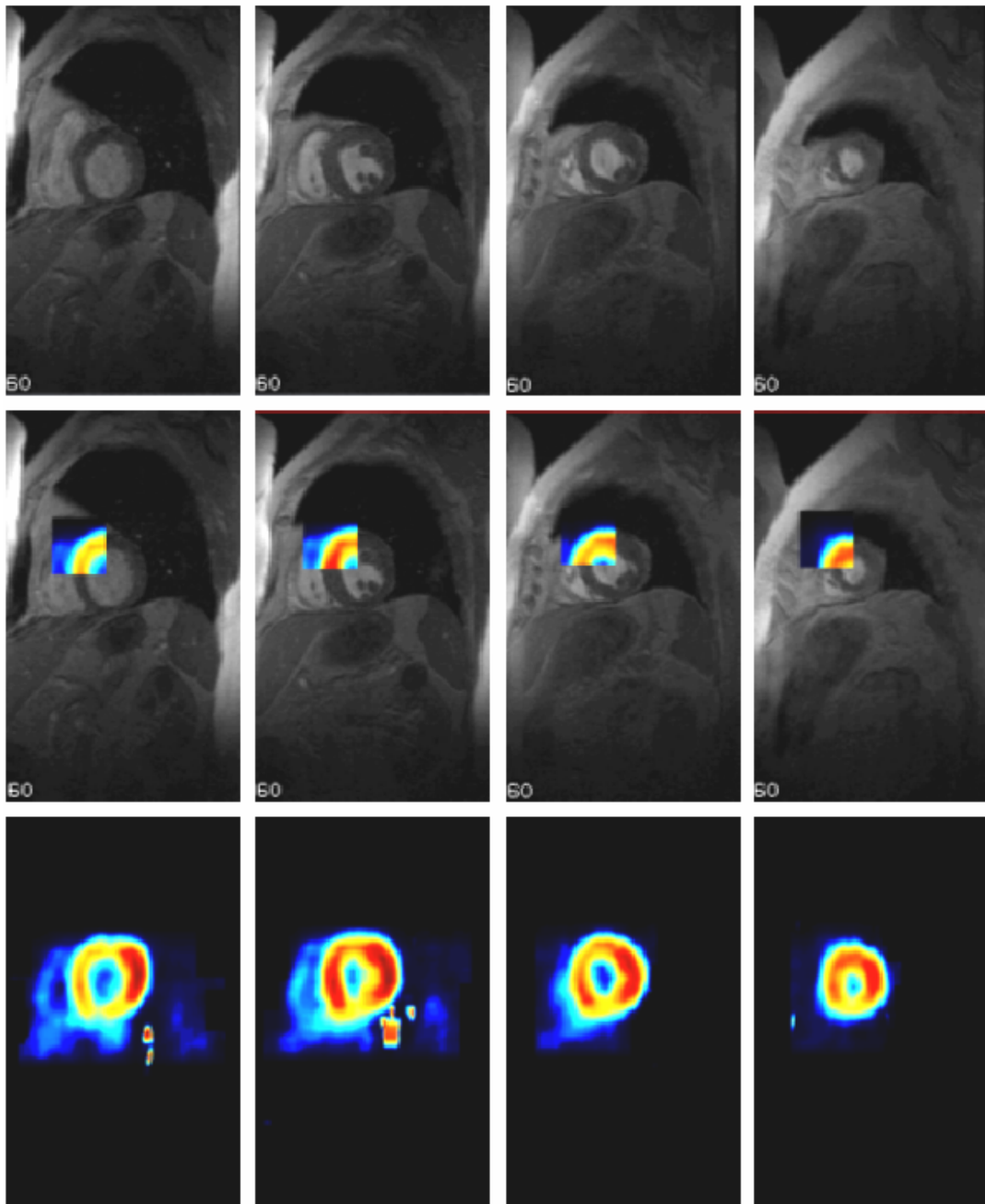


Figure 15 : Coupes IRM-PA (haut) recalées à des images TEP 18F-FDG (bas) pour le cas E2 en télédiastole. La rangée centrale illustre le recouvrement des 2 modalités d'images pour une petite portion du myocarde ventriculaire gauche.

### 3.2.4 Evaluation de la méthode de recalage rigide IRM-TEP

L'évaluation de la méthode de recalage rigide IRM-TEP publiée dans [Mäkelä, 2001] est présentée dans [Mäkelä, 2003b]. Elle est résumée ici. Cette évaluation repose sur la création d'un jeu de données de référence TEP-IRM en quasi-parfaite correspondance [Pauna, 2003]. Des images RM transverses provenant du thorax d'un volontaire sain ont été acquises sur un imageur Siemens, Magnetom Vision 1.5 T (Siemens, Erlangen, Allemagne) à l'Hôpital Cardiologique de Lyon. Une série de 15 images transverses contiguës pondérées en T1 avec synchronisation à l'ECG couvrant le coeur a été acquise en apnée avec une antenne corps (Fig. 16a). La résolution des images est de  $0.97 \text{ mm}^2$  dans le plan. L'épaisseur des coupes est de 8 mm. Les images RM sont segmentées et étiquetées (Fig. 16b). Le résultat est introduit dans un simulateur TEP décrit ci-dessous. Les images TEP simulées de transmission (Fig. 16c) et d'émission  $^{18}\text{F}$ -FDG (Fig. 16d), ainsi que les images RM originales fournissent le jeu de données de référence pour l'évaluation du recalage.

En collaboration avec le CERMEP à Lyon, la simulation des images TEP de transmission et d'émission  $^{18}\text{F}$ -FDG est réalisée à l'aide du simulateur TEP SORTEO (Simulator of Realistic Tridimensional Emitting Objects) [Reilhac, 1999, 2002]. SORTEO est un simulateur Monte Carlo qui utilise en entrée un fantôme numérique réaliste 3-D du thorax et de ses principales structures. Ce fantôme provient ici de la segmentation des images RM de référence en 9 classes (muscle, poumons, foie, graisse, rachis (os), myocarde du VG, cavité du VG, myocarde du VD et la cavité du VD). Il prend en compte la radioactivité spécifique et l'atténuation de chaque tissu. La simulation de l'image TEP d'émission  $^{18}\text{F}$ -FDG est réalisée à l'aide d'un traceur radioactif F-18.

La simulation de l'image TEP de transmission est obtenue par la simulation d'une source radioactive externe de Ge-68 provenant d'études expérimentales.

Les images TEP simulées reconstruites de transmission et d'émission ( $^{18}\text{F}$ -FDG) (FBP avec filtre Hanning) ont une taille de pixel et une épaisseur de coupe respectives de  $3.52 \times 3.52 \text{ mm}^2$  et de 2.43 mm. Les IRM et les images TEP simulées de transmission et d'émission sont interpolées (interpolation trilineaire) à la même taille isotrope de voxel, soit  $1,95 \text{ mm}^3$ , avec une taille de matrice de  $256 \times 256 \times 58$ . La construction du jeu de données de référence fait l'objet de la thèse de N. Pauna et constitue le point central d'une stratégie générale d'évaluation de méthode de mise en correspondance basé sur la simulation réaliste d'images [Pauna, 2003]. L'évaluation du simulateur TEP a été réalisée dans [Reilhac, 1999, 2002].

Cinquante transformations, obtenues par échantillonnage aléatoire du vecteur de transformation à 6 paramètres, sont appliquées aux données TEP de transmission et d'émission. Selon les conditions cliniques actuelles, les translations sont limitées à  $\pm 5$  cm le long de chacun des trois axes et les rotations autour de chaque axe varient entre

$\pm 5$  degrés. La sélection des transformations suit une distribution de Gauss et les contraintes précédentes : distributions normales  $N(0, 1.67)$  cm pour les translations et  $N(0, 1.67)$  degrés pour les rotations.

Les 50 jeux d'images TEP de transmission et d'émission simulées transformées sont recalées avec l'image RM de référence en utilisant la méthode de recalage rigide de surfaces [Mäkelä, 2001]. La précision du recalage est évaluée en calculant l'erreur RMS sur tous les points appartenant à la totalité de l'image (environ 4 millions de points), la zone thoracique (nombre de points,  $n = 907481$ ), la zone cardiaque ( $n = 75944$ ) et la zone du VG ( $n = 26517$ ).

L'erreur RMS est obtenue à partir de l'équation suivante :

$$RMS = \sqrt{\frac{1}{n} \sum_{i=1}^n \|P_i - \hat{I}(T(P_i))\|^2} \quad (2)$$

où  $P_i$  désigne un voxel,  $T(P_i)$  est le voxel transformé utilisant la transformation connue  $T$ , et  $\hat{I}$  est la transformation du recalage estimé par la méthode de recalage de surfaces.

Les résultats du recalage sont présentés dans le tableau 2. Les valeurs moyennes et l'écart type des erreurs RMS sont calculés pour toutes les régions d'intérêt. Les méthodes d'optimisation suivantes sont testées : deux méthodes standard d'optimisation, Powell et Simplexe [Press, 1992], et une méthode d'optimisation non standard, dénommée *méthode d'optimisation sur grille discrète* (présentée dans le chapitre précédent). Dans les optimisations de type grille, l'espace de recherche est limité à des translations  $\pm 25$  voxels (environ  $\pm 5$  cm) pour les 3 directions ( $x, y, z$ ) et des rotations de  $\pm 5$  degrés autour des trois axes.

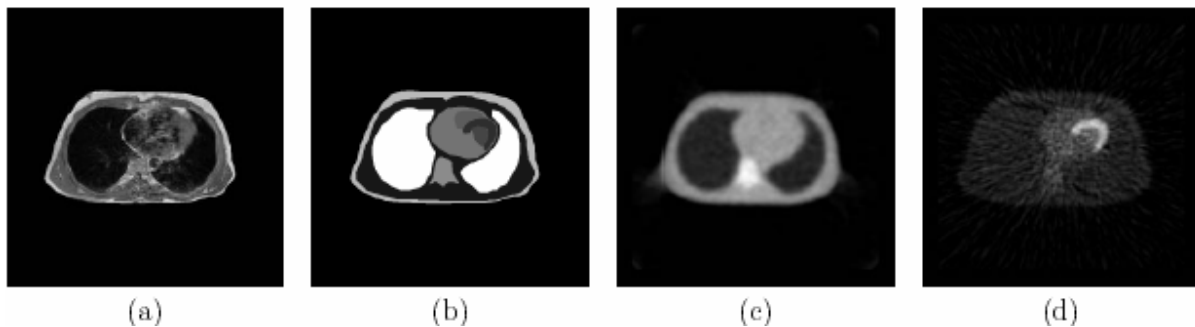


Figure 16 : Données de référence IRM-TEP. Coupes 2D tranverses des volumes 3D (a) IRM, (b) IRM segmentée (entrée du simulateur SORTEO), (c) TEP de transmission simulée, (d) TEP d'émission  $^{18}\text{F}$ -FDG simulée

Tableau 2 : *Précision de la méthode de recalage de surfaces (moyenne et écart-type de l'erreur RMS en mm) pour 50 transformations testées. Pour chacune des quatre régions d'intérêt (image complète, thorax, cœur et VG) l'erreur RMS moyenne et l'écart type sont donnés pour les 3 méthodes d'optimisation testées.*

Optimisation	Image complète (n = 3801088)	Thorax (n = 907481)	Cœur (n = 75944)	Ventricule gauche (n = 26517)
Grille	13.2 ± 3.4	10.7 ± 2.7	8.2 ± 2.3	7.7 ± 2.6
Powell	13.5 ± 4.2	10.9 ± 3.3	8.3 ± 2.9	7.8 ± 2.9
Simplexe	14.9 ± 4.1	11.7 ± 3.1	10.5 ± 3.3	10.9 ± 3.6

### 3.3 Recalage des images RM et des données de la MCG

Le recalage des IRM et des données de la MCG repose sur des repères externes. Le recalage est requis pour deux raisons. Premièrement, dans la résolution du problème inverse de localisation des sources, des modèles individuels de thorax, obtenus à partir d'images RM thoraciques, nécessaires pour la résolution du problème inverse, sont transformés dans le système coordonnées du dispositif de mesure électromagnétique. Deuxièmement, les densités de courant calculées et qui représentent l'information fonctionnelle de l'excitation électro-magnétique cardiaque sera superposée aux structures anatomiques présentes dans les images RM.

La position du système d'enregistrement MCG par rapport au patient est déterminée en fixant trois antennes de repérage (dipôles magnétiques) sur la peau (Fig. 17). Les champs magnétiques produits par les antennes sont alors utilisés pour calculer la position du capteur par rapport aux antennes de repérage [Montonen, 2000]. Les trois antennes de repérage sont aussi utilisées pour définir les coordonnées des capteurs MCG par rapport aux 9 repères MCG qui sont utilisés pour recaler le système de capteurs MCG avec les images RM.

Les repères MCG et les petites antennes de repérage sont localisées avec un système de numérisation 3-D (3SPACE ISOTRAK II, Polhemus Inc., Colchester, VT, USA) [Polhemus, 1993]. La position des repères MCG est également marquée sur la peau. Juste avant l'examen en IRM, neuf repères IRM sont placés sur les positions marquées sur la peau.

Les repères IRM sont construits à partir de deux tubes perpendiculaires remplis de liquide (1 mmol/l de  $MnCl_2$ ), insérés à l'intérieur d'un morceau de plastique de 4.0 x 4.0 x 0.7 cm. La forme en croix d'un repère est clairement visible sur les



images RM. Les repères pour l'IRM sont localisés manuellement sur les images RM, à l'aide d'un logiciel dédié. Les points de repères (x, y, z) dans les systèmes de coordonnées MCG et IRM respectivement, sont recalés à l'aide de la méthode des moindres carrés non itérée [Arun, 1987]. Seules les transformations rigides sont prises en compte.

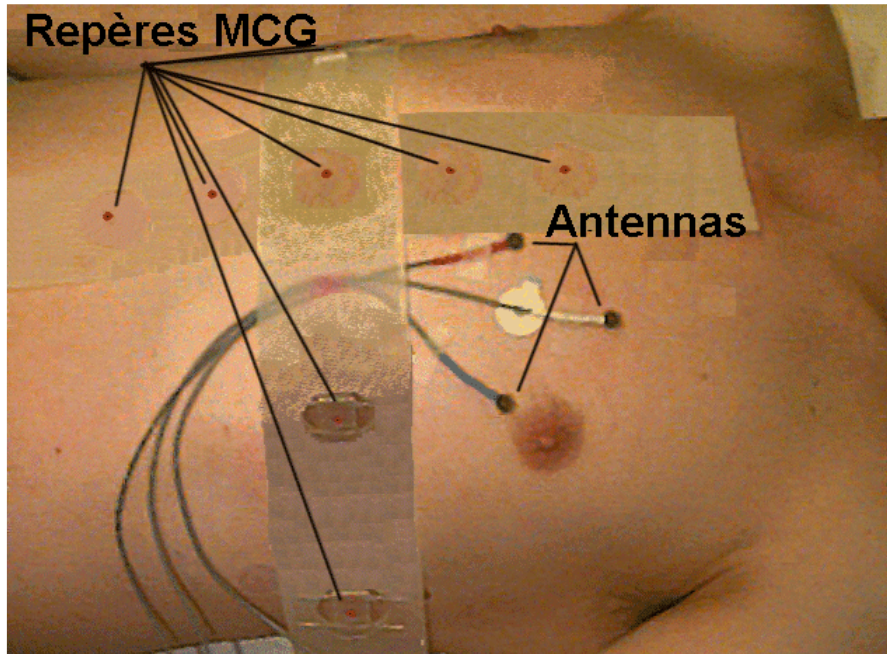


Figure 17 : Mise en place des neuf repères MCG et des trois antennes de repérage sur la poitrine d'un patient. Les pièces rondes en plastique maintenues dans deux bandes de silicone en caoutchouc indiquent la localisation des repères MCG. Leurs points centraux sont numérisés, puis les positions sont marquées sur la peau. Les trois antennes de repérage sont utilisées pour définir les coordonnées des capteurs de la MCG par rapport au repère de coordonnées MCG.

Dans [Mäkelä, 2002b], l'impact relatif des différentes sources d'erreurs dans la méthode de recalage IRM-MCG est évalué. L'objectif de cette publication est d'analyser les sources d'erreurs les plus graves de la méthode de recalage et de réduire, si possible, leur amplitude. Des mesures sont réalisées avec un fantôme et sur un volontaire. L'étude de l'erreur de recalage inclut des sources d'erreurs et des mesures variées et est divisée en cinq volets :

- A) La reproductibilité de la localisation 3-D à l'aide d'un crayon de numérisation.
- B) L'erreur d'alignement du patient.
- C) L'erreur provenant du repositionnement des repères IRM.
- D) L'effet de différentes formes de lits.
- E) L'erreur de localisation des repères IRM dans les images.

La somme de toutes les composantes d'erreurs de recalage est de 6 mm environ et la contribution des différentes sources d'erreurs à l'erreur totale est approximativement égale.



## 4. Cartographies fonctionnelles en 3-D

### 4.1 Principe

Les informations fonctionnelles en imagerie cardiaque sont couramment exploitées par des représentations du cœur en 2-D, comme la représentation polaire (œil de bœuf, bull's eye en anglais) bien connue.

De telles représentations sont très pratiques, mais elles n'incluent pas l'anatomie cardiaque spécifique du patient. La morphologie du cœur en 3-D peut être extraite d'images RM. C'est ce que nous proposons dans ce chapitre. L'anatomie cardiaque ainsi obtenue sert alors de support pour la visualisation et l'interprétation de l'information fonctionnelle issue de modalités complémentaires, après recalage. Il en résulte des cartographies anatomo-fonctionnelles 3-D individualisées du cœur.

Les cartographies 3-D incluent des informations provenant des données recalées IRM, TEP-FDG et MCG. Pour créer les cartographies, les images RM-PA sont segmentées à l'aide d'un modèle de cœur déformable biventriculaire (Fig. 18) [Pham, 2001 ; 2002]. La segmentation est basée sur un modèle volumique *a priori* de cœur à deux ventricules qui est déformé dans l'image afin qu'il s'adapte aux contours cardiaques. La déformation est contrôlée par l'élasticité du matériau utilisé pour le modèle dans une procédure classique de minimisation d'énergie pour lequel différents schémas numériques basés sur la méthode des éléments finis (MEF) ont été testés. Ce modèle déformable élastique a été développé dans le cadre de la thèse de Q. C. Pham [Pham, 2002].

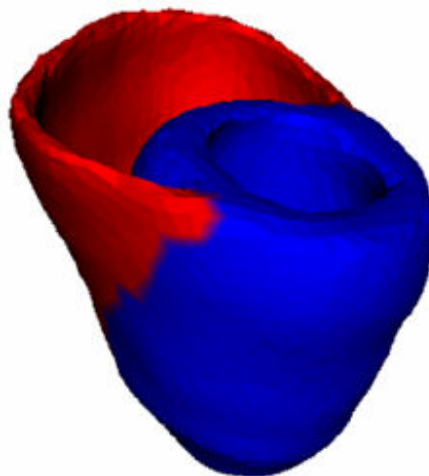


Figure 18 : *Modèle de cœur déformable biventriculaire [Pham, 2002].*

À partir de la segmentation de l'anatomie cardiaque avec ce modèle, une surface interne (médiane) est automatiquement calculée entre les surfaces ventriculaires gauches endocardiques et épiscopardiques du modèle. Le calcul de la surface interne médiane est réalisé tout d'abord en calculant une normale en chaque nœud de la surface endocardique, puis en calculant le point moyen entre la surface endocardique et l'intersection de la normale avec la surface épiscopardique (Fig. 19).

Le modèle incluant la surface interne est alors transformé de l'image RM-PA vers l'image TEP-FDG d'émission en utilisant les paramètres de recalage rigide estimés (Fig. 20). Une valeur moyenne de captation du  $^{18}\text{F}$ -FDG est calculée en chaque nœud de la surface interne dans un voisinage réduit  $5 \times 5 \times 5$ . On combine la captation du FDG et la surface médiane du VG, les surfaces ventriculaires droite et péricardique pour former une représentation 3-D de l'anatomie et du métabolisme du cœur. Pour obtenir les cartographies fonctionnelles 3-D correspondantes de l'activité électromagnétique cardiaque, des estimations des densités de courant en MCG sont calculées pour les nœuds de la surface interne.

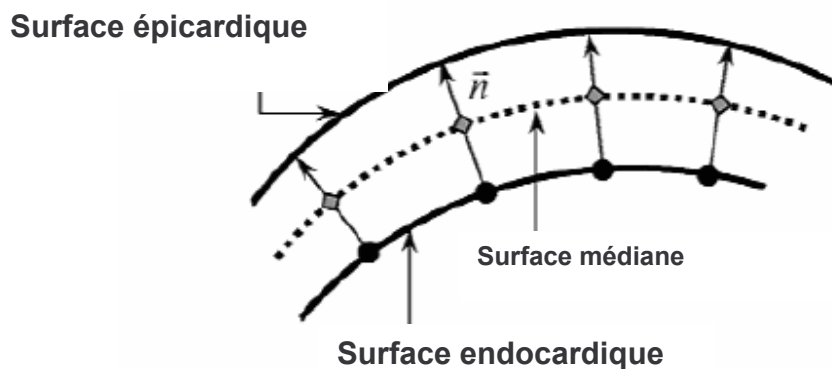


Figure 19 : Calcul de la surface médiane [Mäkelä, 2003a].

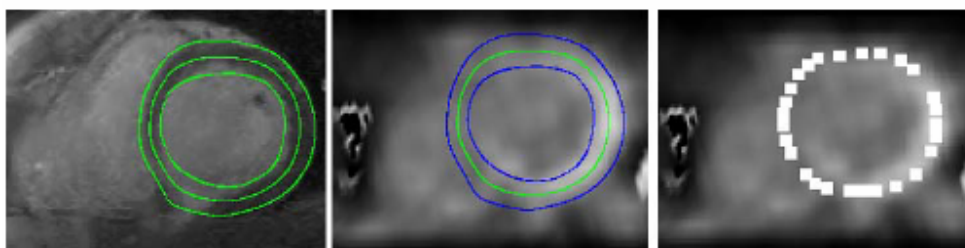


Figure 20 : Calcul des valeurs de captation glucidique sur la surface médiane : (a) Intersection des surfaces endocardique (contour le plus interne), épiscopardique (contour le plus externe) et surface médiane calculée (contour intermédiaire) avec un plan de coupe IRM en petit axe, (b) les mêmes contours sont présentés dans l'image TEP-FDG recalée en PA correspondante (c) la valeur moyenne de la captation du FDG est calculée au niveau des nœuds de la surface médiane dans un voisinage de petite taille.

## 4.2 Cartographies anatomo-fonctionnelles : quelques exemples

Les résultats de la fusion de données sont présentés dans les figures suivantes :  
Les Fig. 21, 22 et 23 (gauche) illustrent l'activité métabolique en TEP-FDG et les Fig. 21 (milieu), 22 (droite) et 24, les cartographies MCG pour les cas E1 et E2. Les surfaces ventriculaires droites et péricardiques sont présentées en transparence. Les régions du VG présentant une faible captation du FDG sont en bleu foncé et les valeurs basses de MCG en vert foncé dans les vues en 3-D (Fig. 21 et 22 à gauche). Pour l'évaluation initiale de la méthode, les résultats sont comparés à des représentations polaire 2D (œil de bœuf) réalisées manuellement (Fig. 21 et 23 à droite) [Mäkelä, 2003a]. Les flèches indiquent des régions qui se correspondent dans les représentations 2D et 3D.

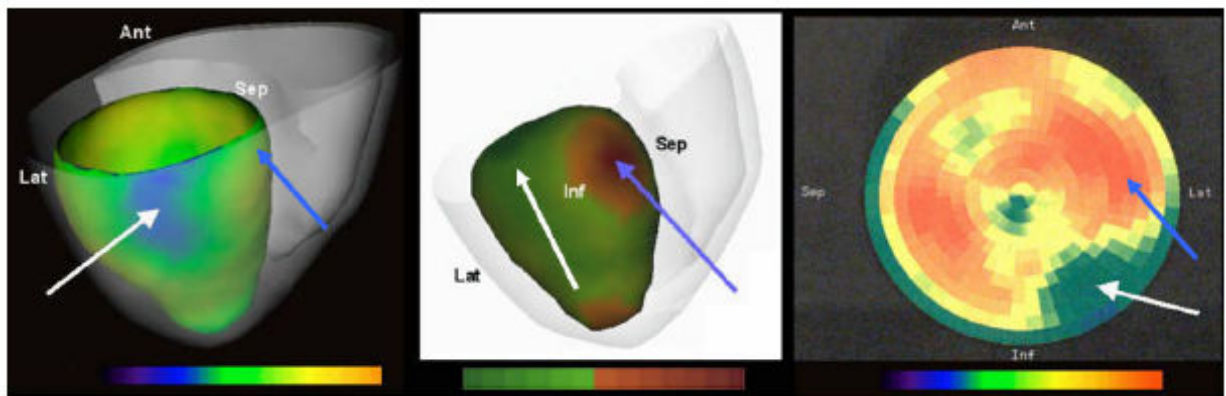


Figure 21 : Représentations en 3-D de la captation du FDG (gauche) et des valeurs de densité de courant (milieu) sur un modèle de cœur biventriculaire du patient E1. Pour la comparaison des modes de présentation de l'information, la représentation polaire 2D réalisée manuellement (logiciel Siemens ; Turku PET center) de l'image TEP-FDG correspondante est représentée à droite. Une zone nécrosée postéro-latérobasale est identifiée ; elle est colorée en bleu au niveau de la base sur la représentation en 3-D (à gauche, flèche blanche) et en vert foncé dans l'image polaire (à droite, flèche blanche). Dans les données MCG (milieu), les amplitudes de courant les plus faibles sont aussi représentées en vert foncé (flèche blanche) et les amplitudes les plus élevées peuvent être observées en rouge au niveau basal (flèche bleue).

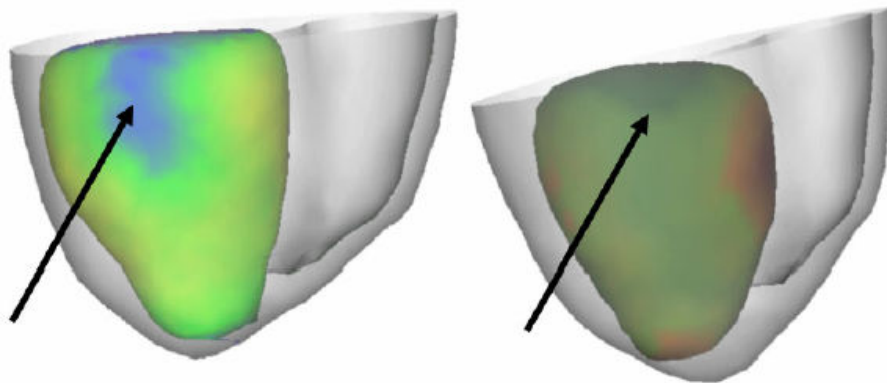


Figure 22 : Représentations en 3-D de la captation du FDG (gauche) et de la densité de courant (droite) pour le patient E1 selon un autre point de vue pour une meilleure visualisation de la zone lésionnelle.

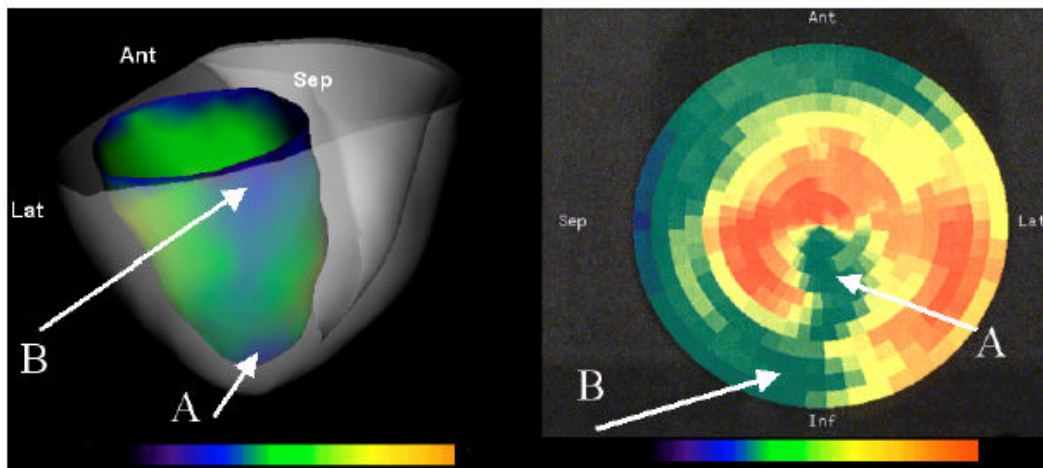


Figure 23 : Représentations en 3-D de la captation du FDG (gauche) sur le modèle de cœur biventriculaire du patient E2. La représentation polaire réalisée manuellement de l'image TEP-FDG correspondante est présentée à droite.

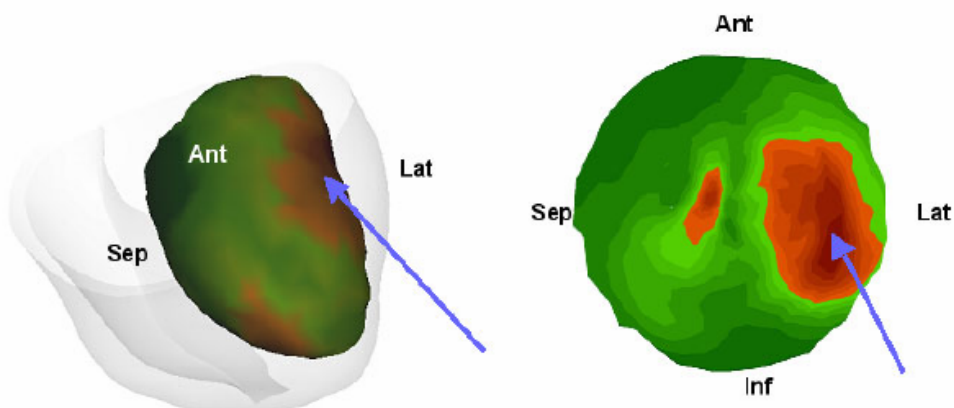


Figure 24 : Gauche : Représentation en 3-D des valeurs de densité de courant sur le modèle de cœur biventriculaire du patient E2. Droite : représentation polaire 2D réalisée de façon interactive à partir de la surface interne en 3-D.

## 5. Méthode de recalage élastique pour les images cardiaques RM et TEP

L'analyse des résultats du recalage rigide montre qu'il peut exister des divergences locales lors de la superposition des informations TEP et IRM (voir par exemple, Fig. 14, rangée du milieu à droite). Les caractéristiques d'acquisition sont en effet relativement différentes dans ces deux modalités. De façon à améliorer les analyses ultérieures, il est nécessaire de corriger ce problème. C'est la raison pour laquelle une nouvelle méthode de recalage élastique a été mise au point.

### 5.1 Principe

Il s'agit d'une combinaison d'informations mutuelles, d'informations de gradient et de lissage de transformation utilisée pour guider la déformation d'une image vers une autre.

Le recalage élastique est obtenu en minimisant l'énergie totale,  $E_{total}$ , de la fonction d'énergie suivante :

$$E_{total} = E_{MI} + \alpha E_{grad} + \beta E_{model}, \quad (3)$$

où  $E_{MI}$  et  $E_{grad}$  sont respectivement les composantes d'énergie d'information mutuelle et du gradient conjoint [Pluim, 2000]. Le paramètre  $E_{model}$  est une composante d'énergie qui contraint la transformation à rester lisse. Les termes  $\alpha$  et  $\beta$  sont des paramètres de pondération définis par l'utilisateur.

La composante d'informations mutuelles  $E_{MI}$ , est calculée à partir de l'équation :

$$E_{MI} = \sum_{a,b} p_{AB}(a,b) \log \frac{p_{AB}(a,b)}{p_A(a)p_B(b)}, \quad (4)$$

où  $p_A(a)$  et  $p_B(b)$  sont des probabilités marginales et  $p_{AB}(a, b)$  représente la distribution de probabilité jointe.

Dans la suite de ce travail, le volume à niveaux de gris du modèle est appelé *volume M*, et les données volumiques acquises chez un patient et auquel le modèle est apparié sont appelées *volume D*. Le terme  $p_A(a)$  est la probabilité que la valeur du niveau de gris d'un voxel soit dans le volume M et le terme  $p_{AB}(a, b)$  est la probabilité que des voxels

correspondants dans les volumes M et D aient des niveaux de gris  $a$  et  $b$ , *respectivement*.

Le terme d'énergie d'informations mutuelles,  $E_{MI}$ , mesure la dépendance statistique entre deux variables aléatoires ou la quantité d'informations qu'une variable contient à propos de l'autre [Fitzpatrick, 2000], [Hajnal, 2001], [Maes, 1997], [Wells, 1996], [Woods, 2000a]. Le terme d'énergie d'information mutuelle peut être qualitativement considéré comme une mesure de la façon dont une image explique l'autre image. L'information mutuelle est maximisée lorsque l'alignement est optimal. Peu d'hypothèses sont faites concernant la nature de la relation entre les intensités des images recalées [Hill, 2000], [Maes, 1997].

La composante d'énergie  $E_{grad}$  est dérivée des gradients des contours dans les images recalées. Les informations de gradient reposent sur l'hypothèse que les contours du modèle doivent s'apparier soit sur des contours identiques, soit sur des contours orientés en direction opposée dans les données. La composante d'énergie  $E_{grad}$  est calculée comme suit :

$$E_{grad} = \frac{1}{N} \sum_{(\mathbf{m}, \mathbf{d}) \in (M \cap D)} \frac{\nabla \mathbf{m} \cdot \nabla \mathbf{d}}{|\nabla \mathbf{m}| |\nabla \mathbf{d}|} \min(|\nabla \mathbf{m}|, |\nabla \mathbf{d}|), \quad (5)$$

où  $N$  est le nombre de points du modèle recouvrant le volume D. Etant donné qu'un minimum du gradient est utilisé dans deux volumes, les variations d'intensité doivent être fixées de façon pratiquement similaire dans les deux volumes. Étant donné que l'échelle de gris d'un tissu dépend de la séquence d'imagerie ou de la modalité, les gradients sur les contours du tissu peuvent avoir des directions opposées dans différents volumes. Si c'est le cas avec les volumes M et D, l'équation 5 est modifiée en prenant la valeur absolue du produit scalaire.

La composante d'énergie  $E_{model}$  régularise la transformation en la contraignant pour qu'elle reste lisse. La transformation T peut être contrainte à rester lisse en incorporant la composante d'énergie  $E_{model,1}$  :

$$E_{model,1} = \frac{1}{N} \sum_{x,y,z} [(\frac{\partial^2 \mathbf{T}}{\partial x^2})^2 + (\frac{\partial^2 \mathbf{T}}{\partial y^2})^2 + (\frac{\partial^2 \mathbf{T}}{\partial z^2})^2 + 2(\frac{\partial^2 \mathbf{T}}{\partial x \partial y})^2 + 2(\frac{\partial^2 \mathbf{T}}{\partial x \partial z})^2 + 2(\frac{\partial^2 \mathbf{T}}{\partial y \partial z})^2], \quad (6)$$

où la somme porte sur tous les voxels dans le volume modèle et  $N$  est le nombre de points. Le terme d'énergie est l'équivalent en 3-D de l'énergie de flexion 2-D d'une plaque mince. Pour accélérer les calculs, seuls les trois premiers termes sont utilisés en pratique. Alternativement, si un modèle des surfaces est disponible, le lissage de la



transformation peut être contrôlé en contraignant la modification de la forme des surfaces du modèle.

La déformation des images à recaler est réalisée dans un processus multi-résolution. Elle est réalisée à l'intérieur de sphères dont la position et le rayon sont variables (Fig. 25). Par défaut, la localisation des sphères est choisie de manière aléatoire dans un *volume* modèle M. L'utilisateur peut définir le nombre de positions testées ( $N_{loc}$ ). Dans la Fig. 25, la grille au centre de la sphère, indiquée par un cercle, représente l'espace de recherche et visualise les nouvelles positions possibles du centre en 2-D. Le volume modèle à niveaux de gris est apparié de façon élastique à un volume de données. Si une surface n'est pas incluse dans le modèle, seul le lissage de la transformation peut être contrôlé. Toutefois, si des informations de surface sont incluses dans le modèle, sous la forme de triangulations par exemple, les localisations peuvent être choisies au niveau des positions des points appartenant à la surface (i. e. les sommets des triangulations). De même, si la surface est disponible, on recommande la méthode régularisant les directions des normales car elle réduit largement le temps de calcul.

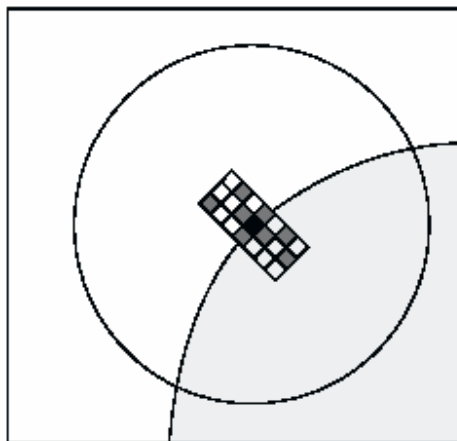


Figure 25 : *Un espace de recherche en 2-D au centre de la sphère de déformation et les positions testées ( $N_{loc} = 8$ ).*

Le modèle M doit contenir des surfaces dans les régions pour lesquelles il est demandé un recalage de qualité. Par exemple, si les contours du thorax doivent être recalés à partir de l'image, la transformation à l'intérieur et en dehors des contours n'est pas d'un grand intérêt. L'utilisation des surfaces localise la déformation vers les régions les plus intéressantes et accélère le processus car une grande partie du volume, comme le fond, est alors exclue.

Toutefois, les sphères aux niveaux de résolution les plus faibles contiennent habituellement la totalité, ou la plus grande partie, du volume du modèle et permettent ainsi une transformation globale pour les régions éloignées des contours.

Si le volume modèle à recalculer est un atlas, c'est-à-dire un volume dans lequel les classes des tissus sont connues, le résultat de l'appariement élastique produit aussi une segmentation.

## 5.2 Résultats de recalages élastiques

La méthode a été utilisée pour le recalage d'images cardiaques intra-patient RM et TEP-FDG et d'images RM inter-patient de la tête.

La Fig. 26 présente le résultat du recalage élastique d'images RM PA et TEP-FDG d'émission en petit axe du coeur. Les images peuvent être préalablement recalées de façon rigide. Les flèches présentes dans les images montrent une zone où le recalage élastique a nettement amélioré les résultats du recalage rigide.

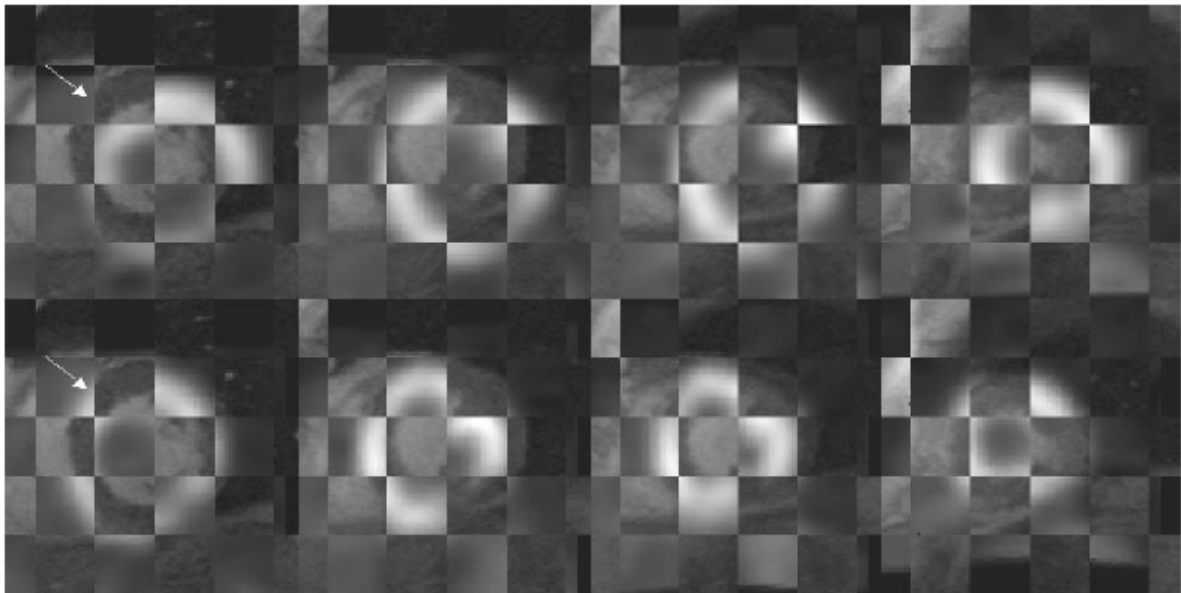


Figure 26 : *Recalage élastique d'images cardiaques TEP-FDG d'émission et IRM en petit axe pour le patient E3. Pour quatre niveaux de coupe, (haut) Recalage rigide, (bas) Recalage élastique.*

Dans la Fig. 26, la rangée supérieure montre une représentation en mosaïque après recalage rigide et la rangée inférieure, après recalage élastique. Le ventricule gauche est relativement bien apparié. Par exemple, le recalage est meilleur après recalage élastique au niveau du septum (flèches blanches). Dans le cas présent, les images n'ont pas été recalées de façon rigide avant l'appariement élastique. Lorsque le recalage rigide est utilisé, les images apparaissent souvent déjà bien alignées avant la transformation élastique et l'amélioration est peu visible. L'évaluation précise des résultats est cependant difficile, les images TEP étant fortement lissées. En conséquence, les performances et les conditions d'utilisation du recalage élastique dans

la cas de l'imagerie cardiaque doivent être soigneusement évaluées dans de futures études.

Dans la Fig. 27, la rangée supérieure montre des images cérébrales du modèle initial entrelacées avec les données du patient en mosaïque. La rangée inférieure présente les mêmes volumes après recalage élastique du modèle avec les données du patient. L'inspection visuelle montre que les contours des structures anatomiques semblent bien alignés après appariement élastique, c'est-à-dire que les contours sont raisonnablement continus entre les cases contiguës de l'échiquier.

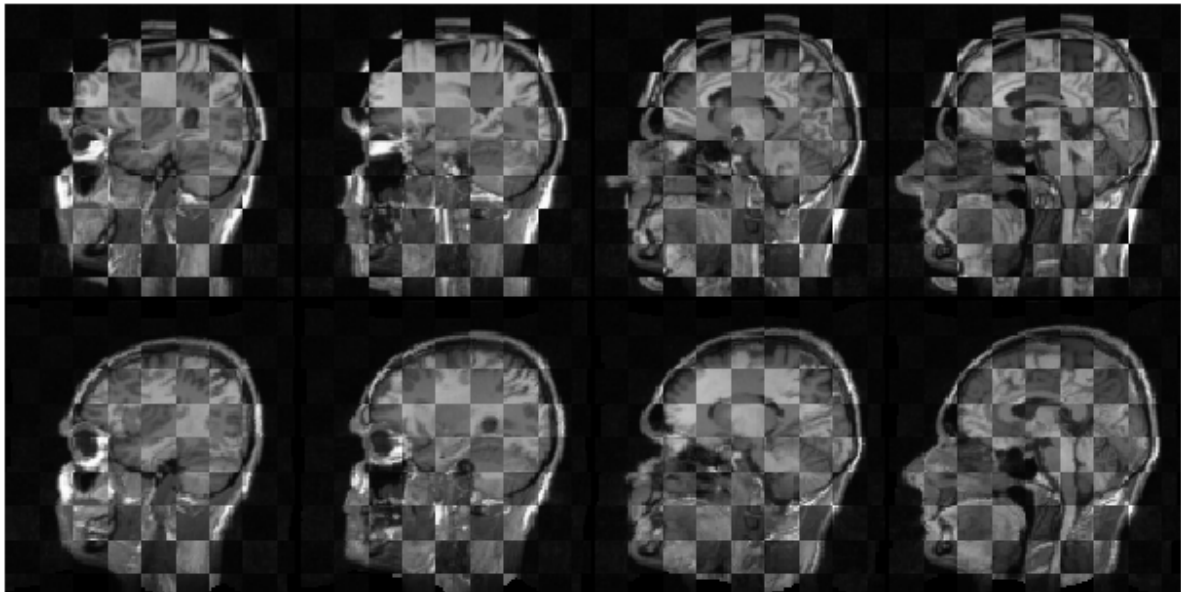


Fig. 27 : Appariement de volumes IRM de la tête (coupes). La rangée supérieure montre les données du modèle et celles du patient entrelacées avant recalage et la rangée inférieure, après recalage élastique.

## 6. Discussion

Le recalage d'images cardiaques est un problème complexe, notamment à cause des conditions d'acquisition des images et des mouvement respiratoire et cardiaque. Un certain nombre de contraintes d'acquisition et de solutions possibles sont revues ci-après.

- ***Les limites de l'étude et quelques solutions***

1) Dans la méthode de recalage rigide présentée dans cette thèse, l'hypothèse principale est que le patient ne bouge pas pendant et entre les acquisitions d'images RM transverses et en PA. On suppose également que le patient ne bouge pas pendant et entre l'imagerie TEP de transmission et d'émission 18F-FDG. En IRM cardiaque, l'immobilisation du corps par rapport à l'antenne de surface pourrait empêcher le mouvement du patient. Des systèmes de contention du patient, tels que des coussins ou matelas à aspiration qui épousent l'anatomie du patient (vacuum cushions en anglais), utilisés en radiothérapie, pourraient aussi permettre de réduire les artefacts dûs aux mouvements pendant l'imagerie TEP de transmission et d'émission. L'acquisition des images TEP de transmission avant et après l'acquisition des images d'émission pourrait fournir une estimation du mouvement du patient pendant et entre les acquisitions d'images [Bettinardi, 1993]. Ceci permettrait une correction du mouvement, mais augmenterait la dose de radiations administrées au patient. Des méthodes ont aussi été proposées pour le recalage des images TEP d'émission 18F-FDG et de transmission [Bettinardi, 1993], [Costa, 1994] ainsi que pour réduire le temps d'acquisition en imagerie TEP de transmission, diminuant ainsi la probabilité d'artefacts de mouvement pendant l'imagerie de transmission [Alenius, 1999]. Un appariement parfait entre les imageries de transmission et d'émission est essentiel dans les études réalisées en corps entier dans lesquelles la correction de l'atténuation est primordiale en raison de la présence de tissus très hétérogènes (muscle, os, poumon, etc.) [Bettinardi, 1993].

2) Des images RM transverses en synchronisation à l'ECG ont été obtenues chez 10 patients en utilisant des séquences d'acquisition en respiration libre. La durée de l'imagerie du thorax était d'1 minute environ. En comparaison, les images TEP de transmission peuvent être vues comme des images intégrées sur un temps d'acquisition relativement long (environ 20 minutes). Ceci peut conduire à des différences entre ces deux méthodes d'imagerie portant sur la forme du thorax et la position du diaphragme.

La méthode de recalage rigide est basée sur la détermination des surfaces thoraciques et pulmonaires. Par conséquent, le diaphragme doit avoir des positions similaires dans les deux modalités d'imagerie, ce qui ne peut être assuré en pratique. Une solution possible pourrait consister en des procédures similaires de synchronisation de la respiration (ou d'apnées par sections) dans les deux modalités d'imagerie ou l'utilisation de méthodes de recalage élastique. En général, la partie basse des poumons est bien

visible dans les images TEP de transmission chez les 10 patients. Dans certains cas, on a relevé de très petites portions d'images où la base d'un ou des deux poumons n'était pas visible. Dans ces cas, le modèle déformable extrapole la petite partie inférieure de la base du poumon et ceci peut entraîner des erreurs de recalage.

3) Le recalage d'images RM-PA et TEP d'émission 18F-FDG a été réalisé entre des images télé-diastoliques pour l'IRM et des images non synchronisées pour la TEP. L'instant télé-diastolique des images de ciné-IRM a été sélectionné car les images 18F-FDG TEP non synchronisées proviennent de l'intégration de la captation sur plusieurs cycles cardiaques, et peut être considéré comme représentant principalement la phase diastolique. L'acquisition d'images TEP d'émission synchronisées pourraient améliorer le recalage en réduisant l'effet du mouvement cardiaque dans les images acquises. Les images TEP d'émission synchronisées apporteraient aussi des informations fonctionnelles pendant le cycle cardiaque.

4) Etant donné que les bras du patient entraînent une atténuation du signal au cours de l'imagerie d'émission et de transmission TEP, les patients ont les bras maintenus au-dessus de la tête pendant la réalisation de la procédure. Cette position peut elle-même changer la position du cœur et des poumons par rapport à l'imagerie RM, au cours de laquelle les patients conservent les bras le long du corps [Dahlbom, 2000]. Il n'a pas été possible d'utiliser la même position en IRM qu'en imagerie TEP, car l'imagerie RM, pour des études de viabilité, peut durer jusqu'à 60 minutes. De même, le diamètre des tunnels des imageurs RM est trop petit pour que certains patients puissent rester couchés dans cette position. Les techniques de recalage élastique pourraient permettre de résoudre de petites différences anatomiques rencontrées dans ces situations [Tai, 1997].

5) Les images RM et TEP acquises dans le cadre de cette étude soulèvent plusieurs exigences pour l'algorithme de recalage. L'algorithme de recalage ne converge pas nécessairement vers le résultat correct si le vecteur de paramètres initial est trop loin du résultat optimal. Avec les images TEP de transmission et les images RM transverses utilisées pour le calcul de la transformation rigide, le vecteur de paramètres initial étaient suffisamment proche de l'optimum local pour faire converger l'algorithme, et, le repositionnement manuel des images avant recalage ne s'est pas avéré nécessaire. Les surfaces extraites ne doivent pas présenter de symétries de révolution (par exemple, pour des objets cylindriques, la solution n'est pas unique) ce qui n'est habituellement pas le cas avec le thorax qui inclut les poumons. Chaque point de surface utilisé lors du recalage devrait avoir un point de correspondance unique dans l'autre image. Dans les dix cas étudiés, les images TEP de transmission et d'émissions 18F-FDG ont un champ de vue plus petit que dans les images RM. Par conséquent, dans certains cas, une partie des points des surfaces de l'image TEP de transmission a

été exclue de façon semi-automatique du calcul des paramètres de recalage si elles ne présentaient pas de contours correspondants dans les images RM.

6) Les images RM des patients couvrent la totalité de la zone thoracique, tandis que les images TEP de transmission et d'émission 18F-FDG utilisées pour l'évaluation de la méthode de recalage ne couvrent que la région du coeur. Dans les images TEP de transmission chez les patients, la base des poumons est en général plus visible que dans les images de transmission simulées, ce qui a aidé le recalage basé sur les surfaces des images du patient. De même, le champ de vue plus important des images RM chez les patients (la totalité du thorax) a probablement aidé au recalage par rapport aux images simulées dans lesquelles seule la zone cardiaque a été imagée. Toutefois, les images de simulation n'incluent pas d'artefacts de mouvements provoqués par la respiration, les mouvements cardiaques et les mouvements du patient qui sont présents dans les images des patients. Chez certains patients, le temps de réalisation de l'imagerie était trop long (1 minute environ) pour qu'ils maintiennent l'apnée, car la totalité du thorax était imagée. Pour les images RM utilisées dans le simulateur TEP, seule la zone cardiaque est couverte et les acquisitions ont été réalisées en apnée. Les bras ont été segmentés dans les images RM utilisées dans le simulateur TEP, étant donné que les bras sont normalement maintenus au-dessus de la tête pour éviter toute atténuation supplémentaire dans la zone cardiaque pendant l'acquisition des images TEP de transmission et d'émission 18F-FDG.

7) Des simulations d'images TEP (émission, transmission) ont été réalisées à partir d'images RM segmentées dans le cadre de l'évaluation. La segmentation des images RM (en 9 classes) est sujette à des erreurs et peut donc entraîner des différences dans les images simulées lors d'une comparaison à l'image RM originale.

- **Les résultats de recalage**

La méthode de recalage rigide de surfaces des images RM et TEP 18F-FDG a été évaluée avec des images simulées et des données obtenues chez dix patients. Les méthodes de recalage basées sur les surfaces sont des méthodes efficaces lorsque les structures recalées sont clairement visibles et faciles à segmenter. En principe, elles ne nécessitent pas de connaissance *a priori* de la nature des images recalées ou des informations provenant de la distribution de l'intensité des images. La précision de la méthode de recalage de surfaces dépend principalement de la précision avec laquelle les surfaces utilisées pour le recalage peuvent être extraites des images. Les résultats des méthodes de recalage basées sur les surfaces avec des images simulées (Table 2) ont montré que l'erreur RMS était plus importante que la taille du voxel des images recalées ( $1.95 \text{ mm}^3$ ) quelque soit la méthode d'optimisation pour les quatre zones cibles (image complète, thorax, coeur et VG). Les meilleurs résultats pour le recalage de surfaces sur 50 cas au niveau du coeur ont été obtenus avec l'optimisation sur grille discrète, avec une erreur RMS de  $8.2 \pm 2.3 \text{ mm}$ . Dans la méthode de recalage de



surfaces et optimisation sur grille discrète, l'espace de recherche était limité à des translations de  $\pm 25$  voxels (environ  $\pm 5$  cm) par rapport à la position originale pour toutes les directions et  $\pm 5$  degrés pour les rotations autour des trois axes. Pour le recalage des images de patients, l'optimisation de type grille avec un espace de recherche limité a aussi donné des résultats visuellement satisfaisants dans 9 cas sur 10. Dans le cas d'un patient, le recalage de l'image de transmission a réussi, mais des artefacts dans les données TEP-FDG d'émission ont été détectés. La raison probable de ce problème est probablement une conséquence des mouvements entre (ou pendant) l'imagerie TEP de transmission et d'émission.

La méthode d'optimisation sur une grille discrète s'est montrée la plus robuste lors d'une inspection visuelle du recalage des images de patients ; deux mises en correspondance sur 10 ont conduit à un recalage visuellement non satisfaisant avec les minimisations de Powell et du Simplexe. Une des raisons expliquant la robustesse de la méthode de type grille est la limitation de l'espace de recherche permettant l'obtention de résultats raisonnables.

- ***Caractéristiques et performances de la méthode de recalage***

La méthode de recalage rigide mise au point pour les images 18F-FDG TEP et RM diffère des méthodes précédemment introduites (par exemple, [Pallotta, 1995], [Gilardi, 1998]), notamment en raison de la segmentation automatique par un modèle déformable du thorax et des poumons dans les images TEP de transmission et les images RM transverses. Un autre avantage de la méthode de recalage est qu'elle ne donne pas uniquement des images RM et TEP transverses recalées mais aussi des images RM et TEP en petit axe, couramment exploitées en routine clinique. La méthode de recalage peut s'appliquer au recalage d'images RM-TEMP ou TEP-TEMP si l'image de transmission TEMP est disponible. Les images TEP d'émission cardiaques avec synchronisation à l'ECG pourraient aussi améliorer les résultats du recalage, permettant le recalage des images RM et TEP d'émission aux mêmes phases du cycle cardiaque.

La vitesse de l'algorithme de recalage dépend de différents facteurs, tels que la nécessité d'un recours à un prétraitement, la complexité et le nombre d'évaluations de la fonction de coût effectuées par l'algorithme d'optimisation [Bankman, 2000]. Comparé à l'algorithme ICP (Iterative Closest Point en anglais) [Besl and McKay, 1992], l'approche de recalage IRM-TEP basée sur les surfaces présentée ici nécessite la pré-segmentation des données. La cartographie des distances est calculée une fois lors d'une étape de prétraitement. Ensuite, l'estimation des distances entre le modèle et les points de données est immédiate. Dans l'algorithme ICP, les distances entre les surfaces sont explicitement calculées à de chaque itération. Ainsi, en comparaison avec ICP, le coût de l'évaluation de la distance est beaucoup moindre dans l'algorithme de carte des distances de chanfrein, mais l'approche requiert davantage de prétraitement [Bankman, 2000]. Pour la segmentation automatique des images RM et des images TEP de transmission (256 x 256 x 217 voxels), il faut moins de 3 minutes sur un poste de travail de type PC (Pentium III cadencé à 800 MHz). Avec la même taille d'images et sur le même matériel, le temps d'exécution pour le recalage (optimisation

sur grille discrète) est de 50 secondes environ à partir de 1 000 points pour calculer les paramètres de la transformation rigide. Dans nos expériences, la stratégie de recherche proposée pour les paramètres de recalage pour la méthode d'optimisation sur grille discrète offre des résultats rapides et fiables.

La méthode de recalage rigide de surfaces [Mäkelä, 2001] a également été comparée à des mises en correspondance basées sur la similarité de voxels avec l'information mutuelle [Maes, 1997], [Wells, 1996], l'information mutuelle normalisée (IMN) [Studholme, 1997, 1999] et le rapport de corrélation (RC) [Roche, 1998, 2001] dans [Mäkelä, 2003b]. Les méthodes basées sur l'intensité de l'image ne nécessitent pas d'extraction *a priori* des structures recalées (la segmentation des surfaces) et représentent ainsi des méthodes prometteuses pour le recalage automatique des images. Dans le cas de l'information mutuelle, peu d'hypothèses sont faites sur la nature de la relation entre les intensités des images recalées. Par conséquent, l'information mutuelle est intéressante, en particulier pour le recalage inter-modalité [Maes, 1997]. Dans la mesure du RC [Roche, 1998, 2001], une image est considérée comme étant un modèle d'une autre image et on admet une dépendance fonctionnelle entre les intensités des images.

Les résultats des méthodes de recalage IRM-TEP basées sur l'intensité de l'image ont été évalués de la même façon qu'avec la méthode de recalage de surfaces (chapitre 3.2). Les résultats les plus précis ont été obtenus avec des méthodes de recalage basées sur IMN et RC. Pour IMN et RC avec l'optimisation du Simplexe, l'erreur RMS pour la zone cardiaque avec 50 images simulées était respectivement de  $2.9 \pm 0.5$  mm et de  $2.9 \pm 0.4$  mm. Le recalage avec l'information mutuelle a échoué (contrôle visuel) dans près de 90% des cas (simplexe) et l'erreur RMS était au moins dix fois plus importante qu'avec IMN et RC. L'erreur RMS pour la méthode de recalage rigide de surfaces avec espace de recherche limité était quant à elle de  $8.2 \pm 2.3$  mm. La comparaison montre que la méthode de recalage de surfaces est plus robuste que la méthode basée sur l'information mutuelle, mais que sa précision est significativement plus faible que les méthodes basées sur IMN et RC.

Lorsqu'on considère le recalage des images TEP d'émission directement avec des images RM en utilisant l'information mutuelle, IMN et RC, seul un cinquième des cas environ a été concluant (inspection visuelle) avec à la fois les images simulées et les images de patients. Ces résultats indiquent que l'utilisation des images TEP de transmission en tant que « médiateur » représente une façon plus précise et plus fiable de mettre en correspondance des images TEP d'émission et des images RM.

- **Cartographies anatomo-fonctionnelles**

Dans [Mäkelä, 2003a], une approche de construction de cartographies 3-D incluant des informations anatomiques et fonctionnelles à partir des images recalées RM, TEP-FDG et des données MCG a été développée. La méthode de fusion des données combine des informations structurelles provenant des images RM et des informations

fonctionnelles provenant de la TEP et de la MCG. Avec la présente approche, la localisation des anomalies métaboliques et de conduction est simple, le modèle biventriculaire avec une surface médiane du VG permettant l'identification non ambiguë des territoires myocardiques. Dans la littérature, l'activité électrique et le métabolisme ont généralement été étudiés séparément, principalement en raison du fait que les systèmes d'acquisition sont différents et impliquent des spécialistes différents. D'un point de vue physiopathologique, il est clair que toutes les activités sont liées entre elles. En conséquence, notre objectif, ici, a été de permettre l'étude de la corrélation entre les activités électriques (données MCG) et métaboliques (imagerie TEP 18F-FDG) qui peuvent révéler de nouveaux aspects de processus cardiaques complexes. La méthode de fusion des données donne une bonne compréhension spatiale de la captation du 18F-FDG et des valeurs MCG du cœur et pourrait aider à poser un meilleur diagnostic clinique, notamment, dans des études de viabilité myocardique [Nenonen, 2001]. La méthode 3-D présentée offre de bonnes possibilités, notamment pour la comparaison visuelle de données provenant de différentes modalités d'imagerie. Dans le même cadre de travail, il est naturel d'envisager l'inclusion d'autres données fonctionnelles complémentaires, telles que des informations liées à la mécanique ou à la perfusion myocardique, ainsi qu'à des informations temporelles en exploitant l'acquisition d'images TEP en synchronisation à l'ECG, par exemple [Behloul, 2001]. La fiabilité de la méthode dépend globalement de la précision du recalage rigide TEP-IRM, de la qualité de la segmentation des structures du cœur et de l'extraction de la surface médiane du VG.

La précision des méthodes dépend aussi des caractéristiques intrinsèques des modalités d'imagerie considérées. Les dispositifs d'imagerie TEP ont généralement une résolution spatiale de 4 à 10 mm [Hartiala, 1995]. Dans la MCG, des précisions de 5 à 25 mm ont été rapportées en comparant les résultats de la localisation MCG à : i) la chirurgie cardiaque, ii) l'ablation d'un cathéter, iii) des études électrophysiologiques invasives, iv) les résultats de la localisation ECG, et v) la connaissance physiologique (rayons X- ou IRM) [Fenici, 1998], [Pesola, 1999]. La méthode de visualisation en 3-D présentée avec la surface médiane du VG semble le moyen le plus direct d'obtenir des cartographies fonctionnelles du VG en empêchant un « effet de bord » qui pourrait survenir avec un recalage légèrement imprécis.

#### • **Analyse d'erreurs**

L'analyse de l'erreur de recalage des données anatomiques IRM avec des données fonctionnelles de la MCG, basée sur des repères externes, a été présentée dans [Mäkelä, 2002b]. L'importance relative des différentes sources d'erreurs a été évaluée. La somme de toutes les composantes d'erreurs de recalage est de 6 mm. Cette valeur explique bien l'erreur RMS des neuf repères recalés dans nos études menées chez 50 patients où l'erreur obtenue était de 6 mm environ [Pesola, 2000]. Une réduction drastique de l'erreur RMS totale n'est pas facile à réaliser car toutes les sources d'erreur interviennent à part égale. Néanmoins, l'effet des différences dans les formes de lits de mesure pourrait être réduit en fabriquant un support semi-rigide qui copierait la forme du

lit IRM et pourrait être utilisé pendant les acquisitions en MCG. De même, l'utilisation de coupes obliques semble être supérieure aux coupes orthogonales lors de la localisation des repères dans les images RM. Des acquisitions IRM en apnées courtes et la localisation en 3-D des repères MCG pourraient aussi aider à réduire l'erreur de recalage.

- ***Exploitation clinique***

Dans [Lauerma, 2000], les résultats combinés de trois modalités d'imagerie RM (dobutamine, ciné d'effort, premier passage et imagerie T1 pondérée avec rehaussement par produit de contraste) ont été comparés aux résultats de la TEP 18F-FDG avec évaluation du myocarde non viable dans des maladies de l'artère coronaire. Les données 18F-FDG TEP ont été utilisées comme référence afin d'analyser la capacité des méthodes IRM à détecter les zones de myocarde non viables. La visualisation des images recalées IRM-TEP a clairement montré une diminution de l'activité dans les zones infarctées potentielles. La combinaison de l'analyse du rehaussement de premier passage et l'évaluation de la mobilité de la paroi à l'effort augmente considérablement la spécificité de l'IRM dans la détection de secteurs non viables.

Enfin, une méthode de recalage élastique a été mise au point [Lötjönen and Mäkelä, 2001]. Dans la méthode de recalage élastique, une analyse visuelle qualitative des images cardiaques RM-TEP en petit axe, recalées de façon élastique, s'est avérée satisfaisante pour les cas testés. La méthode de recalage élastique réduit de petites différences de forme du cœur et du thorax entre les images recalées. Cependant, l'évaluation de la méthode n'a été réalisée que visuellement, une validation plus approfondie, par exemple, en s'appuyant sur des images simulées doit être réalisée.

## 7. Conclusions

Plusieurs aspects liés aux méthodes de recalage et de fusion de données en imagerie thoracique et cardiaque ont été présentés et discutés dans cette thèse, du développement et de l'implantation des méthodes jusqu'aux études cliniques. Cette thèse comporte une vue d'ensemble d'éléments déjà publiés, et aussi des compléments et six publications.

De nouvelles méthodes ont été mises au point, pour le recalage et la fusion d'images RM, TEP 18F-FDG et de données MCG. Les méthodes de recalage et de fusion des données ont obtenu de bons résultats. La production de cartographies anatomiques et fonctionnelles en 3-D a été assez complexe à mettre en oeuvre; elle a nécessité l'intégration de techniques de recalage, de segmentation, de calcul des valeurs de MCG et de fusion des données pour une visualisation en 3-D via les cartographies. Des méthodes alternatives existent pour chaque étape, et notamment dans le domaine du recalage d'images multimodalités.

Le choix d'une méthode de recalage d'images cardiaques est difficile. Il n'existe pas, à l'heure actuelle, de méthode suffisamment générale et puissante pour traiter la grande variété des situations cliniques. On est alors amené à concevoir une méthode spécialisée pour un cas particulier de recalage. Un recalage d'images cardiaques basé sur des repères cutanés externes ne garantit pas le recalage du cœur à l'intérieur du corps en raison des mouvements cardiaques et des structures thoraciques. Un recalage basé sur des repères anatomiques est difficile en raison du peu de structures anatomiques suffisamment précises visibles dans les images cardiaques, qui peuvent également être plus ou moins présentes dans certaines modalités et dans certaines conditions pathologiques telles que l'ischémie. Les méthodes de recalage de surfaces s'appuyant sur les contours thoraciques peuvent être utilisées s'il n'est pas possible d'obtenir d'informations structurelles directement à partir des surfaces du cœur. Les méthodes de recalage d'images cardiaques basées sur les surfaces thoraciques et pulmonaires, qui sont clairement visibles dans les images RM et TDM du thorax et dans les images de transmission TEP et TEMP sont recommandées [Pallotta, 1995]. Néanmoins, ces méthodes sont aussi sujettes à des erreurs induites par des artefacts liés aux différents mouvements (respiration, battements du cœur) [Goerres, 2002]. Le recalage direct des surfaces du cœur peut générer un meilleur recalage de la région d'intérêt, mais le choix des surfaces à recaler est important et dépend de l'application et des modalités utilisées. Les mesures de similarité de voxels, comparées aux méthodes de recalage basées sur les caractéristiques géométriques (comme les surfaces) présentent un avantage important dans la mesure où elles ne nécessitent pas d'extraction a priori de caractéristiques (segmentation et extraction de primitives). Dans les techniques récentes basées sur les mesures de similarité issues de la théorie de l'information, comme l'information mutuelle, peu d'hypothèses sont émises sur la nature

de la relation entre les intensités de l'image et l'image recalée [Maes, 1997]. Ces méthodes sont particulièrement prometteuses pour le recalage d'images cardiaques multimodales. En raison du très récent développement des méthodes de recalage basées sur ces nouvelles mesures, les applications au recalage des images cardiaques sont encore rares.

Compte tenu de nos premières expériences [Mäkelä, 2003b], il apparaît que le recalage multimodale d'images cardiaques IRM-TEP, avec les mesures IMN et RC, ait donné des résultats plus précis que le recalage rigide des surfaces thoraciques. Ce qui est confirmé par les expériences menées par Nicoleta Pauna dans le cadre de ses travaux sur l'évaluation des méthodes de recalage [Pauna, 2004].

Notons que les méthodes développées ont été utilisées à des fins de recherche [Mäkelä, 2003a], [Nenonen, 2001], ainsi que dans des études cliniques [Lauerma, 2000].

En toute rigueur, le recalage rigide des images cardiaques ne décrit pas correctement la relation spatiale entre les images. Le recalage élastique des images cardiaques se justifie en raison des mouvements respiratoire et cardiaque ; entre la télé-diastole et la télé-systole (pendant le cycle cardiaque), le plan des valves du cœur se déplace de 9 à 14 mm vers l'apex, et la paroi myocardique s'épaissit (elle passe de 10 mm à plus de 15 mm approximativement). De plus, les problèmes dus aux conditions d'imagerie, aux différents artefacts de mouvement et à l'élasticité du corps, des poumons et du cœur engendrent des déformations tissulaires qu'il n'est pas possible de compenser avec des méthodes de recalage rigide. Les méthodes élastiques seraient aussi utiles dans les cas où un grand nombre de jeux de données serait recalé sur le même atlas, permettant ainsi de recueillir des informations statistiques liées aux paramètres fonctionnels et structurels [Thirion, 2001] dans le cadre d'étude épidémiologiques, par exemple. Une méthode de recalage élastique a été développée et appliquée au recalage d'images cardiaques intra-patient IRM et TEP-FDG et d'images RM de la tête de sujets différents. La méthode a donné des résultats visuellement satisfaisants dans les deux cas. La méthode de recalage élastique peut compenser de légères différences provoquées par le mouvement cardiaque et la variabilité de la forme dans des études inter-sujets. Il faut cependant réaliser une évaluation beaucoup plus précise de l'impact de ce type de méthode.

Une approche basée sur un modèle *a priori* de cœur 3-D a été développée pour combiner des informations anatomiques IRM et des informations fonctionnelles issues de la TEP et de la MCG. Pour recaler des images RM et des données MCG, une méthode de recalage rigide basée sur des repères externes a été utilisée. Différentes sources d'erreurs pour ce recalage ont été évaluées par des expériences sur fantôme et des études réalisées chez des volontaires. Les résultats obtenus peuvent aider à réduire l'erreur de recalage de la méthode de recalage IRM-MCG. La méthode de fusion de données permet une bonne compréhension spatiale conjointe de deux informations



fonctionnelles complémentaires qui n'avaient pas encore pu être mise en relation auparavant: la captation du  $^{18}\text{F}$ -FDG en TEP et l'activité électro-magnétique en MCG du cœur. Cette méthode apporte ainsi les moyens d'une évaluation clinique plus riche, par exemple, pour l'estimation de la viabilité myocardique.

## Références

- [Alenius, 1999] Alenius, S., Ruotsalainen, U. et Astola, J. Attenuation correction for PET using count-limited transmission images reconstructed with median root prior. *IEEE Trans. Nucl. Science*, 1999, 46(3):1011-1021.
- [Ambroggi, 1989] Ambroggi, L., Musso, E., et Taccardi, B. Comprehensive electrocardiology, 1989, volume 2, chapitre Body-Surface Mapping, pp 1015-1049. Pergamon Press.
- [Andersson, 1995] Andersson, J. L. R., Bagnhammar, B., et Schneider, H. Accurate attenuation correction despite movement during PET imaging. *J. Nucl. Med.*, 1995, 36(4):670-678.
- [Arun, 1987] Arun, K. S., Huang, T. S., et Blostein, S. D. Least-squares fitting of two 3-D point sets. *IEEE Trans. Pattern Anal. Machine Intell.*, 1987, 9(5):698-700.
- [Audette, 2000] Audette, M., Ferrie, F., et Peters, T. An algorithmic overview of surface registration techniques for medical imaging. *Med. Image Anal.*, 2000, 4(4):201-217.
- [Axel, 1989] Axel, L. and L. Dougherty, *MR Imaging of motion with spatial modulation of magnetization*. *Radiology*, 1989. 171: 41-45.
- [Bacharach, 1993] Bacharach, S., Douglas, M., Carson, R., Kalkowski, P., Freedman, N., Perrone, P., et Bonow, R. Three-dimensional registration of cardiac positron emission tomography attenuation scans. *Computer Vision, Graphics et Image Processing*, 1993, 34(2):311-321.
- [Baer, 1996] Baer, F., Voth, E., et LaRosee, K. Comparison of dobutamine transesophageal echocardiography and dobutamine magnetic resonance imaging for detection of residual myocardial viability. *Am. J. Cardiol.*, 1996, 78:417-419.
- [Bankman, 2000] Bankman, I. N. *Handbook of Medical Imaging: Processing and Analysis*. Academic Press, 2000.
- [Behloul, 2001] Behloul, F., Lelieveldt, B. P. F., Boudraa, A., Janier, M., Revel, D., et Reiber, J. H. C. Neuro-fuzzy systems for computer-aided myocardial viability assessment. *IEEE Trans. Med. Imaging*, 2001, 20(12):1302-1313.
- [Besl, 1992] Besl, P. J. et McKay, N. D. A method for registration of 3-D shapes. *IEEE Trans. Pattern Anal. Machine Intell.*, 1992, 14(2):239-256.
- [Bettinardi, 1993] Bettinardi, V., Gilardi, M., Lucignani, G., Landoni, C., et Rizzo, G. (1993). A procedure for patient repositioning and compensation for misalignment between transmission and emission data in PET heart studies. *J. Nucl. Med.*, 34(1):137-142.
- [Beyer, 1999] Beyer, T., Townsend, D., Brun, T., Kinahan, P., Charron, M., Roddy, R., et Jerin, J. (1999). A combined PET/CT scanner for clinical oncology. *J. Nucl. Med.*, 41(8):1369-1379.

- [Bidaut, 2001] Bidaut, L. et Vallée, J.-P. Automated registration of dynamic MR images for the quantification of myocardial perfusion. *Journal of magnetic resonance imaging*, 2001, 13:648-655.
- [Borgefors, 1986] Borgefors, G. Distance transformation in digital images. *Computer Vision Graphics and Image Processing*, 1986, 48:344-371.
- [Borgefors, 1988] Borgefors, G. Hierarchical chamfer matching: A parametric edge matching algorithm. *IEEE Trans. Pattern Anal. Machine Intell.*, 1988, 10(6):849-865.
- [Brown, 1992] Brown, L. A survey of image registration techniques. *ACM Computing Surveys*, 1992, 24(4):325-376.
- [Brownell, 1953] Brownell, G. et Sweet, W. Localization of brain tumors with positron emitters. *Nucleonics*, 1953, 11:40-45.
- [Budinger, 1995] Budinger, T. et VanBrockling, H. The biomedical engineering handbook, *Positron Emission Tomography (PET)*, pp 1134-1150. CRC Press, 1995.
- [Cai, 1999] Cai, J., Chu, J., Recine, D., Sharma, M., Nguyen, C., Rodebaugh, R., Saxena, A., et Ali, A. (1999). CT and PET lung image registration and fusion in radiotherapy treatment planning using the chamfer-matching method. *Int. J. Radiation Oncology Biol. Phys.*, 1999, 43(4):883-891.
- [Canny, 1986] Canny, J. (1986). A computational approach to edge detection. *IEEE Trans. Pattern Anal. Machine Intell.*, 1986, 8(6):679-698.
- [Carrillo, 2001] Carrillo, A., Duerk, J., Lewin, J., et Wilson, D. Semiautomatic 3-D image registration as applied to interventional MRI liver cancer treatment. *IEEE Trans. Med. Imaging*, 2001, 19(3):175-185.
- [Conolly, 1995] Conolly, S., Macovski, A., et Pauly, J. The biomedical engineering handbook, chapitre Magnetic resonance imaging, pp 1006-1014. CRC Press, 1995.
- [Costa, 1994] Costa, W., Haynor, D., et Lewellen, T. Registration of segmented attenuation and emission data in PET. In *Proc. of Nucl. Science Symposium and Medical Imaging Conference*, 1994, pp 1407 - 1411.
- [Dahlbom, 2000] Dahlbom, M. et Huang, S.-C. *Handbook of Medical Imaging: Processing and Analysis*, chapitre Physical and biological bases of spatial distortions in positron emission tomography images, pp 439-448. Academic Press, 2000.
- [Declerck, 1996a] Declerck, J., Feldmar, J., Betting, F., et Goris, M. Automatic registration and alignment on a template of cardiac stress and rest SPECT images. In *Proc. of the workshop on mathematical methods in biomedical image analysis*, 1996, pp 212-221.
- [Declerck, 1996b] Declerck, J., Feldmar, J., Goris, M., et Betting, F. Automatic registration and alignment on a template of cardiac stress

- and rest SPECT images. Research Report 2770, INRIA, 1996.
- [Declerck, 1997] Declerck, J., Feldmar, J., Goris, M., et Betting, F. Automatic registration and alignment on a template of cardiac stress and rest reoriented SPECT images. *IEEE Trans. Med. Imaging*, 1997, 16(6):727-737.
- [Deriche, 1987] Deriche, R. Using Canny's criteria to derive a recursively implemented optimal edge detector. *International Journal of Computer Vision*, 1987, 1:167-187.
- [Dey, 1999] Dey, D., Slomka, P., Hahn, L., et Kloiber, R. Automatic three-dimensional multimodality registration using radionuclide transmission CT attenuation maps: A phantom study. *J. Nucl. Med.*, 1999, 40(3):448-455.
- [Eberl, 1996] Eberl, S., Kanno, I., Fulton, R., Ryan, A., Hutton, B., et Fulham, M. Automated interstudy image registration technique for SPECT and PET. *J. Nucl. Med.*, 1996, 37(1):137-145.
- [Faber, 1991] Faber, T., McColl, R., Opperman, R., Corbett, J., et Peshock, R. Spatial and temporal registration of cardiac SPECT and MR images: methods and evaluation. *Radiology*, 1991, 179(3):857-861.
- [Fenici, 1998] Fenici, R., Nenonen, J., Pesola, K., Korhonen, P., Lötjönen, J., Mäkijärvi, M., Poutanen, V. P., Keto, P., et Katila, T. Non-fluoroscopic localization of an amagnetic stimulation catheter by multichannel magnetocardiography. *PACE*, 1998, 22:1210-1220.
- [Fitzpatrick, 2000] Fitzpatrick, J., Hill, D., et Maurer, C. *Handbook of Medical Imaging*, volume 2, chapitre Image registration, pp 447-513. SPIE Press, 2000.
- [Frangi, 2001] Frangi, A. F., Niessen, W. J., et Viergever, M. A. Three-dimensional modeling for functional analysis of cardiac images, a review. *IEEE Trans. Med. Imaging*, 2001, 20(1):2-25.
- [Gallippi, 2001] Gallippi, C. M. et Trahey, G. E. Automatic image registration for MR and ultrasound cardiac images. In Insana, M. F. and Leahy, R. M., editors, *Lecture Notes in Computer Science 2082: Information Processing in Medical Imaging, IPMI01*, pp 141-147. Springer.
- [Gilardi, 1996] Gilardi, M., Rizzo, G., Savi, A., et Fazio, F. Registration of multi-modal biomedical images of the heart. *Q. J. Nucl. Med.*, 1996, 40(1):142-150.
- [Gilardi, 1998] Gilardi, M. C., Rizzo, G., Savi, A., Landoni, C., Bettinardi, V., Rossetti, C., Striano, G., et Fazio, F. N. Correlation of SPECT and PET cardiac images by a surface matching registration technique. *Computerized Medical Imaging and graphics*, 1998, 22:391-398.

- [Goerres, 2002] Goerres, G. W., Kamel, E., Heidelber, T.-N. H., Schwitter, M. R., Burger, C., et von Schulthess, G. K. PET-CT image co-registration in the thorax: influence of respiration. *Eur. J. Nucl. Med.*, 2002, 29(3):351-360.
- [Habboosh, 1992] Habboosh, A. W. A review of MRI and PET correlation. In *Proc. IEEE Conf. in Bioengineering*, 1992, pp 16-17.
- [Hajnal, 2001] Hajnal, J., Hill, D., et Hawkes, D. *Medical image registration*. CRC Press, 2001.
- [Hämäläinen, 1999] Hämäläinen, M. et Nenonen, J. *Encyclopedia of Electrical Engineering*, volume 12, chapitre Magnetic Source Imaging, 1999, pp 464-479. New York: Wiley & Sons.
- [Hänninen, 2001] Hänninen, H., Takala, P., Mäkijärvi, M., Montonen, J., Korhonen, P., Oikarinen, L., Simelius, K., Nenonen, J., Katila, T., et Toivonen, L. Recording locations in multichannel magnetocardiography and body surface potential mapping sensitive for regional exercise-induced ischemia. *Basic Res. Cardiol.*, 2001, 96:405-414.
- [Hartiala, 1995] Hartiala, J. et Knuuti, J. Imaging of heart by MRI and PET. *Ann. Med.*, 1995, 27:35-45.
- [Herk, 2000] Herk, M. V. *Handbook of Medical Imaging: Processing and Analysis*, chapitre Image registration using chamfer matching, pp 515-527. Academic Press, 2000.
- [Hill, 2000] Hill, D. et Hawkes, D. *Handbook of Medical Imaging: Processing and Analysis*, chapitre Across-modality registration using intensity-based cost functions, pp 537-553. Academic Press, 2000.
- [Hill, 2001] Hill, D. L. G., Batchelor, P. G., Holden, M. H., et Hawkes, D. J. *Medical image registration. Physics in medicine and biology*, 2001, 46(1):1-45.
- [Hoh, 1993] Hoh, C., Dahlbom, M., Harris, G., Choi, Y., Hawkins, R., Philps, M., and Maddahi, J. (1993). Automated iterative three-dimensional registration of positron emission tomography images. *J. Nucl. Med.*, 1993, 34(11):2009-2018.
- [Kim, 1991] Kim, R., Aw, T., Bacharach, S., et Bonow, R. Correlation of cardiac MRI and PET images using lung cavities as landmarks. In *Proc. IEEE Conf. Computers in Cardiology*, 1991, pp 49-52.
- [Klein, 2002a] Klein, G. J. et Huesman, R. H. Four-dimensional processing of deformable cardiac PET data. *Medical Image Analysis*, 2002, 6:29-46.
- [Klein, 2002b] Klein, G. J., Reutter, B. W., et Huesman, R. H. Four-dimensional affine registration models for respiratory-gated PET. *IEEE Trans. Medical Imag.*, 2002, 21(7):756-760.
- [Kramer, 1989] Kramer, E., Noz, M., Sanger, J., Megibow, A., et Maguire, G. CT-SPECT fusion to correlate radiolabeled monoclonal antibody uptake with abdominal CT findings. *Radiology*, 1989, 172(10):861-865.

- [Lauerma, 2000] Lauerma, K., Niemi, P., Hänninen, H., Janatuinen, T., Voipio-Pulkki, L., Knuuti, J., Toivonen, L., Mäkelä, T., Mäkijärvi, M., et Aronen, H. Multimodality MR imaging assessment of myocardial viability: combination of first-pass and late contrast enhancement to wall motion dynamics and comparison with FDG-PET. *Radiology*, 2000, 217:729-736.
- [Lauterbur, 1973] Lauterbur, P. Image formation by induced local interactions: Examples employing nuclear magnetic resonance. *Nature*, 1973, 242:190-191.
- [Lester, 1998] Lester, H. et Arridge, S. A survey of hierarchical non-linear medical image registration. *Pattern recognition*, 1998, 32:129-149.
- [Levin, 1988] Levin, D., Pelizzari, C., Chen, G., Chen, C.-T., et Cooper, M. D. Retrospective geometric correlation of MR ,CT and PET images. *Radiology* , 169(3):817-823.
- [Lötjönen et Mäkelä, 2001] Lötjönen, J. et Mäkelä, T. Elastic matching using a deformation sphere. In Niessen, W. and Viergever, M., editors, *Lecture Notes in Computer Science 2208: Medical Image Computing and Computer-Assisted Intervention, MICCAI'01*, 2001, pp 541-548. Springer.
- [Lötjönen, 1998] Lötjönen, J., Reissman, P.-J., Magnin, I. E., Nenonen, J., et Katila, T. A triangulation method of an arbitrary point set for biomagnetic problems. *IEEE Trans. Magn.*, 1998, 34(4):2228-2233.
- [Lötjönen, 1999] Lötjönen, J., Reissman, P.-J., Magnin, I. E., et Katila, T. Model extraction from magnetic resonance volume data using the deformable pyramid. *Med. Image Anal.*, 1999, 3(4):387-406.
- [Maes, 1997] Maes, F., Collignon, A., Vandermeulen, D., Marchal, G., et Suetens, P. Multimodality image registration by maximization of mutual information. *IEEE Trans. Med. Imaging*, 1997, 16(2):187-198.
- [Maintz, 1998] Maintz, J. B. A. et Viergever, M. A. A survey of medical image registration. *Med. Image Anal.*, 1998, 2(1):1-36.
- [Mäkelä, 2001] Mäkelä, T., Clarysse, P., Lötjönen, J., Sipilä, O., Lauerma, K., Hänninen, H., Pyökkimies, E.-P., Nenonen, J., Knuuti, J., Katila, T., et Magnin, I. E. A new method for the registration of cardiac PET and MR images using deformable model based segmentation of the main thorax structures. In *Medical Image Computing and Computer-Assisted Intervention (MICCAI'01)* , volume 2208 of *Lecture Notes in Computer Science (LNCS)*, 2001, pp 557-564. Springer.
- [Mäkelä, 2002a] Mäkelä, T., Clarysse, P., Sipilä, O., Pauna, N., Pham, Q., , Katila, T. et Magnin, I. E. A review of cardiac image registration methods. *IEEE Trans. Med. Imaging*, 2002, 21(9):1011-1021.



- [Mäkelä, 2002b] Mäkelä, T., Lötjönen, J., Sipilä, O., Lauerma, K., Nenonen, J., , Katila, T., et Magnin, I. E. Error analysis of registering of anatomical and functional cardiac data using external markers. In Nowak, H., Haueisen, J., Giesler, F., and Huonker, R., editors, Biomag 2002, Proc. of the 13th International Conf. on Biomagnetism, 2002, pp 842-845.
- [Mäkelä, 2003a] Mäkelä, T., Pham, Q., Clarysse, P., Nenonen, J., Lötjönen, J., Sipilä, O., Hänninen, H., Lauerma, K., Knuuti, J., Katila, T., et Magnin, I. E. A 3-D model-based registration approach for the PET, MR and MCG cardiac data fusion. Medical Image Analysis, 2003, 7:377-389.
- [Mäkelä, 2003b] Mäkelä, T., Pollari, M., Lötjönen, J., Pauna, N., Reilhac, A., Clarysse, P., Magnin, I. E., et Katila, T. (2003b). Evaluation and comparison of surface and intensity based rigid registration methods for thorax and cardiac MR and PET images. In I. E. Magnin et al. editors, Second International Workshop on Functional Imaging and Modeling of the Heart, FIMH 2003, pp 224-233. Springer.
- [Mattes, 2003] Mattes, D., Haynor, D., Vesselle, H., Lewellen, T., et Eubank, W. PET-CT image registration in the chest using free-form deformations. IEEE Trans. Med. Imaging, 2003, 22(1):120 - 128.
- [Maurer, 1993] Maurer, C. et Fitzpatrick, J. M. A review of medical image registration. Interactive image-guided neurosurgery, 1993, pp 17-44.
- [McLeish, 2003] McLeish, K., Hill, D., Atkinson, D., Blackall, J., et Razavi, R. A study of the motion and deformation of the heart due to respiration. IEEE Trans. Med. Imaging, 2003, 21(9):1142 - 1150.
- [Montonen, 2000] Montonen, J., Ahonen, A., Hämäläinen, M., Ilmoniemi, R., Laine, P., Nenonen, J., Paavola, M., K. Simelius, K., Paavola, M., Simola, K. S. J., et Katila, T. (2000). Magnetocardiographic functional imaging studies in biomag laboratory. In Aine, C., editor, Biomag96, Proc. Tenth Internat. Conf. on Biomagnetism , pp 494-497.
- [Nekolla, 2000] Nekolla, S., Ibrahim, T., Balbach, T., et Klein, C. Understanding cardiac imaging techniques - from basic pathology to image fusion , chapitre Coregistration and fusion of cardiac magnetic resonance and positron emission tomography studies, pp 144-154. IOS Press, Amsterdam, 2000.
- [Nelder, 1965] Nelder, J. et Mead, R. A simplex method for function minimization. Comp. J. , 7:308-313, 1965.
- [Nenonen, 1994] Nenonen, J. (1994). Solving the inverse problem in magnetocardiography. IEEE Eng. Med. Biol., 13:487-496.

- [Nenonen, 1997] Nenonen, J. T. Multimodal cardiac source imaging in the biomag laboratory. *Biomedizinische technik*, 1997, 42(1):29-32.
- [Nenonen, 2001] Nenonen, J., Pesola, K., Hänninen, H., K. Lauerma, K., Takala, P., Mäkelä, T. J., Mäkijärvi, M., Knuuti, J., Toivonen, L., et Katila, T. Current-density estimation of exercise-induced ischemia in patients with multivessel coronary artery disease. *Journal of Electrocardiography*, 2001, 34(suppl.):37-42.
- [O'Connor, 1998] O'Connor, M., Kanal, K., Gebhard, M., et Rossman, P. Comparison of four motion correction techniques in SPECT imaging of the heart: a cardiac phantom study. *J. Nucl. Med.*, 1998, 39:2027-2034.
- [O'Connor, 2000] O'Connor, M. (Evaluation of motion-correction techniques in cardiac SPECT. *J. Nucl. Med.*, 2000, 41(7):1298.
- [O'Dell, 1995] O'Dell, W. G., Moore, C. C., Hunter, W. C., Zerhouni, E. A., et McViegh, E. R. Three-dimensional myocardial deformations: calculation with displacement field fitting to tagged MR images. *Radiology*, 1995, 195:829-835.
- [Pallotta, 1995] Pallotta, S., Gilardi, M. C., Bettinardi, V., Rizzo, G., Landoni, C., Striano, G., Masi, R., et Fazio, F. Application of a surface matching image registration technique to the correlation of cardiac studies in positron emission tomography by transmission images. *Physics in Medicine and Biology*, 1995, 40:1695-1708.
- [Patton, 2000] Patton, J., Delbeke, D., et Sandler, M. Image fusion using an integrated, dual-head coincidence camera with X-ray tube-based attenuation maps. *J. Nucl. Med.*, 2000, 41(8):1364-1368.
- [Pauna, 2003] Pauna, N., Croisille, P., Costes, N., Reilhac, A., Mäkelä, T., Cozar, O., Janier, M., et Clarysse, P. A strategy to quantitatively evaluate MRI/PET cardiac registration methods using a monte carlo simulator. In I. E. Magnin et al., editors, *Second International Workshop on Functional Imaging and Modeling of the Heart, FIMH 2003*, pp 194-204. Springer, 2003.
- [Pauna, 2004] Pauna, N., Evaluation des méthodes de mise en correspondance en imagerie multimodale IRM/TEP thoracique et cardiaque. PhD thesis, spécialité Ingénierie Médicale et Biologique, Université Claude Bernard, Lyon I, France.
- [Pelizzari, 1989] Pelizzari, C. A., Ghen, G. T. Y., Spelbring, D. R., Weichselbaum, R. R., et Chen, C. T. Accurate three-dimensional registration of CT, PET and/or MR images of the brain. *J Comput Assist Tomogr.*, 1989, 13(1):20-26.
- [Pesola, 1999] Pesola, K., Nenonen, J., Fenici, R., Lötjönen, J., Mäkijärvi, M., Fenici, P., Korhonen, P., Lauerma, K., Valkonen, M.,

- Toivonen, L., et Katila, T. (1999). Bioelectromagnetic localization of a pacing catheter in the heart. *Phys. Med. Biol.*, 1999, 44:2565-2578.
- [Pesola, 2000] Pesola, K., Lötjönen, J., Nenonen, J., Magnin, I., Lauerma, K., Fenici, R. et Katila, T. The effect of geometry and topology differences in boundary element models on magnetocardiographic localization accuracy. *IEEE Trans. Biomedical Eng.*, 2000, 47(9):1237-1247.
- [Pham, 2001] Pham, Q. C., Vincent, F., Clarysse, P., Croisille, P., et Magnin, I. E. A FEM-based deformable model for the 3-D segmentation and tracking of the heart in cardiac MRI. In *Image and Signal Processing and Analysis ISPA 2001*, pp 250-254.
- [Pham, 2002] Pham, Q. (2002). Segmentation et mise en correspondance en imagerie cardiaque multimodale conduites par un modele anatomique bi-cavites du coeur. PhD thesis, Institut National Polytechnique de Grenoble, France.
- [Pluim, 2000] Pluim, J., Maintz, J., et Viergever, M. Image registration by maximization of combined mutual information and gradient information. *IEEE Trans. Med. Imaging*, 2000, 19(8):809-814.
- [Polhemus, 1993] Polhemus (1993). 3SPACE ISOTRAK II User's Manual. Polhemus Inc., Colchester, Vermont, U.S.A.
- [Powell, 1962] Powell, M. An iterative method of finding stationary values of a function of several variables. *Comp. J.*, 1962, 5:147-151.
- [Press, 1992] Press, W. H., Teukolsky, S. A., Vetterling, W. T., et Flannery, B. P. *Numerical Recipes in C: The art of scientific computing* 2<sup>nd</sup> Edition. Cambridge Univ. Press, 1992, Cambridge.
- [Pretorius, 1997] Pretorius, P. H. ., Xia, W., Kinag, M. A., Tsui, B. M. W., Pan, T. S., et Villegas, B. J. Evaluation of right and left ventricular volume and ejection fraction using a mathematical cardiac torso phantom. *J. Nucl. Med.*, 1997, 38(10):1528-1535.
- [Raichura, 2001] Raichura, N., Entwisle, J., Leverment, J., et Beardsmore, C. Breath-hold MRI in evaluating patients with pectus excavatum. *British Journal of Radiology*, 2001, 74(884):701-708.
- [Ratib, 2000] Ratib, O. *Handbook of Medical Imaging: Processing and Analysis*, chapitre Quantitative analysis of cardiac function, pp 359-374. Academic Press, 2000.
- [Reilhac, 1999] Reilhac, A., Gregoire, M.-C., Costes, N., Lavenne, F., Pierre, C., Diou, A., et Pujol, J.-F. A PET monte carlo simulateur from numerical phantom: Validation against the EXACT ECAT HR + scanner. In *Proc. IEEE Medical Imaging Conference*, Seattle, Washington, USA, 1999, pp 1527-1531.
- [Reilhac, 2002] Reilhac, A., Lartizien, C., Costes, N., Sans, S., Comtat, C., et Evans, A. Accounting for singles rates related phenomena in PET monte-carlo based simulations. In *IEEE Nuclear*

- Sciences Symposium, Norfolk, VA, USA, 2002, pp. 1617-1621.
- [Roche, 1998] Roche, A., Pennec, X., Malandain, G., et Ayache, N. The correlation ratio as a new similarity measure for multimodal image registration. In Wells, W. M., Colchester, A., and Delp, S., editors, *Lecture Notes in Computer Science 1496: Medical Image Computing and Computer-Assisted Intervention, MICCAI98*, 1998, pp 1115-1124. Springer.
- [Roche, 2001] Roche, A., Pennec, X., Malandain, G., et Ayache, N. Rigid registration of 3-D ultrasound with MR images : A new approach combining intensity and gradient information. *IEEE Trans. Med. Imaging*, 2001, 20(10):1038-1049.
- [Rogers, 1991] Rogers, W. J., Shapiro, E. P., Weiss, J. L., Buchalter, M. B., Rademakers, F. E., Weisfeldt, M. L., et Zerhouni, E. A. Quantification and correction for left ventricular systolic long-axis shortening by magnetic resonance tissue tagging and slice isolation. *Circulation*, 1991, 84(2):721-731.
- [Savi, 1995] Savi, A., Gilardi, M., Rizzo, G., Pepi, M., Landoni, C., Rossetti, C., Lucignani, G., Bartonelli, A., et Fazio, F. Spatial registration of echocardiographic and positron emission tomographic heart studies. *Eur. J. Nucl. Med.*, 1995, 22(3):243-247.
- [Shekhar, 2002] Shekhar, R. et Zagrodsky, V. Mutual information-based rigid and nonrigid registration of ultrasound volumes. *IEEE Trans. Med. Imaging*, 2002, 21(1):9-22.
- [Siemens, 2001] Siemens Applications guide, *MAGNETOM Vision to MAGNETOM Sonata, Fast imaging with TurboFLASH*, pp B.5.1-B.5.10. Siemens AG, 2001, Erlanger, Germany.
- [Siltanen, 1988] Siltanen, P. *Comprehensive Electrocardiology, chapitre Magnetocardiography*. Oxford: Pergamon Press, 1988.
- [Simelius, 1998] Simelius, K. Development of cardiographic mapping techniques for clinical use. *Licenciate thesis*, Helsinki university of Technology, 1998.
- [Sinha, 1995] Sinha, S., Sinha, U., Czernin, J., Porenta, G., et Schelbert, H. Noninvasive assessment of myocardial perfusion and metabolism: feasibility of registering gated MR and PET images. *Am. J. Roentgenol.*, 1995, 36:301-307.
- [Slomka, 1995] Slomka, P., Hurtwitz, G. A., Stephenson, J., et Cradduc, T. (1995). Automated alignment and sizing of myocardial stress and rest scans to three-dimensional normal templates using an image registration algorithm. *J. Nucl. Med.*, 1995, 36:1115-1122.
- [Slomka, 2001] Slomka, P. J., Radau, P., Hurwitz, G. A., et Dey, D. Automated three-dimensional quantification of myocardial perfusion and brain SPECT. *Computerized Medical Imaging and graphics*, 2001, 25(2):153-164.

- [Stone, 1998] Stone, C., McCormick, J., Gilland, D., Greer, K., Coleman, R., et Jaszczak, R. Effect of registration errors between transmission and emission scans on a SPECT system using sequential scanning. *J. Nucl. Med.*, 1998, 39(2):365-373.
- [Studholme, 1997] Studholme, C., Hill, D. L., et Hawkes, D. J. (1997). Automated three-dimensional registration of magnetic resonance and positron emission tomography brain images by multiresolution optimization of voxel measures. *Medical Physics*, 1997, 24(1):25-35.
- [Studholme, 1999] Studholme, C., Hill, D. L., et Hawkes, D. J. An overlap invariant entropy measure of 3d medical image alignment. *Pattern Recognition*, 1999, 32:71-86.
- [Sweet, 1951] Sweet, W. The use of nuclear disintegration in the diagnosis and treatment of brain tumor. *New England Journal of Medicine*, 1951, (247):875-878.
- [Tai, 1997] Tai, Y.-C., Lin, K., Hoh, C., Huang, S., et Hoffman, E. Utilization of 3-D elastic transformation in the registration of chest X-ray CT and whole body PET. *IEEE Trans. Nucl. Med.*, 1997, 44(4):1606-1612.
- [Thirion, 1995] Thirion, J.-P. Fast non-rigid matching of 3-D medical images. *Research Report 2547*, 1995, INRIA.
- [Thirion, 2001] Thirion, J.-P. Understanding cardiac imaging techniques - from basic pathology to image fusion, chapitre Perfusion and motion from gated SPECT, pp 84-93. *IOS Press*, Amsterdam, 2001.
- [Turkington, 1997] Turkington, T., DeGrado, T., Hanson, M., et R.E.Coleman. Alignment of dynamic cardiac PET images for correction of motion. *IEEE Trans. Nucl. Sci.*, 1997, 44(2):235-242.
- [van den Elsen, 1993] Van den Elsen, P., Pol, E.-J., et Viergever, M. Medical image matching - A review with classification. *IEEE Engineering in Medicine and Biology*, 1993, 12(2):16-39.
- [Waiter, 2000] Waiter, G. D., Al-Mohammad, A., Norton, M. Y., Redpath, T. W., Welch, A., et Walton, S. Regional myocardial wall thickening assessed at rest by ECG gated 18-F-FDG positron emission tomography and by magnetic resonance imaging. *Heart*, 2000, 84:332-333.
- [Webb, 1995] Webb, S. *The Physics of Medical Imaging*. Academic Press, 1995.
- [Wells, 1996] Wells, W., Viola, P., Atsumi, H., Nakajima, S., et Kikinis, R. Multi-modal volume registration by maximization of mutual information. *Med. Image Anal.*, 1996, 1(1):35-51.
- [Wirth, 1997] Wirth, M. A., Choi, C., et Jennings, A. Point-to-point registration of non-rigid medical images using local elastic transformation methods. In *IEEE Int. Conf. on Image Processing and its Applications*, 1997, pp 780-784.
- [Woods, 2000a] Woods, R. *Handbook of Medical Imaging: Processing and Analysis* , chapitre Within-modality registration using

- intensity-based cost functions, pp 529-536. Academic Press, 2002.
- [Woods, 2000b] Woods, R. Handbook of Medical Imaging: Processing and Analysis , chapitre Validation of registration accuracy, pp 491-497. Academic Press, 2000.
- [Wrenn, 1951] Wrenn, F. et Handlerp, M. P. The use of positron emitting radioisotopes for localization of brain tumors. Science, 1951, 113: 153-164.
- [Yu, 1995] Yu, J. N., Fahey, F. H., Gage, H. D., Eades, C. G., Harkness, B. A., et Pelizzari, C. A. Intermodality, retrospective image registration in the thorax. J. Nucl. Med., 1995, 36(12):2333-2338.
- [Zerhouni, 1988] Zerhouni, E.A., D. M. Parish, W. J. Rogers, A. Yang, and E. P. Shapiro,, *Human heart: tagging with MR imaging - A method for noninvasive assessment of myocardial motion*. Radiology, 1988. 169: 59-63
- [Zhenghong, 2002] Zhenghong, L. et Berridge, M. PET imaging-based evaluation of aerosol drugs and their delivery devices: nasal and pulmonary studies. IEEE Trans. Med. Imaging, 2002, 21(10):1324-1331.



## Liste des publications insérées

T.J. Mäkelä, P. Clarysse, O. Sipilä, N. Pauna, Q.C. Pham, T. Katila et I.E. Magnin. A review of cardiac image registration methods. IEEE Trans. Med. Imaging, vol. 21, no 9, pp. 1011-1021, 2002.

T.J. Mäkelä, P. Clarysse, J. Lötjönen, O. Sipilä, K. Lauerma, H. Hänninen, E. P. Pyökkimies, J. Nenonen, J. Knuuti, T. Katila et I.E. Magnin, A new method for the registration of cardiac PET and MR images using deformable model based segmentation of the main thorax structures. Lect. Notes Comput. Sci. 2208:Medical Image Computing and Computer Assisted Intervention, MICCAI'01, W. Niessen, M.A. Viergever (Eds.), Springer, pp. 557-564, 2001.

T.J. Mäkelä, Q.C. Pham, P. Clarysse, J. Nenonen, J. Lötjönen, O. Sipilä, H. Hänninen, K. Lauerma, J. Knuuti, T. Katila et I.E. Magnin. A 3-D model-based registration approach for the PET, MR and MCG cardiac data fusion. Medical Image Analysis, vol. 7, pp. 377-389, 2003.

T.J. Mäkelä, J. Lötjönen, O. Sipilä, K. Lauerma, J. Nenonen, T. Katila et I.E. Magnin, Error Analysis of Registering of Anatomical and Functional Cardiac Data Using External Markers, Int. Conf. on Biomagnetism, BIOMAG'02, H. Nowak, J. Haueisen, F. Giesler, R. Huonker (Eds.). Verlag, pp. 842-845, 2002.

T. Mäkelä, M. Pollari, J. Lötjönen, N. Pauna, A. Reilhac, P. Clarysse, I.E. Magnin et T. Katila. Evaluation and comparison of surface and intensity based rigid registration methods for thorax and cardiac MR and PET images. Lect. Notes Comput. Sci. 2674: International Workshop on Functional Imaging and Modeling of the Heart, FIMH'03, Springer, pp. 224-233, 2003.

J. Lötjönen et T.J. Mäkelä, Elastic matching using a deformation sphere, Lect. Notes Comput. Sci. 2208: Medical Image Computing and Computer Assisted Intervention, MICCAI'01, W. Niessen, M.A. Viergever (Eds.), Springer, pp. 541-548, 2001.

K. Lauerma, P. Niemi, H. Hänninen, T. Janatuinen, L-M. Voipio-Pulkki, J. Knuuti, L. L. Toivonen, T.J. Mäkelä, M. Mäkijärvi et H.J. Aronen. Multimodality MR Imaging Assessment of Myocardial Viability: Combination of First-Pass and Late Contrast Enhancement to Wall Motion Dynamics and Comparison with FDG PET-Initial Experience. Radiology, vol. 217, pp. 729-736, 2000.



# A Review of Cardiac Image Registration Methods

Timo Mäkelä\*, *Student Member, IEEE*, Patrick Clarysse, Outi Sipilä, Nicoleta Pauna, Quoc Cuong Pham, Toivo Katila, *Member, IEEE*, and Isabelle E. Magnin, *Member, IEEE*

**Abstract**—In this paper, the current status of cardiac image registration methods is reviewed. The combination of information from multiple cardiac image modalities, such as magnetic resonance imaging, computed tomography, positron emission tomography, single-photon emission computed tomography, and ultrasound, is of increasing interest in the medical community for physiologic understanding and diagnostic purposes. Registration of cardiac images is a more complex problem than brain image registration because the heart is a nonrigid moving organ inside a moving body. Moreover, as compared to the registration of brain images, the heart exhibits much fewer accurate anatomical landmarks. In a clinical context, physicians often mentally integrate image information from different modalities. Automatic registration, based on computer programs, might, however, offer better accuracy and repeatability and save time.

**Index Terms**—Cardiac image registration, computed tomography (CT), magnetic resonance imaging (MRI), positron emission tomography (PET), single-photon emission computed tomography (SPECT), ultrasound (US).

## NOMENCLATURE

CC	Correlation coefficient.
CT	X-ray computed tomography.
ECG	Electrocardiography.
ED	End-diastolic.
ES	End-systolic.
FDG	Fluorodeoxyglucose.
ICP	Iterative closest point.
LA	Long axis.
LV	Left ventricle.
MRI	Magnetic resonance imaging.
PET	Positron emission tomography.
rms	Root mean square.
SA	Short axis.
SAD	Sum of absolute differences.
SPECT	Single-photon emission computed tomography.
SSC	Stochastic sign change.
SSD	Sum of squared intensity differences.

Manuscript received November 3, 2001; revised July 6, 2002. This work was supported in part by the Scientific Department of the French Embassy in Finland, the Region Rhône Alpes, the ADéMO project, and The Foundation of Technology in Finland. Asterisk indicates corresponding author.

\*T. Mäkelä is with the Laboratory of Biomedical Engineering, Helsinki University of Technology, P.O. Box 2200, FIN-02015 HUT, Finland, and CREATIS, UMR CNRS #5515, 69621 Villeurbanne Cedex, France (e-mail: timo.makela@hut.fi).

P. Clarysse, N. Pauna, Q. C. Pham, and I. E. Magnin are with CREATIS, UMR CNRS #5515, 69621 Villeurbanne Cedex, France.

O. Sipilä is with the Department of Radiology, Helsinki University Central Hospital, FIN-00029 HUS, Finland.

T. Katila is with the Laboratory of Biomedical Engineering, Helsinki University of Technology, FIN-02015 HUT, Finland, and BioMag Laboratory, Helsinki University Central Hospital, FIN-00029 HUS, Finland.

Digital Object Identifier 10.1109/TMI.2002.804441

SVD	Singular value decomposition.
US	Ultrasound.
VIR	Variance of intensity ratio.

## I. INTRODUCTION

**D**IFFERENT imaging modalities bring complementary information that can be advantageously used to establish a diagnosis or assist the clinician for a therapeutic gesture. To locally compare two or more measurements of different nature, a number of registration algorithms have been developed, especially in brain imaging.

In the widespread ischemic heart diseases, the consequence of reduced blood flow to the heart muscle can be studied using several medical imaging modalities, each of which gives a specific view of this complex phenomenon. The first consequence is a deterioration of the myocardial perfusion, which can be analyzed with nuclear medicine imaging techniques (SPECT and PET) or with MRI [1], [2]. The deficit of perfusion induces metabolic changes in myocardial tissues highlighted using FDG PET studies [1]. A further consequence of a myocardial ischemia is the reduced capacity of the heart to eject blood into the body. This can be evaluated by analyzing the myocardial contractile function using MRI or US. Recent studies have demonstrated the interest of concurrently analyzing those different aspects in order to assess the myocardial viability, which will determine the proper therapeutic action [3], [4]. Therefore, there is a growing interest in the development of cardiac image registration methods that could bring into the same anatomical reference all the available functional measurements.

Cardiac image registration is a more complex problem than brain image registration, in particular because of the nonrigid and mixed motions of the heart and the thorax structures. Moreover, as compared to the brain, the heart exhibits fewer accurate anatomical landmarks. Also, cardiac images are usually acquired with a lower resolution than brain images. Fig. 1 illustrates a typical acquisition protocol with ECG-gated cardiac MRI. This highlights certain problems induced by the spatiotemporal image acquisition that hamper image registration.

In clinical practice, physicians mentally integrate information from different images acquired from a patient, often with different imaging modalities. Images are shown in various orientations and positions and at different scales. Semi-interactive registration methods rely on the expert's ability to interactively select corresponding slices using anatomical knowledge. In cardiac image registration, the semi-interactive methods are often used to register gated SA images [5], [6].

Several survey papers have been published in the field of medical image registration [7]–[10]. Also, some review articles

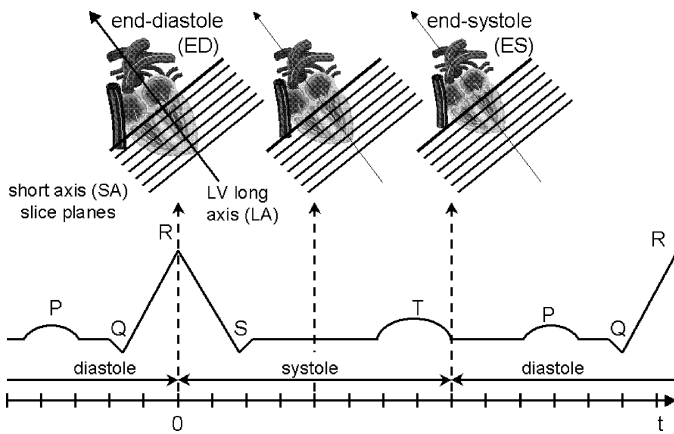


Fig. 1. Illustration of a classical acquisition of SA images with a ECG-gated cine MR sequence. The same slice is acquired at successive time points of the cardiac cycle. However, due to the motion of the heart, we do not observe the same anatomical region within the same slice. Moreover, several cardiac cycles are required to reconstruct slices. When possible, patients are asked to retain their breath (15–20 s) during acquisition.

and books closely related to medical image registration and fusion can be mentioned, such as [11]–[17]. Very few review papers focusing on cardiac image registration have been published [18], [19]. Gilardi *et al.* [18] reviewed the techniques and clinical applications for the integration of multimodal biomedical images of the heart. Habboosh *et al.* [19] briefly discussed the aspects of cardiac PET and MRI correlation. In the review article of Maintz *et al.* [8], registration methods for cardiac images were also referenced in a separate section.

This paper aims to provide a survey concerning cardiac image registration, including the most recent articles and discussing also implementation and validation issues. For the four-dimensional (4-D) registration of intramodality cardiac images, the problem is often addressed in a cardiac motion tracking framework. In this survey, the 4-D motion tracking problem is not considered at the methodological level. Instead, we refer to some recent papers in this field [14], [20]–[23].

In this paper, cardiac image registration methods are divided into two main categories: 1) those based on geometric image features (Section II-A) and 2) those based on voxel similarity measures (Section II-B). The geometric image feature-based methods are divided into registration of *a set of points* and *edges or surfaces*. Registration methods based on voxel similarity measures include *moments and principal-axes methods*, *intensity difference and correlation methods*, and *methods based on mutual information*. After presenting the current status of cardiac image registration methods, we discuss implementation issues, such as interpolation and optimization (Section II-C). Validation of the registration methods is presented in Section III. The overview of cardiac and thorax registration methods and their main parameters are summarized in Table I. Some of the brain, thorax, and abdominal image registration articles are referenced when methods have been, or can easily be, applied to heart image registration.

In the reviewed papers, mainly MR, CT, PET, and SPECT imaging modalities have been considered. There are very few references related to registration with cardiac US images. This is due to the characteristics of the US images that make them diffi-

cult to process automatically. Moreover, despite the existence of three-dimensional (3-D) echocardiographic systems [24], two-dimensional (2-D) image acquisitions are routinely performed. At most, a collection of radial planes is acquired, resulting in a quite different geometry as compared to the other imaging modalities.

## II. CARDIAC IMAGE REGISTRATION: PRINCIPLES AND APPLICATIONS

### A. Registration Methods Based on Geometric Image Features

Registration methods based on geometric image features can be divided into registration of *a set of points* and registration of *edges or surfaces*.

1) *Point-Based Registration*: Point-based registration methods often use external markers or anatomical landmarks. Corresponding point sets are usually manually defined in the reference and floating images. The advantages of the point-based registration methods are that they can be applied to any imaging modalities where markers or landmarks are visible and that the calculation of the registration parameters between two point sets is usually fast. A noniterative least squares method can be used to register corresponding point sets [12], [25]. The method uses an SVD of a 3 by 3 covariance matrix to find a unique solution for the registration parameters between two point sets. In cardiac image registration, the method has been used, e.g., in phantom experiments for validating rigid registration error [26].

Registration methods based on *external skin markers* (fiducial markers) are widely applied in medical image registration because they allow matching of any imaging modalities in which the positions of markers can be accurately defined. Registration based on skin markers is independent of the alteration in the image patterns, induced by the pathologies [18]. Skin markers must be easy to use and accurate to reattach, but they should not interfere with the diagnostic content of the images. Since the flexibility of the body can cause errors in registration, it is important to choose relatively stable parts of the body for markers placement [27]. Ideally, markers should not be removed between imaging sessions to ensure the same placements in different modalities [28]. Registration of external skin markers does not guarantee registration of the heart within the body, since heart position changes with body position, respiration, and cardiac contraction [29]. The disadvantage of the skin markers is also that they cannot be utilized retrospectively. External markers have been applied especially as a gold standard method in phantom measurements to validate the accuracy of rigid cardiac and thorax registration methods [26], [30]–[33] and in clinical images, e.g., to validate the accuracy of rigid registration of head images [34]. For rigid thorax CT and SPECT image registration, the combination of both external markers and landmarks has also been utilized [35], [36].

In *landmark-based registration*, corresponding anatomical points have to be visible in both registered images. For heart images, there are usually only few spatially accurate anatomical landmarks. In pathological conditions, such as ischemia, the functional alterations can also hide anatomical landmarks [18].

TABLE I  
OVERVIEW OF EVALUATED CARDIAC AND THORAX IMAGE REGISTRATION METHODS

Reference	Modalities	Object	Trans.	Struc.	Method	Valid.	Error	Error type
Registration methods based on geometric image features								
Point-based registration								
Wirth <i>et al.</i> [42]	CT-MR	Thorax	Elastic	Landmarks	Interpolation & Elastic funct.	-	-	-
Thorax surface based registration								
Yu <i>et al.</i> [33]	CT-PET	Thorax	Rigid	T & L	“head-and-hat”	P	(x,y) 2.3 mm, (y) 3.0 mm	mean (rms)
Cai <i>et al.</i> [46]	CT-PET	Lungs	Rigid	T & L	Chamfer	P & Pa. & S	(x,y) 2-3 mm, (y) 3-4 mm, (rot.)1.5°	mean
Pallotta <i>et al.</i> [26]	PET-PET	Heart	Rigid	T & L	Chamfer	P & S	3 mm, (rot.) 1°	mean (rms)
Gilardi <i>et al.</i> [31]	SPECT-PET	Heart	Rigid	T & L	Chamfer	P & Pa.	2.19 ± 0.52 mm	mean (rms)±s.d.
Mäkelä <i>et al.</i> [47]	MR-PET	Heart	Rigid	T & L	Chamfer	Surfaces	(x,y,z) 2.8 ± 0.5 mm	(x,y) mean (rms), (z) mean
Heart surface based registration								
Faber <i>et al.</i> [29]	MR-SPECT	Heart	Rigid	HS	“head-and-hat”	P	2.7 mm	mean (rms)
Sinha <i>et al.</i> [40]	MR-PET	Heart	Rigid	HS	“head-and-hat”	L	1.95 mm ± 1.6 mm	mean (rms)
Nekolla <i>et al.</i> [57]	PET-SPECT	Heart	Rigid	HS	-	Surfaces	2.5 mm	mean
Declerck <i>et al.</i> [50]	SPECT-SPECT	Heart	Elastic	HS	ICP	Pa.	-	-
Registration methods based on voxel similarity measures								
Intensity difference and correlation methods								
Gallippi <i>et al.</i> [75]	MR-MR (time series)	Heart	Rigid & Elastic	-	C	M	1.23 ± 0.06 mm 3.25 ± 1.04 mm	left-right (mean) anterior-poster. (mean)
Bidaut <i>et al.</i> [37]	MR-MR (perfusion)	Heart	Rigid	-	SSD	L	3.0 mm (x), 1.6 mm (y), 2.2 mm (z)	mean (rms) (maximum)
Bacharach <i>et al.</i> [76]	PET-PET	Heart	Rigid	-	CC	M	(x,y,z) 1 mm, (rot.) 1.5°	mean
Turkingston <i>et al.</i> [71]	PET-PET	Heart	Rigid	-	C	P	(x, y) 1.7 mm, (z) 4.2 mm	mean
Klein <i>et al.</i> [23]	PET-PET	Heart	Elastic (4-D)	-	LS	P	(x) 1.9 mm, (y) 2.4 mm, (z) 6.8 mm	mean (max.)
Hoh <i>et al.</i> [67]	MR-SPECT	Heart	Rigid	-	SAD, SSC	M	(x,y) 0.5 ± 0.5 mm, (z) 1.1 ± 1.1 mm, (rot) 0.9 ± 1.1°	mean ± s.d.
Dey <i>et al.</i> [32]	CT-SPECT	Heart & Thorax	Rigid	-	SAD VIR	P P	2.5 ± 1.2 mm 3.3 ± 1.3 mm	mean (rms) mean (rms)
Eberl <i>et al.</i> [30]	SPECT-SPECT	Heart	Rigid	-	SAD	P	3.1 ± 1.7 mm 1.3° (rot)	mean ± s.d.
Slomka <i>et al.</i> [66]	SPECT-SPECT	Heart	Affine	-	SAD	P	1.5 mm(x,y,z) 2.0° (rot), 5.3 % (size)	mean (max.)
Mutual information								
Carrillo <i>et al.</i> [38]	MR-MR	Abdom.	Rigid	-	MI	L	(x,y,z) 3.05 mm	mean

Object = Main object to be registered.

Trans. = Transformation method.

Struc. = Structures used in registration (T = Thorax, L = Lungs, HS = heart surfaces).

Method = Method used in registration (C = cross-correlation, LS = least squares voxel difference, MI = mutual information).

Valid. = Validation method (P = Phantom, Pa. = Patient, S = Simulated images, M = Misaligned images, L = Landmarks).

Error: rot. = Rotational error.

Error type: s.d. = Standard deviation.

Landmarks have been exploited to estimate rigid registration error in [30], [31], [35], [37], and [38]. Savi *et al.* [39] rigidly registered cardiac PET and US images by using homologous anatomical landmarks (the two papillary muscles and the inferior junction of the right ventricle) of the heart. Rigid US-PET image registration was first performed in a plane identified by three landmarks. The obtained registration parameters were then applied to the whole PET volume. Sinha *et al.* [40] validated the rigid heart surface-based cardiac MR and PET image registration method by analyzing registration error using cardiac landmarks (papillary muscles, the insertion point of the right ventricle into the septum, the most inferior aspect of the septum, and the most inferior aspect of the lateral wall). Identification of landmarks was prone to errors because of their finite width and complex shapes. Especially in multimodal cardiac image registration, the accurate localization of the same

anatomical landmarks can be difficult. Sometimes automatically detected points and lines can be used as landmarks [41]. Wirth *et al.* [42] utilized landmark-based elastic registration to register a thorax MR image to the coordinates of a CT image of the same subject. In this method, 36 corresponding landmarks in thorax and lung surfaces were elastically matched, and the rest of the points were mapped using interpolation or elastic mapping functions. The method registered corresponding points well, but general validation of the method accuracy was not performed.

2) *Edge- and Surface-Based Registration*: The chamfer matching method [43], [44] is often used to register surfaces and point sets. In this method, the sum of the distances between the transformed points and a distance map built upon the segmented surface using the chamfer distance transformation is minimized [45]. For cardiac image registration, chamfer

matching methods have mainly been utilized for rigid registration methods based on the thorax structures [26], [31], [46], [47]. Also the ICP algorithm of Besl *et al.* [48] has been used to elastically register surfaces and lines [49], [50]. In the ICP method, the distances between structures are explicitly computed at every iteration of the registration algorithm and the sum of distances minimized. The “head-and-hat” algorithm [51], [52] has also been commonly proposed to register medical images and was first presented to register brain images. This algorithm models the contours from one of the images (usually higher resolution) as a surface (the “head”) and the contours of the other image set as a series of points (the “hat”). The algorithm then determines the optimum rigid transformation, which minimizes the mean squared deviation between the points of the hat and the surfaces of the head by using the Powell minimization algorithm [53], [54]. The “head-and-hat” method has been applied for registering surfaces from cardiac MR and PET images [40] and thorax CT and PET images [33].

*a) Registration methods based on thorax surfaces:* Cardiac image registration methods based on the registration of the thorax surfaces have been proposed because it is often difficult to extract structural information from the heart surfaces directly. Thorax and lung surfaces are, in general, well visible in MR and CT images and in PET and SPECT transmission images. In the registration methods based on the thorax surfaces, every surface point that is involved in registration should have a unique corresponding point in the other image. In practice, this usually means that the axial extension in the reference study must be greater than in the study to be matched [18]. Sometimes, artificial edges of the images have to be excluded from the registration parameters’ calculation. Surfaces from the transmission images have been utilized for intramodality registration of cardiac PET images [26] and for intermodality registration of cardiac PET and SPECT images [31], MR and PET images [47], and thorax CT and PET images [33], [46], [55]. Thorax and lung surfaces have often been obtained using the simple thresholding method of Yu *et al.* [33], where a threshold value of 50% of the maximum soft-tissue value was selected to segment the PET and SPECT transmission images [31], [46] and thorax CT images [33], [46]. Also, deformable models have been applied to segment thorax structures from PET transmission and MR images [47]. In this rigid registration method, chamfer matching was used to register segmented surfaces from PET transmission image with the MR transaxial image. Also, SA PET images were calculated from registered transaxial images by using header information between MR transaxial and SA images.

*b) Registration methods based on heart surfaces:* Registration of the heart surfaces may result in better registration of the area of interest [31]. The choice of the surfaces to be registered (e.g., epicardial and/or endocardial) is important. Faber *et al.* [29] presented a method for the intersubject rigid registration of 4-D gated cardiac SPECT perfusion images to the coordinates of the gated MR image. Left ventricular ED and ES endocardial surfaces were automatically detected from both image modalities using a model-based surface detector [56]. The best single transformation was searched to register SPECT ED and ES surfaces with corresponding surfaces in an MR image. Registration of the center of mass of the surfaces was used as an initial align-

ment, and the “head-and-hat” algorithm [51], [52] was used to find more accurate registration parameters. After registration, quadrilinear interpolation was applied to the SPECT image to obtain a temporal correlation with time frames of an MR image. Sinha *et al.* [40] presented a method to register gated cardiac FDG PET images to the coordinates of gated MR images. In this method, contours of the left ventricular wall were defined from both imaging modalities by using an interactive algorithm with morphologic operators. Registration parameters were defined by using the “head-and-hat” surface matching approach [51]. In the MunichHeart software [57], endocardial and epicardial contours were manually delineated from SA MR images and registered with the same contours extracted from PET or SPECT images using the maximum count detection algorithm [58]. Declerck *et al.* [49], [50] presented an automated elastic registration method to align images from rest and stress myocardial perfusion SPECT studies. In this method, feature points of the cardiac SPECT image surfaces were extracted using a Canny–Deriche edge detector [59], [60]. The features were then registered using the ICP method [48]. Images were also elastically registered with a template image by using local spline transformations. The method was also applied to cardiac SPECT perfusion followup studies [61]. Thirion *et al.* [62], [63] presented a deformable model-based elastic registration method for intramodality registration of diastolic and systolic CT or SPECT images. Andersson *et al.* [64] utilized heart edge information for the cardiac PET emission images to rigidly reduce movement artifacts. The method was also applied to rigidly realign cardiac PET emission and transmission images [65].

### B. Registration Methods Based on Voxel Similarity Measures

Registration methods based on voxel similarity measures can be divided into methods based on *moments and principal axes*, *intensity difference and correlation methods*, and methods based on *mutual information*.

*1) Methods Based on Moments and Principal Axes:* Image registration methods based on moments and principal axes use statistical factors derived from image data [7]. Moments describe the spatial distribution of the mass (intensity) of the image. Methods based on the principal axes register images by bringing the principal axes of the inertia tensors of corresponding objects in the images into coincidence. Accurate registration based on principal axes requires that the entire object be present in both imaging sets. Therefore, applications of these methods are limited. The principal-axes approach has been used to initially register myocardial SPECT stress and rest scans to templates [66], using SAD and SSC methods (see Section II-B2) to obtain more accurate registration. For the registration of thorax images, the principal-axes approach was proposed as an initial registration between CT and transmission SPECT images [32], while SAD and VIR measures (see Section II-B2) were applied to obtain the final registration.

*2) Intensity Difference and Correlation Methods:* Image intensity difference and correlation methods attempt to determine the best registration by maximizing the similarity between images that differ primarily because of different image-acquisition conditions, like noise [7]. The assumption of these methods is usually that pixel values in the registered images are strongly



correlated. Therefore, these methods are particularly powerful for intramodality registration methods.

*a) Intramodality registration:* Hoh *et al.* [67] compared the SAD and SSD similarity measures for the rigid registration of cardiac PET emission images. In the SAD method, registered images are subtracted pixel-by-pixel, and the mean value of the sum of the absolute intensity difference of all the pixels in the subtracted image is computed. The SSD is similar to the SAD measure, but the squared intensity difference is calculated instead of the absolute difference. The SSD is the optimum measure when registered images differ only by Gaussian noise [12], [68]. In the paper by Hoh *et al.* [67], the effect of various defects and misalignments was simulated. No significant differences in the translation or rotation errors of the SAD and SSD algorithms were found. Slomka *et al.* [66] compared the SAD and SSC methods for affine registration of SPECT emission images to templates. An initial registration was obtained using alignment of the principal axes. Registered images were first subtracted, and the SSC was determined by counting along each pixel row the number of times the pixel gray level in the subtracted images went from negative to positive or from positive to negative [67]. At the optimum registration, there is a maximum of total sign changes. Slomka *et al.* [66] argued that the SAD provided better results than the SSC. This method was later enhanced and proposed for voxel-by-voxel quantification of SPECT images as a clinical tool [69]. In the enhanced method, not only did the registration algorithm compensate for shape differences by affine registration, but also a template erosion technique was used (role similar to warping adjustments) for fine tuning of the registration. The SSD-based similarity measure has also been applied in rigid motion correction (caused mainly by breathing) of gated heart perfusion MR images [37]. Perfusion MR imaging often takes more than 3 min. Breath holding is not possible during the imaging protocol, nor can respiratory gating be used since a high temporal resolution is needed. Therefore, dynamic gated heart images and temporal resolution are degraded by respiratory-induced movements during the whole sequence [37]. In the recent paper by Klein *et al.* [23], [70], a novel affine 4-D registration algorithm was proposed for motion compensation of gated cardiac PET emission images to give better estimation of perfusion and metabolic parameters. The method registers different cardiac PET emission image time frames with the end-diastolic time frame. It uses nonuniform elastic material model (12-parameter global affine motion model) and iteratively calculates registration parameters of the model using a cost function that combines a least squares voxel difference measure with penalty terms assuming constant velocity and an affine model. The method does not require the precise a priori segmentation of the object.

Turkington *et al.* [71] utilized cross-correlation measure for the rigid alignment of dynamic cardiac PET images to cardiac templates. The method used only translations, assuming that the orientation of the heart remains the same during the study. The cross-correlation technique has also been proposed for rigid motion correction of cardiac SPECT images [72], [73]. Bettinardi *et al.* [74] utilized the cross-correlation measure to rigidly register two PET transmission images for patient repositioning. Cross-correlation measure was also used for the correction of the patient motion in the PET heart studies with the help of PET

transmission images, taken before and after emission imaging [74]. Gallippi *et al.* [75] utilized modified correlation measure to match local brightness statistics of the registered images. The method was applied to rigidly register intramodality cardiac MR or US time series images. Bacharach *et al.* [76] utilized CC measure to rigidly register two cardiac PET emission scans of the same subject acquired at different times. The method was based on the registration of corresponding transmission data sets. The optimum alignment was defined as the one that produced the maximum value of the CC between the two data sets. CC is an optimal measure for registration in the case of a linear relationship between the intensity values in the images to be registered [11], [12], [68], [77]. This is seldom the case between different image modalities, and the CC is thus mainly used for intramodality registration.

*b) Intermodality registration:* In the paper by Dey *et al.* [32], SAD and VIR methods were compared for the rigid registration of thorax CT and SPECT images. In the VIR method, the sum of the normalized standard deviations is calculated to define registration parameters. The method was first proposed by Woods *et al.* [78], [79] for registering intramodality brain PET images [78] and intermodality brain PET and MR images [79]. In the latter, the VIR algorithm minimizes the normalized standard deviation of PET voxel values for each MR intensity value, but the method could also be used for these images vice versa [12]. Dey *et al.* [32] utilized SPECT transmission image as a linking mediator to register thorax CT and SPECT emission images. In this VIR method, the Simplex algorithm was applied for the minimization of the cost function, while in the original VIR method [79], the Newton-Raphson method [54] was used. An approximate image alignment was made using a technique based on the principal-axes transformation [80]. VIR provided better convergence than SAD and may perform better for CT and SPECT image registration, but the method was only tested on phantom images. In the paper by Eberl *et al.* [30], the SAD, SSC, VIR, and *sum of pixel-by-pixel product* measures were compared for rigid registration of intramodality cardiac SPECT emission images or intermodality cardiac PET and SPECT emission images. SAD was recognized to be the most accurate and reliable method. The use of SAD and VIR thus depends on the type of images to be registered.

In [81], the cross-correlation measure was utilized to rigidly register cardiac MR and PET emission images by using PET transmission image as a linking mediator for registration. Edge information and a region growing algorithm were combined to segment lung cavities from both MR and PET transmission images. The segmented cavities were then utilized as landmarks for registration. Matching of the center of mass of segmented cavities was exploited as an initial registration, and the cross-correlation function was employed for maximizing overlapping areas of the lung cavities for accurate registration. The method was validated only qualitatively, using visual inspection.

*3) Mutual Information:* Mutual information is an information theory measure of the statistical dependence between two random variables or the amount of information that one variable contains about the other [11], [12], [82]–[84]. Mutual information can be qualitatively considered as a measure of how well one image explains the other. The mutual information is maxi-

mized at the optimal alignment [77]. No assumptions are made regarding the nature of the relation between the image intensities in the registered images [82]. Therefore, the mutual information method is promising in particular for intermodality registration.

Intermodality registration differs from intramodality registration because different medical imaging modalities usually have different intensity characteristics and different resolutions, noise characteristics, and fields of view. Several normalized versions of the mutual information has been proposed because changes in overlap of very low-intensity regions of the image can disproportionately contribute to the mutual information measure [10]–[12].

Registration based on mutual information has been proposed to register thorax CT and PET images, rigidly [85] and elastically [86]. In the latter, the rigid registration method [85] was first applied as an initialization prior to the elastic registration. A nonlinear thin-plate-spline warping was done using lung contours detected on PET transmission scans and CT volumes. Nonlinear deformation significantly improved the alignment of PET with breath-hold CT. Carrillo *et al.* [38] used mutual information, VIR, and the CC methods for registering abdominal thorax MR images. Results were compared with the manual registration method. The best registration results were obtained using the mutual information with the Powell minimization algorithm. In [87], a method that associates mutual information, gradient information, and the smoothness of the registration transformation was presented to elastically register inpatient cardiac MR and PET images. A rigid thorax surface-based cardiac registration method [47] was used for the initial registration of the images.

### C. Implementation: Interpolation and Optimization

In a registration process, the image interpolation and minimization algorithm are key points. We give hereafter some comments on these important topics.

1) *Interpolation*: Interpolation is required when an image needs to be translated, rotated, scaled, warped, or otherwise deformed before it can match a reference image or an atlas [88]. In volumetric imaging, interpolation is often used to compensate for nonisotropic data sampling. This is typically the case with cardiac and thorax images where the in-slice resolution can be much higher (e.g., 1 mm) than the interslice resolution (e.g., 8 mm). In intermodality registration, one image may be of substantially lower resolution than the other, and in cardiac image registration, lower resolution images (e.g., SPECT or PET) are often transformed to the sample space of the higher resolution modality (e.g., CT or MR) [29], [40]. To obtain the same isotropic voxel dimension in cardiac and thorax image registration, trilinear interpolation is often used [47], [88]. Nekolla *et al.* [57] created a scaled isotropic set from individual SA MR and PET images using a cubic interpolation. In [37], bicubic interpolation was used for interpolation of SA MR perfusion images. Faber *et al.* [29] used quadrilinear interpolation to interpolate a 4-D SPECT image to the coordinates of a corresponding MR image. For cardiac nuclear medicine images, cubic convolution interpolation method has been recognized as efficient [89].

2) *Optimization*: For rigid 3-D image registration, the optimal transformation usually minimizes a cost function with

six degrees of freedom (three translations and three rotations), giving a six-dimensional parameter space. Elastic registration algorithms have more degrees of freedom, in which case the parameter space has correspondingly more dimensions [10]–[12]. Because the heart is a nonrigid moving object, elastic registration is ideally needed. An exhaustive search to find the global minimum of the cost function is usually computationally too extensive and time consuming. Nonoptimal optimization methods, like Powell [53], [54] and Simplex [54], [90] methods, are applied to find an optimum faster than with the exhaustive search. The Powell method has been selected for the minimization of cardiac image registration methods in [29], [33], [38], and [46] and for thorax image registration methods in [32], [85], and [86]. The Simplex method has been used for cardiac image registration in [30], [66], [67], and [69].

Multiresolution methods can be implemented to increase the probability of finding the global optimum in the parameter space and to make the registration procedure faster. In the multiresolution approach, the images are first registered at a low resolution, and the transformation solution is applied to the next resolution level. The process is repeated until the highest resolution level is reached. For cardiac image registration, the multiresolution approach has been applied in [26], [37], [47], and [86]. To our knowledge, no comparative studies on the performance of minimization methods for cardiac image registration have been published to date.

## III. VALIDATION OF REGISTRATION METHODS

A method can not be accepted as a clinical tool without careful validation. Validation of registration accuracy is a difficult task because the ground truth (i.e., gold standard) is generally not available [11], [12], [91]. Registration methods are often validated using external markers, anatomical landmarks, or external fiducial frames as the gold standards [91]. Visual inspection is the most obvious method for evaluation of the registration accuracy but can be considered as an informal and insufficient approach.

A direct comparison of the measurements reported in the literature is not straightforward because of the nonunique definition of accuracy and of the different methods adopted to measure it [31]. In cardiac image registration, the main interest is the registration accuracy in the heart area (target registration error) [12]. The mean and rms errors are commonly used measures for registration errors [11], [12], [91]. In rigid-body registration, error in the parameters of the spatial transformation model, such as errors in  $x$ -axis translation, are also commonly reported. However, the decomposition of a rigid-body movement into elementary rotations and translations is not unique, i.e., the result depends on the order of the elementary operations [92].

To reduce registration errors caused by cardiac movement and respiration, ECG gating and breath holding (or breath gating) are sometimes used. The problem for cardiac image registration of ECG-gated cine MR images is often that the same anatomical region is not observed within the same slice of the cine images. Recent MRI “slice following” techniques should make temporal registration easier, showing the same anatomical locations of the heart through cine image sequence. In thorax surface-based

cardiac registration methods, movement of the thoracic wall and diaphragm is quite different in magnitude in all directions. Movements can lead to distortions and asymmetrical position changes that can cause errors while determining the registration parameters [93]. The movements near the diaphragm are largest, reaching several centimeters [94]. Cardiac PET and SPECT images are often integral images through time (static images). This causes extra difficulties for registering, e.g., with gated MR images. In the case where both registered images are integral images through time, the errors caused by breathing and cardiac motion can be considered to be similar in both images [31].

In registration methods in which a transmission image (PET, SPECT) is used as a linking mediator to register corresponding emission image, the assumption is that the patient does not move during and between image acquisition. Because the image-acquisition times in cardiac PET and SPECT transmission and emission images are often several minutes, movement artifacts often occur. In modern PET imaging scanners, emission and transmission images are acquired without taking the patient out of the scanner between acquisitions. Yu *et al.* [95] argue that careful application of laser alignment is an adequate method of registration in the PET imaging systems where the patient is taken out of the scanner between transmission and emission acquisitions during the uptake period. Methods have also been presented for the rigid registration of PET emission and transmission images [74], [96]. If the movement between SPECT transmission and the emission image is more than 2–3 cm, it can also seriously affect the attenuation correction of the emission image and, thus, its quality [97].

#### A. Phantom Studies

Phantom studies are important for the estimation of the registration accuracy because a phantom can remain perfectly still and can be displaced and sometimes even rotated with considerable accuracy. Phantom-based validation is utilized especially for estimating the accuracy of intramodality registration methods. For registration methods based on thorax surfaces, the registration accuracy has been usually validated using thorax phantoms [26], [30]–[33], [35], [46], [74]. For example, the Alderson thorax phantom [31], [98], a physical torso phantom with lungs, cardiac, and spine inserts (Data Spectrum) [32] and Jaszczak thorax phantom (Data Spectrum) [35] have been applied. In [71], a heart phantom was used. Simulations of images and different error sources can be used to estimate cardiac registration accuracy [26], [55]. Klein *et al.* [23], [70] utilized a mathematical cardiac phantom [99] to validate a 4-D motion correction algorithm of cardiac PET images. Integrated imaging devices such as combined PET/CT scanners [100], [101] could also provide gold standards for registration [94].

The accuracy of thorax surface-based registration methods depends on the modalities and structures to be registered. Pallotta *et al.* [26] compared the registration accuracy of the method where segmented PET transmission images were linking mediators to register corresponding PET emission images. A synthetic thorax phantom was used to validate the registration accuracy by using only external thorax surfaces (E), internal lung surfaces (I), or both thorax and lungs (EI). Seven markers were positioned to the external surfaces of the synthetic thorax phantom.

Average values for the mean residual marker displacement over ten experiments were  $3.41 \pm 1.41$  mm,  $2.27 \pm 0.76$  mm, and  $2.19 \pm 0.52$  mm for E, I, and EI surfaces, respectively. The rotational error was smaller than  $1.5^\circ$  in each case. The result indicated that the more the surfaces were integrated in the registration, the more accurate the result.

#### B. Registration Accuracy

##### 1) Intramodality Registration:

a) *MRI*: Bidaut *et al.* [37] rigidly registered intramodality gated heart perfusion MR images by using SSD measure and obtained 3.0-mm accuracy in  $x$ , 1.6-mm accuracy in  $y$ , and 2.2-mm accuracy in  $z$  directions. Gallippi *et al.* [75] utilized correlation measure and warping to register cardiac MR time-series images. Mean left–right registration error of  $1.23 \pm 0.06$  mm and mean anterior–posterior error of  $3.25 \pm 1.04$  mm were reported. With intramodality mutual information-based registration of abdominal MR images, Carrillo *et al.* [38] reported 3-mm accuracy by using anatomical landmarks.

b) *PET*: Hoh *et al.* [67] registered cardiac PET emission images using SAD and SSC measures. For both methods, accuracy was typically  $0.5 \pm 0.5$  mm in the inplane direction,  $1.1 \pm 1.1$  mm in the interplane direction, and  $0.9 \pm 1.1^\circ$  for all rotational directions. Turkington *et al.* [71] used cross-correlation measure for the alignment of dynamic cardiac PET emission scans to templates and showed that the rigid registration technique was reliable within one voxel ( $1.7 \times 1.7 \times 4.2$  mm<sup>3</sup>). Pallotta *et al.* [26] obtained with synthetic thorax phantom  $2.19 \pm 0.52$  mm rms error for rigid registration of cardiac PET emission images with  $1.5^\circ$  rotational error, while using both thorax and lung surfaces from corresponding transmission images for registration. Klein *et al.* [23], [70] reported a 1.9-, 2.4-, and 6.8-mm maximum registration error for the  $x$ ,  $y$ , and  $z$  directions, respectively, after the use of a 4-D PET motion compensation algorithm. For the CC-based PET transmission image registration of corresponding cardiac PET emission images, Bacharach *et al.* [76] reported 1-mm accuracy in  $x$ ,  $y$ , and  $z$  directions and  $1.5^\circ$  in the three angles of rotation.

c) *SPECT*: Eberl *et al.* [30] rigidly registered intramodality SPECT emission images by using SAD measure and obtained  $2.1 \pm 1.2$  mm accuracy by using a phantom experiment.

##### 2) Intermodality Registration:

a) *MR-PET*: Sinha *et al.* [40] reported a  $1.95 \pm 1.6$  mm<sup>2</sup> accuracy for a rigid heart surface-based registration method of ECG-gated cardiac MR and FDG PET images. This error was estimated only in the  $(x, y)$  plane using 80 internal landmarks from six volunteer scans. In [47], a  $2.8 \pm 0.5$  mm error was reported for the rigid registration of cardiac MR and PET images. The reported error was a surface distance registration error between thorax and lung surfaces. The measure depended also on deformable model-based segmentation results, but provided also a reasonable measure of the registration accuracy of the MR and PET cardiac (thorax) images.

b) *MR-SPECT*: For rigid heart surface-based registration of MR and SPECT images, Faber *et al.* [29] reported a 2.7-mm registration accuracy.

c) *CT-PET*: In the rigid thorax and lung CT and PET image registrations, where a PET transmission image was used as a linking mediator to register PET emission image to CT image coordinates, accuracy of 1–3 mm in the transaxial plane and 2–4 mm in the longitudinal direction was reported in [33], [46], and [55], with about  $1.5^\circ$  rotational error [46].

d) *CT-SPECT*: For the rigid registration of thorax CT and SPECT emission images with the help of SPECT transmission images, the VIR and SAD methods were found to have about the same accuracy (about 3.5 mm), but VIR provided better convergence [32].

e) *PET-SPECT*: For rigid cardiac PET and SPECT image registration based on the segmentation of thorax and lung surfaces from transmission images, the accuracy was reported to be on the order of 3 mm in longitudinal direction and 5 mm in the transaxial plane [31]. For rigid cardiac PET and SPECT emission image registration based on SAD measure, Eberl *et al.* [30] reported  $3.1 \pm 1.7$  mm accuracy. Nekolla *et al.* [57] rigidly registered heart surfaces from PET and SPECT images, and a mean distance between the two registered heart surfaces was less than 2.5 mm. The surface distance error measure depended on segmentation results but provided a reasonable measure of the registration accuracy.

#### IV. CONCLUSION

Registration of different cardiac imaging modalities is the preliminary and mandatory step to combining anatomical and functional cardiac information. The integration of multiple complementary data into a common reference allows a more comprehensive analysis of the cardiac functions and pathologies. The accurate spatial coregistration of different imaging modalities also provides additional useful clinically relevant information, or information relevant to cardiac research, which is not available while looking at images from a single modality.

We have presented a survey of various cardiac image registration methods, which were coarsely divided into registration methods based on *geometric image features* and *voxel similarity measures*. In the first category, registration relies on the extraction of geometric features; in the latter, preliminary extraction of the features is not needed.

The choice of a cardiac registration method is difficult since, at the present time, no general fully automatic method exists that could handle the wide variety of encountered clinical situations (modalities, acquisition protocols, etc.). Moreover, it should also be driven by the evaluation of the methods' performances with the same common databases for which the ground truth is available. Such a reference does not exist either. We give hereafter some critical comments about the main categories of cardiac image registration methods.

- 1) External skin marker-based registration of cardiac images does not guarantee registration of the heart within the body, since heart position changes with body position (e.g., prone or supine), respiration, and cardiac contraction [29]. Also, skin markers cannot be utilized retrospectively.
- 2) Landmark-based registration of the heart is also difficult because there are few spatially accurate anatomical land-

marks in cardiac images. Landmarks can also be less visible with certain modalities and in some pathological conditions, such as ischemia.

- 3) Thorax surface-based methods can be used if it is not possible to obtain structural information from the heart surfaces directly. In thorax surface-based cardiac image registration methods, it is recommended to use both thorax and lung surfaces, which are well visible in thorax MR and CT images and in PET and SPECT transmission images [26]. Still, these methods are prone to errors induced by respiration and different movement artifacts [94].
- 4) Registration of the heart surfaces directly will result in the better registration of the area of interest. The choice of the surfaces to be registered (e.g., epicardial and/or endocardial) is important and depends on the application and modalities to be used. Gated acquisitions combined with breath-hold (or breath-gated) image acquisition [94] give in many cases acceptable results even with rigid cardiac registration methods.
- 5) The voxel similarity measures, compared to geometric image feature-based registration methods, have the important advantage that they do not require a priori extraction of the registered features (e.g., segmentation). The use of image intensity difference and correlation methods relies on the assumption that pixel values in the registered images are strongly correlated. This is usually not the case with intermodality registration. In modern information-theoretic voxel similarity methods, like mutual information, no assumptions are made regarding the nature of the relation between the image intensities in the registered images [82]. These methods are particularly promising for the intermodality cardiac image registration. Because of the recent development of the mutual information-based methods, applications to cardiac image registration are still rare. One of the aims of recent research in the voxel similarity measure-based registration area has been to devise general algorithms that will work on a wide variety of image types, without application-specific preprocessing [12].

Rigid cardiac image registration generally does not describe the spatial relationship between images adequately. Elastic (nonrigid) cardiac image registration is needed especially because of cardiac motion; between end-diastole and end-systole (during cardiac cycle), the heart valvular plane moves 9–14 mm toward the apex and the myocardial walls thicken from approximately 10 to over 15 mm [23], [102], [103]. Also, the problems due to imaging conditions, different movement artifacts, and elasticity of the body, lungs, and heart cause different tissue deformations that are not possible to compensate for using rigid registration methods. There is considerable research going on in extending the use of intensity-based registration algorithms to nonrigid transformations [12].

Deformable model-based approaches (deformable registration algorithms) for cardiac image registration are particularly promising for elastic 4-D registration of the cardiac images (e.g., to compensate for movement artifacts) [23], [70]. Model-based approaches can also lead to the integration of information from different imaging modalities into an individualized heart model,

including anatomical and functional information [69], [104]. This kind of model can be applied in computer-assisted diagnosis, treatment planning, and surgery. Data fusion techniques, based, i.e., on neural networks and fuzzy logic, can be used to interpret and summarize the large amount of information from registered images and to help establish a diagnostic or select a therapy [4], [105]. Methods combining similarity measures with a priori knowledge from geometric models can also provide new possibilities, especially for elastic registration [87], [106].

The validation of the registration accuracy is particularly important. Virtual and physical phantoms may provide the gold standard for validation. Also, image databases may in the future provide a source for the objective comparison of different cardiac registration methods.

Cardiac image registration remains a challenge because of the numerous specific problems mainly related to the different motion sources (patient, respiration, heart) and to the specificity of each imaging modality. Up to now, no general method is able to automatically register any modality with any other modality. Cardiac image registration methods also always require a compromise among accuracy, precision, reliability, robustness, and issues such as automation, interactivity, speed, patient-friendliness, etc. It is also important to keep in mind that the registration techniques and results should be useful and usable in clinical practice.

#### ACKNOWLEDGMENT

The authors are grateful to the anonymous reviewers for their suggestions to improve this paper.

#### REFERENCES

- [1] J. Hartiala and J. Knuuti, "Imaging of heart by MRI and PET," *Ann. Med.*, vol. 27, pp. 35–45, 1995.
- [2] N. Wilke, M. Jerosch-Herold, A. E. Stillman, K. Kroll, N. Tsekos, H. Merkle, T. Parrish, X. Hu, Y. Wang, J. Bassingthwaite, R. J. Bache, and K. Ugurbil, "Concepts of myocardial perfusion imaging in magnetic resonance imaging," *Magn. Res. Quart.*, vol. 10, pp. 249–286, 1994.
- [3] H. R. Schelbert, "Metabolic imaging to assess myocardial viability," *J. Nucl. Med.*, vol. 35, pp. 8–14, 1994.
- [4] F. Behloul, B. P. F. Lelieveldt, A. Boudraa, M. Janier, D. Revel, and J. H. C. Reiber, "Neuro-fuzzy systems for computer-aided myocardial viability assessment," *IEEE Trans. Med. Imag.*, vol. 20, pp. 1302–1313, Dec. 2001.
- [5] F. Behloul, M. Janier, P. Croisille, C. Poirier, A. Boudraa, R. Unterreiner, J. Mason, and D. Revel, "Automatic assessment of myocardial viability based on PET-MRI data fusion," in *Int. Conf. IEEE Engineering in Medicine and Biology Soc.*, 1998, pp. 429–495.
- [6] G. D. Waiter, A. Al-Mohammad, M. Y. Norton, T. W. Redpath, A. Welch, and S. Walton, "Regional myocardial wall thickening assessed at rest by ECG gated (18)F-FDG positron emission tomography and by magnetic resonance imaging," *Heart*, vol. 84, pp. 332–333, 2000.
- [7] C. Maurer and J. M. Fitzpatrick, "A review of medical image registration," *Interact. Image-Guided Neurosurg.*, pp. 17–44, 1993.
- [8] J. B. A. Maintz and M. A. Viergever, "A survey of medical image registration," *Med. Image Anal.*, vol. 2, no. 1, pp. 1–36, 1998.
- [9] P. A. van den Elsen, E.-J. D. Pol, and M. A. Viergever, "Medical image matching—A review with classification," *IEEE Eng. Med. Biol.*, vol. 12, no. 2, pp. 16–39, 1993.
- [10] D. L. G. Hill, P. G. Batchelor, M. H. Holden, and D. J. Hawkes, "Medical image registration," *Phys. Med. Biol.*, vol. 46, no. 1, pp. 1–45, 2001.
- [11] J. V. Hajnal, D. L. G. Hill, and D. J. Hawkes, *Medical Image Registration*. Boca Raton, FL: CRC Press, 2001.
- [12] J. M. Fitzpatrick, D. L. G. Hill, and C. R. Maurer, *Handbook of Medical Imaging*. Bellingham, WA: SPIE Press, 2000, vol. 2, ch. Image Registration, pp. 375–435.
- [13] I. N. Bankman, *Handbook of Medical Imaging: Processing and Analysis*: Academic Press, 2000.
- [14] A. F. Frangi, W. J. Niessen, and M. A. Viergever, "Three-dimensional modeling for functional analysis of cardiac images, a review," *IEEE Trans. Med. Imag.*, vol. 20, pp. 2–25, Jan. 2001.
- [15] M. Audette, F. Ferrie, and T. Peters, "An algorithmic overview of surface registration techniques for medical imaging," *Med. Image Anal.*, vol. 4, no. 4, pp. 201–217, Feb. 2000.
- [16] H. Lester and S. R. Arridge, "A survey of hierarchical nonlinear medical image registration," *Pattern Recognit.*, vol. 32, pp. 129–149, 1998.
- [17] L. G. Brown, "A survey of image registration techniques," *ACM Comput. Surv.*, vol. 24, no. 4, pp. 325–376, 1992.
- [18] M. C. Gilardi, G. Rizzo, A. Savi, and F. Fazio, "Registration of multimodal biomedical images of the heart," *Q. J. Nucl. Med.*, vol. 40, no. 1, pp. 142–150, 1996.
- [19] A. W. Habboosh, "A review of MRI and PET correlation," in *Proc. IEEE Conf. Bioengineering*, 1992, pp. 16–17.
- [20] G. Z. Yang, P. Burger, J. Panting, P. D. Gatehouse, D. Rueckert, D. J. Pennel, and D. N. Firmin, "Motion and deformation tracking for short-axis echo-planar myocardial perfusion imaging," *Med. Image Anal.*, vol. 2, no. 3, pp. 285–302, Mar. 1998.
- [21] J. C. McEachen II, A. Nehorai, and J. S. Duncan, "Multiframe temporal estimation of cardiac nonrigid motion," *IEEE Trans. Med. Imag.*, vol. 9, pp. 651–665, Apr. 2000.
- [22] X. Papademetris, A. J. Sinusas, D. P. Dione, and J. S. Duncan, "Estimation of 3D left ventricular deformation from echocardiography," *Med. Image Anal.*, vol. 5, pp. 17–28, 2001.
- [23] G. J. Klein and R. H. Huesman, "Four-dimensional processing of deformable cardiac PET data," *Med. Image Anal.*, vol. 6, pp. 29–46, 2002.
- [24] T. R. Nelson, D. B. Downay, D. H. Pretorius, and A. Fenster, *Three-Dimensional Ultrasound*. Philadelphia, PA: Lippincott Williams & Wilkins, 1999.
- [25] K. S. Arun, T. S. Huang, and S. D. Blostein, "Least-squares fitting of two 3-D point sets," *IEEE Trans. Pattern Anal. Machine Intell.*, vol. PAMI-9, pp. 698–700, May 1987.
- [26] S. Pallotta, M. C. Gilardi, V. Bettinardi, G. Rizzo, C. Landoni, G. Striano, R. Masi, and F. Fazio, "Application of a surface matching image registration technique to the correlation of cardiac studies in positron emission tomography by transmission images," *Phys. Med. Biol.*, vol. 40, pp. 1695–1708, 1995.
- [27] Q. Li, L. Zamorano, Z. Jiang, F. Vinas, and F. Diaz, "The application accuracy of the frameless implantable marker system and analysis of related affecting factors," in *Lecture Notes in Computer Science 1496: Medical Image Computing and Computer-Assisted Intervention, MICCAI98*, W. M. Wells, A. Colchester, and S. Delp, Eds., 1998, pp. 253–260.
- [28] O. Sipilä, "Methodological aspects for improving clinical value of SPECT and MRI," Ph.D. dissertation, Helsinki Univ. Technol., Helsinki, Finland, 2000.
- [29] T. L. Faber, R. W. McColl, R. M. Opperman, J. R. Corbett, and R. M. Peshock, "Spatial and temporal registration of cardiac SPECT and MR images: Methods and evaluation," *Radiology*, vol. 179, no. 3, pp. 857–861, 1991.
- [30] S. Eberl, I. Kanno, R. R. Fulton, A. Ryan, B. F. Hutton, and M. J. Fulham, "Automated interstudy image registration technique for SPECT and PET," *J. Nucl. Med.*, vol. 37, no. 1, pp. 137–145, 1996.
- [31] M. C. Gilardi, G. Rizzo, A. Savi, C. Landoni, V. Bettinardi, C. Rossetti, G. Striano, and F. N. Fazio, "Correlation of SPECT and PET cardiac images by a surface matching registration technique," *Comput. Med. Imag. Graph.*, vol. 22, pp. 391–398, Dec. 1998.
- [32] D. Dey, P. J. Slomka, L. J. Hahn, and R. Klotz, "Automatic three-dimensional multimodality registration using radionuclide transmission CT attenuation maps: A phantom study," *J. Nucl. Med.*, vol. 40, no. 3, pp. 448–455, 1999.
- [33] J. N. Yu, F. H. Fahey, H. D. Gage, C. G. Eades, B. A. Harkness, and C. A. Pelizzari, "Intermodality, retrospective image registration in the thorax," *J. Nucl. Med.*, vol. 36, no. 12, pp. 2333–2338, Dec. 1995.
- [34] J. West, J. M. Fitzpatrick, M. Y. Wang, B. M. Dawant, C. R. Maurer Jr., R. M. Kessler, R. J. Maciunas, C. Barillot, D. Lemoine, A. Collingnon, F. Maes, P. Suetens, D. Vandermeulen, P. A. van den Elsen, S. Napel, T. S. Sumanaweera, B. Harkness, P. F. Hemler, D. L. G. Hill, D. J. Hawkes, C. Studholme, J. B. A. Maintz, M. A. Viergever, G. Malandain, X. Pennec, M. E. Noz, G. Q. Maguire Jr., M. Pollack, C. A. Pelizzari, R. A. Robb, D. Hanson, and R. P. Woods, "Comparison and evaluation of retrospective intermodality image registration techniques," *J. Comput. Assist. Tomogr.*, vol. 21, pp. 554–566, 1997.

- [35] E. L. Kramer, M. E. Noz, J. J. Sanger, A. J. Megibow, and G. Q. Maguire, "CT-SPECT fusion to correlate radiolabeled monoclonal antibody uptake with abdominal CT findings," *Radiology*, vol. 172, no. 10, pp. 861–865, 1989.
- [36] H. Loats, "CT and SPECT image registration and fusion for spatial localization of metastatic processes using radiolabeled monoclonals," *J. Nucl. Med.*, vol. 34, pp. 562–566, 1993.
- [37] L. M. Bidaut and J.-P. Vallee, "Automated registration of dynamic MR images for the quantification of myocardial perfusion," *J. Magn. Res. Imag.*, vol. 13, pp. 648–655, 2001.
- [38] A. Carrillo, J. L. Duerk, J. S. Lewin, and D. L. Wilson, "Semiautomatic 3-D image registration as applied to interventional MRI liver cancer treatment," *IEEE Trans. Med. Imag.*, vol. 19, pp. 175–185, Mar. 2001.
- [39] A. Savi, M. C. Gilardi, G. Rizzo, M. Pepi, C. Landoni, C. Rossetti, G. Lucignani, A. Bartonelli, and F. Fazio, "Spatial registration of echocardiographic and positron emission tomographic heart studies," *Eur. J. Nucl. Med.*, vol. 22, no. 3, pp. 243–247, 1995.
- [40] S. Sinha, U. Sinha, J. Czernin, G. Porenta, and H. R. Schelbert, "Noninvasive assessment of myocardial perfusion and metabolism: Feasibility of registering gated MR and PET images," *Amer. J. Roentgenol.*, vol. 36, pp. 301–307, 1995.
- [41] X. Pennec, N. Ayache, and J.-P. Thirion, *Handbook of Medical Imaging: Processing and Analysis*. New York: Academic, 2000, ch. Landmark-based registration using features identified through differential geometry, pp. 499–513.
- [42] M. A. Wirth, C. Choi, and A. Jennings, "Point-to-point registration of nonrigid medical images using local elastic transformation methods," in *IEEE Int. Conf. Image Processing and Its Applications*, 1997, pp. 780–784.
- [43] G. Borgefors, "Distance transformation in digital images," *Comput. Vision Graph. Image Process.*, vol. 48, pp. 344–371, 1986.
- [44] —, "Hierarchical chamfer matching: A parametric edge matching algorithm," *IEEE Trans. Pattern Anal. Machine Intell.*, vol. 10, pp. 849–865, Nov. 1988.
- [45] M. Van Herk, *Handbook of Medical Imaging: Processing and Analysis*. New York: Academic, 2000, ch. Image registration using chamfer matching, pp. 515–527.
- [46] J. Cai, J. C. Chu, D. Recine, M. Sharma, C. Nguyen, R. Rodebaugh, A. Saxena, and A. Ali, "CT and PET lung image registration and fusion in radiotherapy treatment planning using the chamfer-matching method," *Int. J. Radiat. Oncol. Biol. Phys.*, vol. 43, no. 4, pp. 883–891, 1999.
- [47] T. J. Mäkelä, P. Clarysse, J. Lötjönen, O. Sipilä, K. Lauerma, H. Hänninen, E.-P. Pyötkimies, J. Nenonen, J. Knuuti, T. Katila, and I. E. Magnin, "A new method for the registration of cardiac PET and MR images using deformable model based segmentation of the main thorax structures," in *Lecture Notes in Computer Science 2208: Medical Image Computing and Computer-Assisted Intervention, MICCAI01*, W. J. Niessen and M. Viergever, Eds., 2001, pp. 557–564.
- [48] P. J. Besl and N. D. McKay, "A method for registration of 3-D shapes," *IEEE Trans. Pattern Anal. Machine Intell.*, vol. 14, pp. 239–256, Feb. 1992.
- [49] J. Declerck, J. Feldmar, M. L. Goris, and F. Betting, "Automatic registration and alignment on a template of cardiac stress and rest SPECT images," INRIA, Res. Rep. 2770, 1996.
- [50] —, "Automatic registration and alignment on a template of cardiac stress and rest reoriented SPECT images," *IEEE Trans. Med. Imag.*, vol. 16, pp. 727–737, Dec. 1997.
- [51] C. A. Pelizzari, G. T. Y. Ghen, D. R. Spelbring, R. R. Weichselbaum, and C. T. Chen, "Accurate three-dimensional registration of CT, PET and/or MR images of the brain," *J. Comput. Assist. Tomogr.*, vol. 13, no. 1, pp. 20–26, 1989.
- [52] D. N. Levin, C. A. Pelizzari, G. T. Y. Chen, C.-T. Chen, and M. D. Cooper, "Retrospective geometric correlation of MR, CT and PET images," *Radiology*, vol. 169, no. 3, pp. 817–823, 1988.
- [53] M. J. Powell, "An iterative method of finding stationary values of a function of several variables," *Comp. J.*, vol. 5, pp. 147–151, 1962.
- [54] W. H. Press, S. A. Teukolsky, W. T. Vetterling, and B. P. Flannery, *Numerical Recipes in C: The Art of Scientific Computing*, 2nd ed. Cambridge, U.K.: Cambridge Univ. Press, 1992.
- [55] Y.-C. Tai, K. P. Lin, C. K. Hoh, S. C. Huang, and E. J. Hoffman, "Utilization of 3-D elastic transformation in the registration of chest X-ray CT and whole body PET," *IEEE Trans. Nucl. Sci.*, vol. 44, pp. 1606–1612, Aug. 1997.
- [56] T. L. Faber, E. M. Stokely, R. M. Peshock, and J. R. Corbett, "A model based four-dimensional left ventricular surface detector," *IEEE Trans. Med. Imag.*, vol. 10, pp. 321–329, Sept. 1991.
- [57] S. Nekolla, T. Ibrahim, T. Balbach, and C. Klein, *Understanding Cardiac Imaging Techniques—From Basic Pathology to Image Fusion*. Amsterdam, The Netherlands: IOS Press, 2001, vol. 322, ch. Coregistration and fusion of cardiac magnetic resonance and positron emission tomography studies, pp. 144–154.
- [58] S. Nekolla, C. Miethaner, N. Nguyen, S. Ziegler, and M. Schwaiger, "Reproducibility of polar map generation and assessment of defect severity and extent assessment in myocardial perfusion imaging using positron emission tomography," *Eur. J. Nucl. Med.*, no. 25, pp. 1313–1321, 1998.
- [59] J. Canny, "A computational approach to edge detection," *IEEE Trans. Pattern Anal. Machine Intell.*, vol. PAMI-8, pp. 679–698, Nov. 1986.
- [60] R. Deriche, "Using Canny's criteria to derive a recursively implemented optimal edge detector," *Int. J. Comput. Vision*, vol. 1, pp. 167–187, 1987.
- [61] J.-P. Thirion, *Understanding Cardiac Imaging Techniques—From Basic Pathology to Image Fusion*. Amsterdam, The Netherlands: IOS Press, 2001, ch. Perfusion and motion from gated SPECT, pp. 84–93.
- [62] —, "Fast non-rigid matching of 3-D medical images," INRIA, Res. Rep. 2547, 1995.
- [63] —, "Image matching as a diffusion process: An analogy with Maxwell's demons," *Med. Image Anal.*, vol. 2, no. 3, pp. 243–260, 1998.
- [64] J. L. R. Andersson, "A rapid and accurate method to realign PET scans utilizing image edge information," *J. Nucl. Med.*, vol. 36, no. 4, pp. 657–669, 1995.
- [65] J. L. R. Andersson, B. E. Bagnhammar, and H. Schneider, "Accurate attenuation correction despite movement during PET imaging," *J. Nucl. Med.*, vol. 36, no. 4, pp. 670–678, 1995.
- [66] P. J. Slomka, A. H. Gilbert, J. Stephenson, and T. Cradduc, "Automated alignment and sizing of myocardial stress and rest scans to three-dimensional normal templates using an image registration algorithm," *J. Nucl. Med.*, vol. 36, pp. 1115–1122, 1995.
- [67] C. K. Hoh, M. Dahlbom, G. Harris, Y. Choi, R. A. Hawkins, M. E. Philips, and J. Maddahi, "Automated iterative three-dimensional registration of positron emission tomography images," *J. Nucl. Med.*, vol. 34, no. 11, pp. 2009–2018, 1993.
- [68] P. A. Viola, "Alignment by maximization of mutual information," Ph.D. dissertation, Massachusetts Inst. Technol., Cambridge, MA, 1995.
- [69] P. J. Slomka, P. Radau, G. A. Hurwitz, and D. Dey, "Automated three-dimensional quantification of myocardial perfusion and brain SPECT," *Comput. Med. Imag. Graph.*, no. 25, pp. 153–164, 2001.
- [70] G. J. Klein, B. W. Reutter, and R. H. Huesman, "Four-dimensional affine registration models for respiratory-gated PET," *IEEE Trans. Med. Imag.*, vol. 48, pp. 756–760, Mar. 2002.
- [71] T. G. Turkington, T. R. DeGrado, M. W. Hanson, and R. E. Coleman, "Alignment of dynamic cardiac PET images for correction of motion," *IEEE Trans. Nucl. Sci.*, vol. 44, pp. 235–242, Apr. 1997.
- [72] M. K. O'Connor, K. M. Kanal, M. W. Gebhard, and P. J. Rossman, "Comparison of four motion correction techniques in SPECT imaging of the heart: A cardiac phantom study," *J. Nucl. Med.*, vol. 39, pp. 2027–2034, 1998.
- [73] M. K. O'Connor, "Evaluation of motion-correction techniques in cardiac SPECT," *J. Nucl. Med.*, vol. 41, no. 7, p. 1298, 2000.
- [74] V. Bettinardi, M. C. Gilardi, G. Lucignani, C. Landoni, and G. Rizzo, "A procedure for patient repositioning and compensation for misalignment between transmission and emission data in PET heart studies," *J. Nucl. Med.*, vol. 34, no. 1, pp. 137–142, 1993.
- [75] C. M. Gallippi and G. E. Trahey, "Automatic image registration for MR and ultrasound cardiac images," in *Lecture Notes in Computer Science 2082: Information Processing in Medical Imaging, IPMI01*, M. F. Insana and R. M. Leahy, Eds., 2001, pp. 141–147.
- [76] S. L. Bacharach, M. A. Douglas, R. E. Carson, P. J. Kalkowski, N. M. Freedman, P. Perrone, and R. O. Bonow, "Three-dimensional registration of cardiac positron emission tomography attenuation scans," *Comput. Vision, Graph. Image Process.*, vol. 34, no. 2, pp. 311–321, 1993.
- [77] D. L. G. Hill and D. J. Hawkes, *Handbook of Medical Imaging: Processing and Analysis*. New York: Academic, 2000, ch. Cross-modality registration using intensity-based cost functions, pp. 537–553.
- [78] R. P. Woods, S. R. Cherry, and J. C. Mazziotta, "Rapid automated algorithm for aligning and reslicing PET images," *J. Comput. Assist. Tomogr.*, vol. 17, no. 4, pp. 620–633, 1992.
- [79] R. P. Woods, J. C. Mazziotta, and S. R. Cherry, "MRI-PET registration with automated algorithm," *J. Comput. Assist. Tomogr.*, vol. 17, no. 4, pp. 536–546, 1993.
- [80] N. Alpert, J. Bradshaw, D. Kennedy, and J. Correia, "The principal axes transformation—A method for image registration," *J. Nucl. Med.*, vol. 31, no. 1, pp. 717–721, 1990.



- [81] R. Kim, T. Aw, S. Bacharach, and R. Bonow, "Correlation of cardiac MRI and PET images using lung cavities as landmarks," in *Proc. IEEE Conf. Computers in Cardiology*, 1991, pp. 49–52.
- [82] F. Maes, A. Collignon, D. Vandermeulen, G. Marchal, and P. Suetens, "Multimodality image registration by maximization of mutual information," *IEEE Trans. Med. Imag.*, vol. 16, pp. 187–198, Apr. 1997.
- [83] W. M. Wells, P. Viola, H. Atsumi, S. Nakajima, and R. Kikinis, "Multi-modal volume registration by maximization of mutual information," *Med. Image Anal.*, vol. 1, no. 1, pp. 35–51, 1996.
- [84] R. P. Woods, *Handbook of Medical Imaging: Processing and Analysis*. New York: Academic, 2000, ch. Within-modality registration using intensity-based cost functions, pp. 529–536.
- [85] P. J. Slomka, D. Dey, C. Przetak, and R. Baum, "Automated 3-D spatial integration of 18-F FDG wholebody PET with CT," *J. Nucl. Med.*, vol. 41, no. 6, p. 59P, 2000.
- [86] —, "Automated nonlinear 3-D registration of 18-F FDG wholebody PET with thoracic CT," *J. Nucl. Med.*, vol. 42, no. 5, p. 11P, 2001.
- [87] J. Lötjönen and T. J. Mäkelä, "Elastic matching using a deformation sphere," in *Lecture Notes in Computer Science 2208: Medical Image Computing and Computer-Assisted Intervention, MICCAI01*, W. Niessen and M. Viergever, Eds., 2001, pp. 541–548.
- [88] P. Thévenaz, T. Blu, and M. Unser, *Handbook of Medical Imaging: Processing and Analysis*. New York: Academic, 2000, ch. Image interpolation and resampling, pp. 393–418.
- [89] M. Haddad, "Impact of reorientation algorithms on quantitative myocardial SPECT perfusion imaging," *J. Nucl. Med.*, vol. 39, no. 11, pp. 1864–1869, 1998.
- [90] J. Nelder and R. A. Mead, "A simplex method for function minimization," *Comp. J.*, vol. 7, pp. 308–313, 1965.
- [91] R. P. Woods, *Handbook of Medical Imaging: Processing and Analysis*. New York: Academic, 2000, ch. Validation of registration accuracy, pp. 491–497.
- [92] —, *Handbook of Medical Imaging: Processing and Analysis*. New York: Academic, 2000, ch. Spatial transformation models, pp. 465–490.
- [93] M. Dahlbom and S.-C. Huang, *Handbook of Medical Imaging: Processing and Analysis*. New York: Academic, 2000, ch. Physical and biological bases of spatial distortions in positron emission tomography images, pp. 439–448.
- [94] G. W. Goerres, E. Kamel, T.-N. H. Heidelber, M. R. Schwitter, C. Burger, and G. K. von Schulthess, "PET-CT image co-registration in the thorax: Influence of respiration," *Eur. J. Nucl. Med.*, vol. 29, no. 3, pp. 351–360, 2002.
- [95] J. N. Yu, F. H. Fahey, H. D. Gage, C. G. Eades, and J. W. Keyes, "Evaluation of emission-transmission registration in thoracic PET," *J. Nucl. Med.*, vol. 35, no. 11, pp. 1777–1781, 1994.
- [96] W. L. Costa, D. R. Haynor, and T. K. Lewellen, "Registration of segmented attenuation and emission data in PET," in *Proc. Nucl. Science Symp. Medical Imaging Conf.*, 1994, pp. 1407–1411.
- [97] C. D. Stone, J. W. McCormick, D. R. Gilland, K. L. Greer, R. E. Coleman, and R. J. Jaszczyk, "Effect of registration errors between transmission and emission scans on a SPECT system using sequential scanning," *J. Nucl. Med.*, vol. 39, no. 2, pp. 365–373, 1998.
- [98] S. W. Alderson, L. H. Lanzl, M. Rollins, and J. Spira, "An instrumented phantom system for analog computation of treatments plans," *Amer. J. Roentgenol. Radium Ther. Nucl. Med.*, vol. 87, pp. 185–195, 1962.
- [99] P. H. Pretorius, W. Xia, M. A. Kinag, B. M. W. Tsui, T. S. Pan, and B. J. Villegas, "Evaluation of right and left ventricular volume and ejection fraction using a mathematical cardiac torso phantom," *J. Nucl. Med.*, vol. 38, no. 10, pp. 1528–1535, 1997.
- [100] T. Beyer, D. W. Townsend, T. Brun, P. E. Kinahan, M. Charron, R. Roddy, and J. Jerin, "A combined PET/CT scanner for clinical oncology," *J. Nucl. Med.*, vol. 41, no. 8, pp. 1369–1379, 1999.
- [101] J. Patton, D. Delbeke, and M. P. Sandler, "Image fusion using an integrated, dual-head coincidence camera with X-ray tube-based attenuation maps," *J. Nucl. Med.*, vol. 41, no. 8, pp. 1364–1368, 2000.
- [102] W. J. Rogers, E. P. Shapiro, J. L. Weiss, M. B. Buchalter, F. E. Rade-makers, M. L. Weisfeldt, and E. A. Zerhouni, "Quantification of and correction for left ventricular systolic long-axis shortening by magnetic resonance tissue tagging and slice isolation," *Circulation*, vol. 84, no. 2, pp. 721–731, 1991.
- [103] W. G. O'Dell, C. C. Moore, W. C. Hunter, E. A. Zerhouni, and E. R. McViegh, "Three-dimensional myocardial deformations: Calculation with displacement field fitting to tagged MR images," *Radiology*, vol. 195, pp. 829–835, 1995.
- [104] T. J. Mäkelä, Q. C. Pham, P. Clarysse, J. Lötjönen, K. L. H. Hänninen, J. Nenonen, J. Knuuti, T. Katila, and I. E. Magnin, "A 3-D model-based approach for the PET-functional and MR-anatomical cardiac imaging data fusion," in *Lecture Notes in Computer Science 2230: 1st Int. Workshop Functional Imaging and Modeling of the Heart, FIMH 2001*, T. Katila, I. E. Magnin, P. Clarysse, J. Montagnat, and J. Nenonen, Eds., 2001, pp. 83–90.
- [105] C. Muller, M. Rombaut, and M. Janier, "Dempster shafer approach for high level data fusion applied to the assessment of myocardial viability," in *Lecture Notes in Computer Science 2230: 1st Int. Workshop Functional Imaging and Modeling of the Heart, FIMH 2001*, T. Katila, I. E. Magnin, P. Clarysse, J. Montagnat, and J. Nenonen, Eds., 2001, pp. 104–112.
- [106] T. McNerney and D. Terzopoulos, "Deformable models in medical image analysis: A survey," *Med. Image Anal.*, vol. 1, no. 2, pp. 91–108, 1996.

# A New Method for the Registration of Cardiac PET and MR Images Using Deformable Model Based Segmentation of the Main Thorax Structures

Timo Mäkelä<sup>1,2</sup>, Patrick Clarysse<sup>2</sup>, Jyrki Lötjönen<sup>3</sup>, Outi Sipilä<sup>4</sup>,  
Kirsi Lauerma<sup>4</sup>, Helena Hänninen<sup>5,7</sup>, Esa-Pekka Pyökkimies<sup>1</sup>,  
Jukka Nenonen<sup>1</sup>, Juhani Knuuti<sup>6</sup>, Toivo Katila<sup>1,7</sup>, and Isabelle E. Magnin<sup>2</sup>

<sup>1</sup> Laboratory of Biomedical Engineering, Helsinki University of Technology,  
P.O.B. 2200, FIN-02015 HUT, Finland

{Timo.Makela, Toivo.Katila}@hut.fi

<sup>2</sup> CREATIS, INSA, Batiment Blaise Pascal, 69621 Villeurbanne Cedex, France  
{Patrick.Clarysse, Isabelle.Magnin}@creatis.insa-lyon.fr

<sup>3</sup> VTT Information Technology, P.O.Box 1206, FIN-33101 Tampere, Finland  
Jyrki.Lotjonen@vtt.fi

<sup>4</sup> Department of Radiology, Helsinki University Central Hospital,  
P.O.B. 340, FIN-00029 HUS, Finland

<sup>5</sup> Division of Cardiology, Helsinki University Central Hospital, P.O.B. 340,  
FIN-00029 HUS, Finland

<sup>6</sup> Turku PET Centre, c/o Turku University Central Hospital,  
Box 52, FIN-20521, Finland

<sup>7</sup> BioMag Laboratory, Helsinki University Central Hospital, P.O.B. 503,  
FIN-00029 HUS, Finland

**Abstract.** Integration of magnetic resonance (MR) and positron emission tomography (PET) images of the heart has proved its usefulness for the estimation of the myocardial viability. In this paper, a method for the rigid registration of cardiac MR and PET images is presented. It is based on the matching of the surfaces of thorax structures extracted by a deformable model from PET transmission and MR transaxial images. MR short axis registration with PET emission image is easily derived and allows the study viability in the proper anatomic conditions. The method has been evaluated on ten patients suffering from three vessel coronary artery disease. Qualitative results were good with 9 over the 10 available cases. A quantitative estimation of the registration quality confirmed the nice abilities of this approach.

## 1 Introduction

The combination of multiple cardiac image modalities like Magnetic Resonance Imaging (MRI) and Positron Emission Tomography (PET), has gained an increasing interest for physiologic understanding and diagnostic purposes, specially

for viability studies. The combination requires the geometric alignment i.e. registration of multimodal images. This is a difficult problem mainly due to the continuous motion of the heart. Methods to correlate PET cardiac studies by using a surface based image registration technique of PET transmission images has been presented in [1] and [2]. In this work, we propose a new method for cardiac transaxial and short axis (SA) MR and PET image registration. A preliminary approach has been presented in [3]. Here, the method has been greatly improved by substituting the manual segmentation of the thorax structures by a deformable model based automatic segmentation. The data and the method are presented in section 2. The registration results are presented in section 3 and discussed in section 4.

## 2 Material and Method

### 2.1 Data

The data set is composed of MR and PET images of ten patients suffering from three vessel coronary artery disease [4]. Mean age was 69 (8 men, 2 women). All patients underwent MR and fluorine-18-deoxyglucose (FDG) PET imaging within 10 days. The MR imaging was performed at the Department of Radiology of Helsinki University Central Hospital with a 1.5 T Siemens Magnetom Vision imager (Siemens, Erlangen, Germany). A series of 39 ECG-gated contiguous transaxial images was acquired during free respiration using TurboFLASH sequence with the body array coil (Fig. 1a). The pixel size and the slice thickness were  $1.95 \times 1.95$  mm and 10 mm, respectively. Five ECG-gated breath-hold cine SA slices covering the ventricles were also acquired. The pixel size for SA slices was  $1.25 \times 1.25$  mm and the slice thickness 7 mm with a gap of 15 mm between slices (Fig. 1b).

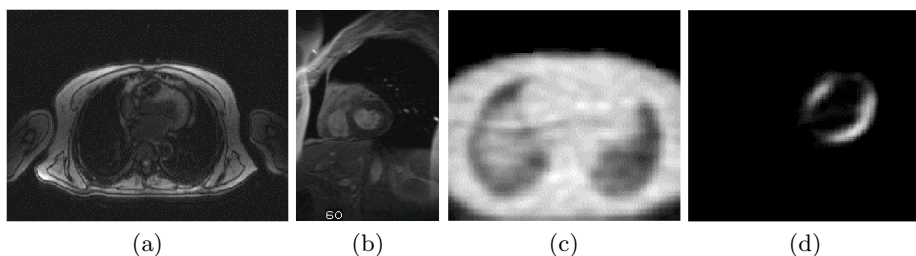


**Fig. 1.** (a) Transaxial and (b) SA MR images of the thorax and heart, (c) PET transmission and (d) emission images.

PET imaging was performed at the Turku PET Centre using a Siemens ECAT 931/08-12 (Siemens/CTI, Knoxville, USA) PET scanner. A series of 16 contiguous transmission and emission images was acquired. The pixel size and the slice thickness were  $2.41 \times 2.41$  mm and 6.75 mm, respectively (Fig. 1c, d).

## 2.2 Registration Protocol

The proposed registration method is based on the matching of the thorax and lungs surfaces which are visible in both PET transmission and MR transaxial images. The registration protocol first matches PET transmission and transaxial MR images and then computes the SA PET slices that correspond to the SA MR slices. The main steps are:

- 1) Image resizing to get the same isotropic voxel dimensions. Tri-linear interpolation was used.
- 2) Segmentation of the thorax and lungs was performed for the transaxial MR and PET transmission images by a deformable model based method [5] which is summarized in subsection 2.3.
- 3) Selection of a set of points from the segmented surfaces of the thorax and lungs in the PET model. The uniformly distributed nodes of the deformable model were used.
- 4) Calculation of the rigid registration parameters (3 translations, 3 rotations) to find the best matching between the point set and the surface of the segmented MR image. The minimization algorithm is explained in subsection 2.4.
- 5) Registration of the PET emission image to the transaxial MR image using the computed registration parameters.
- 6) Registration of SA MR images with PET data. Slice position information contained in the MR image header provides the transformation between transaxial MR and SA MR slices. The SA PET slices corresponding to SA MR images are computed using the estimated parameters of the transformation.

## 2.3 Deformable Model Based Segmentation

The segmentation of the thorax structures is based on the elastic deformation of a topologic and geometric prior model using a multiresolution approach [5]. A thorax model including full triangulated thorax and lungs surfaces was used with transaxial MR images (Fig. 2a). With the transmission PET images, a truncated model with only a part of the thorax was used (Fig. 2b).

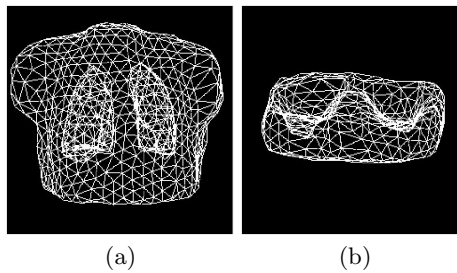


**Fig. 2.** Geometric and topologic prior model of the thorax for (a) transaxial MR and (b) transmission PET image segmentation.

The deformation algorithm adapts the prior model to locally fit the salient edges in the image within a minimization process. The energy to be minimized is

$$E_{total} = E_{image} + \gamma E_{model}, \quad (1)$$

where  $E_{image}$  represents the matching error between the prior model and the partial edges in the data volume.  $E_{model}$  tends to preserve the model's shape by restricting the deformation of the prior model. It describes the deviation of the model's surface normals from their original orientation. The image energy results from a distance map [6] built upon edges extracted either by a Canny-Deriche method [7] or image thresholding. In order to select corresponding edges with the model, oriented distance maps [5] were used. The parameter  $\gamma$  sets the contribution of the two energy components. A multiresolution process speeds up the minimization of the energy and improves the convergence.

## 2.4 Estimation of the Rigid Transformation

The 6 rigid registration parameters (3 translations, 3 rotations) result from the best match between the set of the nodes of the triangulated surfaces extracted from the PET transmission image and the surfaces of the segmented MR image. The optimal transformation minimizes the sum of the distances between the transformed points and a distance map built upon the segmented MR surfaces using the chamfer distance transformation [6].

For the sake of simplicity, the minimization algorithm is described here only for 2 parameters representing, for example, the translation in x- and y-directions on a 2-D plane. The extension to 6 parameters is straightforward. The parameters to be optimized form the parameter vector  $(t_1, t_2)$ . The optimal parameter vector is iteratively searched in the discrete search space. The initial position for the parameter vector is  $(t_{1o}, t_{2o})$  (Fig. 3). The iteration steps for the search of a new parameter vector are as follows:

- 1) Possible values for the parameter  $t_k$ ,  $k \in [1, 2]$  are  $t_k - gd_k$ ,  $t_k - (g-1)d_k, \dots, t_k, \dots, t_k + gd_k$ , where  $g$  is a user-defined positive integer parameter affecting the number of the possible new values, and parameter  $d_k$  (positive real number) represents the magnitude by which the parameter  $t_k$  is varied.
- 2) For all  $(2g+1)^n$  combinations of the parameter vector, where  $n$  is the number of parameters (big dots in Fig. 3), the cost function is computed.
- 3) A user-defined number of combinations,  $m$ , having the lowest registration error, are selected for the new initial parameter vectors (selected positions of step 1, Fig. 3).
- 4) Each  $d_k$ -component is divided by 2.
- 5) Steps 1-2 are repeated for all  $m$  initial parameter vectors. Then, steps 3-4 provides an new local optima. Therefore, the number of initial parameter vectors remains constant during the iterations. Iterations are repeated until the cost function does not decrease more than a user-predefined value  $\epsilon$ .

The algorithm does not necessarily converge to a global minimum of the cost function. However, the method samples the search-space more than a basic gradient descent method and allows find a minimum with a higher probability. The sampling of the search space is controlled by the parameters  $g$  and  $d_k$ . In addition, the computation time is only a few seconds, which is generally not the case with global optimization algorithms.

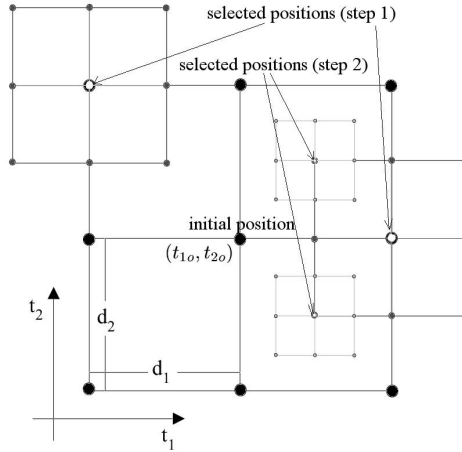


**Fig. 3.** Principle for the search of the optimal translation parameters.

### 3 Results

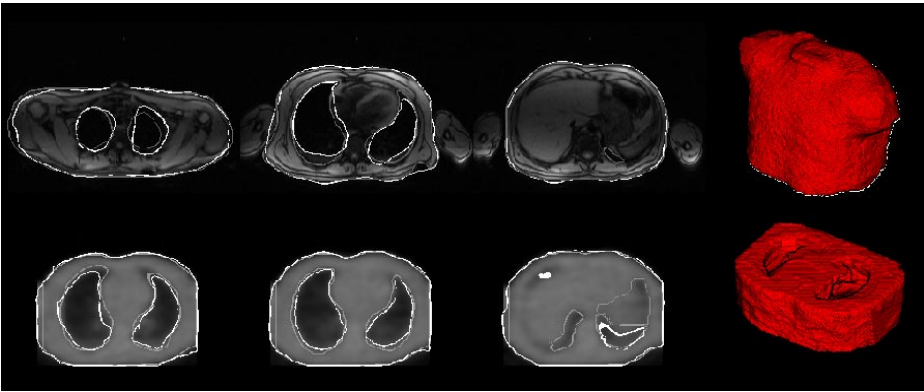
#### 3.1 Segmentation Results

Three multiresolution levels were used (for image data, model and deformation grid). Canny-Deriche method or image thresholding were used for the edge extraction. Fig. 4 presents the segmentation results of case E1 for MR (top) and PET transmission image (down). Segmentation results (white contours) are compared to manual delineation (gray contours).

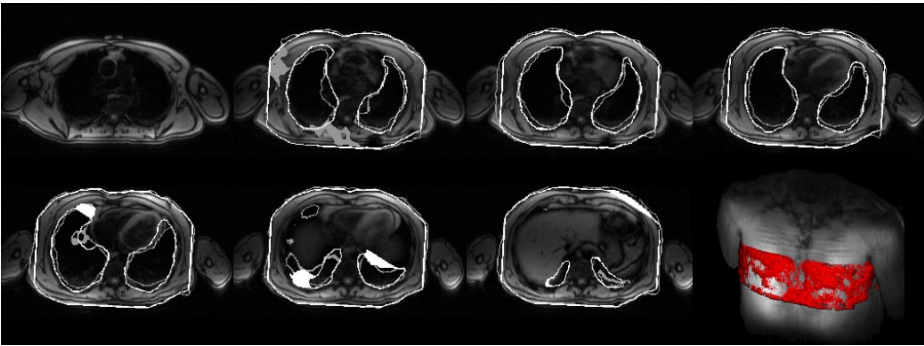
#### 3.2 Registration Results

Fig. 5 presents the registration result obtained with the E1 case. SA PET images which correspond to the MR SA image planes are computed using the obtained registration parameters. In Figs. 6 and 7 registered end-diastolic MR and PET emission images are presented in the transaxial and SA planes, respectively.





**Fig. 4.** Segmentation results of transaxial MR (top) and PET transmission (down) images for case E1. White contours correspond to the deformable model based segmentation and gray contours show the manual delineation. A 3-D visualization [8] of the corresponding deformable model based segmentation is shown on the right.



**Fig. 5.** Contours from registered PET images are superimposed onto the MR transaxial image plane. Automatically segmented contours are shown in white and manually delineated in gray. Bottom right corner: A 3D visualization illustrates the positioning of the registered PET transmission data relative to the ray traced MR thorax image.

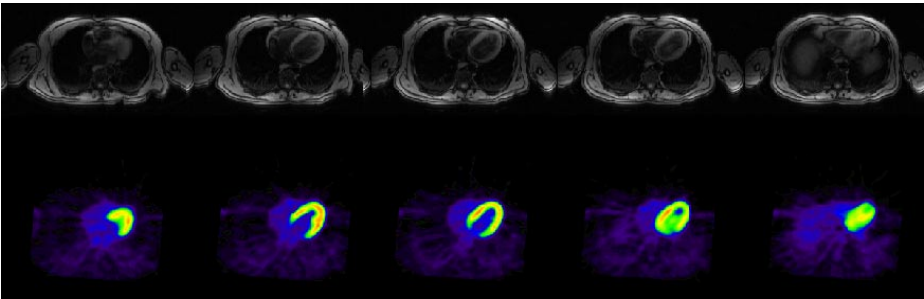


**Fig. 6.** Registered transaxial end-diastolic MR (top) and PET emission (bottom) image slices for the E1 case.

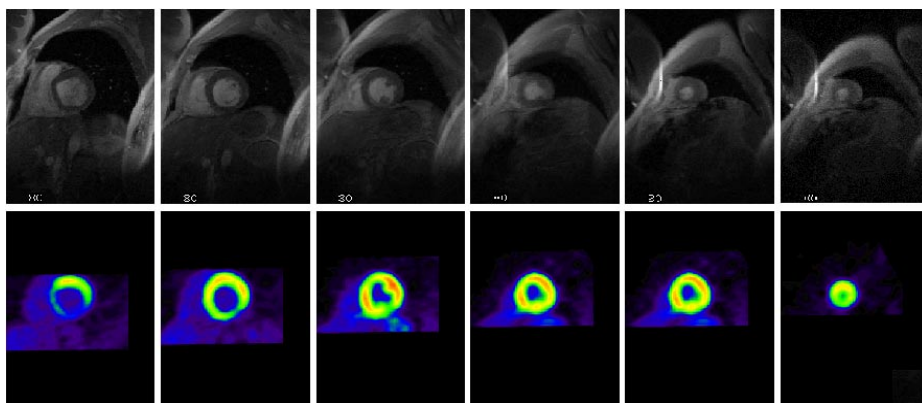


**Fig. 7.** Registered end-diastolic SA MR (top) and PET emission (bottom) image slices.

## 4 Discussion and Conclusion

The proposed method was applied to the 10 available cases. It did give visually good results for 9 cases out of the 10. In the failing case, there were unexpected artifacts in the FDG PET data. In order to quantitatively evaluate the algorithm, the statistics of the distance between registered PET surface points and segmented MR image surface were computed. When using deformable model based automatic segmentation, registration error was  $2.8 \pm 0.5$  mm (minimum 1.9 and maximum 3.8 mm). With the manual delineation of the thorax structures, registration error was  $2.4 \pm 0.9$  mm (minimum 0.5 and maximum 3.5 mm). Although this computed error term mainly quantify the difference between segmentation results of PET and MR thorax models, it gives a reasonable index of the quality of the registration in the absence of a reference data set.

Due to the presence of arms in MRI and their absence in PET, we did exclude points of the PET model located on the thorax sides for the calculation of the registration parameters. Initial parameter vector should also be close enough for the algorithm to converge to optimal result. This was the case in all of the studies since the positioning of the patient was identical in both imaging modalities, and as a result, the initial alignment of the MR distance map volume and the PET model was similar.

We did not observe major differences between registration based on manual delineation and automatic segmentation. In some cases, registration based on manual delineation performed better. One possible reason for this is that sometimes the automatic deformable model based segmentation locally fails to follow deep cavities. One additional segmentation step using a denser deformation grid could help to solve this problem.

The automatic segmentation of the MR and PET images with size  $256 \times 256 \times 217$  voxels takes less than 3 minutes on a PC workstation (PIII, 800 MHz). With the same image size, the execution time for registration was about 50

seconds when about 400 points were selected to compute the rigid transformation parameters. The speed of registration algorithm depends on factors like the need of the preprocessing, the complexity of the cost function and the number of the cost function evaluations performed by the optimization algorithm [10]. Compared to the iterative closest point (ICP) algorithm [9], our approach also requires the segmentation of the data. In our method, the distance map is computed once as a preprocessing step and after that the estimation of the distances between the model and the data points is immediate. On the contrary, in the ICP algorithm, distances are explicitly computed at every iteration. In our experiments the proposed registration parameter search strategy did provide a fast and reliable results. In future works, we will compare current method to other registration methods and also validate this method by using simulated images.

## References

1. Pallotta S., Gilardi M. C., Bettinardi V., Landoni C., Striano G., Masi R. and Fazio F.: Application of a surface matching image registration technique to the correlation of cardiac studies in positron emission tomography (PET) by transmission images. *Phys. Med. Biol.*, **40** (1995) 1695–1708.
2. Kim R., Aw T., Bacharach S., Bonow R.: Correlation of cardiac MRI and PET images using lung cavities as landmarks. *Computers in Cardiology*, (1991) 49–52.
3. Mäkelä T., Clarysse P., Lötjönen J., Sipilä O., Hänninen H., Nenonen J., Lauerma K., Knuuti J., Katila T. and Magnin I. E.: A method for registration of cardiac MR and PET images for the myocardial viability study. In: Marzullo, P. (ed.): *NATO advanced research workshop - Understanding Cardiac Imaging Techniques From Basic Pathology to Image Fusion*. NATO Science Series: Life and Behavioural Sciences. Vol. 332. IOS Press (2001) 155–165.
4. Lauerma K., Niemi P., Hänninen H., Janatuinen T., Voipio-Pulkki L., Knuuti J., Toivonen L., Mäkelä T., Mäkijärvi M. A. and Aronen H. J.: Multimodality MR imaging assessment of myocardial viability: combination of first-pass and late contrast enhancement to wall motion dynamics and comparison with FDG-PET. *Radiology*, **217** (2000) 729–736.
5. Lötjönen J., Reissman P.-J., Magnin I.E. and Katila T.: Model extraction from magnetic resonance volume data using the deformable pyramid. *Medical Image Analysis*, **4** (1999) 387–406.
6. Borgefors G.: Hierarchical chamfer matching: A parametric edge matching algorithm. *IEEE Trans. Pattern Anal. Machine Intell.*, **6** (1988) 849–865.
7. Canny J.: A computational approach to edge detection. *IEEE Trans. Pattern Anal. Machine Intell.*, **8** (1986) 679–698.
8. Pyökkimies E. P., Salli E. and Katila T. Fast image order volume rendering algorithm for multimodal image visualization. In: Nenonen J., Ilmoniemi R.J. and Katila T. (eds.): *Biomag2000*, Proc. 12th Int. Conf. on Biomagnetism, (2001) 1043–1045.
9. Besl P.J. and McKay N.D.: A method for registration of 3-D shapes. *IEEE Trans. Pattern Anal. Machine Intell.*, **14** (1992) 239–256.
10. Van Herk M.: Image registration using chamfer matching. In: Bankman I. N. (ed.): *Handbook of medical imaging*. Academic Press (2000) 515–527 .

## A 3-D model-based registration approach for the PET, MR and MCG cardiac data fusion

Timo Mäkelä<sup>a,b,c,\*</sup>, Quoc Cuong Pham<sup>b</sup>, Patrick Clarysse<sup>b</sup>, Jukka Nenonen<sup>a,c</sup>,  
Jyrki Lötjönen<sup>d</sup>, Outi Sipilä<sup>e</sup>, Helena Hänninen<sup>f</sup>, Kirsi Lauerma<sup>e</sup>, Juhani Knuuti<sup>g</sup>,  
Toivo Katila<sup>a,c</sup>, Isabelle E. Magnin<sup>b</sup>

<sup>a</sup>Laboratory of Biomedical Engineering, Helsinki University of Technology, P.O.B. 2200, FIN-02015 HUT Helsinki, Finland

<sup>b</sup>CREATIS, INSA, Batiment Blaise Pascal, 69621 Villeurbanne Cedex, France

<sup>c</sup>BioMag Laboratory, Helsinki University Central Hospital, P.O.B. 503, FIN-00029 HUS Helsinki, Finland

<sup>d</sup>VTT Information Technology, P.O.B. 1206, FIN-33101 Tampere, Finland

<sup>e</sup>Department of Radiology, Helsinki University Central Hospital, P.O.B. 340, FIN-00029 HUS Helsinki, Finland

<sup>f</sup>Division of Cardiology, Helsinki University Central Hospital, P.O.B. 340, FIN-00029 HUS Helsinki, Finland

<sup>g</sup>Turku PET Centre, c/o Turku University Central Hospital, Box 52, FIN-20521 Turku, Finland

### Abstract

In this paper, a new approach is presented for the assessment of a 3-D anatomical and functional model of the heart including structural information from magnetic resonance imaging (MRI) and functional information from positron emission tomography (PET) and magnetocardiography (MCG). The method uses model-based co-registration of MR and PET images and marker-based registration for MRI and MCG. Model-based segmentation of MR anatomical images results in an individualized 3-D biventricular model of the heart including functional parameters from PET and MCG in an easily interpretable 3-D form.

© 2003 Elsevier B.V. All rights reserved.

### 1. Introduction

Ischemic diseases and their dramatic consequence, the myocardial infarct, are the leading cause of mortality in industrial countries. From the physio-pathological point of view, ischemia results from a disequilibrium between myocardial perfusion, metabolism and contractile function. Following an ischemic event, the question of myocardial viability arises. Both ischemia diagnosis and viability estimation rely on the joint analysis of the perfusion, metabolism and contractile function, each of which being quantified with specific imaging modalities (Fig. 1). Consequences onto the electric and magnetic activity of the heart have also been observed. Therefore, computer-based methods are required to automatically perform multi-modal cardiac image registration in 3-D. This is the purpose of this work.

Anatomical (structural) information of the heart is

usually provided by magnetic resonance imaging (MRI) and ultrasound (US). Metabolism can be analyzed with positron emission tomography (PET), perfusion with thallium single photon emission computed tomography (SPECT), MRI, or PET, and contractile function by using MRI and US. Fluorodeoxyglucose (FDG) PET imaging is

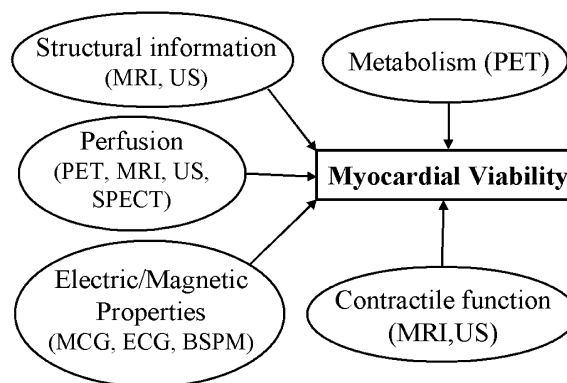


Fig. 1. Variety of imaging modalities required for the cardiac viability assessment.

\*Corresponding author. Tel.: +358-9-451-3174; fax: +358-9-451-3182.

E-mail address: timo.makela@hut.fi (T. Mäkelä).

considered as the gold standard to determine viable areas of the heart (Hartiala and Knuuti, 1995). The electrical activity of the heart creates both an electric and a magnetic field and can be measured by using electrocardiography (ECG) and magnetocardiography (MCG), respectively (Siltanen, 1988). In MCG and ECG *inverse problems*, a current distribution inside of the heart is estimated from noninvasively measured signals by solving a regularized inverse problem (Hämäläinen and Nenonen, 1999; MacLeod and Brooks, 1998). Thus, multichannel MCG and ECG studies can be applied in locating abnormal electrical activity in the heart (Nenonen et al., 2001). The MCG signals are generated by the same bioelectric currents as the ECG, but the MCG may show ischemia-induced deviations from the normal direction of depolarization and repolarization in a different way than ECG (Hänninen et al., 2001). In the literature, electrical activity and metabolism have usually been studied separately, principally because the acquisition system are quite different and involve different specialists. From the physiopathological point of view, it is clear that all the activities are related one to each other. Therefore, our objective here was to allow for the study of the correlation between the electrical (MCG data) and metabolic (PET imaging) activities which may reveal new aspects of hearts complex pathological processes. To our knowledge, this kind of comparison has not been done before. The presented 3-D method gives good possibilities especially for visual comparison of data from different imaging modalities. Whereas PET imaging is used to study the cardiac metabolism, the multichannel ECG and MCG mappings allow a comprehensive study of the electromagnetic fields of the heart. These mapping techniques give unique additional information on the electromagnetic manifestations of myocardial ischemia and viability. At present, the nuclear imaging modalities are mainly used in elective manner, applied only rarely in clinical decisions concerning cardiac care unit patients, whereas ECG monitoring is widely used in emergency care units. In the future, technical development will hopefully allow the MCG mapping function as clinical tool without need for shielding. Multichannel ECG and MCG studies, used with standard torso models (to obtain individual torso model one needs usually MR images), could then give estimation of ischemia (and viability). The 3-D model based approaches could be first used with functional data from ECG and/or MCG, and then be extended during the clinical studies with other modalities, such as MR and nuclear medicine studies. In this paper, we will use MRI for obtaining the heart's anatomy. Myocardial functional data are issued from FDG-PET for the metabolism and MCG data for the heart's electrical activity.

In viability studies, mental registration of the information from different imaging modalities is routinely performed by clinicians. Automatic registration, based on computer programs, is however expected to offer better accuracy, repeatability, and to save time. Registration of

cardiac images is a more complex problem than brain image registration because of the mixed motions of the heart and the thorax structures. Moreover, as compared to the registration of brain images, the heart exhibits much fewer accurate anatomical landmarks and the images are usually acquired with lower resolution. A review of cardiac image registration approaches can be found in (Mäkelä et al., 2002a). These methods are usually based on manual intervention (Behloul et al., 2001; Waiter et al., 2000), automatic registration of thorax surfaces (Pallotta et al., 1995; Gilardi et al., 1998; Yu et al., 1995; Tai et al., 1997; Cai et al., 1999; Mäkelä et al., 2001a) or heart surfaces (Faber et al., 1991; Sinha et al., 1995; Andersson et al., 1995; Declerck et al., 1997; Thirion, 1995, 2001; Nekolla et al., 2000). Another category of methods relies on the matching of image intensities (Hoh et al., 1993; Bettinardi et al., 1993; Slomka et al., 1995; Eberl et al., 1996; Dey et al., 1999; Carrillo et al., 2001; Lötjönen and Mäkelä, 2001). In (Behloul et al., 2001), maximal myocardial deformation from tagged MRI and FDG-PET metabolism were combined using neuro-fuzzy rules to generate polar maps representing the viability. The registration was performed manually with the help of the long axis angles defined in the MRI protocol. In the 'MunichHeart' software, endocardial and epicardial contours were manually delineated in short axis (SA) MR images and registered with the same contours extracted from PET or SPECT using the maximum count detection algorithm (Nekolla et al., 1998, 2000).

In this work, we propose a method for extracting an individualized 3-D anatomical heart model which combines myocardial metabolic data from PET and electrical measurements from MCG. A first approach of the method was presented in (Mäkelä et al., 2001b). Here, it is improved by adding functional MCG results to the model. The method provides a 3-D geometric representation of the heart onto which functional information can be displayed. The data are presented in Section 2. An overview of the approach is given in Section 3, and the different steps are described in Section 4. The extraction of an individualized heart model is explained in Section 5. The construction of functional cartographies are described in Section 6. Results are presented in Section 7 and discussed in Section 8.

## 2. Cardiac imaging protocol

The cardiac data were composed of MR and PET images and MCG data of 10 patients (identified by P1 to P10) suffering from 3 vessels coronary artery disease, diagnosed with coronary angiography and regional dyskinesia in cineangiograms (Lauerma et al., 2000). The mean age was 69 (8 men, 2 women). All patients underwent MR and fluorine-18-deoxyglucose (FDG) PET imaging within 10 days. MCG measurements were also acquired.



- **MR images.** The MR data were acquired with a 1.5 T Siemens Magnetom Vision imager (Siemens, Erlangen, Germany) at the Department of Radiology in Helsinki University Central Hospital (HUCH). A series of 39 ECG-gated contiguous transaxial images was acquired during free respiration using a TurboFLASH sequence (Fig. 2(a)). The pixel size and the slice thickness were  $1.95 \times 1.95$  mm and 10 mm, respectively. Five ECG-gated breath-hold cine SA sections were also acquired (Fig. 2(b)). The pixel size for SA slices was  $1.25 \times 1.25$  mm and the slice thickness 7 mm with a gap of 15 mm between slices. About 15 time points were taken for each section with a repetition time of 40 ms.
- **PET images.** The static cardiac PET data were acquired with a Siemens ECAT 931/08-12 (Siemens/CTI, Knoxville, TN, USA) PET scanner at the Turku PET Centre (Turku, Finland). A series of 15 contiguous transmission and emission images were acquired (Fig. 2(c) and (d)). Transmission images were used for attenuation correction of emission images and also provided structural information that was utilized for registration purposes. The emission image, which can be assumed to be in good registration with the transmission image (Kim et al., 1991), gives absolute quantification of glucosis uptake. For both transmission and emission images, the pixel size and the slice thickness were  $2.41 \times 2.41$  mm and 6.75 mm, respectively.
- **MCG data.** The MCG measurements were performed at rest and after stress with the 67-channel cardiomagnetometer (4-D NeuroImaging, Helsinki, Finland) at the BioMag Laboratory (Montonen et al., 2000) at HUCH. Acute ischemia was induced by exercise testing with a non-magnetic stress ergometer (Hänninen et al., 2001), pedaled in supine position.

The ST-segment difference signals of averaged post-

stress and rest recordings were used in computing current density estimates (CDE) (Nenonen et al., 2001). In this work, the depolarization (QRS complex) data at rest was utilized. Patient-specific boundary-element torso models were acquired from magnetic resonance images, including the triangulated thorax and LV surfaces (Lötjönen et al., 1999, Pham et al., 2001). The torso was assigned a constant electrical conductivity of 0.2 S/m. Discrete CDE values were computed on the LV at midwall locations. The ill-posed inverse problem was regularized with three different methods (Tikhonov regularization with an identity or a surface Laplacian operator, and a maximum a posteriori estimator, MAP; for details, see (Nenonen et al., 2001)). In the present study, we selected MCG results obtained with the MAP estimator.

### 3. Method overview

The aim of the overall approach is to extract a 3-D anatomical model of the heart from patient MR images and to incorporate functional data, such as FDG uptake, information of the magneto-electric properties of the heart and other clinically relevant parameters to the model. The process is summarized in Fig. 3.

First, MR transaxial images were co-registered (rigid transformation) with the PET transmission image (Mäkelä et al., 2001a). The obtained registration parameters were used to register transaxial MR images and the PET emission image. PET slices that correspond to SA MR images were calculated by using MR header information. Then, a 3-D biventricular deformable model was initialized in the SA MR images to segment the myocardium. The deformed model was transformed into the registered SA PET image to obtain FDG uptake values. The model was also transformed to the transaxial MR image and MCG values were calculated for the LV midwall locations. The main steps of the method are described in the following sections.

## 4. Registration

### 4.1. PET-MRI registration

The rigid registration method for cardiac PET and MR images was fully described in (Mäkelä et al., 2001a). The registration method is based on the matching of the thorax and lungs surfaces which are visible in both PET transmission and MR transaxial images. The registration protocol first matches PET transmission and transaxial MR images by using a surface-based registration algorithm and then computes the SA PET slices corresponding to the SA MR slices. The emission and transmission PET and transaxial MR images were first interpolated to the same isotropic

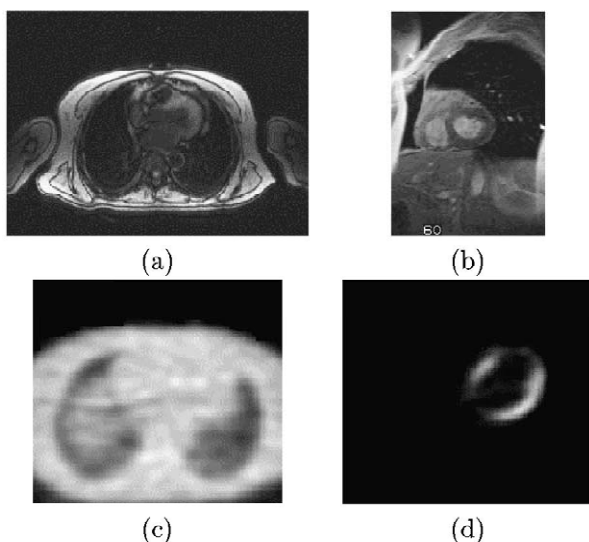


Fig. 2. (a) Transaxial and (b) SA MR images, (c) transmission and (d) emission PET images.

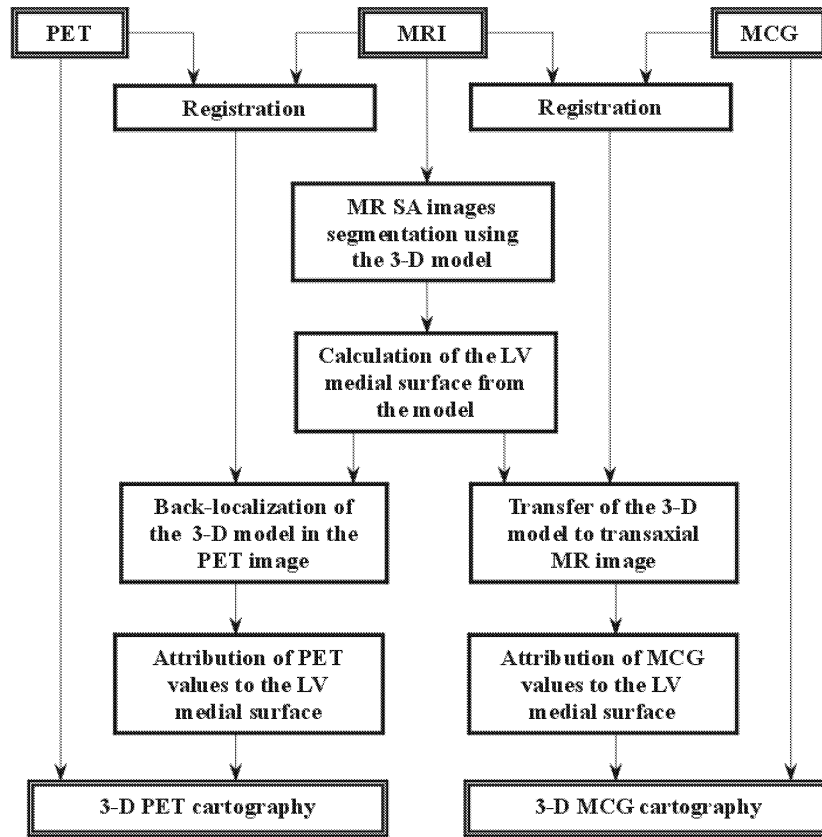


Fig. 3. Extraction of the 3-D anatomical and functional model of the heart including PET-FDG uptake and MCG values: main steps of the process.

voxel dimensions using tri-linear interpolation. Then, the PET transmission and emission images, which had smaller physical dimensions than MR image, was set to the geometric center of the MR image space. The thorax and lung surfaces were segmented from PET transmission image using the deformable model based segmentation method proposed in (Lötjönen et al., 1999). Segmentation of the thorax structures (thorax and lungs surfaces) was based on the elastic deformation of a topologic and geometric prior model using a multiresolution approach. A thorax model including a full triangulated thorax and the lungs surfaces was used with MR images (Fig. 4(a)) while with the PET transmission images, the model was trun-

cated (Fig. 4(b)). The initialization of the models can be made in three ways in our software: (1) manually, (2) matching bounding boxes set around the model and binarized (thresholded) volume, or (3) making rigid registration with the model and binarized volume. In this work, the initialization was done manually. However, we have also used successfully the second approach in more than 50 cases as the thorax is segmented from MR images. Although the bounding boxes do not allow any rotation correction, it has performed well because subjects are always lying on the bed in an approximately same orientation. The segmentation algorithm can cope initialization errors up to a few degrees and several centimeters as demonstrated also in the original article (Lötjönen et al., 1999).

The free-form based deformation algorithm adapts the prior model to locally fit the salient edges in the image within a minimization process. The energy to be minimized is

$$E_{\text{total}} = E_{\text{image}} + \gamma E_{\text{model}}, \quad (1)$$

where  $E_{\text{image}}$  represents the matching error between the prior model and the partial edges in the data volume.  $E_{\text{model}}$  tends to preserve the model's shape by restricting the deformation of the prior model. It describes the deviation of the model's surface normals from their original orientation. The image energy results from a

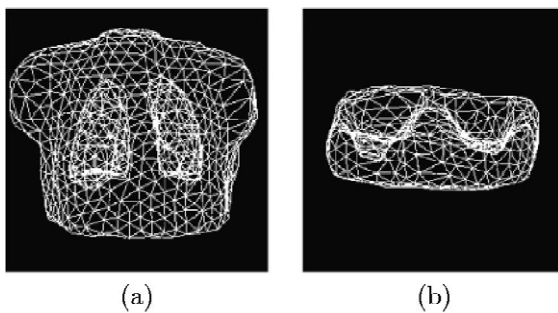


Fig. 4. Geometric and topologic prior model of the thorax for the (a) MR and (b) PET transmission image segmentation.



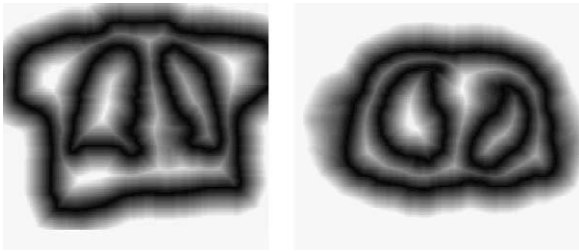


Fig. 5. MR distance maps. The registration algorithm minimizes the distance of the thorax surface points in PET relatively to this distance map.

distance map (Borgefors, 1988) built upon edges extracted either by a Canny–Deriche method (Canny, 1986) or image thresholding (Fig. 5). In order to select edges corresponding to the model, oriented distance maps (Lötjönen et al., 1999) were computed. The parameter  $\gamma$  sets the contribution of the two energy components. A multiresolution process speeds up the minimization process and improves the convergence. Figs. 6(a) and (b) show segmentation results for the thorax structures in MR and PET transmission images.

The parameters of the rigid transformation parameters (three translations, three rotations) between the two image sets are derived from the minimization of the distance between the point set from segmented PET transmission image surfaces and a distance map (Borgefors, 1988) built

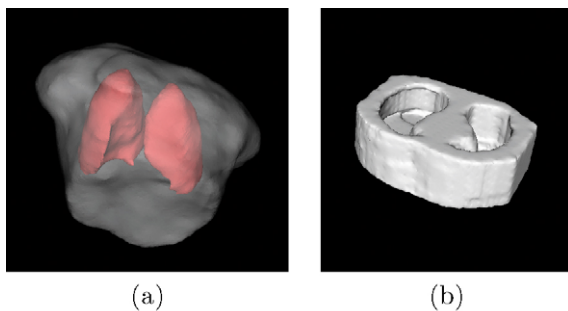


Fig. 6. Segmented (a) MR and (b) PET transmission images.

upon the segmented transaxial MR surfaces (Fig. 5). The uniformly distributed nodes of the deformable model were used as point set from PET transmission image surface. PET transmission and MR transaxial images are acquired in a similar geometry; the model is therefore initialized in a position close to the registration solution. The minimization algorithm is more detailed in (Mäkelä et al., 2001a).

PET emission image was registered with transaxial MR image using the computed registration parameters. The PET transmission image was thus used as a linking mediator to register PET emission image to MR image coordinates.

After registration of the PET emission image with the transaxial MR image, the SA PET slices that corresponded to the SA MR images were computed using MR header information of transaxial and SA MR images (Fig. 7). Note that, as PET acquisition was not gated in this study, the PET images were registered with the SA MR data at end-diastole. This cardiac instant best corresponds to the average PET image.

#### 4.2. MCG–MRI registration

MCG measurements were registered with MRI data by using external markers. The position of the MCG recording system with respect to the patient is determined by attaching three marker coils (magnetic dipoles) to the skin. The magnetic fields produced by the coils are then used to compute the sensor locations relatively to the marker coils (Montonen et al., 2000). The three marker coils were also used to define the MCG sensor coordinates with respect to the MCG markers, a set of nine external marker positions which were selected for registering the MCG sensor system to MR images (Fig. 8).

The locations of the MCG markers were defined by attaching a cross-shaped object consisting of two silicone strips of rubber on the skin of the thorax. The separation between neighboring MCG markers was 5 cm in the head-feet direction and 10 cm in the left-right direction. The locations of the MCG markers and the small marker

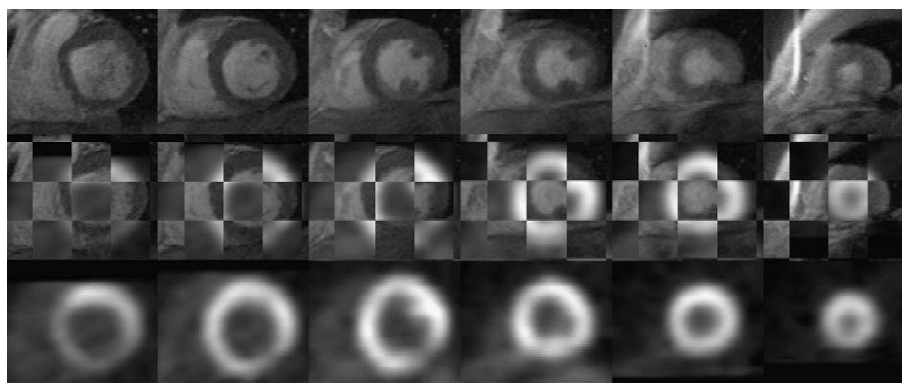


Fig. 7. A stack of registered end-diastolic SA MR (top) and PET emission (bottom) image slices for the P1 case. In the middle row, the images were overlaid in block format to visualize registration results.

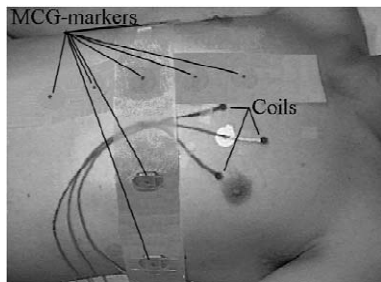


Fig. 8. Placements of the nine MCG markers and three marker coils on the chest in a typical patient study. The round pieces of plastic in two silicone strips of rubber denote the MCG marker locations. Their centerpoints are digitized, and the pieces are removed from the strips before stamping the locations with ink visible in UV light. The three marker coils are used to define the MCG sensor coordinates in respect to the MCG markers.

coils were defined with a 3-D digitization system (3SPACE ISOTRAK II; Polhemus, Colchester, VT, USA). The digitized MCG marker positions were stamped with non-toxic ink, visible only in ultraviolet light. Prior to MR imaging, the nine MRI markers were placed on the stamped positions on the skin. The MRI markers were constructed from two perpendicular tubes filled with 1 mmol/l  $\text{MnCl}_2$  fluid, inserted inside a piece of plastic of  $4.0 \times 4.0 \times 0.7$  cm. The cross-shaped figure of a marker was well visible in the MR images. The MRI markers were located manually from MR images, using a dedicated software. The nine marker coordinate sets ( $x$ ,  $y$ ,  $z$ ) in the MCG and MRI coordinate systems, respectively, were registered using a non-iterative least-squares method (Arun et al., 1987). Only rigid transformations including global rotations and translations were considered. MCG–MRI registration protocol has been applied to more than 50 patient studies (Pesola et al., 2000). With our patient studies we have obtained the root mean square (RMS) error of the nine registered markers to be about 6 mm. The registration error includes various error sources such as the effect of breathing, reattachment of the markers between MCG and MR measurements, localization of the markers from MR images and shape changes in thorax between the measurements because of the flexibility of the shoulders and the skin (Mäkelä et al., 2002b). One of the reasons why the RMS error values are relatively low in our measurements is that the markers in our protocol were attached in positions which were not very sensitive to different alignment errors.

## 5. Capturing the heart anatomy

MR images provide relevant information on the cardiac anatomy. In this section, we present a method for extracting a 3-D individualized anatomical model of the heart from MR short axis images, based on an Elastic Active Region Model (ARM) which is an extension of our

previous work (Pham et al., 2001). Several groups have proposed superficial deformable models to segment the cardiac chambers in three dimensions (McInerney and Terzopoulos, 1996). More recently, Montagnat and Delingette (2000) introduced simplex meshes for segmenting the LV surfaces from 4-D cardiac sequences in MR, SPECT and ultrasound imaging. The reader can find in (Frangi et al., 2001) a good review of 3-D heart modeling approaches used for the purpose of segmentation. Contrary to superficial models, the ARM relies on a volumetric deformation of a geometric heart model. It allows to simultaneously extract the LV and RV endocardial surfaces, as well as the epicardium, while enforcing regularity between these surfaces. In addition, it is formulated in the mechanical framework of elastic bodies that is often used in the context of motion estimation (Papademetris et al., 2001). The ARM is also closely related to the work of Sermesant et al. (2001) who introduced an electro-mechanical model of the heart. In this model, the contraction is controlled by simulating the propagation of electrical waves and taking into account the interaction with ultrasound images. Nevertheless, in this work, the objective is not to provide a complete biomechanical model of the heart, but to accurately segment MR cardiac images by means of a simple but natural description of the heart. The segmentation process can be divided in two main steps. First, the template is spatially positioned by registering it with the image to be segmented. Then, starting from this initial configuration, it is elastically deformed to fit the cardiac structures. Each step will be described in the following.

### 5.1. The 3-D biventricular template

A priori information on the shape of the object of interest strongly constrains the segmentation. We thus developed a 3-D geometric accurate representation of the heart ventricles. This volumetric template was created from a MR reference dataset. The heart of a healthy volunteer was imaged using a cine-MR protocol and the end-diastolic time frame was selected, as we only focus on the images corresponding to the end-diastole. A medical expert interactively delineated the epi- and endocardial contours of the two ventricles on each of the 2-D short axis slices. The corresponding surfaces were then reconstructed and the interior meshed with tetrahedra using the GHS3D software (INRIA, Gamma Project, France). The 3-D biventricular template is shown in Fig. 9.

### 5.2. Interpolating 3-D MR volumes

In order to take advantage of a fully three-dimensional interaction between the model and the short axis images of the heart, 3-D isotropic volumes were interpolated from stacks of 2-D short axis slices. SA images present a good spatial resolution in the acquisition plane, but a poor one in the transversal direction. For the studied cases, the inter-

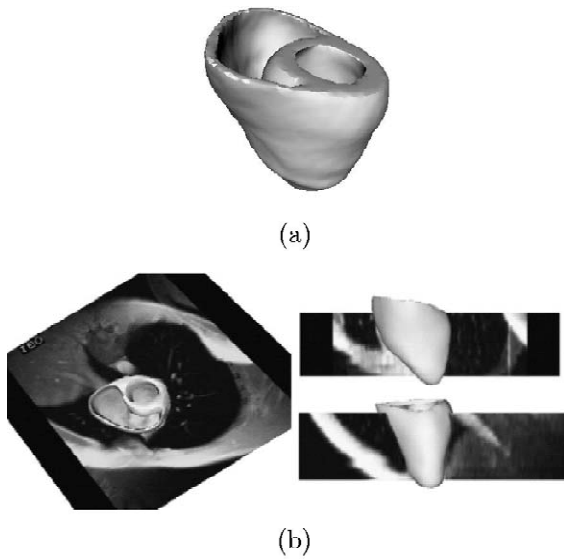


Fig. 9. (a) 3-D prior biventricular model (19 524 nodes, 94 402 tetrahedral elements), (b) model immersed in the MR data.

slice distance was 15 mm, whereas the pixel size was less than 1.5 mm. In such conditions, we experimentally observed that the shape based interpolation technique (Grevera and Udupa, 1996) gave better results than polynomial interpolations on our data.

### 5.3. The model initialization as a registration step

The model is rigidly positioned with respect to the image to be as close as possible to the cardiac structures to be segmented. This is done by searching for the 6 parameters of the rigid spatial transformation  $T$  (3 transla-

tions, 3 rotations) applied to the model, that minimizes the following energy:

$$E_{\text{ini}}(T) = E_{\partial\Omega}(T) E_W(T). \quad (2)$$

Like in (Pluim et al., 2000), the energy to be minimized is a product of an energy based on an intensity criterion and an energy deriving from the image gradient. Here,  $E_{\partial\Omega}(T)$ , computed on the boundary of the template, represents a distance from the model to detected contours in the image. In practice, we take the mean square Euclidean distance from the boundary nodes to the image edges. The region energy  $E_W(T)$  is a similarity measure between the image intensities. It is estimated in a floating meshed domain  $W$  surrounding the template ( $\Omega \subset W$ ) and can either be the sum of the square intensity differences (SSD) sampled on the nodes of  $W$ , or the mutual information (MI) between the two gray level distributions. In most of the cases, good results are obtained with the SSD criterion which is known to be efficient in the monomodal case (Fitzpatrick and Maurer, 2000). The total initialization energy is minimized using the Powell's optimization method (Press et al., 1988) which does not require the computation of the function's gradient. Fig. 10 shows initialization results for two patients.

### 5.4. The deformation model

The second step of the segmentation process is seen as the deformation of an elastic body submitted to an external force field. The myocardium is modeled as a linear elastic continuous medium. Under the small deformation assump-

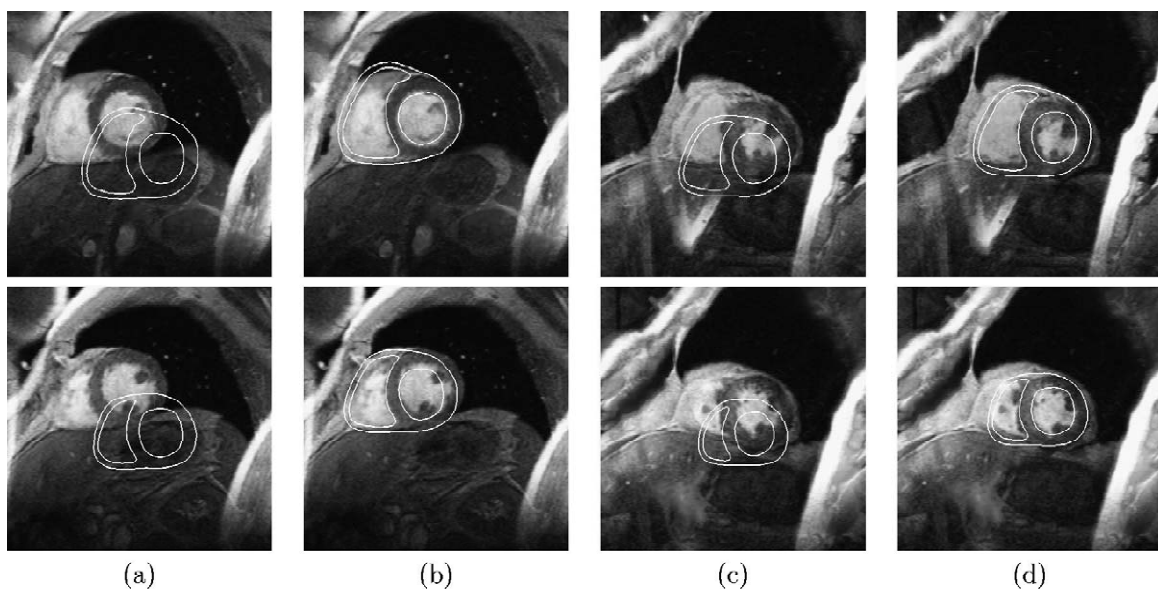


Fig. 10. Initialization step. (a) Patient P1, before registration, (b) patient P1, after registration, (c) patient P2, before registration, (d) patient P2, after registration. First row: basal cross-section; second row: mid-ventricular level.



tion, the linearized form of the Green–Lagrange strain tensor is used:

$$[\epsilon] = \frac{1}{2}(\nabla \mathbf{u} + \nabla \mathbf{u}^T), \quad (3)$$

where  $\mathbf{u}$  denotes the displacement vector. The stress is related to the strain by the constitutive law of the material. For a homogeneous isotropic material, it takes the form

$$\boldsymbol{\sigma} = \mathbf{R}\boldsymbol{\epsilon} = \mathbf{R}\mathbf{S}\mathbf{u}, \quad (4)$$

where  $\boldsymbol{\sigma} = (\sigma_{11}, \sigma_{22}, \sigma_{33}, \sigma_{12}, \sigma_{23}, \sigma_{31})^T$  and  $\boldsymbol{\epsilon} = (\epsilon_{11}, \epsilon_{22}, \epsilon_{33}, \epsilon_{12}, \epsilon_{23}, \epsilon_{31})^T$  are, respectively, the stress and the strain vectors,  $\mathbf{R}$  the elasticity matrix depending on two mechanical parameters (either the Lamé coefficients  $\lambda$  and  $\mu$ , or the Young modulus  $E$  and the Poisson ratio  $\nu$ ), and  $\mathbf{S}$  a differential operator. If we note  $\Omega$  the considered domain,  $\partial\Omega$  its boundary, and  $\mathbf{t}$  the superficial external forces applied on the boundary, the equilibrium state corresponds to the minimum of the following potential energy:

$$E_{\text{glob}}(\mathbf{u}) = \underbrace{\frac{1}{2} \int_{\Omega} \boldsymbol{\sigma} \boldsymbol{\epsilon} \, d\mathbf{x}}_{E_{\text{elast}}(\mathbf{u})} - \alpha \underbrace{\int_{\partial\Omega} \mathbf{t}(\mathbf{I} + \mathbf{u}) \cdot \mathbf{u} \, d\mathbf{s}}_{E_{\text{data}}(\mathbf{u})}. \quad (5)$$

The first term  $E_{\text{elast}}(\mathbf{u})$  is an elastic energy which regularizes the deformations imposed by the external energy  $E_{\text{data}}(\mathbf{u})$ , evaluated in the deformed configuration (if we assume that the displacements are small). In the case of large displacements, the geometric non-linearity should be taken into account by updating the elastic energy during the deformation process. The external force field deriving from the image is chosen such that it tends to attract the model's boundary towards salient features existing in the image. One way to compute a 3-D force field is to calculate the gradient of a potential image  $\mathbf{t}(\mathbf{x}) = -\nabla P(\mathbf{x})$  which can be, for example, either the norm of the image gradient, an edge map extracted with a Canny–Deriche operator and smoothed with a gaussian filter, or a distance map (chamfer or Euclidean distance). The Gradient Vector Flow (GVF), proposed by Xu and Prince (1998), directly provides a force field which allows a better convergence, especially in the case of concavities. In our experiments, the GVF computed from the norm of the image gradient was used in most of the cases.

Eq. (5) is discretized using the Finite Element Method (FEM) with linear basis functions (Zienkiewicz and Taylor, 1987). The energy to be minimized thus becomes

$$E_{\text{glob}}(\mathbf{U}) = \frac{1}{2} \mathbf{U}^T \mathbf{K} \mathbf{U} + \alpha \mathbf{F} \cdot \mathbf{U}, \quad (6)$$

with  $\mathbf{U}$  being the global displacement vector,  $\mathbf{F}$  the global force vector and  $\mathbf{K}$  the stiffness matrix. A minimum is reached for

$$\mathbf{K} \mathbf{U} = \mathbf{F}. \quad (7)$$

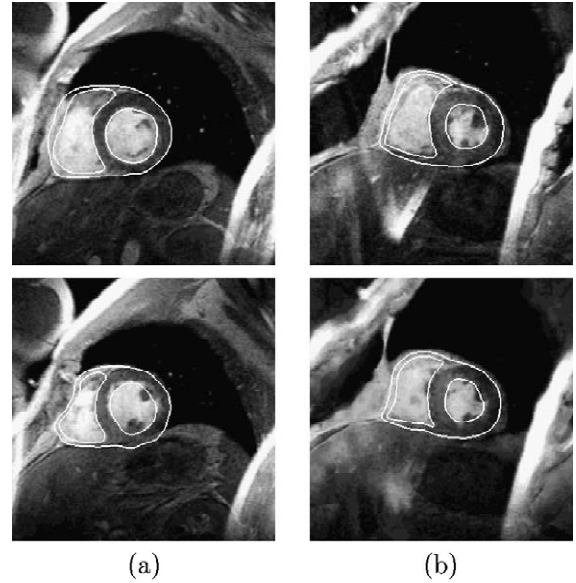


Fig. 11. Segmentation results. (a) Patient P1, (b) patient P2. First row: basal slice; second row: mid-ventricular level.

As  $\mathbf{F}$  is a function of the displacement, Eq. (7) is solved iteratively using a semi-implicit Euler scheme. Final segmentation results after the model deformation are shown in Fig. 11 for the two same cases.

## 6. Functional model of the heart

### 6.1. FDG-PET cartography

After the registration and segmentation steps, functional data was attributed to the elements and nodes of the 3-D biventricular model. Also some parameters with clinical interest was derived from MR imaging. First, the model was labeled so that it was possible to separate the right and left ventricles and obtain internal and external surfaces. Moreover, cavity volumes, myocardial mass and local wall thickness were computed. In order to enrich the model with metabolic information, the model was transformed into the registered PET-FDG emission image. A LV medial surface was automatically calculated between LV endo- and epicardial surfaces (Fig. 12).

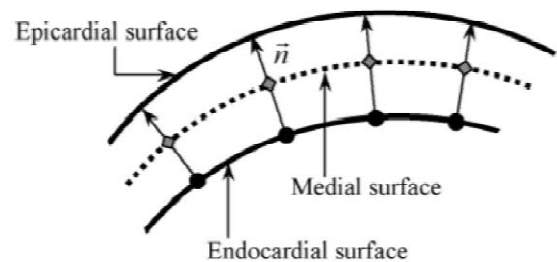


Fig. 12. Calculation of the medial surface using the segmented epicardial and endocardial surfaces.

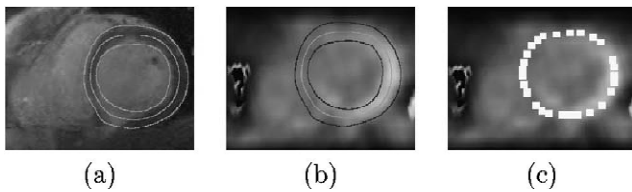


Fig. 13. (a) Intersection of endocardial (inner contour), epicardial (outermost contour) and calculated medial (middle contour) surfaces with a MR SA slice, (b) the same contours are shown in the corresponding registered PET SA image (medial contour in the middle) and (c) the mean value of the FDG-uptake was computed at the medial surface nodes in a small neighborhood.

The medial surface nodes were calculated by, first computing the 3-D normal to each node of the endocardial surface and, secondly, calculating the middle point of the segment normal to the endocardial surface and its intersection with the epicardial surface (Fig. 13(a)). Surfaces were transformed to registered PET emission image and a FDG uptake mean value was computed at each node of the medial surface (Fig. 13(b), middle contour) in a  $5 \times 5 \times 5$  neighborhood, which corresponds to  $6.25 \times 6.25 \times 6.25$  mm physical dimensions (Fig. 13(c)).

## 6.2. Magneto-electric cartography

MCG inverse current-density estimates were calculated for the nodepoints of the medial surface. To this aim, the medial surface was transformed from MR SA plane to transaxial MR coordinate system by using MR header information. The MCG measurements were regularized with a MAP estimator.

## 7. Results

### 7.1. FDG-PET cartography

Fig. 14(left) and Fig. 15(left) illustrate the FDG metabolic activity over the LV medial surface for 2 cases. Right ventricular and epicardial surfaces are shown in transparency. In Fig. 14(right) and Fig. 15(right), the corresponding PET bull's eye (polarmap) presentations are shown for a qualitative evaluation of the 3-D displays (Siemens software, Turku PET Centre). Bull's eye images are commonly used method for displaying functional information of the heart. The center corresponds to the

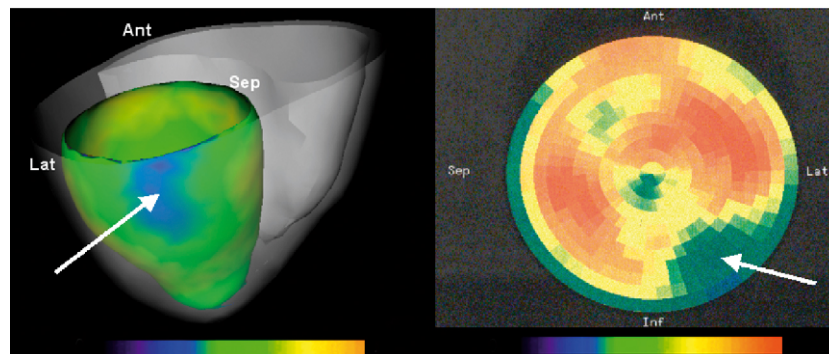


Fig. 14. 3-D representation of the FDG PET uptake values on the biventricular heart model (left) for patient P1. Interactively made bull's eye representation (Siemens software) of the corresponding PET image is presented on the right. The polarmap shows PET values at mid-wall location. Scar area can be seen in dark green at the basal level of the 3-D display (arrows).

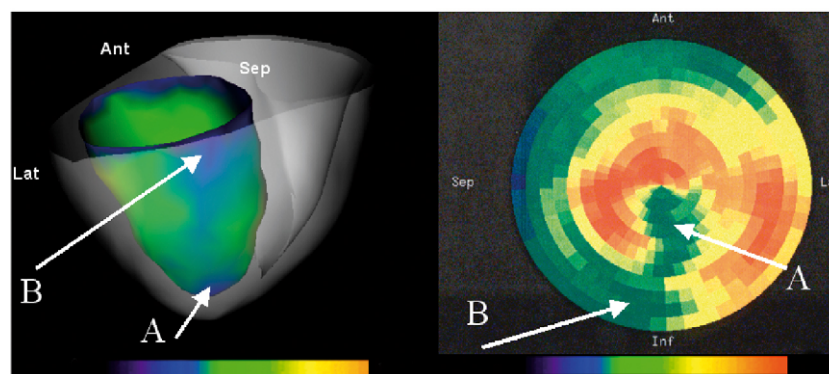


Fig. 15. Left: 3-D representation of the FDG PET uptake values on the biventricular heart model for patient P2. Right: corresponding bull's eye representation (Siemens software) with values estimated at mid-wall location. The low LV FDG uptake areas (arrows A, B) can be seen clearly in darker colors in the figures.

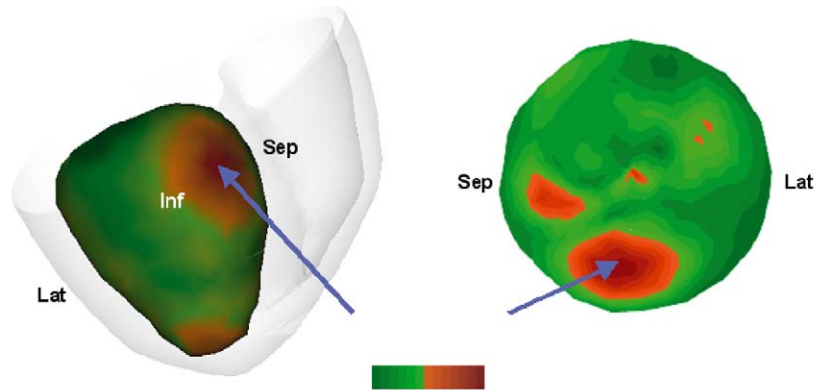


Fig. 16. Left: 3-D representation of the MCG values on the biventricular heart model for patient P1. Right: interactively made corresponding bull's eye representation calculated from the 3-D medial surface. Highest current magnitudes can be seen in red at the basal level of the presentations (arrows) and lowest current magnitudes in dark green.

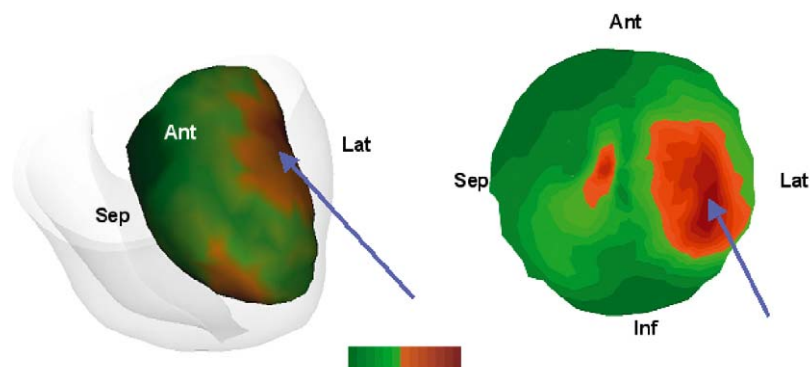


Fig. 17. Left: 3-D representation of the MCG values on the biventricular heart model for patient P2. Right: interactively made corresponding bull's eye representation calculated from the 3-D medial surface.

apex and the outermost ring represents the basal slice. In such polarmaps, metabolic activity is estimated at left-ventricular mid-wall.

The corresponding low LV FDG uptake areas can clearly be seen in both the bull's eye images (dark green in Figs. 14 and 15(right)) and in the 3-D model displays (arrows in Figs. 14 and 15(left)). Visualizations of the 3-D model were performed using the VTK software library.<sup>1</sup>

## 7.2. Magneto-electric cartography

MCG results are presented on the medial surface for P1 in Fig. 16 and P2 in Fig. 17. For both cases, the 3-D visualization is presented on the left and the corresponding bull's eye representation computed from the extracted 3-D medial surface on the right. The MCG results were computed from the resting state data at a single time instant in the middle of the QRS complex. The results have to be regarded illustrative in that sense that the electrical activity in the right ventricle was neglected in the inverse calculations.

## 8. Discussion and conclusion

In this paper, we presented a new approach for the combination of anatomical and functional data from various cardiac imaging modalities. It relies on the registration of thorax structures (thorax surfaces) which are extracted from MR anatomical and PET transmission images. In order to provide 3-D displays of the heart that are easily interpretable by the physician, an individualized 3-D biventricular heart model is extracted from the SA MR images. The various geometrical and functional parameters can therefore be represented onto this model through the LV medial surface (Figs. 14–17). Following our previous efforts, we show in this paper the ability of the method to integrate information about the magneto-electric activity of the heart from MCG. The fusion of metabolic data from PET and magneto-electrical potential onto the same individualized 3-D heart model from MRI has been illustrated on two pathological cases. With such an approach, the localization of metabolic and conduction defects is straightforward since the biventricular model allows for the unambiguous identification of myocardial territories. Within the same framework, it is natural to envisage the inclusion of other complementary functional data such as

<sup>1</sup>The visualization Toolkit (VTK), <http://www.kitware.com>.

information related to the myocardial deformation or perfusion (Behloul et al., 2001).

The reliability of the method mainly depends on the accuracy of the rigid PET-MRI registration. The registration results of 10 cases were visually inspected by a medical expert. Nine over the 10 available cases were considered to provide satisfactory correspondence results. In the remaining bad case, unexpected artifacts were observed in FDG-PET data. In a previous paper (Mäkelä et al., 2001a), we proposed a quantification of the registration accuracy based on the calculation of a distance between segmented surfaces in PET and MRI. The mean distance was 3 mm with a maximum of 4 mm. This is only an indication of the performance of the registration algorithm since it highly depends upon the segmentation of the thorax structures. It also provides a simple mean to detect possible registration failure. A more systematic and accurate validation of the registration method is currently conducted through image simulations. Also intensity based methods, like mutual information, are potential alternative to determine registration parameters in this kind of registration methods where the PET transmission image is used as a linking mediator to register PET emission image to MR image coordinates. In some cases, intensity based methods can even allow to register the emission image directly with the anatomical image.

PET imaging devices have typically 4–10 mm spatial resolution (Hartiala and Knuuti, 1995). In general, the ability of our 3-D model based method to detect functional abnormalities is limited by the spatial resolution of the PET imaging device. In MCG, accuracies of 5 to 25 mm have been reported by comparing the MCG localization results to: (i) cardiac surgery, (ii) catheter ablation, (iii) the results of invasive electrophysiological studies, (iv) ECG localization results, and (v) physiological knowledge (X-ray or MRI). Besides patient studies, the ability of the MCG to locate artificial current dipoles has been tested with physical thorax phantoms. A non-magnetic pacing catheter in a realistically shaped thorax phantom resulted in equal accuracies of 5–10 mm between MCG and ECG mapping data (Fenici et al., 1998). On the other hand, the same catheter in 15 patients showed significantly better localization accuracy with MCG data (7 mm) than with simultaneously recorded ECG mapping data (25 mm) (Pesola et al., 1999).

The MCG results in this work were evaluated on the median LV surface during the cardiac depolarization. The resting-state MCG data in the peak of the QRS contains contributions from both ventricles, while the LV contribution dominates. In this study the RV was not included in the inverse MCG computations. The main motivation to use only the LV surface came from our previous study where we investigated the MCG data after physical exercise test in the same patient population (Nenonen et al., 2001). In that study the ST segment was analyzed and difference signals were computed (post-exercise minus

rest). This difference was associated with exercise-induced ischemia which was known to arise in the left ventricle on the basis of PET and MRI (Lauerma et al., 2000). While the whole MCG (and ECG) source imaging methodology is still under rapid development (Hämäläinen and Nenonen, 1999) the results show that MCG, due to a millisecond time resolution, may be able to provide new valuable information on cardiac function, especially when constrained with accurate anatomy from MRI and combined with other medical imaging data.

The temporal correspondence of the PET and MR images has been overcome by assuming the correspondence between the MR transaxial, end-diastolic SA images, and the PET acquisitions, as it is usually admitted in clinical practice. In fact, transaxial MR images were obtained with a snapshot technique during free respiration while PET measurements were accumulated during a relatively long period of time (about 10 min). This might generate differences in the thorax and lungs shape and, consequently, cause registration errors. ECG-gated PET with non-rigid registration could certainly help to better handle the temporal correspondence problem.

The results of the automatic extraction of the biventricular model using the ARM were quite satisfactory for the two processed cases as shown in Fig. 11. This step, which is independent of the others, is important since (i) it extracts an individualized anatomical model from which volumes, masses, wall thickness can be derived, (ii) it provides the region of interest where the functional parameters from PET and MCG are estimated. We are currently quantifying the performance of the ARM in terms of accuracy (as compared to manual tracing) and robustness, especially as a function of model initialization. In addition, acquisition sequences such as stimulated echo sequences (e.g. TrueFISP, bFFE, Fiesta) provide better resolution and contrast and may improve the reliability and the accuracy of the segmentation results.

The medial surface seems to us the most straightforward way to obtain functional cartographies preventing from border effects that could occur from slight mis-registration. In this work, we implemented a simple geometrical approach to compute this surface. Other methods such as the centersurface (Bolson et al., 1995) could also be applied. In order to keep the volumetric property of the model, the next step will consist in the anatomical reparameterization of the heart's geometry so that the functional parameters can be easily depicted on the myocardial borders as well as inside the wall by interactively peeling the model, for instance.

In conclusion, we have presented a model-based approach for the combination onto patient-specific heart model of both anatomical and diverse functional data from multimodality cardiac imaging. In this work, one of the main purposes was to automatically register metabolic PET and electromagnetic measurements from MCG. Similar approach could also be used to combine other modalities



such as SPECT and multichannel ECG studies. We believe that the presented approach can help the radiologist or cardiologist to rapidly apprehend the functional state of the myocardium through 3-D intuitive cartographies. It is therefore possible to accurately compare the different imaged functions (metabolism, magneto-electric activity) in the context of physio-pathological studies on the ischemic diseases, for instance, which consequences on the cardiac muscle are complex and not yet fully understood. In order to enrich the model, other parameters related to the heart motion and perfusion will be integrated in the near future.

## Acknowledgements

This study was partly granted by the Scientific Department of the French Embassy in Finland, the Region Rhône Alpes, through the ADÉMO project and The Foundation of Technology in Finland. This work was performed within the framework of the joint incentive action 'Beating Heart' of the research groups ISIS, ALP and MSPC of the French National Center for Scientific Research (CNRS).

## References

- Andersson, J.L.R., Bagnhammar, B., Schneider, H., 1995. Accurate attenuation correction despite movement during PET imaging. *J. Nucl. Med.* 36 (4), 670–678.
- Arun, K.S., Huang, T.S., Blostein, S.D., 1987. Least-squares fitting of two 3-D point sets. *IEEE Trans. Pattern Anal. Machine Intell.* 9 (5), 698–700.
- Behloul, F., Lelieveldt, B.P.F., Boudraa, A., Janier, M., Revel, D., Reiber, J.H.C., 2001. Neuro-fuzzy systems for computer-aided myocardial viability assessment. *IEEE Trans. Med. Imaging* 20 (12), 1302–1313.
- Bettinardi, V., Gilardi, M., Lucignani, G., Landoni, C., Rizzo, G., 1993. A procedure for patient repositioning and compensation for misalignment between transmission and emission data in PET heart studies. *J. Nucl. Med.* 34 (1), 137–142.
- Bolson, E., Sheehan, F., Legget, M., Jin, H., McDonald, J., Sampson, P., Martin, R., Bashein, G., Otto, C., 1995. Applying the centersurface model to 3-D reconstructions of the left ventricle for regional function analysis. In: *Computers in Cardiology*. IEEE Computer Society, Long Beach, CA, pp. 63–66.
- Borgefors, G., 1988. Hierarchical chamfer matching: a parametric edge matching algorithm. *IEEE Trans. Pattern Anal. Machine Intell.* 10 (6), 849–865.
- Cai, J., Chu, J., Recine, D., Sharma, M., Nguyen, C., Rodebaugh, R., Saxena, A., Ali, A., 1999. CT and PET lung image registration and fusion in radiotherapy treatment planning using the chamfer-matching method. *Int. J. Radiat. Oncol. Biol. Phys.* 43 (4), 883–891.
- Canny, J., 1986. A computational approach to edge detection. *IEEE Trans. Pattern Anal. Machine Intell.* 8 (6), 679–698.
- Carrillo, A., Duerk, J., Lewin, J., Wilson, D., 2001. Semiautomatic 3-D image registration as applied to interventional MRI liver cancer treatment. *IEEE Trans. Med. Imaging* 19 (3), 175–185.
- Declerck, J., Feldmar, J., Goris, M., Betting, F., 1997. Automatic registration and alignment on a template of cardiac stress and rest reoriented SPECT images. *IEEE Trans. Med. Imaging* 16 (6), 727–737.
- Dey, D., Slomka, P., Hahn, L., Kloiber, R., 1999. Automatic three-dimensional multimodality registration using radionuclide transmission CT attenuation maps: a phantom study. *J. Nucl. Med.* 40 (3), 448–455.
- Eberl, S., Kanno, I., Fulton, R., Ryan, A., Hutton, B., Fulham, M., 1996. Automated interstudy image registration technique for SPECT and PET. *J. Nucl. Med.* 37 (1), 137–145.
- Faber, T., McColl, R., Opperman, R., Corbett, J., Peshock, R., 1991. Spatial and temporal registration of cardiac SPECT and MR images: methods and evaluation. *Radiology* 179 (3), 857–861.
- Fenici, R., Nenonen, J., Pesola, K., Korhonen, P., Lötjönen, J., Mäkiärvä, M., Poutanen, V.P., Keto, P., Katila, T., 1998. Non-fluoroscopic localization of an amagnetic stimulation catheter by multichannel magnetocardiography. *PACE* 22, 1210–1220.
- Fitzpatrick, J., Hill, D., Maurer, C., 2000. Image registration. In: *Handbook of Medical Imaging*, Vol. 2. SPIE Press, pp. 375–435.
- Frangi, A.F., Niessen, W.J., Viergever, M.A., 2001. Three-dimensional modeling for functional analysis of cardiac images, a review. *IEEE Trans. Med. Imaging* 20 (1), 2–25.
- Gilardi, M.C., Rizzo, G., Savi, A., Landoni, C., Bettinardi, V., Rossetti, C., Striano, G., Fazio, F.N., 1998. Correlation of SPECT and PET cardiac images by a surface matching registration technique. *Comput. Med. Imag. Graph.* 22, 391–398.
- Grevera, G.J., Udupa, J.K., 1996. Shape-based interpolation of multi-dimensional grey-level images. *IEEE Trans. Med. Imaging* 15 (6), 881–892.
- Hämäläinen, M., Nenonen, J., 1999. Magnetic source imaging. In: *Encyclopedia of Electrical Engineering*, Vol. 12. Wiley, New York, pp. 464–479.
- Hänninen, H., Takala, P., Mäkiärvä, M., Montonen, J., Korhonen, P., Oikarinen, L., Simelius, K., Nenonen, J., Katila, T., Toivonen, L., 2001. Recording locations in multichannel magnetocardiography and body surface potential mapping sensitive for regional exercise-induced ischemia. *Basic Res. Cardiol.* 96, 405–414.
- Hartiala, J., Knuuti, J., 1995. Imaging of heart by MRI and PET. *Ann. Med.* 27, 35–45.
- Hoh, C., Dahlbom, M., Harris, G., Choi, Y., Hawkins, R., Philips, M., Maddahi, J., 1993. Automated iterative three-dimensional registration of positron emission tomography images. *J. Nucl. Med.* 34 (11), 2009–2018.
- Kim, R., Aw, T., Bacharach, S., Bonow, R., 1991. Correlation of cardiac MRI and PET images using lung cavities as landmarks. In: *Proceedings of the IEEE Conference on Computers in Cardiology*, pp. 49–52.
- Lauerma, K., Niemi, P., Hänninen, H., Janatuinen, T., Voipio-Pulkki, L., Knuuti, J., Toivonen, L., Mäkelä, T., Mäkiärvä, M., Aronen, H., 2000. Multimodality MR imaging assessment of myocardial viability, combination of first-pass and late contrast enhancement to wall motion dynamics and comparison with FDG-PET. *Radiology* 217, 729–736.
- Lötjönen, J., Mäkelä, T., 2001. Elastic matching using a deformation sphere. In: Niessen, W., Viergever, M. (Eds.), *Medical Image Computing and Computer-Assisted Intervention*. Lecture Notes in Computer Science 2208. Springer, Berlin, pp. 541–548, MICCAI01.
- Lötjönen, J., Reissman, P.-J., Magnin, I.E., Katila, T., 1999. Model extraction from magnetic resonance volume data using the deformable pyramid. *Medical Image Analysis* 3 (4), 387–406.
- MacLeod, R.S., Brooks, D.H., 1998. Recent progress in inverse problems in electrocardiology. *IEEE Eng. Med. Biol.* 17 (1), 73–82.
- Mäkelä, T., Clarysse, P., Lötjönen, J., Sipilä, O., Lauerma, K., Hänninen, H., Nenonen, J., Knuuti, J., Katila, T., Magnin, I.E., 2001a. A method for registration of cardiac magnetic resonance and positron emission tomography images for assessing myocardial viability. In: *Understanding Cardiac Imaging Techniques – from Basic Pathology To Image Fusion*, Vol. 322. IOS Press, pp. 155–165.
- Mäkelä, T., Clarysse, P., Lötjönen, J., Sipilä, O., Lauerma, K., Hänninen, H., Pyökkimies, E.-P., Nenonen, J., Knuuti, J., Katila, T., Magnin, I.E., 2001b. A new method for the registration of cardiac PET and MR images using deformable model based segmentation of the main thorax

- structures. In: Medical Image Computing and Computer-Assisted Intervention (MICCAI'01). Lecture Notes in Computer Science (LNCS), Vol. 2208. Springer, Berlin, pp. 557–564.
- Mäkelä, T., Clarysse, P., Sipilä, O., Pauna, N., Pham, Q., Katila, T., Magnin, I.E., 2002a. A review of cardiac image registration methods. *IEEE Trans. Med. Imaging* 21 (9), 1011–1021.
- Mäkelä, T., Lötjönen, J., Sipilä, O., Lauerma, K., Nenonen, J., Katila, T., Magnin, I.E., 2002b. Error analysis of registering of anatomical and functional cardiac data using external markers. In: Nowak, H., Haueisen, J., Giesler, F., Huonker, R. (Eds.), *Biomag 2002, Proceedings of the 13th International Conference on Biomagnetism*, pp. 842–845.
- McInerney, T., Terzopoulos, D., 1996. Deformable models in medical image analysis: a survey. *Medical Image Analysis* 1 (2), 91–108.
- Montagnat, J., Delingette, H., 2000. Space and time shape constrained deformable surfaces for 4D medical image segmentation. In: Medical Image Computing and Computer-Assisted Intervention (MICCAI'00). Lecture Notes in Computer Science (LNCS), Vol. 1935. Springer, Berlin, pp. 196–205.
- Montonen, J., Ahonen, A., Hämäläinen, M., Ilmoniemi, R., Laine, P., Nenonen, J., Paavola, M., Simelius, K., Simola, K., Katila, J.T., 2000. Magnetocardiographic functional imaging studies in biomag laboratory. In: *Biomag96, Proceedings of the 10th International Conference on Biomagnetism*, pp. 494–497.
- Nekolla, S., Miethaner, C., Nguyen, N., Ziegler, S., Schwaiger, M., 1998. Reproducibility of polar map generation and assessment of defect severity and extent assessment in myocardial perfusion imaging using positron emission tomography. *Eur. J. Nucl. Med.* 25, 1313–1321.
- Nekolla, S., Ibrahim, T., Balbach, T., Klein, C., 2000. Coregistration and fusion of cardiac magnetic resonance and positron emission tomography studies. In: *Understanding Cardiac Imaging Techniques – from Basic Pathology To Image Fusion*. IOS Press, pp. 144–154.
- Nenonen, J., Pesola, K., Hänninen, H., Lauerma, K., Takala, P., Mäkelä, T.J., Mäkiärvä, M., Knuuti, J., Toivonen, L., Katila, T., 2001. Current – density estimation of exercise-induced ischemia in patients with multivessel coronary artery disease. *J. Electrocardiogr.* 34 (suppl.), 37–42.
- Pallotta, S., Gilardi, M.C., Bettinardi, V., Rizzo, G., Landoni, C., Striano, G., Masi, R., Fazio, F., 1995. Application of a surface matching image registration technique to the correlation of cardiac studies in positron emission tomography by transmission images. *Phys. Med. Biol.* 40, 1695–1708.
- Papademetris, X., Sinusas, A.J., Dione, D.P., Duncan, J.S., 2001. Estimation of 3D left ventricular deformation from echocardiography. *Medical Image Analysis* 5, 17–28.
- Pesola, K., Nenonen, J., Fenici, R., Lötjönen, J., Mäkiärvä, M., Fenici, P., Korhonen, P., Lauerma, K., Valkonen, M., Toivonen, L., Katila, T., 1999. Bio-electromagnetic localization of a pacing catheter in the heart. *Phys. Med. Biol.* 44, 2565–2578.
- Pesola, K., Lötjönen, J., Nenonen, J., Magnin, I., Lauerma, K., Fenici, R., Katila, T., 2000. The effect of geometry and topology differences in boundary element models on magnetocardiographic localization accuracy. *IEEE Trans. Biomed. Eng.* 47 (9), 1237–1247.
- Pham, Q.C., Vincent, F., Clarysse, P., Croisille, P., Magnin, I.E., 2001. A FEM-based deformable model for the 3-D segmentation and tracking of the heart in cardiac MRI. In: *Image and Signal Processing and Analysis ISPA 2001*, pp. 250–254.
- Pluim, J., Maintz, J., Viergever, M., 2000. Image registration by maximization of combined mutual information and gradient information. *IEEE Trans. Med. Imaging* 19 (8), 809–814.
- Press, W., Flannery, B., Teukolsky, S., Vetterling, W., 1988. *Numerical Recipes in C*. Cambridge University Press, Cambridge.
- Sermesant, M., Coudière, Y., Delingette, H., Ayache, N., Désidéri, J., 2001. An electro-mechanical model of the heart for cardiac image analysis. In: Medical Image Computing and Computer-Assisted Intervention (MICCAI'01). Lecture Notes in Computer Science (LNCS), Vol. 2208. Springer, Berlin, pp. 224–231.
- Siltanen, P., 1988. *Comprehensive Electrocardiology*. Pergamon Press, Oxford, Chapter on Magnetocardiography.
- Sinha, S., Sinha, U., Czernin, J., Porenta, G., Schelbert, H., 1995. Noninvasive assessment of myocardial perfusion and metabolism: feasibility of registering gated MR and PET images. *Am. J. Roentgenol.* 36, 301–307.
- Slomka, P., Gilbert, A., Stephenson, J., Cradduc, T., 1995. Automated alignment and sizing of myocardial stress and rest scans to three-dimensional normal templates using an image registration algorithm. *J. Nucl. Med.* 36, 1115–1122.
- Tai, Y.-C., Lin, K., Hoh, C., Huang, S., Hoffman, E., 1997. Utilization of 3-D elastic transformation in the registration of chest X-ray CT and whole body PET. *IEEE Trans. Nucl. Med.* 44 (4), 1606–1612.
- Thirion, J.-P., 1995. Fast non-rigid matching of 3-D medical images. Research Report 2547. INRIA.
- Thirion, J.-P., 2001. Perfusion and motion from gated SPECT. In: *Understanding Cardiac Imaging Techniques – From Basic Pathology to Image Fusion*. IOS Press, pp. 84–93.
- Waiter, G.D., Al-Mohammad, A., Norton, M.Y., Redpath, T.W., Welch, A., Walton, S., 2000. Regional myocardial wall thickening assessed at rest by ECG gated (18)F-FDG positron emission tomography and by magnetic resonance imaging. *Heart* 84, 332–333.
- Xu, C., Prince, J.L., 1998. Snakes, shapes, and gradient vector flow. *IEEE Trans. Image Process.* 7 (3), 359–369.
- Yu, J.N., Fahey, F.H., Gage, H.D., Eades, C.G., Harkness, B.A., Pelizzari, C.A., 1995. Intermodality, retrospective image registration in the thorax. *J. Nucl. Med.* 36 (12), 2333–2338.
- Zienkiewicz, O., Taylor, R., 1987. *The Finite Element Method*. McGraw-Hill, New York.

# Error Analysis of Registering of Anatomical and Functional Cardiac Data Using External Markers

Timo Mäkelä<sup>1,2,3</sup>, Jyrki Lötjönen<sup>4</sup>, Outi Sipilä<sup>5</sup>, Kirsi Lauerma<sup>5</sup>,  
Jukka Nenonen<sup>1,3</sup>, Toivo Katila<sup>1,3</sup>, Isabelle E. Magnin<sup>2</sup>.

<sup>1</sup>Laboratory of Biomedical Engineering, Helsinki University of Technology, Espoo, Finland;  
<sup>2</sup>CREATIS, INSA Lyon, Villeurbanne Cedex, France; <sup>3</sup>BioMag Laboratory and <sup>5</sup>Department of Radiology,  
Helsinki University Central Hospital, Helsinki, Finland; <sup>4</sup>VTT Information Technology, Tampere, Finland

## Abstract

In this work the relative strengths of the different error sources in a skin marker based registration method for functional magnetocardiography (MCG) data and anatomical magnetic resonance (MR) images of the heart were evaluated. The registration method is needed a) to transform individual torso model, obtained from MR thorax images for inverse problem computations made in the coordinate systems of the bioelectromagnetic measurement device and b) to transform MCG solution of functional information of the cardiac electric excitation to anatomy of MR images. The objective was to analyze the most severe error sources in the registration method, and to reduce their magnitude if possible. Measurements were made with a phantom and on a volunteer. The sum of all registration error components was 6 mm. No specific error sources dominated and their contribution to the total error was approximately equal.

## 1 Introduction

Interpretation and comparison of anatomical and functional data from different medical imaging modalities can be accomplished by registration. Registration methods based on skin markers are widely applied because they allow match any imaging modalities in which the positions of markers can be accurately defined. The main objective of this study was to define the relative strengths of the different error sources in a skin marker based registration method for functional magnetocardiography (MCG) data and anatomical magnetic resonance (MR) images of the heart.

## 2 Materials and methods

### 2.1 Registration protocol

#### 2.1.1 MCG recordings

MCG studies were performed in the BioMag laboratory of Helsinki University Central Hospital (HUCH). Multichannel MCG signals were recorded in a magnetically shielded room using a 99-channel cardiomagnetometer (4-D NeuroImaging, Helsinki, Finland) [1]. The position of the MCG recording system with respect to the patient was determined by attaching three marker coils (magnetic dipoles) to the skin. The magnetic fields produced by the coils were then used to calculate the sensor locations relative to the marker coils.

#### 2.1.2 MCG markers

A set of nine external marker positions, here referred as MCG markers, was selected to registrate the MCG sensor system to MR images. The locations of the MCG markers were defined by attaching a cross-shaped object consisting of two silicone strips of rubber on the skin (see Fig 1). The three marker coils were used to define the MCG sensor coordinates in respect to the MCG markers.

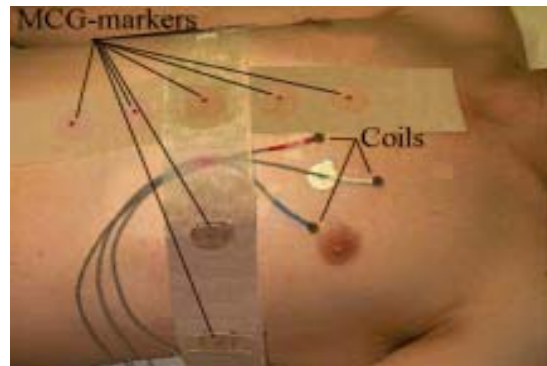


**Fig. 1** Placements of the nine MCG markers and three marker coils on the chest in a typical patient study.

The separation between neighboring MCG markers was 5 cm in the head-feet direction and 10 cm in the left-right direction. The locations of the MCG markers and the marker coils were defined with a 3-D digitization system (3SPACE ISOTRAK II, Polhemus Inc., Colchester, VT, USA). The digitized MCG marker positions were stamped with non-toxic ink, visible only in ultraviolet light.

### 2.1.3 MRI markers

The nine MRI markers were constructed from two perpendicular tubes filled with 1 mmol/l  $\text{MnCl}_2$  fluid, inserted inside a piece of plastic of 4.0 x 4.0 x 0.7 cm. Prior to MR imaging, the nine MRI markers were placed on the stamped positions on the skin. The cross-shaped figure of a marker was well visible in the MR images.

### 2.1.4 Registration

The MRI markers were first located manually from MR images, using a dedicated software. The nine marker coordinate sets (x, y, z) in the MCG and MRI coordinate systems, respectively, were registered using a non-iterative least-squares method [2]. Only rigid transformations including global rotations and translations were considered.

Thus far, our registration protocol has been applied to more than 50 patient studies [3]. The root mean square (RMS) error of the nine registered markers was about 6 mm; ranging from three to more than ten millimeters. The registration error was relatively high and should be reduced, because MCG localization accuracy of < 1 cm are desired for clinical purposes.

## 2.2 Separation of various error sources

A comprehensive study of all error sources in thorax registration would be laborious. In this work, the error sources were divided into five studies: A) the reproducibility of the 3-D localization using the digitization pen, B) the error in alignment of the patient, C) the error arising from repositioning of the MRI markers, D) the effect of different shapes in the measurement beds, and E) the localization error of the MRI markers from the images. Also F) target registration error (TRE) was defined in phantom studies by measuring error of twelve markers in thorax area and four markers in cardiac area which were not used to define registration parameters. Several other error sources can be found, especially from MR imaging, but the selected five studies cover the most significant registration errors in our MCG studies.

An independent measurement of separate error sources is very difficult. For example, the error of the reproducibility of the 3-D localization (study A) can not be avoided during the other studies. Therefore, we chose to quantify the difference between the RMS errors computed for various point sets and not to evaluate the absolute value of each error type individually. Consequently the effects of error sources are not cumulative in a scalar sense, because the errors are vector quantities in 3-D. The main objective of this study is to define the relative strengths of the error sources, instead of absolute magnitudes, in order to reduce the impact of the most severe ones. Estimating the differ-

ences of RMS errors gives a measure of their relative strengths.

## 2.3 Protocol for measuring the error sources

Various error sources were studied using a phantom and a volunteer. The phantom was constructed of wood. Its shape and size were defined from thorax boundaries extracted from MR images of a volunteer. Digitizations were carried out by two persons at the Biomag-laboratory. The MR images were acquired at the Department of Radiology (HUCH). The phantom and the volunteer were positioned supine into a 1.5 T Siemens Magnetom Vision imager (Siemens, Erlangen, Germany). Imaging was performed with the surface coil as a receiver and using a T1 weighted gradient echo sequence. A series of 32 contiguous transaxial images was acquired. Each slice was 10 mm thick. The matrix was 256 x 256 pixels with a 1.76 mm<sup>2</sup> pixel size.

## 2.4 Error studies

### 2.4.1 Study A

The reproducibility of the 3-D localization using the digitization pen was first studied. The MCG markers, a cross-shaped rubber strips including nine markers, were placed on the top of the supine positioned phantom or the volunteer. The MCG markers were digitized four times and the average set was calculated. The RMS error was calculated as an mean value of the RMS errors between digitized sets and the average set. Next the marker positions were stamped to the surface of the phantom or the volunteers skin. Also the stamped positions were digitized four times and the RMS error was calculated similarly than for the MCG marker digitizations. Global measurement procedure was repeated three times and the mean value of the three computed RMS errors were calculated.

### 2.4.2 Study B

The error caused by the alignment of the volunteer was studied next. The stamped positions from the skin of the supine positioned volunteer were digitized four times and the average set was calculated. Thereafter the volunteer arose from bed and get back into supine position for repeating the digitization procedure. Average sets were registered and the RMS error between them calculated. The global measurement procedure was repeated three times and the mean RMS error was calculated. This mean RMS error also included the error of reproducibility of the 3-D localization (study A) and it was subtracted from the computed error to get an estimate of the RMS error caused by the alignment of the volunteer.

### 2.4.3 Study C

The error of repositioning the MRI markers to the stamped positions of the surface of the phantom or the skin of the volunteer was studied next. The MRI markers were attached to the surface of the phantom or the skin of the volunteer and markers were digitized two times and the average set was calculated. Then the MRI markers were detached and reattached, and the measurement was repeated. The average sets were registered and the RMS error between them calculated. The global measurement procedure was repeated three times and the mean RMS error was calculated. The computed RMS error contains also the error of reproducibility of the 3-D localization using the digitization pen (study A) and it was subtracted from the computed error to get an estimate of the inaccuracy in repositioning of the MRI markers.

### 2.4.4 Study D

The shapes of the measurement beds were different; the MRI bed was concave while the MCG bed was flat. Two wooden wedge objects with the shape corresponding to the MRI bed were placed under the sides of the volunteer lying on a flat bed. The stamped positions from the skin of the volunteer were digitized two times and the average set was calculated. Thereafter the volunteer arose from bed, wooden wedge objects were removed and volunteer get back into supine position for repeating the digitization procedure. The average sets were registered and the RMS error between them calculated. The global measurement procedure was repeated four times and the mean RMS error was calculated. The error of reproducibility of the 3-D localization (study A) and the error caused by the alignment (study B) was subtracted from the computed error to get an estimate of the error caused by wooden wedge objects.

### 2.4.5 Study E

The inaccuracy of the 3-D localization of the MRI markers from the MR images was studied in phantom experiment. The center of the cross from MRI marker was well visible in the MR images. The detection was done using two versions of an interactive software allowing a) only orthogonal slices or b) orthogonal and oblique slices. The point set located from MR images was registered with the point set digitized from MCG markers and the RMS error between them calculated. The errors due to the reproducibility of the 3-D localization using the digitization pen (study A) and the error arising from repositioning of the MRI markers (study C) were subtracted from the computed error. This measure gave an estimate of the increase of the error due to the 3-D localization of the markers from the images. In addition, this error contained also other error sources due to MR imaging itself.

### 2.4.6 Study F

Target registration error (TRE) was defined with phantom experiment in thorax and in heart area. A set of nine MCG markers and eight other markers, six markers in thorax area and two in heart area, were digitized from the phantom by using digitization pen. MR markers were attached to the same placements and then imaged in MR scanner and located from the images. The digitized nine MCG markers and corresponding set of MR markers were registered and same registration parameters were used for the other eight markers. The TRE was then calculated as mean RMS error of six thorax area markers and respectively for two heart area markers. The global measurement procedure was repeated two times.

## 3 Results

### 3.1 Study A

With *phantom* the mean RMS error of the 3-D localization from MCG markers was 0.5 mm and from the surface of phantom 0.6 mm.

With *volunteer* the mean RMS error of the 3-D localization from MCG markers was 0.9 mm and from the surface of skin 1.2 mm. The average value for the 3-D localization error for the volunteer was 1.1 mm.

The mean RMS error measure for the phantom demonstrated errors arising from different measurement events and from different users of the digitization pen. The error of the measurement device itself is also included in the error. The RMS error was higher with the volunteer than with the phantom because of the errors from the breathing and the elasticity of the skin.

### 3.2 Study B

The RMS error due to different alignments of the volunteer was 1.3 mm, ranging from 0.7 mm to 2.1 mm. The values were relatively low, because: 1) the markers in our protocol were attached in positions which not sensitive to alignment errors, and 2) the error was not cumulative in scalar sense, as mentioned above. The former reason was demonstrated by attaching 9 extra markers on other regions of the thorax, e.g. the shoulders. This increased the RMS error from 1.3 mm to 2.8 mm for the total of 18 markers.

### 3.3 Study C

For the volunteer, the RMS error of repositioning of the MRI markers was 0.2 mm, ranging from 0.1 mm to 0.5 mm. With the phantom, the error increased compared to volunteer result and was 1.9 mm. A probable reason for this was the large size of the markers (4 x 4 cm) which makes their attachment on the curved surface of the wooden phantom difficult.

### 3.4 Study D

The increase of the RMS error because of the wooden wedge objects was 1.9 mm, ranging from 0.8 mm to 2.9 mm. However, the increase of the RMS error was slightly overestimated because the difference in softness of mattress in measurement beds causes also part of the error but it was not considered separately in our measurements. If the locations of the markers were considered separately, lateral markers were clearly lifted up relative to the markers on the sternum.

### 3.5 Study E

The RMS error without oblique slices was 1.5 mm and with oblique slices, the error was 0.5 mm lower. A sum of all error components for the volunteer was 6.0 mm as summarized in **Table 1**. The error values corresponded well to the average RMS error of about 6 mm in our patient studies. With oblique slices the sum of all error components was 5.5 mm. The static RMS accuracy of the digitization system, the error that could be expected from a specific point to be digitized, was specified by the manufacturer to be in normal mode 2.5 mm over a 10.16 cm - 71.12 cm motion box [4]. In our measurements we did use Polhemus equipment in quiet mode-state which utilizes data averaging to increase resolution by up to factor of three over normal mode.

Error source	Human	Phantom
Study A. The reproducibility of the 3-D localization	1.1 mm	0.6 mm
Study B. The error in alignment of the patient	1.3 mm	-
Study C. The error from repositioning of the MRI markers	0.2 mm	1.9 mm
Study D. The effect of different shapes in the measurement beds	1.9 mm	-
Study E. The localization of the MRI markers from the images	1.5 mm	1.5 mm
<b>Sum of all errors</b>	<b>6.0 mm</b>	<b>4.0 mm</b>

**Table 1.** Summary of the registration error sources.

### 3.6 Study F

The TRE error for totally twelve thorax area markers was 5.9 mm and 5.3 mm for four heart area markers. TRE was slightly smaller in heart than in whole thorax area. This was probably because heart area markers are in the central area of the nine MCG and MRI markers which were used to define registration parameters. TRE error of the phantom experiment was slightly bigger than defined RMS error of the markers used to define registration parameters (4.0 mm).

## 4 Discussion

A drastic reduction of the total RMS error was not easy to accomplish because any error sources appeared to dominate. The effect of two error components was, however, fairly easy to compensate: 1) the effect of the measurement bed shape (1.9 mm) was reduced by making a firm support, which copied the shape of the MRI bed. This support could be placed under a patient before digitization of the MCG markers. 2) The use of oblique slices appeared to be superior to orthogonal slices.

Breath holding was used during the MR imaging but not during the 3-D localization of the MCG markers. The breath holding also during the 3-D localizations would reduce the registration error between digitized point sets from MCG markers and reference point sets from MR images. The digitization system itself might have also error while defining digitization points. The effect of the digitization system error will be visible in the localization error of the MRI markers from the images (study E), since point set digitized from MR images does not include it.

TRE error in general is usually bigger than RMS error of the markers that are used to define registration parameters. Still, about 1 mm difference of the heart area TRE error and RMS error of the markers used to define registration parameters (phantom experiment), gives an estimate that heart area registration error of our system is not very big.

In the registration technique that is used in our patient studies there exists several error sources. The five error sources mentioned above explain well the total RMS error of these studies. The results of our analysis are also applicable to other studies requiring registration between two or more imaging facilities on the basis of external markers.

## 5 Literature

- [1] Montonen, J.; Ahonen, A.; Hämäläinen, M.; Ilmonen, R.; Laine, P.; Nenonen, J.; Paavola, M.; Simelius, K.; Simola, J.; Katila, T.: Magneto-cardiographic functional imaging studies in BioMag Laboratory, in Biomag96, Proc. Tenth Internat. Conf. on Biomagnetism, Aine, C. et al., Eds. New York, Springer, 1996, pp. 494 -497
- [2] Arun, K. S.; Huang, T. S.; Blostein, S. D.: Least-squares fitting of two 3-D point sets, IEEE Trans. Pattern Anal. Machine Intell. 9(1987), H.5, S. 698-700
- [3] Pesola, K.; Lötjönen, J.; Nenonen, J.; Magnin, I.E.; Lauerma, K.; Fenici, R.; Katila, T.: The effect of geometry and topology differences in boundary element models on magneto-cardiographic localization accuracy, IEEE Trans. Biomedical Eng., 47 (2000), P. 9, S. 1237-1247
- [4] 3SPACE ISOTRAK II User's Manual, Polhemus Inc., Colchester, Vermont, U.S.A., 1993

# Evaluation and comparison of surface and intensity based rigid registration methods for thorax and cardiac MR and PET images

Timo Mäkelä<sup>1,2,6</sup>, Mika Pollari<sup>1</sup>, Jyrki Lötjönen<sup>3</sup>,  
Nicoleta Pauna<sup>2</sup>, Anthonin Reilhac<sup>4,5</sup>, and Patrick Clarysse<sup>2</sup>,  
Isabelle E. Magnin<sup>2</sup> and Toivo Katila<sup>1,6</sup>

<sup>1</sup> Laboratory of Biomedical Engineering, Helsinki University of Technology,  
P.O.B. 2200, FIN-02015 HUT, Finland

{Mika.Pollari, Timo.Makela, Toivo.Katila}@hut.fi

<sup>2</sup> CREATIS, INSA, Batiment Blaise Pascal, 69621 Villeurbanne Cedex, France  
{Nicoleta.Pauna, Patrick.Clarysse, Isabelle.Magnin}@creatis.insa-lyon.fr

<sup>3</sup> VTT Information Technology, P.O.Box 1206, FIN-33101 Tampere, Finland  
Jyrki.Lotjonen@vtt.fi

<sup>4</sup> Centre d'Exploration et de Recherche Médicales par Emission de Positons,  
Neurological Hospital, 59 boulevard Pinel, F-69003 Lyon, France

<sup>5</sup> McGill University/McConnell Brain Imaging Centre, Montreal Neurological  
Institute, WB-315,3801 University street, Montreal, Quebec, H3A 2B4, Canada  
anthonin@bic.mni.mcgill.ca

<sup>6</sup> BioMag Laboratory, Helsinki University Central Hospital, P.O.B. 503,  
FIN-00029 HUS, Finland

**Abstract.** In this paper an evaluation and a comparison of surface and image intensity based (mutual information, normalized mutual information and correlation ratio) rigid registration methods for cardiac magnetic resonance and positron emission tomography images are presented. In both types of rigid image registration methods, PET transmission image was used as a linking mediator to register corresponding PET emission image to MR image coordinates. Also direct rigid registration of PET emission image to MR image coordinates was tested. Methods were evaluated with simulated and ten patient MR-PET images and with three optimization methods. Results indicated that NMI and CR methods with simplex optimization provided the most robust and accurate results.

## 1 Introduction

Cardiac image registration is a more difficult problem than brain image registration because of the mixed movement of the heart and thorax structures and, also, because the heart exhibits fewer accurate anatomical landmarks than brain. A recent review of cardiac image registration approaches can be found in [1]. Methods are often based on automatic registration of heart or thorax structures [2]. Another category of methods relies on the registration of image intensities. In



the literature, there are very few papers concerning the registration of cardiac or thorax images using modern image intensity based methods such as Mutual Information (MI) or Normalized Mutual Information (NMI) [3], [4], [5]. To our knowledge, Correlation Ratio (CR) has been reported to be used only for brain image registration [6].

In this work we present an evaluation and a comparison of rigid surface and image intensity based registration methods for cardiac Magnetic Resonance (MR) and Positron Emission Tomography (PET). Surface and image intensity based registration methods are both based on the registration of PET transmission image to the coordinates of transaxial MR image to obtain registration parameters to register PET emission image to MR image coordinates. Surface based registration method uses deformable model based automatic segmentation of the thorax and lungs surfaces from transaxial MR and transmission PET image [7]. Surface based registration method was presented in detailed in [2]. Image intensity based methods (MI, NMI and CR) are used as an alternative for surface based registration method. To find the optimum of the algorithms, Powell [8], simplex [8] and grid based [2] optimization methods were used. Methods were evaluated with simulated images and tested with ten patients MR-PET images. The data are presented in Section 2 and methods in Section 3. The registration results are presented in Section 4 and discussed in Section 5.

## 2 Cardiac image data

### 2.1 Simulated data

In order to evaluate the registration methods, a reference PET-MRI data set was build up [9]. Thorax transaxial MR images were acquired on a healthy volunteer with a 1.5 T Siemens Magnetom Vision Imager (Siemens, Erlangen, Germany) at the Cardiological Hospital of Lyon. A series of 15 T1 weighted ECG-gated contiguous transaxial images covering heart area was acquired during breath hold sequence with the body array coil (Fig. 1a). The pixel size and the slice thickness were 0.97 x 0.97 mm and 8 mm, respectively. MR images were segmented and labeled (Fig. 1b). Arms were excluded from the segmentation. The result was inputted into a PET simulator. Simulated PET images (Fig. 1c and Fig. 1d) and original MR image provided the gold standard for registration.

PET transmission and emission images were simulated using the SORTEO (Simulator Of Realistic Three-dimensional Emitting Objects) PET simulator [10], [11]. SORTEO is a Monte Carlo simulator which uses a 3-D realistic phantom based on the segmented MR images into 9 classes (muscle, lungs, liver, fat, spine (bone), heart left ventricle (LV), the cavity of the LV, right ventricle (RV), the cavity of the RV). It takes into account the specific activity and attenuation of each tissue. The Monte Carlo method simulates photons one by one and tracks them until they are detected or lost, accounting then for all the sources of biases and noises. PET emission image simulation was performed using an F-18 radioactive tracer. Fluorodeoxyglucose (FDG) PET imaging is considered

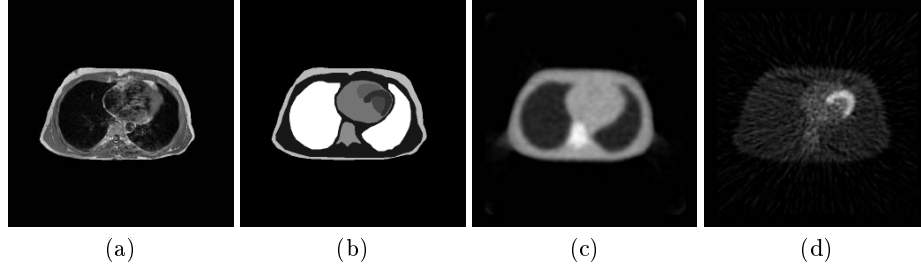


**Fig. 1.** (a) MR image, (b) segmented MR image, simulated PET (c) transmission and (d) emission images.

as a golden standard to determine viable areas of the heart [12]. A PET transmission image simulation was obtained using Ge-68 as an external radioactive source. Reconstructed simulated PET transmission and emission images (FBP with Hanning filter) had pixel sizes and slice thickness of  $3.52 \times 3.52 \text{ mm}^2$  and 2.43 mm, respectively. Both MR and simulated PET images were interpolated (trilinear interpolation) to the same  $256 \times 256 \times 15$  matrix with voxel size  $1.95 \times 1.95 \times 8 \text{ mm}$ . Also isotropic volumes were created with  $256 \times 256 \times 58$  matrix size and  $1.95 \text{ mm}^3$  voxel size.

## 2.2 Patient data

The cardiac patient data consisted of MR and PET images of ten patients suffering from three vessels coronary artery disease, diagnosed with coronary angiography and regional dyskinesia in cineangiograms [13]. All patients underwent MR and fluorine-18-deoxyglucose (FDG) PET imaging within 10 days.

The MR imaging was performed at the Department of Radiology of Helsinki University Central Hospital with a 1.5 T Siemens Magnetom Vision imager (Siemens, Erlangen, Germany). A series of 39 ECG-gated contiguous transaxial images was acquired during free respiration using TurboFLASH sequence (Fig. 2a). The pixel size and the slice thickness were  $1.95 \times 1.95 \text{ mm}^2$  and 10 mm, respectively. Also five ECG-gated breath-hold cine SA sections were also acquired (Fig. 2b). In this work only transaxial images were used.

Static PET imaging was performed using a Siemens ECAT (Siemens/CTI, Knoxville, USA) PET scanner. A series of 16 contiguous transmission and emission images was acquired. The pixel size and the slice thickness were  $2.41 \times 2.41 \text{ mm}^2$  and 6.75 mm, respectively (Fig. 2c, d).

## 3 Methods for PET-MR Image registration

### 3.1 Registration of MR-PET patient images

**Surface based registration** The method for surface based registration for MR and PET images was fully described in [2]. It minimizes the distance between the

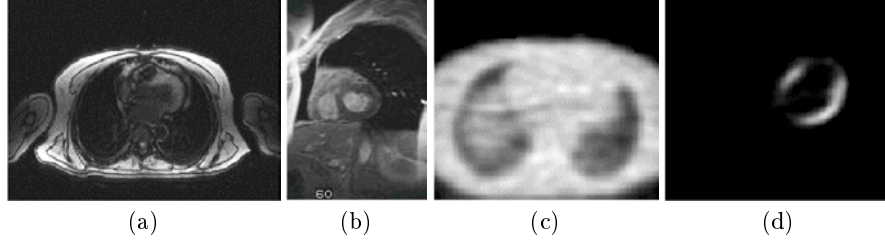


**Fig. 2.** (a) Transaxial and (b) SA MR images, (c) transmission and (d) emission PET images.

point set from segmented PET transmission image surfaces and a distance map [14] built upon the segmented transaxial MR surfaces. The thorax and lungs surfaces are segmented from transaxial MR and transmission PET images by using the deformable model based segmentation method presented in [7]. Here three optimization methods, Powell [8], simplex [8] and non-standard grid based method [2] (notated as grid optimization method in this paper) were used to find minimum of registration algorithms. Grid method evaluates function value iteratively in a user defined amount of points  $T$  and their local neighborhood  $\pm\sigma(t)T$ , where  $\sigma(t)$  is step size for every search direction (6 parameters in rigid registration). The algorithm then chooses from these points the winning nodes ( $N=2$  in this work) for next iteration with smaller local neighborhood. Iterations are repeated until the cost function or local neighborhood reaches a user-predefined value [2].

**Image intensity based registration** Image intensity based method uses MI, NMI or CR measures for registration. The similarity measurements for MI and NMI are described in Eqs. 1-2 as a function of marginal probabilities  $p(a)$ ,  $p(b)$  and a joint probability  $p(a, b)$

$$MI(A, B) = \sum_a \sum_b p(a, b) \log \frac{p(a, b)}{p(a)p(b)}, \quad (1)$$

$$NMI(A, B) = \frac{\sum_a p(a) \log p(a) + \sum_b p(b) \log p(b)}{\sum_{a,b} p(a, b) \log p(a, b)}. \quad (2)$$

The CR measure [6] is based on the minimization of the following Eq.:

$$\mu(A|B) = \frac{Var[E(A|B)]}{Var(A)}. \quad (3)$$

The idea of the image intensity based registration algorithm is similar for the one presented in [15]. Registered images were first scaled and interpolated (trilinear interpolation) by using voxel dimensions. Simulated images had the same dimensions before registration and scaling was not needed. With patient images, PET image was interpolated to isotropic MR image voxel dimensions

with trilinear interpolation. To initialize registration, mass center of the image spaces were registered. During iterative registration procedure, partial volume interpolation was used. Optimization of the registration was done with two standard methods, Powell [8] and simplex [8], and a non standard grid optimization method [2] (see above for a short explanation of grid method). Multiresolution approach was tested with image intensity based registrations, but in practice, only one resolution level was used in this work.

### 3.2 Evaluation method

The evaluation of PET-MR image registration relies on the simulated data set presented in Section 2.1 [9]. Fifty transformations, obtained by randomly sampling the 6 parameter transformation vector, were applied to PET data. The translations were limited to  $\pm 5$  cm along each of the three axis ( $x, y, z$ ) and rotations around each axis ranged between  $\pm 5^\circ$ . The selection of transformations followed Gaussian distribution and obeyed the previous constraints;  $N(0, 1.67)$  cm for translations and  $N(0, 1.67)$  degrees for rotations.

The fifty transformed simulated PET transmission images (and emission images) were registered with the MR images by using the surface or intensity based methods described in Section 3.1. The registration accuracy is evaluated by computing a Root Mean Square (RMS) error on a set of points belonging to the whole image, the thorax, the heart or the LV, respectively. The RMS error was obtained from the equation;

$$RMS = \sqrt{\frac{1}{n} \sum_{i=1}^n \| P_i - \hat{I}(T(P_i)) \|^2}, \quad (4)$$

where  $P_i$  is a voxel-point,  $T(P_i)$  is the transformed voxel-point using the known transformations  $T$ , and  $\hat{I}$  is the evaluated registration transformation calculated using the surface or image intensity based registration method.

## 4 Results

### 4.1 Evaluation using simulated MR-PET image

Results for surface and image intensity based registration using simulated images are presented in Table 1. Evaluation method was described in Section 3.2. Both mean and SDV values of RMS-error (in mm) were calculated for four areas: whole image, thorax area, heart area and LV. Powell, simplex and grid methods were used for optimizations. In the grid based optimizations the search space was limited to  $\pm 5$  cm translations for all 3 directions ( $x, y, z$ ) and  $\pm 5^\circ$  of rotations around all three axis.

**Table 1.** Registration accuracy (RMS-error in mm) of simulated images with surface and image intensity based registration methods. For each optimization method both an average error of all registrations and an average value over successful registrations (marked with \*) are given. The registration was considered to be successful if the registration did reduce RMS error of the misregistered image. Initial misregistrations were selected from gaussian distributions as described in Section 3.2. In the Table, best cases are marked in bold (Surf.=Surface, Pow.=Powell, Simp.=Simplex).

	Image RMS	Thorax RMS	Heart RMS	LV RMS
	<i>Mean <math>\pm</math> SDV</i>	<i>Mean <math>\pm</math> SDV</i>	<i>Mean <math>\pm</math> SDV</i>	<i>Mean <math>\pm</math> SDV</i>
<b>Surf. Pow.</b> (50/50)	22.16 $\pm$ 14.56	15.40 $\pm$ 10.40	11.32 $\pm$ 8.17	11.03 $\pm$ 7.70
Surf. Pow. (43/50)	17.33 $\pm$ 6.97	12.13 $\pm$ 4.63	9.00 $\pm$ 3.55	9.14 $\pm$ 3.91
Surf. Simp. (50/50)	27.32 $\pm$ 14.99	20.90 $\pm$ 12.89	17.45 $\pm$ 12.87	16.90 $\pm$ 13.08
Surf. Simp.* (35/50)	20.23 $\pm$ 7.25	14.82 $\pm$ 5.06	11.92 $\pm$ 5.38	12.08 $\pm$ 6.48
Surf. Grid (50/50)	25.78 $\pm$ 15.16	19.30 $\pm$ 12.31	14.13 $\pm$ 11.63	13.13 $\pm$ 11.57
Surf. Grid* (37/50)	19.31 $\pm$ 8.58	14.24 $\pm$ 6.11	10.27 $\pm$ 4.73	9.94 $\pm$ 5.04
MI Simp. (50/50)	246.24 $\pm$ 184.91	114.82 $\pm$ 89.11	98.55 $\pm$ 105.45	103.05 $\pm$ 113.76
MI Simp.* (5/50)	6.74 $\pm$ 2.50	5.95 $\pm$ 2.71	4.83 $\pm$ 1.52	5.48 $\pm$ 2.30
MI Grid (50/50)	95.21 $\pm$ 37.08	51.17 $\pm$ 21.33	37.54 $\pm$ 29.05	36.42 $\pm$ 30.22
MI Grid* (39/50)	19.72 $\pm$ 6.40	18.07 $\pm$ 8.89	17.59 $\pm$ 7.14	17.41 $\pm$ 6.10
NMI Pow. (50/50)	475.52 $\pm$ 252.88	271.95 $\pm$ 149.71	164.16 $\pm$ 88.96	218.96 $\pm$ 124.45
NMI Pow.* (39/50)	4.88 $\pm$ 2.55	4.11 $\pm$ 2.24	4.33 $\pm$ 2.41	4.42 $\pm$ 2.47
<b>NMI Simp.</b> (50/50)	6.96 $\pm$ 2.40	5.02 $\pm$ 1.32	4.57 $\pm$ 1.43	4.36 $\pm$ 1.89
<b>CR Simp.</b> (50/50)	6.98 $\pm$ 14.89	5.82 $\pm$ 14.60	5.35 $\pm$ 15.48	5.46 $\pm$ 16.05
CR Simp.* (49/50)	4.85 $\pm$ 2.19	3.72 $\pm$ 1.12	3.12 $\pm$ 0.71	3.15 $\pm$ 0.80

## 4.2 Registration of ten MR-PET patient images

Results for ten patient MR-PET image registrations are presented in Table 2. Patient images were first registered with surface or image intensity based registration methods to obtain registration parameters. Registration parameters were then used to transform corresponding manually segmented PET transmission image (point set from PET transmission image surface) to the coordinates of manually segmented MR image. Mean distance of point set from PET transmission image surface and manually segmented MR image surface was calculated using chamfer distance map algorithm [14]. With patient image registrations also three different optimization methods were used (Powell, simplex and grid). Grid optimization used limited search space as in the case of simulated images.

## 5 Discussion and Conclusion

For simulated images CR and NMI image intensity based registrations with simplex minimization (Table 1) had smaller RMS-errors for all areas than biggest voxel size (8 mm in the z-dimension). Best result was obtained using NMI with simplex minimization and mean RMS error of all fifty registrations was for heart

**Table 2.** Registration results of ten patient images for surface and image intensity based registration methods. Error term quantifies the mean distance of the surfaces (manually segmented images) after registration of manually segmented images with the parameters obtained from surface or image intensity based registration methods. In the results which were marked with (\*) some cases were excluded if they were visually unsatisfactorily registered (and mean error was more than 30 mm). Best results are marked in bold.

	$Mean \pm SDV(inmm)$
Surface Powell* (8/10)	$14.23 \pm 2.99$
Surface Simplex* (8/10)	$11.62 \pm 3.73$
<b>Surface Grid</b> (10/10)	$7.46 \pm 2.46$
<b>MI Powell*</b> (9/10)	$7.17 \pm 3.05$
MI Grid* (9/10)	$7.93 \pm 1.67$
MI Simplex* (9/10)	$9.94 \pm 5.50$
NMI Powell* (9/10)	$10.68 \pm 5.62$
NMI Simplex* (9/10)	$9.98 \pm 5.33$
<b>CR Powell</b> (10/10)	$9.85 \pm 5.19$
CR Simplex* (9/10)	$9.60 \pm 5.36$

area  $4.57 \pm 1.43$  mm (mean  $\pm$  SDV). Both NMI and CR with simplex optimization proved also to be very robust; NMI method gave successful registration for all cases and CR method was unsuccessful in only one case. The registration was considered to be successful if the registration did reduce RMS error of the misregistered image (measured from whole image area). MI registration with simplex minimization method was unsuccessful 45 times out of 50. In the case of Powell optimization, both MI and CR registrations methods were unsuccessful every time (not marked in the Table 1) and NMI registration was unsuccessful 11 times out of 50. We added also additional noise (gaussian) to the simulated images (1%, 5%, 10% and 20%) and tested image intensity based methods. The adding of gaussian noise seemed to increase registration accuracy and robustness especially with MI and NMI registration methods. Additional noise might smooth the cost function and thus improve registration results. In the image intensity based registration methods there can also be small interpolation effects which can also effect to the results. We tested the method presented by Holden *et al.* [16] to reduce interpolation errors. However, the effect of interpolation error seemed to be small compared to the registration error.

Results of the surface based registration with simulated images (Table 1) showed that the mean registration error for surface based method was greater than the voxel size of the registered images (8 mm in the z-direction) with all optimization methods. Best results for surface based registration was obtained with the Powell optimization method with a mean RMS error of  $11.32 \pm 8.17$  mm for the whole heart area (for all fifty cases). Powell optimization was also the most robust optimization algorithm of surface based methods with 43 successful registrations (in RMS sense) over fifty registrations.

When registering emission images (simulated images) directly with MR images using image intensity based methods, only about fifth of the cases succeeded (in RMS sense). When considering all registrations (50/50) error values for heart area were  $61.02 \pm 71.05$  mm,  $66.46 \pm 34.91$ ,  $87.54 \pm 63.25$  for NMI, CR and MI registrations, respectively. With succeeded cases (in RMS sense) errors for heart area were  $7.85 \pm 1.21$  mm (15/50 succeeded),  $6.83 \pm 1.38$  (10/50) and  $8.47 \pm 3.57$  (8/50) for NMI, CR and MI registrations, respectively. With patient images, results were similar (only visual verification was used). Thus, results indicated that the use of transmission image as a linking mediator is more accurate and reliable way to register PET image and MR image. The problem while using PET transmission image as a linking mediator to register PET emission image to MR image coordinate is that there might be movement artifacts between (or during) PET transmission and emission imaging. Two transmission images, one before and one after emission imaging, could help to reduce this type of movement artefacts.

Registration methods were also tested using simulated images with isotropic voxel sizes. Original image had  $256 \times 256 \times 15$  matrix size with voxel size of  $1.95 \times 1.95 \times 8$  mm and isotropic image (trilinear interpolation) had  $256 \times 256 \times 58$  matrix size with isotropic voxel size of  $1.95 \text{ mm}^3$ . Best results with isotropic voxel sizes were obtained with NMI ( $2.89 \pm 0.44$  mm) and CR ( $2.89 \pm 0.41$  mm) image intensity based methods (error of all fifty registrations in heart area using simplex minimizations) while with non-isotropic voxel sizes errors were respectively  $4.57 \pm 1.43$  (NMI) and  $5.35 \pm 15.48$  mm (CR). With surface based registration the registration error in heart area (all fifty cases with grid minimizations) was for isotropic voxel size image  $8.23 \pm 2.28$  mm and with non-isotropic voxel sizes image  $11.32 \pm 8.17$  mm. Results indicated, that the use of isotropic voxel sizes might help both image intensity and surface based registration methods. However, execution time of registration with image intensity based method was with isotropic voxel sizes about five times more than with original image dimensions.

When using intensity based methods, the registration time of  $256 \times 256 \times 15$  matrix size simulated images was about 25 minutes with grid minimization and about 4 minutes with Powell and simplex minimizations (1.3 GHz PC). In surface based registration of simulated images, the registration time of Powell and simplex optimizations was 1-3 seconds and for the grid optimization about 1 minute. With surface based registration method a point set of about 1000 points from surface or PET transmission image was registered with MR image surface. Surface based registration needed also automatic segmentation of the MR and PET images which both took about 3 minutes for both MR and PET images.

For patient image registration we estimated in our previous work [2] the quality of surface based registration method using surface distance error after registration. Deformable model based segmentation of surfaces was used for both defining surface based registration parameters and for calculating the surface distance error after registration. Surface distance error with grid optimization was  $2.8 \pm 0.5$  mm. In this work, we also used deformable model based method for segmentations of patient images and to obtain surface based registration



parameters, but resulting registrations parameters were then used to transform corresponding manually segmented PET transmission images (point set from PET transmission image surface) to the coordinates of manually segmented MR images. The distance error term of registered manually segmented images was then calculated (Table 2). The computed surface distance error term quantify also the difference between segmentation results of PET and MR thorax images but gives also a reasonable index of the quality of the patient image registration. Results of surface distance errors of patient images indicated that image intensity based methods performed all pretty well but CR with the Powell optimization was the most robust. Results with simulated images and patient images were a little bit contradictory with Powell optimization methods (Powell optimization did not work well with simulated images). MI registration did not work well with simulated images but did perform well with patient images. The noise in the patient MR and PET images might smooth the cost function of MI and help it not to be attracted to a local minima. With surface based registration of patient images grid based optimization gave smallest error values and was also the most robust. Probable reason for this was the limited search space of grid optimization allowing only reasonable results. Results of image intensity based CR method with Powell optimization and surface based registration method with grid optimization were also visually satisfying in 9 of the 10 cases. In one PET image registration, unexpected artifacts in the PET emission image was observed and the visual assessment of that registration result was difficult to confirm; the PET transmission image was visually well registered also in that case.

Image intensity based methods do not need *a priori* extraction of registered structures (e.g. segmentation of surfaces) and are thus promising methods for the automatic registration of images. Still, image intensity based methods need *a priori* knowledge of the nature of registered images to find proper cost function and optimization method for registration. Surface based methods can be sometimes efficient methods when registered structures are clearly visible and easy to segment. For cardiac MR and PET image registrations, it seems that NMI and CR methods with simplex optimizations are more reliable than MI or Powell optimizations. Patient and simulated image registration results were nevertheless slightly contradictory, especially with MI registrations. Surface based methods, with optimization methods allowing limited search space, gave also robust results. Limited search space could also be used with image intensity based registration methods. Also elastic transformations would be good to use e.g. to reduce the effect of breathing in the registration of patient images and will be considered in our future studies.

## References

1. Mäkelä, T., Clarysse, P., Sipilä, O., Pauna, N., Pham, Q., Katila, T., Magnin, I. E. A review of cardiac image registration methods. *IEEE Trans. Med. Imaging*, **21** (2002) 1011-1021.

2. Mäkelä, T. J., Clarysse, P., Lötjönen, J., Sipilä, O., Lauerma, K., Hänninen, H., Pyökkimies, E.-P., Nenonen, J., Knuuti, J., Katila, T., and Magnin, I. E. A new method for the registration of cardiac PET and MR images using deformable model based segmentation of the main thorax structures. In Niessen, W. and Viergever, M., editors, *Lecture Notes in Computer Science 2208:MICCAI01*, (2001) 557–564.
3. Carrillo, A., Duerk, J., Lewin, J., Wilson, D. Semiautomatic 3-D image registration as applied to interventional MRI liver cancer treatment. *IEEE Trans. Med. Imaging* **19** (2001) 175–185.
4. Slomka P. J., Dey D., Przetak C., and Baum R., Automated nonlinear 3-D registration of 18-F FDG wholebody PET with thoracic CT, *J. Nucl. Med.*, **42**:5 (2001) 11P.
5. Zhenghong, L., Berridge, M.S. PET imaging-based evaluation of aerosol drugs and their delivery devices: nasal and pulmonary studies. *IEEE Trans. Med. Imaging* **21** (2002) 1324–1331.
6. Roche A. and Pennec X. and Malandain G. and Ayache N.: Rigid Registration of 3-D Ultrasound With MR Images: A New Approach Combining Intensity and Gradient Information. *IEEE Trans. Med. Imaging* **20** (2001) 1038–1049.
7. Lötjönen J., Reissman P.-J., Magnin I.E. and Katila T.: Model extraction from magnetic resonance volume data using the deformable pyramid. *Medical Image Analysis*, **4** (1999) 387–406.
8. Press, W. H., Teukolsky, S. A., Vetterling, W. T., and Flannery, B. P. *Numerical Recipes in C: The art of scientific computing 2nd Edition*. Cambridge Univ. Press, Cambridge, (1992).
9. Pauna N., Croisille P., Costes N., Reilhac A., Mäkelä T., Onuc C., Janier M., Clarysse P. A strategy to quantitatively evaluate MRI/PET cardiac registration methods using a Monte Carlo simulator. Accepted to FIMH2003.
10. Reilhac A., Gregoire M.-C., Costes N., Lavanne, F., Pierre C., Diou A., and Pujol J.-F. A PET Monte Carlo simulator from numerical phantom: Validation against the EXACT ECAT HR+ scanner. In *Proc. IEEE Nuclear Sciences Symposium*, vol 3 (1999) 1527–1531.
11. Reilhac A., Lartizien C., Costes N., Sans S., Comtat C., Evans A.: Accounting for singles rates related phenomena in PET Monte-Carlo based simulations. In *IEEE Nuclear Sciences Symposium*, (2002), in press.
12. Hartiala, J. and Knuuti, J. (1995). Imaging of heart by MRI and PET. *Ann. Med.*, **27** (1995) 35–45.
13. Lauerma K., Niemi P., Hänninen H., Janatuinen T., Voipio-Pulkki L., Knuuti J., Toivonen L., Mäkelä T., Mäkijärvi M. A. , Aronen H. J.: Multimodality MR imaging assessment of myocardial viability: combination of first-pass and late contrast enhancement to wall motion dynamics and comparison with FDG-PET. *Radiology*, **217** (2000) 729–736.
14. Borgefors G.: Hierarchical chamfer matching: A parametric edge matching algorithm. *IEEE Trans. Pattern Anal. Machine Intell.*, **6** (1988) 849–865.
15. Maes F., Collignon A., Vandermeulen D., Marchal G. and Suetens P. Multimodality Image Registration by Maximization of Mutual Information. *IEEE Trans. Med. Imaging* **16**:2 (1997) 187–198.
16. Holden M. and Hill D. and Denton E. and Jarosz J. and Cox T. and Rohlmg T. and Goodey J. and Hawkes D. Voxel similarity measures for 3-D serial MR brain image registration. *IEEE Trans. Med. Imaging* **19**:2 (2000) 94–102.

# Elastic Matching Using a Deformation Sphere

J. Lötjönen<sup>1</sup> and T. Mäkelä<sup>2,3,4</sup>

<sup>1</sup> VTT Information Technology, P.O.B. 1206, FIN-33101 Tampere, Finland  
{Jyrki.Lotjonen@vtt.fi}

<sup>2</sup> Laboratory of Biomedical Engineering, Helsinki University of Technology, P.O.B. 2200,  
FIN-02015 HUT, Finland

<sup>3</sup> CREATIS, INSA, Batiment Blaise Pascal, 69621 Villeurbanne Cedex, France

<sup>4</sup> BioMag Laboratory, Helsinki University Central Hospital, P.O.B. 503,  
FIN-00029 HUCS, Finland

**Abstract.** A novel method is proposed for elastic matching of two data volumes. A combination of mutual information, gradient information and smoothness of transformation is used to guide the deformation of another of the volumes. The deformation is accomplished in a multiresolution process by spheres containing a vector field. Position and radius of the spheres are varied. The feasibility of the method is demonstrated in two cases: matching inter-patient MR images of the head and intra-patient cardiac MR and PET images.

## 1 Introduction

Proper interpretation and comparison of medical volumes from different modalities can be accomplished by transforming all data into common spatial alignment, also referred to as registration [1]. In many cases, a satisfactory solution can be found by using rigid registration, i.e. a volume is only translated and rotated. The registration algorithms can be coarsely divided into three groups which register: 1) a set of landmark points, such as external markers and anatomic landmarks [2], 2) geometric image features, such as edges [3], and 3) image intensity based similarity measures, such as mutual information (MI) [4,5]. Algorithms combining these groups exist too, e.g. Pluim *et al.* [6] used geometric features and intensity based similarity measures.

Elastic registration or matching is required as inter-patient volumes or regions containing non-rigid objects are registered. The goal is to remove structural variation between the two volumes to be registered. Many approaches have been proposed for the problem in recent years [7,8,9,10,11,12]. In the method proposed by Christensen *et al.* [7], physical properties of either elastic solids or viscous fluids were simulated as the model was deformed. The criterion for the deformation was to minimize the difference in voxel gray values between two volumes while constraining the transformation to be smooth. Wang and Staib [8] used intensity similarity combined with statistical shape information. The formulation of the elastic model was similar to the one used by Christensen *et al.* but the information on typical deformations, derived from individuals, was incorporated to guide the deformation. Thirion [9] developed a fast 3D matching method based on Maxwellian demons. The displacement vectors for the model were derived from an optical flow equation and smoothed by Gaussian filtering. MI was utilized in non-rigid registration by Gaens *et al.* [10]. In their approach, neighborhood

regions around each point of a discrete lattice were locally translated so that MI was increased. Then, the calculated displacement, filtered by a Gaussian kernel, was applied to the points in the neighborhood. The process was iterated by decreasing gradually the size of the neighborhood and by using a multiresolution approach. Rueckert *et al.* [11] proposed a method where they applied MI and imposed the smoothness of the transformation to constrain the matching. The deformation of data was accomplished using a free-form deformation (FFD) deformation grid. Collins *et al.* [12] maximized a correlation between voxels in two volumes while simultaneously smoothing the transformation by the average displacement vector around each voxel of interest. FFD was used to deform the model. A multiresolution approach was applied.

If one volume to be registered is an atlas, i.e. a volume where the tissue classes of the voxels are known, the result of elastic matching provides also a segmentation. The use of elastic models or deformable models, such as snakes, in the segmentation is a widely studied field in medical image processing [13].

We propose a method by which a model volume with gray-scale information or an atlas consisting of gray-scale data and a set of triangulated surfaces is elastically matched to a data volume. In order to perform the registration, a weighted sum of three energy components is maximized. The first component is the MI between the images [4] while the second component is derived from the intensity gradients of the images [6]. The third component controls either the smoothness of the transformation [11] or the shape of the surfaces in the atlas [14]. The model is deformed using deformation spheres where the transformation is computed only for the model points inside the spheres. A high number of spheres with varying position and radius is used. In addition, a multiresolution approach is adopted.

## 2 Methods

In this study, the model used is a gray-scale volume taken from an individual. If the segmentation of the objects of interest is available, triangulated surfaces of these objects are incorporated in the model, i.e. the model is an atlas. In practice, the model contains also a gradient volume computed from the gray-scale data using a Canny-Deriche operator.

The multi-resolution approach is adopted. A low resolution volume is produced by Gaussian filtering and subsampling a high resolution volume. The matching is done first at the lowest resolution level. As the maximum energy is attained, the process is repeated for a higher resolution level.

Rigid registration is required before elastic transformation if the two volumes have significantly different initial positions. For reference, the mispositioning of the lungs by 5 cm was, however, recovered by the elastic matching in our tests.

In the following, the gray-scale volume of the model is referred to as a *volume M*, and the data volume taken from a patient, and to which the model is matched, *volume D*. Consequently, a sample point, i.e. a voxel, from the volume  $M$  is  $\mathbf{m} = (m_1, m_2, m_3)$  and from the volume  $D$  is  $\mathbf{d} = (d_1, d_2, d_3)$ . The transformation applied to the sample points in the model volume is denoted by  $\mathbf{T} : (\mathbf{m}_1, \mathbf{m}_2, \mathbf{m}_3) \rightarrow (\mathbf{d}_1, \mathbf{d}_2, \mathbf{d}_3)$ .

## 2.1 Energy Function

The motivation in using more than one energy term is to create an energy function with less local minima and therefore to make matching more robust [6]. The energy components provide complementary information on the matching: the gradient component incorporates spatial information while the regularization of the transformation aims to preserve, in a way, the prior knowledge of the shape of the object.

**Mutual information.** MI measures the degree of dependence between the volumes and . MI is high if the gray-scale value of the voxel in can be estimated with a high accuracy as the gray-scale value of the corresponding voxel in is known. If the gray-scale values of the volumes and are considered random variables and , respectively, the MI, proposed in [4] and denoted here by energy  $E$  , is computed from the equation:

$$E = \sum_{a,} ( , ) g \frac{( , )}{( ) ( )}, \quad (1)$$

where  $( )$  and  $( )$  are marginal probabilities and  $( , )$  is the joint probability distribution.  $( )$  is the probability that the gray-scale value of a voxel is in volume .  $( , )$  is the probability that the corresponding voxels in the volumes and have the gray-scale values and .

**Joint gradient information.** The points in the model should match similarly oriented points in the data. The method used is a simplified version of [6]. The energy component  $E_{grad}$  derived from the gradients is computed as follows:

$$E_{grad} = \frac{1}{\sum_{(m,d)} ( , )} \frac{m}{m} \frac{d}{d} m n( m , d ). \quad (2)$$

where is the number of model points overlapping the volume . Because a minimum of gradients is used in two volumes, the intensity ranges need to be set nearly similar in the both volumes.

Since the gray-scale value of a tissue depends on imaging sequence or imaging modality, the gradients on the edges of the tissue may have opposite directions in different volumes. If this is the case with volumes and , Eq. 2 is modified by taking an absolute value from the dot-product.

**Regularization of transformation.** The transformation  $\mathbf{T}$  can be constrained to be smooth by incorporating the energy component  $E_{model,1}$  [11]:

$$E_{model,1} = \frac{1}{\sum_{i,j}} [(\frac{\mathbf{T}}{2})^2 + (\frac{\mathbf{T}}{2})^2 + (\frac{\mathbf{T}}{2})^2 + 2(\frac{\mathbf{T}}{2})^2 + 2(\frac{\mathbf{T}}{2})^2 + 2(\frac{\mathbf{T}}{2})^2], \quad (3)$$

where the sum is over all voxels in the model volume and is the number of points summed. The energy term is the 3D counterpart of the 2D bending energy associated to a thin-plate metal. To speed up computations only three first terms are used in practice.

Alternatively, if the surface model is available, the smoothness of the transformation can be controlled by constraining the change in the shape of the model surfaces. In our

study [14] where a boundary element template was matched to volume data, various regularization strategies were tested. The method with the aim of preserving the orientation of the model's surface normals was preferred. This method is applied also in this study. The energy component is computed as follows:

$$E_{model,2} = \frac{1}{t} \sum_{i=1}^{tr} \mathbf{n}_i \cdot \mathbf{n}_i^o, \quad (4)$$

where  $t$  is the total number of triangles in the model,  $\mathbf{n}_i$  and  $\mathbf{n}_i^o$  are the deformed and the original directions of the normal of the triangle  $i$ , respectively.

**Total energy.** The model is deformed by maximizing the following energy function:

$$E_{total} = E + E_{grad} + E_{model}, \quad (5)$$

where  $\alpha$  and  $\beta$  are user-defined weight parameters for the energy components.

## 2.2 Model Deformation

In our earlier study [14], a boundary element template was deformed using a FFD grid. Since the relative positions of the control points and the model points can not be arbitrarily chosen, the opportunity to control the transformation is limited. In this work, a volumetric transformation is used but the transformation can be better focused on the regions of interest. The potential of the method to include statistical shape information on the deformation is discussed in Section 4.

All model points, including voxels and surface points, inside a deformation sphere are transformed. The center  $\mathbf{c} = (c_1, c_2, c_3)$  and the radius  $r$  of the sphere can be freely chosen. In practice, a high number of spheres (tens of thousands) are applied sequentially. The transformation vector  $\mathbf{t}$  for a model point at  $(x, y, z)$  inside the sphere is computed as follows:

$$\mathbf{t} = \frac{k \frac{(x-c_1)^2 + (y-c_2)^2 + (z-c_3)^2}{r^2} + 1}{1.0 + k}, \quad (6)$$

where  $\mathbf{t}$  is a movement vector posed to the center of the sphere and  $k$  is a parameter which specifies the sharpness of the weight function. A 2D version of the weight function with  $k = 3$  is visualized in Fig. 1.a.

The vector  $\mathbf{t}$  is chosen in such a way that it maximizes the energy in Eq. 5. In practice, the center of the sphere is displaced to several locations, the model is deformed and energy computed, and the location having the highest energy is chosen. The user can define the number of locations tested ( $n_{lo}$ ) around the center as well as the maximum displacement for the center  $(\Delta c)$ , e.g.  $\Delta c = 0.3$ . The six closest neighbors in 3D are always included in the set of tested locations. In Fig. 1.b, the grid around the center of the sphere, shown by a circle in 2D, represents the search space and visualizes the possible new locations for the center. The locations tested are shown by gray squares and the center by a black square. The motivation for testing several locations is that the simple gradient descent method is known to attach relatively easily to local energy minima or maxima. In this strategy, the energy function is maximized more globally.

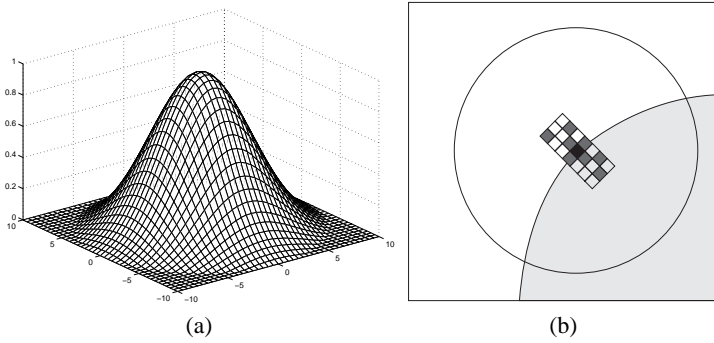


**Fig. 1.** (a) A 2D weight function for the deformation ( $\sigma = 10$ ). (b) A 2D search space visualized in the center of the sphere ( $\sigma_{lo} = 8$ ).

By default, the maximum displacement  $\sigma$  is equal in all directions. In other words, the search space is cubic. However, many methods applying deformable models prefer deformations in the direction of the surface normals. This approach can be followed, if the surface is available in the model. The approach is accomplished as follows. First, define all surface points inside the sphere and compute the average of the surface normals by weighting each normal according to the weight in Eq. 6. Denote the length of the average vector by  $\bar{\sigma}$ . Then, define  $\sigma = \bar{\sigma}$  in the direction of the average and  $\sigma = (1 - \bar{\sigma})$  in orthogonal directions. In Fig. 1.b, the surface is represented in 2D by the contour around the light gray object. Since the average of the surface normals inside the sphere is approximately in the diagonal direction, the value of  $\bar{\sigma} \approx 1$ . Therefore, the search space is highly anisotropic and the diagonal displacements are privileged.

By default, the locations of the spheres are randomly chosen inside the model volume  $V$ . However, if the surface information is included in the model, the locations are randomly chosen at the positions of the surface points. The model should contain surfaces for the regions which are required to be well matched in the final result. For example, if the lung borders are to be segmented from the image, the transformation inside and outside the borders are not of great interest. The use of the surfaces locates the deformation to the most interesting regions, and it speeds up the process because a great part of the volume is excluded, such as background. However, the spheres used at the lowest resolutions levels contain usually the whole or the most of the model, and allow therefore global transformation also for the regions far from the edges.

In the beginning of the deformation, the radius of the spheres is high. As the energy does not change more than a user-specified limit  $\epsilon$  during an iteration, the radius of the sphere is reduced. The user can set the maximum and minimum radius. The number of spheres used in one iteration is relative to the volume of the model divided by the volume of the sphere.



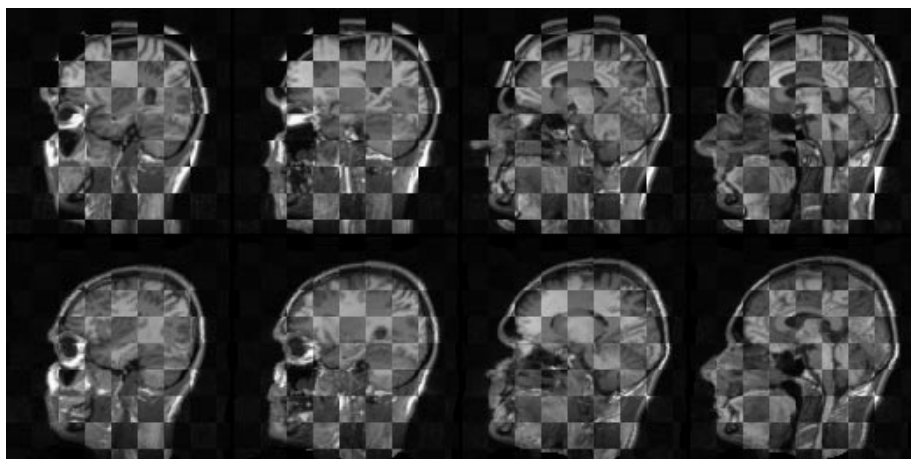


**Fig. 2.** Matching of two T1-weighted MR volumes from the head. The top row shows the model and patient data interlaced before matching and the bottom row after elastic matching.

### 3 Results

The method was developed for two purposes. 1) An automated method was needed by which individualized geometric models can be built for bioelectromagnetic inverse problems from magnetic resonance (MR) images. 2) Elastic matching of cardiac MR and positron emission tomography (PET) images taken from a patient was also needed.

In Fig. 2, the top row shows the original model and patient data interlaced using a chessboard visualization. The bottom row presents the same volumes after the model was elastically matched with the patient data. By visual inspection the edges of anatomic objects appear well aligned after elastic matching, i.e. edges are reasonably continuous between the chess-boxes. The typical run time of the program is 5–15 minutes using a 600 MHz Pentium as the size of the volumes is about  $128 \times 128 \times 100$ . In this case, the surface information was available and four resolution levels were used. The weights used in Eq. 5 were  $w_1 = 2$  and  $w_2 = 10$ . However, the result does not change appreciably as the weight values several times higher or lower are used. The radius of deformation spheres varied from 20 to 6 voxels.

Fig. 3 visualizes a result for cardiac MR-PET matching as the MR volume was the model. The top row shows the volume interlaced before elastic matching and the bottom row after matching. The left ventricle is matched reasonably well, e.g. the matching of the septum is indicated by the white arrows. In this case, the images were not rigidly registered before elastic matching. As the rigid registration is used, the images appear often well aligned already before the elastic transformation. The accurate assessment of the result is difficult because of highly blurred PET images. Therefore, the conditions for the use of elastic matching should be carefully evaluated in future studies.

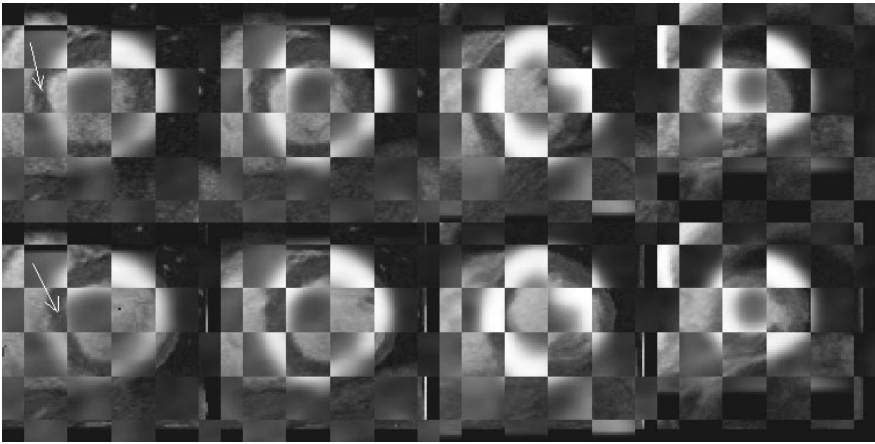


**Fig. 3.** *Matching of cardiac MR and PET volumes from the left ventricle. The top row shows the model and patient data interlaced before elastic matching and the bottom row after matching.*

## 4 Discussion

Elastic matching and segmentation of data volumes is often a pre-requisite for a successful diagnosis and treatment of a patient. This work proposes a method by which this image processing problem can be solved with a reasonable accuracy in a few minutes. So far, the method has been, however, tested only for a few volumes and the results are therefore preliminary.

Although the program allows several parameters to tune the matching, the values do not need to be often varied in practice. Proper parameter values for the energy components depend on imaging modality. If intra-modality anatomic images, such as MRI or computerized tomography (CT), are used, gradient information is weighted more in Eq. 5. However, mutual information should have a major impact on images which have very smooth gradients, such as PET images. The more pathologic the images are, i.e. the images to be matched are highly different or noisy, the more the transformation should be regulated.

Two methods to compute  $E_{model}$  was presented. If a surface is not included in the model, only the smoothness of the transformation can be controlled. If the surface is available, the method regulating the normal directions is recommended, because it makes the run time remarkably shorter.

The method will be further improved by including statistical shape information. This can be done by defining typical transformations for various positions of the model. In the current version of the method, the deformations in the direction of the surface normals are preferred. However, information could be incorporated from test data for which the typical transformations are known, and constrain deformations to typical orientations. In the current version, all transformation vectors inside the sphere are parallel. Typical transformations could be better simulated, if curved transformations inside the

sphere were applied. In addition, more general shapes than a sphere could be used to bound deformation regions, such as a “banana-shaped” object. This would allow constraining the deformation to a more specific region if necessary.

## Acknowledgements

The authors express thanks to The Department of Radiology, Helsinki University Central Hospital, Finland, INSERM Unité 280, Lyon, France, and Turku PET Centre, Turku, Finland for providing volume images. The authors thank also Dr Patrick Clarysse for his constructive comments concerning the manuscript. Research was supported by the National Technology Agency, Finland.

## References

1. J.B.A. Maintz and M.A. Viergever. A Survey of Medical Image Registration. *Med. Image Anal.*, 2(1):1–36, 1998.
2. K.S. Arun, T.S. Huang and S.D. Blostein. Least-Squares Fitting of Two 3-D Point Sets. *IEEE Trans. Pattern Anal. Machine Intell.*, 9(5):698–700, 1987.
3. P.A. Van den Elsen, J.B.A. Maintz, E-J.D. Pol and M.A. Viergever. Automatic Registration of CT and MR Brain Images Using Correlation of Geometrical Features. *IEEE Trans. Med. Imag.*, 14(2):384–396, 1995.
4. F. Maes, A. Collignon, D. Vandermeulen, G. Marchal and P. Suetens. Multimodality Image Registration by Maximization of Mutual Information. *IEEE Trans. Med. Imag.*, 16(2):187–198, 1997.
5. P. Viola and W.M. Wells III. Alignment by Maximization of Mutual Information. *Int. J. Comp. Vision*, 24(2):137–154, 1997.
6. J.P.W. Pluim, J.B.A. Maintz and M.A. Viergever. Image Registration by Maximization of Combined Mutual Information and Gradient Information. *IEEE Trans. Med. Imag.*, 19(8):809–814, 2000.
7. G.E. Christensen, M.I. Miller, M.W. Vannier and U. Grenander. Individualizing Neuroanatomical Atlases Using a Massively Parallel Computer. *IEEE Computer*, January, 1996.
8. Y. Wang and L.H. Staib. Elastic Model Based Non-rigid Registration Incorporating Statistical Shape Information. *Lecture Notes in Computer Science 1496: Medical Image Computing and Computer-Assisted Intervention, MICCAI98*, editors W.M. Wells, A. Colchester and S. Delp, Springer, 1162–1173, 1998.
9. J-P. Thirion. Fast Non-Rigid Matching of 3D Medical Images. *INRIA Report 2547*, 1995.
10. T. Gaens, F. Maes, D. Vandermeulen and P. Suetens. *Lecture Notes in Computer Science 1496: Medical Image Computing and Computer-Assisted Intervention, MICCAI98*, editors W.M. Wells, A. Colchester and S. Delp, Springer, 1099–1106, 1998.
11. D. Rueckert, L.I. Sonoda, C. Hayes, D.L.G. Hill, M.O. Leach and D.J. Hawkes. Nonrigid Registration Using Free-Form Deformations: Application to Breast MR Images. *IEEE Trans. Med. Imag.*, 18(8):712–721, 1999.
12. D.L. Collins, C.J. Holmes, T.M. Peters and A.C. Evans. Automatic 3-D Model-Based Neuroanatomical Segmentation. *Human Brain Mapping*, 3:190–208, 1995.
13. T. McInerney and D. Terzopoulos. Deformable Models in Medical Image Analysis: a Survey. *Med. Image Anal.*, 1(2):91–108, 1996.
14. J. Lötjönen, P-J. Reissman, I. E. Magnin and T. Katila. Model Extraction from Magnetic Resonance Volume Data Using the Deformable Pyramid. *Med. Image Anal.*, 3(4):387–406, 1999.

Kirsi Lauerma, MD  
Pekka Niemi, MD  
Helena Hänninen, MD  
Tuula Janatuinen, MD  
Liisa-Marja Voipio-Pulkki, MD  
Juhani Knuuti, MD  
Lauri Toivonen, MD  
Timo Mäkelä, MSc  
Markku A. Mäkijärvi, MD  
Hannu J. Aronen, MD

### Index terms:

Coronary angiography, comparative studies, 54.1244

Coronary vessels, stenosis or obstruction, 54.76

Magnetic resonance (MR), cine study, 524.12144

Magnetic resonance (MR), comparative studies, 524.121412, 524.121413, 524.12143, 524.12144

Magnetic resonance (MR), contrast enhancement, 524.12143

Magnetic resonance (MR), inversion recovery, 524.121413

Myocardium, infarction, 511.711

Myocardium, PET, 511.12163

**Radiology 2000;** 217:729–736

### Abbreviation:

FDG = 2-[fluorine 18]fluoro-2-deoxy-D-glucose

<sup>1</sup> From the Depts of Radiology (K.L., P.N., H.J.A.), and Medicine, Division of Cardiology and BioMag Laboratory, (H.H., L.T., M.A.M.), Helsinki University Central Hospital (HUCH), Haartmaninkatu 4, 00029 Helsinki, Finland; Dept of Clinical Radiology, Kuopio University Hospital, Finland (H.J.A.); Turku PET Centre, Finland (T.J., L.M.V.P., J.K.); and Laboratory of Biomedical Engineering, Helsinki University of Technology, Finland (T.M.). From the 1999 RSNA scientific assembly. Received Nov 29, 1999; revision requested Jan 14, 2000; revision received Apr 3; accepted Apr 21. Supported by HUCH and Orion research funds, HUCH Foundation, Finnish Cardiac Society, Academy of Finland, and Paavo Nurmi Foundation, Helsinki, Finland. **Address correspondence to** K.L. (e-mail: [kirsi.lauerma@hus.fi](mailto:kirsi.lauerma@hus.fi)).

© RSNA, 2000

### Author contributions:

Guarantors of integrity of entire study, K.L., P.N., H.H., H.J.A. The complete list of author contributions appears at the end of this article.

# Multimodality MR Imaging Assessment of Myocardial Viability: Combination of First-Pass and Late Contrast Enhancement to Wall Motion Dynamics and Comparison with FDG PET—Initial Experience<sup>1</sup>

**PURPOSE:** To combine three magnetic resonance (MR) imaging modalities—dobutamine stress cine, first pass, and late contrast material-enhanced T1-weighted imaging—and to compare the results with 2-[fluorine 18]fluoro-2-deoxy-D-glucose (FDG) positron emission tomography (PET) in the assessment of unviable myocardium in coronary artery disease.

**MATERIALS AND METHODS:** Ten patients with multivessel coronary artery disease underwent MR imaging before and 6 months after bypass surgery. Left ventricular cine MR imaging was performed at rest and during dobutamine infusion. Inversion-recovery gradient-echo images were obtained to study myocardial contrast enhancement at first pass and 5 minutes later. FDG PET was performed with orally administered acipimox before surgery.

**RESULTS:** With dobutamine cine MR imaging, unviable myocardium was detected with a sensitivity of 79% and a specificity of 93%; postoperative wall thickening was the standard. First-pass analysis increased these values to 97% and 96%; analysis of late enhancement with T1-weighted imaging, to 62% and 98%. FDG PET had a sensitivity of 81% and a specificity of 86%.

**CONCLUSION:** The combination of first-pass enhancement analysis and wall motion assessment with stress significantly increases the specificity of MR imaging in the detection of unviable sectors.

Assessment of myocardial viability with a clinical magnetic resonance (MR) imager would increase the feasibility of MR imaging in coronary artery disease. Dobutamine stress cine imaging has been used for both ischemia induction (1) and viability assessment (2). Compared with echocardiography, MR imaging is more accurate in viability assessment because MR images can be acquired with reproducible quality independent of the examiner or patient anatomy (3). First-pass contrast enhancement with the use of T1-weighted fast sequences has shown promise in the detection of ischemia and infarction (4), especially when combined with pharmacologic stress and the administration of dipyridamole (5) or adenosine (6), which specifically increase coronary artery flow. Contrast enhancement on T1-weighted images of acutely infarcted myocardium in patients was reported in 1988 (7), but this phenomenon has not been used for clinical purposes. The combination of these techniques at one MR imaging session has been tested in only a few recent studies (8–10).

The purpose of our study was to determine the effect of the addition of information

from first-pass MR imaging and from late enhancement on T1-weighted images to dobutamine stress cine imaging. We compared MR imaging results to those obtained with 2-[fluorine 18]fluoro-2-deoxy-D-glucose (FDG) positron emission tomography (PET), a method that has been shown to depict unviable myocardium with great accuracy (11). Left ventricular wall thickening was assessed with MR imaging 6 months after bypass surgery, and the findings of wall thickening at rest were used as the standard.

## MATERIALS AND METHODS

### Study Protocol

The study protocol was approved by the local ethics committee. Ten consecutive patients with multivessel coronary artery disease and regional wall motion abnormality depicted at angiography and with need of revascularization were included. FDG PET and MR imaging were performed within 10 days. All patients underwent bypass surgery after imaging. Six months after surgery, MR imaging was repeated for assessment of myocardial response to revascularization.

### Patients

Informed consent was obtained from all patients before they entered the study. The mean age of the patients was 69 years (range, 64–71 years); eight were men, two were women. Four patients belonged to group III, five to group II, and one to group I according to the New York Heart Association functional classification. Seven patients had a history of myocardial infarction, and the mean time from last infarction to MR imaging was 16 months (range, 3–60 months). In addition to coronary artery disease, patients had diabetes ( $n = 3$ ), hypertension ( $n = 2$ ), psoriasis ( $n = 2$ ), and/or hypercholesterolemia ( $n = 1$ ).

### Coronary Angiography and Interpretation of Findings

Coronary angiography was performed with 6-F catheters and imaging in multiple projections. Iobitrol (Xenetix; Guerbet, Aulnay-Sous-Bois, France) with 350 mg of iodine per milliliter was used as the intraarterial contrast material. Left ventricular cine angiograms were obtained in the 30° right anterior oblique projection. The images were interpreted by an experienced angiographer (L.T.). The level and degree of stenosis in the main branches of the coronary arteries were

visually estimated, and reduction in coronary artery diameter of more than 70% was considered significant. The presence of dyskinetic anatomic regions was estimated from left ventricular cine angiograms.

### MR Imaging Protocol

Combined MR imaging was performed in all patients before and 6 months after multivascular bypass surgery. An 18-gauge catheter was inserted into the antecubital vein for dobutamine (Dobutect; Leiras, Helsinki, Finland) infusion and gadopentetate dimeglumine (Magnevist; Schering, Helsinki, Finland) injection. Patients were positioned supine on the table of a 1.5-T imager (Magnetom Vision; Siemens, Erlangen, Germany), and imaging was performed with the body array coil as a receiver. Transverse, oblique sagittal, and double-oblique left ventricular long-axis scout images were obtained to determine the final short-axis imaging plane. A left ventricular short-axis orientation was selected for MR imaging to minimize partial volume effects and to enable comparison between myocardial regions perfused by different arteries and between MR imaging and PET findings.

Blood pressure was monitored before and during dobutamine infusion, and continuous heart rate monitoring was performed during MR imaging. In addition, two-way audio communication and video monitoring of the patient were maintained.

Regional systolic wall thickening was monitored with an electrocardiographically gated breath-hold cine sequence. The imaging parameters for the series were as follows: repetition time msec/echo time msec, 40/4.8; matrix,  $126 \times 256$ ; field of view,  $240 \times 320$  mm; and section thickness, 8 mm. Five short-axis sections 15 mm apart were imaged at rest, and three of these with regional hypokinesia were imaged during dobutamine infusion of 5  $\mu$ g per kilogram of body weight per minute.

To monitor the first transit of bolus injection of contrast agent during dobutamine infusion, electrocardiographically gated, inversion-recovery gradient-echo images were acquired in the same three left ventricular short-axis planes with the following parameters: 3.3/1.4; matrix,  $62 \times 128$ ; field of view,  $240 \times 320$  mm; section thickness, 10 mm; and flip angle, 8°. An inversion time of 400 msec was selected to nullify the myocardial signal before contrast material administration. Perfused with gadopentetate dimeglumine, the myocardium would show rela-

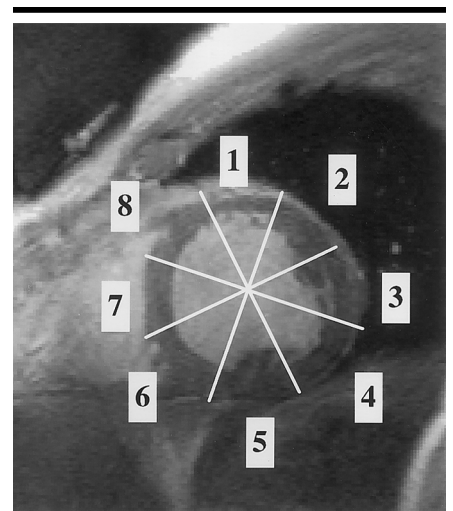


**Figure 1.** Anatomic basis for MR imaging and PET image analysis. Left ventricular short-axis MR images were divided into eight sectors (1–8) in a clockwise fashion by using the interventricular groove as the starting point. On the MR images, systolic wall thickening at rest and with stress, first-pass enhancement, and late enhancement on T1-weighted images were measured in each sector. On PET images, the FDG uptake was determined in corresponding sectors.

tively increased signal intensity because of the predominant T1 shortening.

Sets of 60 images were acquired, with the three sections imaged repeatedly. Each set of images in the three sections was obtained every four to six R-R intervals (approximately 4 seconds), and one inversion-recovery preparation pulse was followed by an imaging sequence for a single section. After the third set of the three sections, gadopentetate dimeglumine (0.05 mmol/kg) was injected intravenously with a rate of 5 mL/sec.

After the first-pass study, dobutamine infusion was discontinued, and 5 minutes later, inversion-recovery gradient-echo images were obtained. Increased signal intensity would be a sign of increased extracellular volume, as in myocardial infarction.

### MR Image Analysis

In each patient, the three left ventricular short-axis sections were divided into eight 45° sectors from the interventricular groove in a clockwise fashion (Fig 1). These sectors were analyzed for systolic wall thickening, first-pass enhancement, and late enhancement with NIH IMAGE 1.59 (Bethesda, Md; available at [rsb.info.nih.gov/ni-h-image](http://rsb.info.nih.gov/ni-h-image)), an image analysis program. One author (K.L.) performed the analysis of each MR modality (enhancement on cine, first-pass, and late T1-

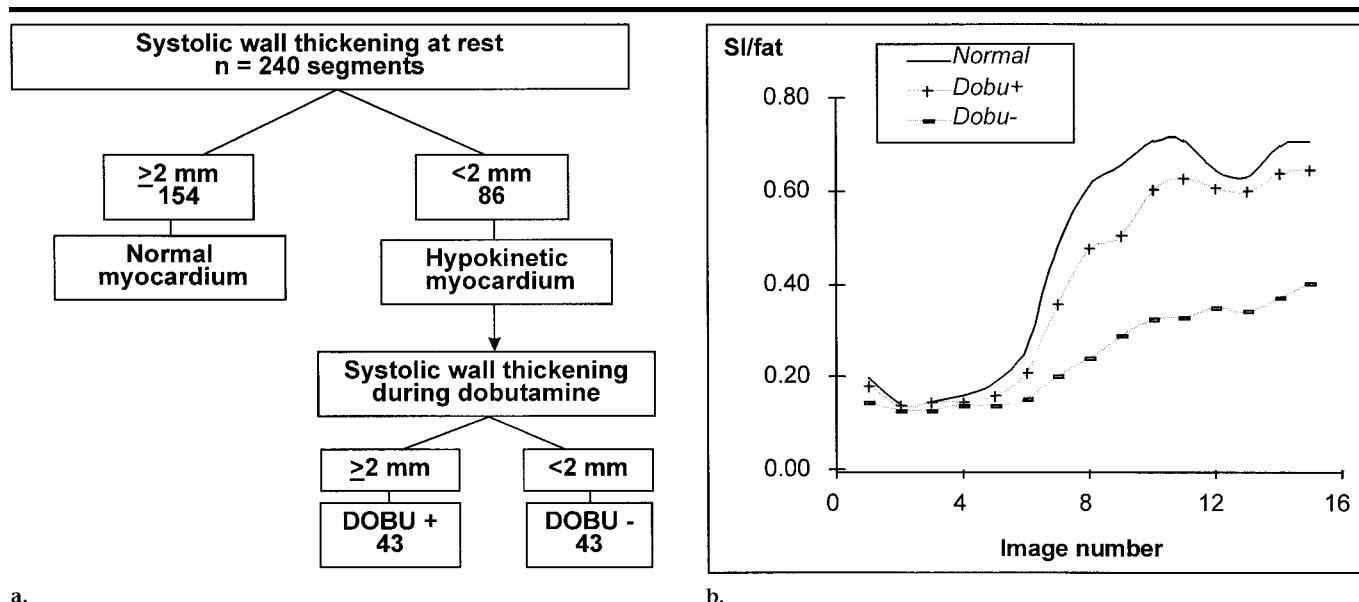


**Figure 2.** Assessment of (a) sectional left ventricular systolic wall thickening and (b) first-pass enhancement. Sectors ( $n = 240$ ) were divided into three groups: normal myocardium (wall thickening  $\geq 2$  mm at rest), *Dobu+* group (wall thickening  $< 2$  mm at rest but  $\geq 2$  mm during dobutamine infusion), and *Dobu-* group (wall thickening  $< 2$  mm at rest and no response to dobutamine). (b) Mean signal intensity-time curves of 43 sectors in each group. Fastest enhancement was observed in normal sectors, and clear hypoperfusion was shown in *Dobu-* sectors. The intensity curve of *Dobu-* sectors differs significantly ( $P < .05$ ) from normal and *Dobu+* curves when tested by using analysis of variance with repeated measures. SI = signal intensity.

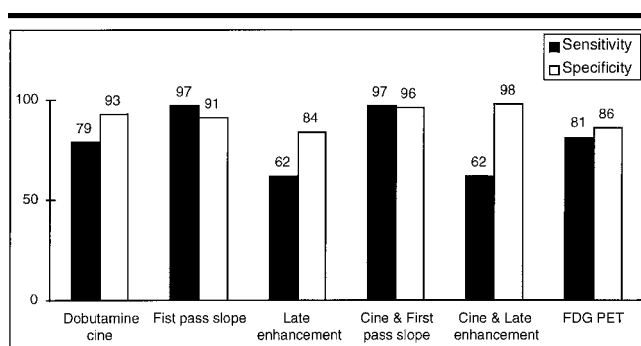


**Figure 3.** Sensitivity and specificity of single and combined MR imaging modalities in the detection of unviable myocardium in patients with regional left ventricular hypokinesia and comparison with FDG PET. Numbers are percentages.

weighted contrast-enhanced images) separately and was blinded to the rest of the results.

### Left Ventricular Systolic Wall Thickening

Diastolic wall thickness for each sector was measured from the first image of the cine sequence; and systolic wall thickness, from the image with the smallest left ventricular chamber volume. Systolic wall thickening was calculated from these values. Sectors were divided into three groups according to systolic wall thickening at rest and during dobutamine infusion.

Sectors with systolic wall thickening of at least 2 mm at rest were considered normal (12). Sectors with systolic wall thickening of less than 2 mm at rest were classified to *Dobu+* and *Dobu-* groups, depending on their response to dobutamine infusion. During infusion, *Dobu+* sectors had systolic wall thickening of at least 2 mm; and *Dobu-* sectors, of less than 2 mm. The hypokinetic sectors (systolic wall thickening  $< 2$  mm) that responded to bypass surgery (systolic wall thickening  $\geq 2$  mm at rest) were classified as hibernating, and those that did not were classified as unviable.

### First-Pass Enhancement

The effect of gadopentetate dimeglumine injection was quantified by measuring signal intensity changes in left ventricular chamber blood, the eight myocardial sectors on each imaged section, and subcutaneous fat. The size ( $40 \text{ mm}^2 \pm 13 \text{ [SD]}$ ; range, 24–71  $\text{mm}^2$ ) and shape of the irregular myocardial regions of interest were kept constant throughout the analysis of each sector, but the sectors were individually traced from image to image because of breathing motion. Signal intensity-time curves were generated for regional first-pass enhancement analysis (Fig 2). The rate of increase in signal intensity in the myocardial sectors was assessed from the upslope of signal intensity-time curves of each perfusion study and was calculated with the equation  $\text{slope} = \text{signal intensity increase} / \text{time}$ , as described previously (5).

### Late Enhancement on T1-weighted Images

The last T1-weighted inversion-recovery gradient-echo images that were obtained 5 minutes after contrast injection were used for the late enhancement analysis. A circumferential 5-mm region of interest was drawn on the myocardium, and care was taken to avoid pixels in the blood pool or epicardial fat. The signal intensity profile was produced by plotting the mean



signal intensity of the three pixels against the angular position (13). The mean plus or minus the SD of signal intensity in the normal myocardium in the lower-intensity region was calculated for each section, and the sectors with a signal intensity of 2 SDs above the mean were classified to represent the areas with larger extracellular volume (Fig 3).

### Left Ventricular Ejection Fraction

All left ventricular short-axis images were planimetered with a mouse-driven cursor, and left ventricular volumes were summed to give the total cavity volume at diastole and systole according to the Simpson rule algorithm.

### FDG PET and Comparison with MR Imaging

All patients underwent FDG PET before bypass surgery (Fig 4). Acipimox (Olbetam, Stabilimento di Ascoli Piceno, Marino del Tronto, Italy; 250 mg) was orally administered to patients 3.0 and 1.5 hours before FDG was injected. Dynamic PET was performed for 60 minutes; the imaging procedure and analysis were described in detail previously (11). FDG was synthesized with an automatic apparatus by using a modified method of Hamacher et al (14). The patients were positioned supine on a 15-section tomograph (Ecat 931/08-12; Siemens/CTI, Knoxville, Tenn) with a measured axial resolution of 6.7 and 6.5 mm in plane, and 250 MBq  $\pm$  35 of FDG was injected intravenously over 30 seconds. Dynamic imaging of the thoracic region was started simultaneously and continued for 60 minutes.

All data were corrected for dead time, decay, and measured photon attenuation. The three myocardial short-axis sections that corresponded to the sections imaged with MR were selected by measuring their distance from left ventricular apex and were divided into eight sectors by one author (T.J.). The sectors were aligned by defining the anterior interventricular groove visible with both imaging methods. Fractional utilization constants of FDG( $K^1$ ) and rates of myocardial glucose utilization were calculated for each sector, and results were compared with viability results obtained from MR imaging. The cutoff value for viability was set to 80% of normal myocardium in the lateral left ventricular wall (11).

### Statistical Analysis

All values were expressed as the mean plus or minus the SD. The significance of differences in signal intensity-time curves,

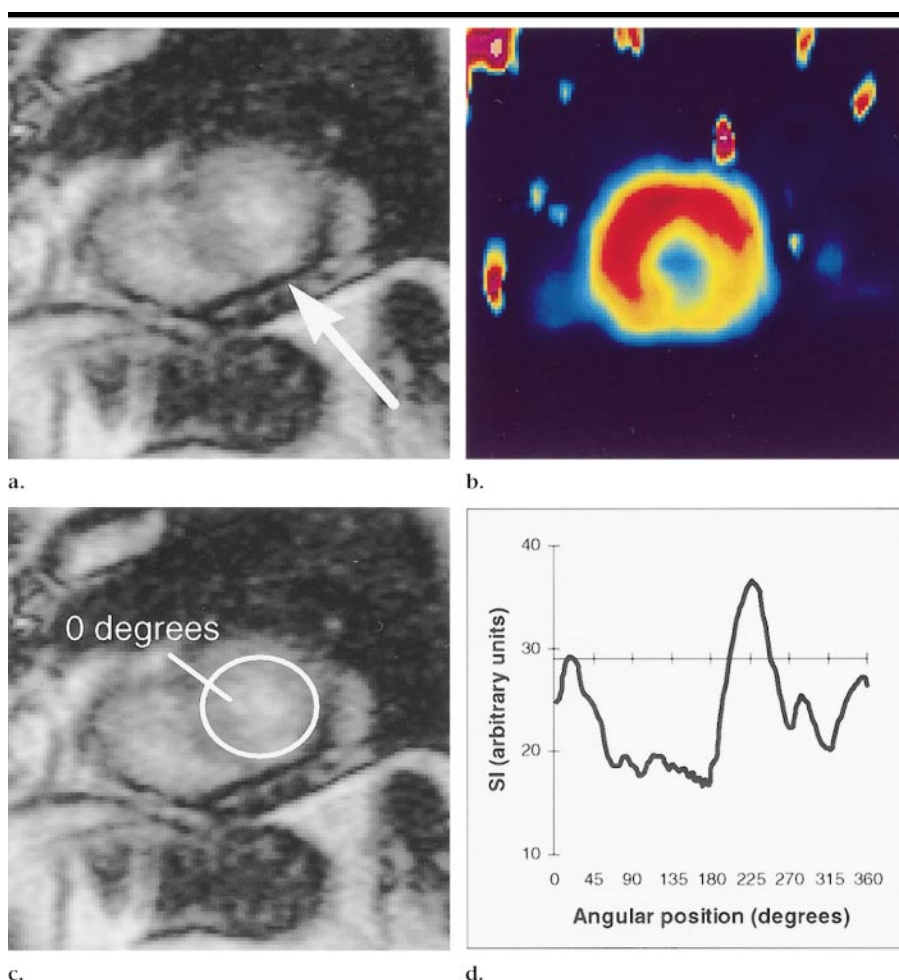


**Figure 4.** Assessment of late enhancement at T1-weighted imaging and comparison with FDG PET. (a, c) Contrast-enhanced T1-weighted MR images were obtained with an inversion-recovery gradient-echo sequence (repetition time msec/echo time msec/inversion time msec, 3.3/1.4/400; flip angle, 8°; section thickness, 10 mm; field of view, 240  $\times$  320 mm; and matrix, 62  $\times$  128.) (a) Image was obtained at the left ventricular short-axis apical level 5 minutes after gadopentetate dimeglumine injection. The arrow indicates the hyperintense zone in the posterior part of the left ventricular wall, which is a marker of larger extracellular volume and possible infarction. (b) FDG PET image shows decreased activity at the same site. (c) Circumferential region of interest was drawn on a from the interventricular groove clockwise to measure the signal intensity, site, and size of the hyperintense zone. (d) Plot of signal intensity (SI) in the circumferential region of interest versus the angular position on the left ventricular wall. The line at 29 arbitrary units indicates the cutoff value calculated as the signal intensity mean plus 2 SD from the value in normal myocardium, and the peak of the curve above it represents the hyperintense zone.

slopes, and late enhancement of sector groups was determined by means of repeated analysis of variance, or ANOVA, measures with multiple comparison of mean values by using the Scheffe  $f$  test. Differences in left ventricular ejection fraction before and after surgery on MR cine images were tested with the paired Student  $t$  test. A significance level of less than 5% was used.

## RESULTS

### Coronary Angiography

At coronary angiography, all patients had at least 70% stenosis in two main

coronary arteries and at least 50% stenosis in the third. On the right anterior oblique projection, all patients had regional dysfunction, six in the posterior wall and four in anterior wall. The mean ejection fraction was 46%  $\pm$  15 (range, 30%–80%).

### MR Imaging

The mean left ventricular ejection fraction measured from short-axis cine sections increased from 44% before to 51% after surgery (ranges, 16%–62% before and 20%–69% after;  $P$  < .004). Systolic wall thickening at rest was normal ( $\geq$



# Anatomic Distribution of False-Positive and False-Negative Sectors in the MR Imaging Assessment of Unviable Myocardium

Location	Dobutamine Stress Cine		First-Pass Contrast-enhanced		Late Contrast-enhanced T1-weighted	
	False-Positive	False-Negative	False-Positive	False-Negative	False-Positive	False-Negative
Apex						
Anterior*	2	0	0	2	9	0
Lateral†	2	0	1	2	5	0
Posterior‡	2	1	0	3	4	2
Middle						
Anterior*	0	1	0	1	3	2
Lateral†	0	0	0	1	2	2
Posterior‡	2	1	0	4	1	1
Base						
Anterior*	2	0	0	2	6	1
Lateral†	0	1	0	0	3	1
Posterior‡	4	2	0	3	1	2

Note.—Data are the number of sectors. Findings at left ventricular cine MR imaging performed 6 months later were used for the standard.

\* 89°–315°.

† 90°–224°.

‡ 225°–314°.

mm) in 154 sectors and hypokinetic (<2 mm) in 86 sectors (Fig 2a). Of the hypokinetic sectors, 43 responded to dobutamine infusion, and 43 did not. Six months after bypass surgery, 211 sectors had normal systolic wall thickening. Twenty-nine were still hypokinetic and were therefore labeled unviable. The 57 preoperatively hypokinetic sectors that had recovered after surgery were labeled hibernating. Figure 3 illustrates the high sensitivity and specificity of dobutamine cine and wall motion analysis (79% and 93%), as well as those of other MR modalities, for the detection of unviable sectors.

The six sectors with a response of at least 2 mm to dobutamine but with no recovery after surgery were observed in four different patients, and the 14 sectors with a response of less than 2 mm to dobutamine but with normal systolic wall thickening after surgery were observed in nine different patients. The majority of the false-positive and false-negative sectors were seen in the posterior left ventricular wall, as listed in the Table. Figure 5 illustrates the depiction of a posterior unviable sector, as confirmed at postoperative cine imaging and FDG PET, with all MR modalities.

First-pass enhancement curves of the sectors that did not respond to dobutamine were significantly lower than those of the sectors that did ( $P = .03$ ) (Fig 2b). As shown in Figure 6a, the slope of the signal intensity–time curve [(intensity change/fat intensity)/seconds] was highest in sectors with normal systolic wall thickening and lowest in sectors with no response to dobutamine ( $P < .002$ ). The range of slopes in normal, hibernating,

and unviable sectors is illustrated in Figure 6b. There was only one unviable sector with a slope of more than 1.0. With a slope of 1 as the cutoff value, sensitivity and specificity in the detection of unviable sectors was 97% and 91% (Fig 3). The 18 viable sectors with slope of less than 1 were seen in seven patients (Table).

There were 52 sectors that had a signal intensity on contrast-enhanced T1-weighted images that was 2 SDs higher than that of normal myocardium. The mean relative signal intensity value in unviable sectors was significantly higher than that of hibernating or normal sectors ( $P < .001$ ) (Fig 6c). The sensitivity and specificity of contrast enhancement on T1-weighted images in the detection of unviable myocardium were lower than those of other MR modalities (Fig 3). The majority of false-positive sectors were seen in the anterior left ventricular wall in all 10 patients, and false-negative sectors were seen in five patients (Table).

The combination of first-pass slope analysis and dobutamine cine systolic wall thickening assessment increased sensitivity and specificity to 97% and 96%, respectively, in the detection of unviable sectors. Late enhancement increased the specificity to 98% but decreased the sensitivity to 62% (Fig 3). In comparison, FDG PET in the same sectors had a sensitivity and specificity of 81% and 86%, respectively.

## DISCUSSION

The question of myocardial viability in coronary artery disease can be answered with the use of scintigraphy and echo

methods, but only with MR imaging can the combination of wall motion, perfusion, and tissue characteristics be assessed with good regional accuracy. Although authors of many review articles (15–17) recommend the use of cine MR imaging in combination with other MR techniques, to our knowledge only a few original reports (8,9) are available. We studied the effect of combining contrast-enhanced MR imaging sequences with low-dose dobutamine cine assessment.

The major finding of this study was the significantly higher first-pass enhancement slope in myocardial hypokinetic sectors that did respond to dobutamine stressing compared with those that did not respond. Also, the slope was greatly decreased in sectors that appeared unviable after bypass grafting. As a single MR imaging modality for assessment of unviable sectors, first-pass imaging provided the best sensitivity and specificity results. Contrast enhancement on T1-weighted images was seen in several sectors that had normal wall thickening or that had recovered after surgery; therefore, this approach should not be used as a single method for viability analysis. The combination of cine, stress, and first-pass imaging was the best approach to MR viability analysis in patients with multivessel coronary artery disease. Compared with FDG PET, multimodality MR imaging had good accuracy in the detection of unviable myocardium.

Our finding that low-dose dobutamine cine imaging and systolic wall thickening assessment depicts hibernating and unviable myocardium with good sensitivity and specificity is in agreement with those of earlier articles (3,18,19). Dobutamine

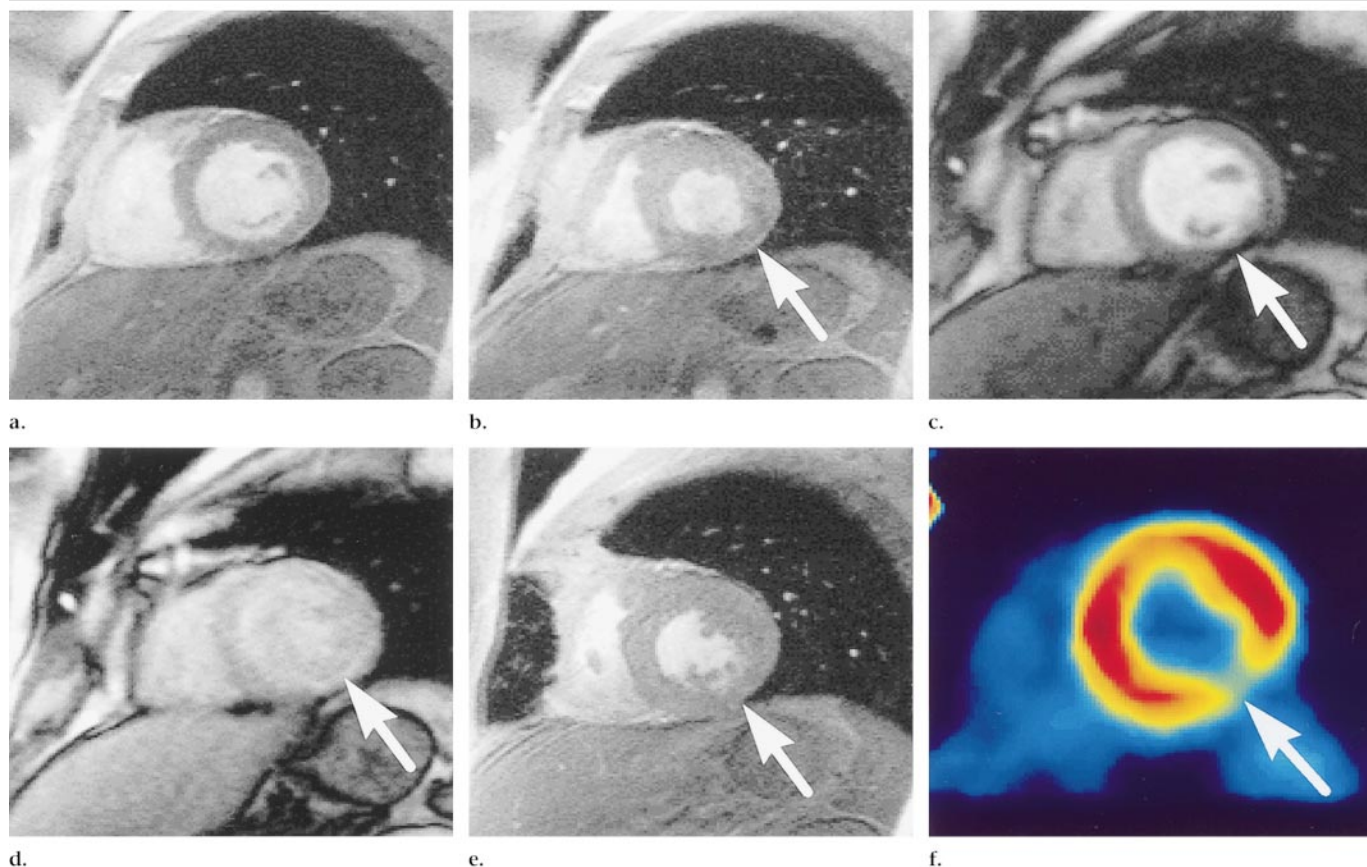


**Figure 5.** Three MR modalities illustrate posterior unviable myocardium in the left ventricular short-axis section imaged at the level of the papillary muscles. (a) End-diastolic cine image. (b) End-systolic cine image obtained during dobutamine infusion. Arrow indicates the site of a nonresponding sector on the posterior wall. (c) First-pass image obtained during early myocardial contrast enhancement. Arrow indicates the sector with a slower-enhancing posterior wall. (d) Arrow indicates the late enhancement in the same sector on this image obtained 5 minutes after contrast agent injection. (e) Image of the same left ventricular short-axis section at end systole obtained 6 months after bypass surgery. There is no recovery of systolic wall thickening in the unviable sector. Arrow indicates the site of the nonresponding sector. (f) Arrow on the PET image indicates low FDG uptake in the corresponding region. (a, b, e) Rest and stress cine images used in the analysis of systolic wall thickening were obtained with an electrocardiographically gated breath-hold sequence (40/4.8; section thickness, 8 mm; field of view,  $240 \times 320$  mm; matrix,  $126 \times 256$ ). (c, d) First-pass MR images and late-enhanced T1-weighted MR images were obtained with an inversion-recovery gradient-echo sequence (3.3/1.4/400; flip angle,  $8^\circ$ ; section thickness, 10 mm; field of view,  $240 \times 320$  mm; and matrix,  $62 \times 128$ ).

infusion with increasing doses does increase the specificity of the wall motion analysis (12), but this method is more time-consuming. On the other hand, first-pass imaging at the single-dose level is fast and requires less image processing and image analysis time.

We found a significant difference in the first-pass enhancement slope of hypokinetic myocardial sectors that did respond to dobutamine when they were compared with the ones that did not and to normal sectors. Similar MR imaging results have not been reported before. We suggest that the difference indicates the dependence of wall motion and perfusion on stress in coronary artery disease. The slope of the enhancement curve is a result of several physiologic factors, such as cardiac output, coronary vasodilatation, and extravasation of low-molecular-

weight contrast agent into the myocardial extracellular space (20). The slope is also dependent on the MR imaging parameters and amount of contrast agent used (21). The slope partly reflects regional perfusion, and, according to our findings, wall motion recruitment is tightly dependent on perfusion reserve.

The unviable sectors had a severely decreased first-pass enhancement slope, which distinguished them from viable sectors, with a good sensitivity and specificity. On the other hand, cine imaging showed the hypokinetic sectors, which would recover after treatment. Therefore, the combination of cine and perfusion imaging would be the best MR imaging tool for use in the assessment of both hibernation and viability. MR cine and perfusion imaging with low-dose dobutamine stressing and contrast material

injection is safe, fast, and feasible, but image analysis without proper postprocessing tools is time-consuming and is the limiting step for clinical applications.

Contrast enhancement on T1-weighted images alone was the least accurate MR modality in detection of unviable sectors. In earlier studies (22), the size of the hyperintense region was larger than the infarction size assessed with control methods. It has been suggested that the tissue surrounding infarction may be edematous and may, therefore, consist of larger extracellular spaces and an increased distribution volume for the contrast agent (23).

In our patients, the enhancement could have been a result of high signal intensity in subendocardial infarction and the surrounding edema. The response to treatment, therefore, would depend on the transmural extent of the infarction (8),

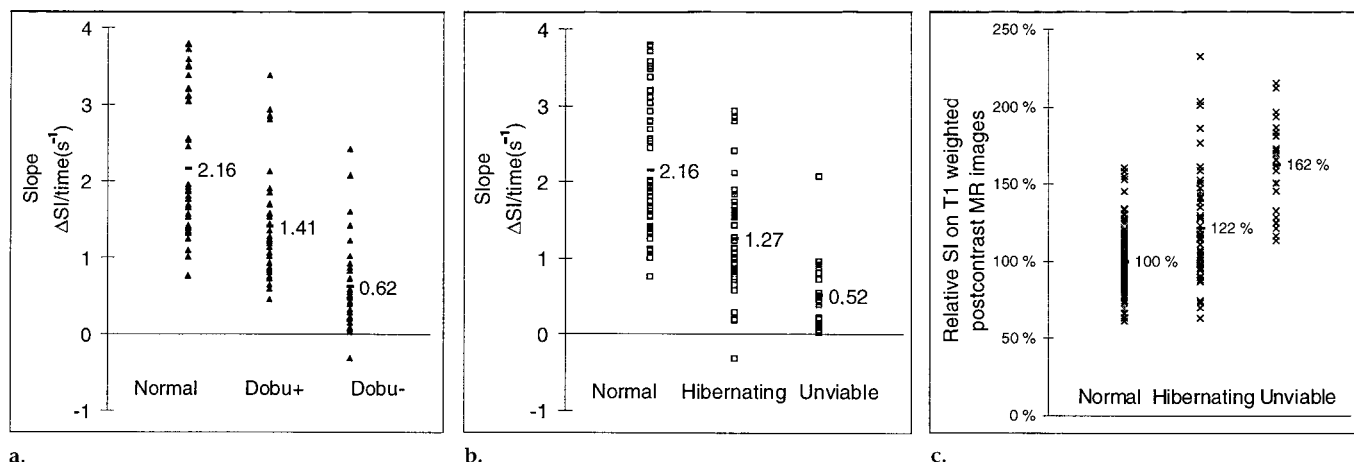


**Figure 6.** Plots show the slope and late enhancement in myocardium during and after the first pass of 0.05 mmol/kg gadopentetate dimeglumine on a series of T1-weighted inversion-recovery gradient-echo (inversion time, 400 msec) images. **(a)** The slope was measured in 43 normal sectors, 43 sectors with decreased (<2 mm) systolic wall thickening at rest that improved by at least 2 mm with low-dose dobutamine infusion (*Dobu+*), and 43 sectors that did not improve (*Dobu-*). The mean in each group is indicated in the plot; the SDs were 0.93, 0.70, and 0.53. **(b)** The slope was measured in 57 normal sectors, 57 sectors that were hypokinetic before but had normal systolic wall thickening after bypass surgery (hibernating), and 29 sectors that were hypokinetic also after surgery (unviable). The mean in each group is indicated in the plot; the SDs were 0.85, 0.73, and 0.43. **(c)** The relative postcontrast enhancement was measured in 57 normal, 57 hibernating, and 29 unviable sectors. The mean in each group is indicated in the plot; the SDs were 18%, 36%, and 30%. *SI* = signal intensity.

which was not assessable with the fast sequence we used. The false-positive sectors on contrast-enhanced images were more often anterior, probably because they were closer to the body array coil. On the other hand, other myocardial diseases such as viral myocarditis (24) and hypertrophic cardiomyopathy (25) have increased signal intensity after contrast agent injection. The high signal intensity on T1-weighted MR images of ischemic myocardium need further study and sector-to-sector comparison with scintigraphic imaging findings.

In the current study, the number of patients was small. Before groups with greater numbers of patients are studied, more automated methods should be developed for quantitative analysis of wall thickening, first-pass imaging, and late enhancement analysis. Because neither angiography nor PET was performed after surgery for control, success in revascularization was not directly assessed. Because first-pass MR imaging with gradient-echo sequences was limited to three left ventricular short-axis sections (5), the entire left ventricular myocardium was not assessed for viability. In the future, faster gradient-echo imaging with inversion recovery (26) or saturation preparation (27), echo-planar sequences (28–30), or a combination of these (31) should be used for whole-heart perfusion and viability imaging.

**Author contributions:** Study concepts, K.L., P.N., H.H., H.J.A., L.M.V.P.; study design, K.L., H.H., H.J.A., L.M.V.P., L.T.; definition of intellectual con-

tent, K.L., P.N., H.H., L.M.V.P., J.K., H.J.A.; literature research, K.L., H.H., T.J.; clinical studies, K.L., P.N., H.H., T.J.; data acquisition, K.L., P.N., H.H., T.J.; data analysis, K.L., T.J., J.K., T.M.; statistical analysis, K.L., T.M.; manuscript preparation, K.L., P.N., H.H., M.A.M., H.J.A.; manuscript editing and review, K.L., P.N., J.K., M.A.M., H.J.A.; manuscript final version approval, all authors.

#### References

- Baer FM, Voth E, Theissen P, Schicha H, Sechtem U. Gradient-echo magnetic resonance imaging during incremental dobutamine infusion for the localization of coronary artery stenoses. *Eur Heart J* 1994; 15:218–225.
- Dendale P, Franken PR, Holman E, et al. Validation of low-dose dobutamine magnetic resonance imaging for assessment of myocardial viability after infarction by serial imaging. *Am J Cardiol* 1998; 82: 375–377.
- Baer FM, Voth E, LaRosee K, et al. Comparison of dobutamine transesophageal echocardiography and dobutamine magnetic resonance imaging for detection of residual myocardial viability. *Am J Cardiol* 1996; 78:415–419.
- Lima JA, Judd RM, Bazille A, et al. Regional heterogeneity of human myocardial infarcts demonstrated by contrast-enhanced MRI: potential mechanisms. *Circulation* 1995; 92:1117–1125.
- Lauerma K, Virtanen KS, Sipila LM, Hekali P, Aronen HJ. Multislice MRI in assessment of myocardial perfusion in patients with single-vessel proximal left anterior descending coronary artery disease before and after revascularization. *Circulation* 1997; 96:2859–2867.
- Cullen JH, Horsfield MA, Reek CR, et al. A myocardial perfusion reserve index in humans using first-pass contrast-enhanced magnetic resonance imaging. *J Am Coll Cardiol* 1999; 33:1386–1394.
- de Roos A, Doornbos J, van der Wall EE, van Voorthuisen AE. MR imaging of acute myocardial infarction: value of Gd-DTPA. *AJR Am J Roentgenol* 1988; 150:531–534.
- Dendale P, Franken PR, Block P, Pratikakis Y, de Roos A. Contrast enhanced and functional magnetic resonance imaging for the detection of viable myocardium after infarction. *Am Heart J* 1998; 135: 875–880.
- Rogers WJ Jr, Kramer CM, Geskin G, et al. Early contrast-enhanced MRI predicts late functional recovery after reperfused myocardial infarction. *Circulation* 1999; 99: 744–750.
- Ramani K, Judd RM, Holly TA, et al. Contrast magnetic resonance imaging in the assessment of myocardial viability in patients with stable coronary artery disease and left ventricular dysfunction. *Circulation* 1998; 98:2687–2694.
- Knuuti MJ, Saraste M, Nuutila P, et al. Myocardial viability: fluorine-18-deoxyglucose positron emission tomography in prediction of wall motion recovery after revascularization. *Am Heart J* 1994; 127: 785–796.
- Baer FM, Theissen P, Schneider CA, et al. Dobutamine magnetic resonance imaging predicts contractile recovery of chronically dysfunctional myocardium after successful revascularization. *J Am Coll Cardiol* 1998; 31:1040–1048.
- Van Rossum AC, Visser FC, Van Eenige MJ, et al. Value of gadolinium-diethylenetriamine pentaacetic acid dynamics in magnetic resonance imaging of acute myocardial infarction with occluded and reperfused coronary arteries after thrombolysis. *Am J Cardiol* 1990; 65:845–851.
- Hamacher K, Coenen HH, Stocklin G. Efficient stereospecific synthesis of no-carrier-added 2-[18F]-fluoro-2-deoxy-D-glucose using aminopolyether supported nucleophilic substitution. *J Nucl Med* 1986; 27:235–238.

15. Kramer CM. Integrated approach to ischemic heart disease: the one-stop shop. *Cardiol Clin* 1998; 16:267-276.
16. van der Wall EE, van Rugge FP, Vliegen HW, et al. Ischemic heart disease: value of MR techniques. *Int J Card Imaging* 1997; 13:179-189.
17. Wilke N, Jerosch-Herold M, Zenovich A, Stillman AE. Magnetic resonance first-pass myocardial perfusion imaging: clinical validation and future applications. *J Magn Reson Imaging* 1999; 10:676-685.
18. Pennell DJ, Underwood SR, Ell PJ, et al. Dipyridamole magnetic resonance imaging: a comparison with thallium-201 emission tomography. *Br Heart J* 1990; 64:362-369.
19. Pennell DJ, Underwood SR, Longmore DB. Detection of coronary artery disease using MR imaging with dipyridamole infusion. *J Comput Assist Tomogr* 1990; 14: 167-170.
20. Arheden H, Saeed M, Higgins CB, et al. Measurement of the distribution volume of gadopentetate dimeglumine at echoplanar MR imaging to quantify myocardial infarction: comparison with <sup>99m</sup>Tc-DTPA autoradiography in rats. *Radiology* 1999; 211:698-708.
21. Canet E, Douek P, Janier M, et al. Influence of bolus volume and dose of gadolinium chelate for first-pass myocardial perfusion MR imaging studies. *J Magn Reson Imaging* 1995; 5:411-415.
22. Lauerma K, Saeed M, Wendland MF, et al. The use of contrast-enhanced magnetic resonance imaging to define ischemic injury after reperfusion: comparison in normal and hypertrophied hearts. *Invest Radiol* 1994; 29:527-535.
23. Inoue S, Murakami Y, Ochiai K, et al. The contributory role of interstitial water in Gd-DTPA-enhanced MRI in myocardial infarction. *J Magn Reson Imaging* 1999; 9:215-219.
24. Friedrich MG, Strohm O, Schulz-Menger J, et al. Contrast media-enhanced magnetic resonance imaging visualizes myocardial changes in the course of viral myocarditis. *Circulation* 1998; 97:1802-1809.
25. Aso H, Takeda K, Ito T, et al. Assessment of myocardial fibrosis in cardiomyopathic hamsters with gadolinium-DTPA enhanced magnetic resonance imaging. *Invest Radiol* 1998; 33:22-32.
26. Fritz-Hansen T, Rostrup E, Ring PB, Larsson HB. Quantification of gadolinium-DTPA concentrations for different inversion times using an IR-turbo flash pulse sequence: a study on optimizing multislice perfusion imaging. *Magn Reson Imaging* 1998; 16:893-899.
27. Penzkofer H, Wintersperger BJ, Knez A, Weber J, Reiser M. Assessment of myocardial perfusion using multisection first-pass MRI and color-coded parameter maps: a comparison to <sup>99m</sup>Tc Sesta MIBI SPECT and systolic myocardial wall thickening analysis. *Magn Reson Imaging* 1999; 17:161-170.
28. Edelman RR, Li W. Contrast-enhanced echo-planar MR imaging of myocardial perfusion: preliminary study in humans. *Radiology* 1994; 190:771-777.
29. Schwitter J, Debatin JF, von Schulthess GK, McKinnon GC. Normal myocardial perfusion assessed with multishot echoplanar imaging. *Magn Reson Med* 1997; 37:140-147.
30. Debatin JF, McKinnon GC, von Schulthess GK. Technical note: approach to myocardial perfusion with echo planar imaging. *Magma* 1996; 4:7-11.
31. Ding S, Wolff SD, Epstein FH. Improved coverage in dynamic contrast-enhanced cardiac MRI using interleaved gradient-echo EPI. *Magn Reson Med* 1998; 39: 514-519.